Benemérita Universidad Autónoma de Puebla

Facultad de Ciencias Físico Matemáticas

Hydrodynamics properties of dark matter

Tesis presentada al

Posgrado en Física Aplicada

como requisito parcial para la obtención del grado de

Doctor en Ciencias

por

Jessica N. López Sánchez

Asesorada por

Dra. Ana A. Avilez López

Puebla Pue.
July, 2023

Benemérita Universidad Autónoma de Puebla

Facultad de Ciencias Físico Matemáticas

Hydrodynamics properties of dark matter

Tesis presentada al

Posgrado en Física Aplicada

como requisito parcial para la obtención del grado de

Doctor en Ciencias

por

Jessica N. López Sánchez

Asesorada por

Dra. Ana A. Avilez López

Dr. Óscar M. Martínez Bravo

Puebla Pue.
July, 2023

A Dali y Leo.

Título: Hydrodynamics properties of dark matter
Estudiante: Jessica N. López Sánchez

COMITÉ

Dr. Cupatitzio Ramírez Romero Presidente	Dra. Irais Bautista Guzmán Secretario
Dra. Tula Bernal Marín Vocal	Dr. Miguel A. García Aspeitia Vocal
Dra. Verónica Lora Castellanos Vocal	Dra. Mercedes P. Velázquez Quesada Suplente
Dra. Ana A. Avilez López Asesor	Dr. Óscar M. Martínez Bravo Asesor

Contents

Acknowledgments **vii**

Abstract **ix**

Resumen **xi**

Introduction **xiii**
0.0.1 Hubble's law . . . xv
0.1 A brief introduction to the history of the universe . . . xvi
0.2 The Standard Model of Cosmology . . . xxiv
0.2.1 Einsten's theory . . . xxiv
0.2.2 Geometry of spatially homogeneous and isotropic universes and the FLRW metric . . . xxv
0.2.3 Dynamics and Evolution of the Background Universe: The Friedmann equations . . . xxvi
0.2.4 Redshift and distances . . . xxvii
0.2.5 Evolution of the species in a FLRW universe . . . xxviii
0.2.6 Cosmic Evolution of the scale factor and the density parameters of species xxix
0.3 The problem of Dark Matter . . . xxx
0.3.1 Formation of the Relic abundance . . . xxx
0.3.2 Observational evidence . . . xxxii
0.3.3 Dark matter tensions . . . xxxv
0.4 Goals and outline of the thesis . . . xxxviii

Bibliografía **xliv**

1 Cosmological perturbations theory and structure formation **1**
1.1 Linear Theory . . . 2
1.1.1 Perturbations Theory . . . 2
1.2 The Boltzmann equation . . . 4
1.2.1 Boltzmann equation for non-relativistic matter . . . 5
1.2.2 Cold Dark Matter . . . 7
1.2.3 Massless neutrinos . . . 7
1.2.4 Photons . . . 8
1.2.5 Baryons . . . 9
1.3 Matter Power Spectrum . . . 9
1.3.1 Transfer function . . . 10
1.4 Evolution of non-linear structures . . . 10
1.4.1 Spherical collapse . . . 10
1.4.2 *The halo model* . . . 11
1.5 Numerical simulations of structure formation . . . 12

1.5.1 The Gadget code . . . 12
1.6 Different types of dark matter . . . 17
1.6.1 Warm Dark Matter . . . 17
1.6.2 Generalized Dark Matter . . . 18
1.6.3 Scalar Field Dark Matter . . . 19
1.7 Dark matter halos properties . . . 21
1.7.1 Navarro Frenk White density profile . . . 21
1.7.2 Zhao profile . . . 22
1.7.3 Soliton profile . . . 23

Bibliografía **27**

2 Study of the properties of dark matter as a non-perfect fluid: GDM model **27**
2.1 The Generalized Dark Matter model . . . 28
2.1.1 Equations of the perturbations . . . 28
2.1.2 Dynamics of gauge-invariant potentials . . . 30
2.2 Structure formation in GDM scenarios . . . 32
2.2.1 Matter Power Spectrum . . . 32
2.2.2 Cosmological parameters and initial conditions . . . 33
2.2.3 Halo Mass Function . . . 34
2.2.4 Stellar mass function . . . 40
2.3 Study of astrophysical systems in GDM scenarios: Hickson Compact Groups . . . 40
2.3.1 Compact groups of galaxies . . . 40
2.3.2 HCG classification criteria . . . 43
2.3.3 Classification algorithms for simulated galaxy catalogs . . . 44
2.3.4 Spatial properties of simulated HCGs . . . 46
2.3.5 Host halos . . . 46
2.3.6 On the relevance of the different filters when identifying HCGs . . . 46
2.3.7 Comparison with observations . . . 50
2.3.8 Time Evolution of simulated HCGs . . . 51
2.4 Conclusions . . . 51

Bibliografía **58**

3 Small-scale system dynamics: SFDM and CDM **59**
3.1 Scalar Field Dark Matter at small scales . . . 60
3.1.1 Time evolution . . . 61
3.1.2 Evolution of a binary configuration . . . 64
3.1.3 Embedded SP configurations inside a Soliton Halo . . . 64
3.2 CDM at small scales . . . 68
3.2.1 Halo stability . . . 68
3.3 Comparison between CDM and SFDM . . . 70
3.3.1 Coarse-graining method . . . 70
3.3.2 Boosted configuration . . . 72
3.3.3 Binary Collision . . . 72
3.4 Conclusions and perspectives . . . 79

Bibliografía **83**

4 Study of galactic systems and their DM properties **83**
4.0.1 Bulge-disk decomposition . . . 84
4.0.2 Scale relations . . . 85
4.0.3 Simulation framework . . . 87
4.1 Machine Learning Algorithms to estimate the mass components of galaxies . . . 90
4.1.1 The Guo's galaxy catalog . . . 90
4.1.2 Description of the algorithms . . . 92
4.1.3 Testing the algorithms performance . . . 93
4.1.4 Comparison with the SDSS catalog . . . 95
4.1.5 Mass-magnitude relation . . . 95
4.1.6 Bulge-disk relation . . . 98
4.1.7 Halo abundance matching . . . 99
4.2 Rotation curves for observational galaxies . . . 100
4.2.1 Stellar velocity maps for galaxies in MaNGA . . . 102
4.2.2 MCMC Method for Rotation Curve Fitting . . . 103
4.2.3 Bulge-disk decomposition . . . 104
4.2.4 Dark matter rotation curve . . . 105
4.3 Fitting different dark matter profiles . . . 107
4.4 Conclusions . . . 107

Bibliografía **114**

5 Conclusions and perspectives **115**

A Some conditions for the ics in cosmological simulations **119**

Bibliografía **118**

B The DBSCAN algorithm **121**

C Numerical methods: Adaptive moving mesh refinement method **123**

Acknowledgments

I wish to express my sincere gratitude to all the people who have been part of my life during this period. I would first like to thank my advisors Ana and Óscar for their time, advice and patience during these four years, for their expert guidance and dedication throught this entire research process. Their support has been invaluable in achieving not only the results presented in this document, but also in the person I am at this moment.
I also want to thank my dissertation committee, for their time, critical review, and valuable suggestions, which have contributed to improve the quality of this work. My thanks are extended to my colleagues and collaborators, who have provided technical support and collaboration at different stages of this research.

At the same time, I want to express my gratitude to the technical staff and the respective institutions that gave me access to advanced computing systems such as Phoebe in CEICO, LNS in BUAP and Laboratorio de Inteligencia Articial de Supercómputo Big Mamma in IFM-UMSNH for providing me with the necessary resources to carry out this research work. Also, I am thankful to CONACYT for the Scholarship Program for Graduate Studies.
Finally, I am thankful to my friends and family for their unconditional support and understanding throughout this process. Believe me, their encouragement and patience have been of great importance in difficult times as well as in moments of joy and celebration.

Abstract

The Standard Model of Cosmology relies on the existence of a dark matter component that drives structure and galaxy formation. However, some tensions at small scales give rise to numerous explanations, many of them related to the nature of dark matter. In this thesis, the effect of different dark matter candidates on the formation and evolution of astrophysical systems has been studied, from a numerical approach. First, the properties of the Generalized Dark Matter (GDM) model were explored, which depends on three free parameters that produce a cut-off effect in the linear matter power spectrum. This condition is reflected in the suppression of small-scale. In particular, the so-called Hickson Compact Groups have been identified in three different scenarios of GDM: GDM I, II, and III. The first one has a very subtle cut-off associated, while the last one has a very pronounced cut at small scales. There are different mechanisms of agglomeration, for those models with a large amount of galaxy-halo self-agglomerate because of their abundance while fewer galaxies need massive halos acting as a dominant potential well. Additionally, a larger amount of compact groups are counted in GDM models in comparison to CDM. This difference suggests that these groups can proliferate within GDM despite the suppressed substructure, which indicates a possible modification in their formation process.

The second part of the work consists of small-scale simulations where the Scalar Field Dark Matter model was used. The first part deals with the implementation of a numerical code to solve the Schrodinger-Poisson system in three dimensions. In addition, some well-known examples are displayed to test the performance of the code. Then an analysis has been carried out to compare the result of the evolution of different assemblies of configurations considering two models of a different nature CDM and SFDM. For that, equivalent conditions must be established, for SFDM a soliton profile was considered while for CDM the density distribution was constructed by fitting the soliton using the Zhao profile. The examples were two central and one off-center collision. In both cases, the movement of the halos is the same, but SFDM shows more effects at the moment of the collision. Such halos, after contact, are more dispersed and also show interference patterns due to the wave behavior of the scalar field. More sophisticated simulations that emulate real astrophysical systems are planned. To do this, it is necessary to explore the dynamics of the galactic components at the observational level.

The last part of this work is related to the analysis of the galactic components from observations. On one hand, different machine learning algorithms were implemented and trained using the *ugriz*-magnitudes derived from Mock catalogs to estimate the mass of the bulge, disk, and halo. This represents an alternative to the methods used at the observational level or in cosmological simulations since there are no strong restrictions for the physics of baryons. On the other hand, the stellar velocity maps from galaxies in MaNGA have been used to reconstruct the total rotation curve. It is necessary to perform the bulge-disk decomposition in order to account for the baryonic contribution and extract the dark matter. Then, the density distribution was computed and fitted using two different density profiles, namely Zhao and Soliton. The analysis of the baryon dynamics at the observational level is necessary to explore the behavior of the density profiles and their parameters associated with isolated galaxies but also for galaxies in a dense environment. This part of the work is still in progress. The purpose is to use this information to construct more realistic initial conditions to perform numerical simulations with different dark matter candidates.

Resumen

El Modelo Cosmológico Estándar está basado en la existencia de una componente de materia oscura que determina la estructura y formación de galaxias. Sin embargo, existen algunas tensiones a pequeñas escalas que dan lugar a numerosas explicaciones relacionadas con la naturaleza del candidato. En esta tesis se ha estudiado, desde un enfoque numérico, el efecto de diferentes candidatos a materia oscura en la formación y evolución de sistemas astrofísicos. En primer lugar, se exploraron las propiedades del modelo de Materia Oscura Generalizada (GDM), que depende de tres parámetros libres que producen un efecto de corte en el espectro de potencia lineal. Esta condición se ve refleja en la supresión de estructuras a pequeñas escalas. En particular, se han identificado los denominados Grupos Compactos de Hickson en tres escenarios diferentes, GDM I, II y III. El primero tiene asociado un corte muy sutil, mientras que el último tiene un corte muy pronunciado a escalas pequeñas. Se ha encontrado que existen diferentes mecanismos de aglomeracion para aquellos modelos que tienen una gran cantidad de subestructura, éstos se auto-aglomeran debido a su abundancia, mientras que aquellos modelos con menos galaxias necesitan halos más masivos que actúan como pozos de potencial dominantes. Además, se encontró un mayor conteo para algunos modelos de GDM en comparación con CDM. Esta diferencia indica que estas agrupaciones pueden prolifear dentro de GDM a pesar de la supresión de subestructura.

La segunda parte del trabajo consiste en el estudio de simulaciones a pequeñas escalas donde se usó el Modelo de Materia Oscura Escalar (SFDM). La primera parte está relacionada con la implementación de un código numérico para resolver el sistema Schrödinger-Poisson en tres dimensiones. Además, se muestran algunos ejemplos conocidos para probar el rendimiento del código. Posteriormente se realizó un análisis para comparar el resultado de la evolución de diferentes ensambles de configuraciones considerando dos modelos de diferente naturaleza CDM y SFDM. Para ello es necesario establecer condiciones equivalentes, para SFDM se consideró un perfil tipo *core* mientras que para CDM se construyó la distribución de densidad ajustando el *core* utilizando el perfil de Zhao. Los ejemplos fueron dos colisiones centrales y una fuera del centro. En ambos casos, el movimiento de los halos es el mismo, pero SFDM muestra más efectos en el momento de la colisión. Dichos halos, después del contacto, están más dispersos y también muestran patrones de interferencia debido al comportamiento ondulatorio del campo escalar. Se planean simulaciones más sofisticadas que emulen sistemas astrofísicos realistas.

La última parte de este trabajo está relacionada con el análisis de componentes galácticas. Por un lado, se implementaron y entrenaron diferentes algoritmos de aprendizaje automático utilizando las *ugriz*-magnitudes, derivadas de los catálogos sintéticos, para estimar la masa del bulbo, el disco y el halo. Esto representa una alternativa a los métodos utilizados en observaciones o simulaciones, ya que no se imponen fuertes restricciones para la física de bariones. Por otro lado, los mapas de velocidad estelar de galaxias en MaNGA se han utilizado para reconstruir la curva de rotación total. Es necesario realizar la descomposición disco-bulbo para tener en cuenta la contribución bariónica y extraer la de materia oscura. Luego, la distribución de densidad se calculó y ajustó utilizando los perfiles de densidad, Zhao y *core*. El análisis de la dinámica bariónica es necesario para explorar el comportamiento de los perfiles de densidad y sus parámetros tanto para galaxias individuales como de ambiente. Esta parte del trabajo aún está en progreso. El propósito es utilizar esta información para construir condiciones iniciales más realistas con diferentes candidatos a materia oscura.

Introduction

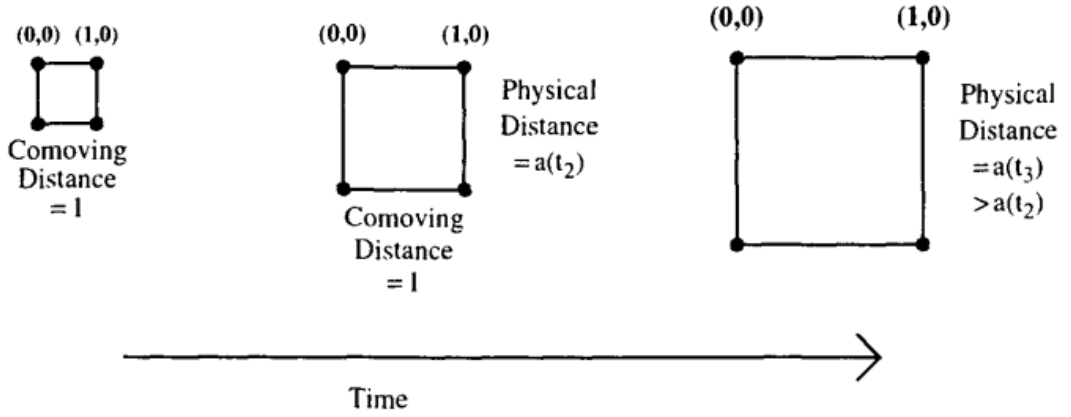

Figure 1: A sketch of the expansion of the universe. The comoving distance between points on the grid as the universe expands. However, the physical distance changes with the scale factor as time evolves. Source [13]

During the last century, the General Theory of Relativity [29, 5] represented one of the most important starting points towards a theory capable to describe the Universe, which can be contrasted to the observations. Subsequently, the discovery of an expanding Universe as well as the extreme conditions in the early epoch, opened a door to explain many questions raised up to that moment, even of philosophical origin. In fact, the *Big Bang* theory rests on three pillars based on the observations: The Hubble Diagram which shows an expanding Universe, the abundance of the primordial elements in accordance with the Nucleosynthesis theory [6] and, finally, the black-body radiation [12] as a footprint of the early stages of the Universe: the Cosmic Microwave Background (CMB) [16]. Subsequent research around these three fundamental pillars, gives rise to theories such as the possible existence of dark matter (and dark energy), the inflation process to generate the first fluctuations, the mechanism to give mass to the neutrinos, or the explanation about the accelerated expansion of the universe [37].

The Standard Model of Cosmology is based on the *Cosmological Principle* under General Relativity, which states that the universe is homogeneous and isotropic. Isotropy implies the universe looks the same in any direction at any point and, thus, there are no special directions. Homogeneity implies that on large scales, the distribution of matter is approximately the same in any region of the universe and, hence, there are no special locations in the universe over scales $R \sim 200h^{-1}$Mpc. Additionally, the model has two main ingredients, the cosmological constant Λ and Cold Dark Matter (CDM). The ΛCDM model is constructed based on the evidence of an expanding universe. This effect is described by introducing the **scale factor** a which describe how the size of the universe is changing with respect to time relative to its size at the current time. To understand this concept, it is convenient to define the *comoving* D_c and *proper* D_p *distances*. The last one is the distance between test particles and it increases over time as the universe expands. On the contrary, the comoving distance remains fixed at all times and can be expressed as $D_p(t) = a(t)D_c$. By convention, at the current cosmological time $a = 1$. In other words, in the present day, both notions of distance coincide. To illustrate these concepts Fig. 1 shows a grid whose coordinates are comoving and therefore, the distances between them are constant. However, the physical distance is proportional to the scale factor and evolves with time.

To measure the variation in the scale factor and its connection to energy, it is useful to establish the concept of the Hubble rate

$$H(t) \equiv \frac{\dot{a}}{a}. \tag{1}$$

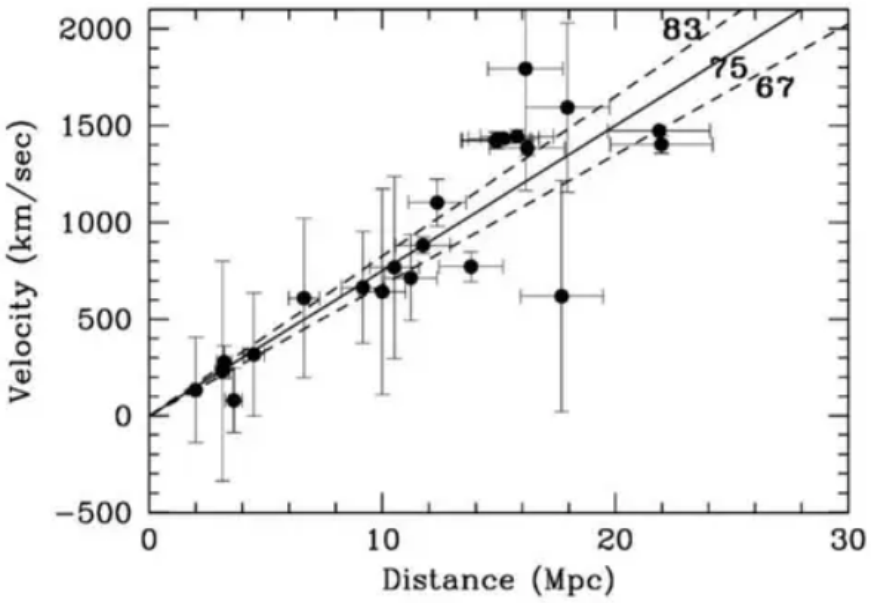

Figure 2: Relation between the recession velocity of Cepheid variable stars and the distance from them to us. The greater the recession velocity, the greater the distance from us. This would indicate that the galaxies are moving away. The points representing the observations follow an approximate shape of a straight line.

0.0.1 Hubble's law

The empirical relation that provides observational evidence for the expansion of the universe is Hubble's law. This relationship states that light coming from distant galaxies is proportional to their distance. Indeed, most of the nearby galaxies are moving away from us. The mathematical expression reads as follows

$$v = H_0 D, \tag{2}$$

where v is the recession velocity due to the redshift, H_0 is the Hubble constant and D is the distance inferred from changes in luminosity by the inverse of the square of distance law. Fig. 2 shows the Hubble law derived using Cepheid stars. The slope of the line represents the Hubble constant.

In order to determine the Hubble constant the Cepheid stars, supernovae type Ia and quasars have played a crucial role. These systems are a type of variable stars that pulsate in brightness with a regular and predictable period. Due to their predictable period-luminosity relationship, such stars act as *standard candles*. The value of H_0 estimated from distance measurements of galaxies is around [31]

$$H_0 = (73.2.4 \pm 0.5)\text{km s}^{-1}\text{Mpc}^{-1}. \tag{3}$$

Alternatively, the Hubble constant can be obtained from measurements from the CMB temperature fluctuations. The precise shape of the curve (known as the acoustic power spectrum) is determined by several parameters, including, for instance, the ratio of baryonic matter and dark matter, and the Hubble constant. The value reported is [1]

$$H_0 = (67.4 \pm 0.5)\text{km s}^{-1}\text{Mpc}^{-1}. \tag{4}$$

The difference between these values may seem small, but it is significant considering the reduced uncertainties in the measurements. This is known as the *Hubble tension* and suggests that there may be some unknown physics or systematic uncertainties affecting the measurements.

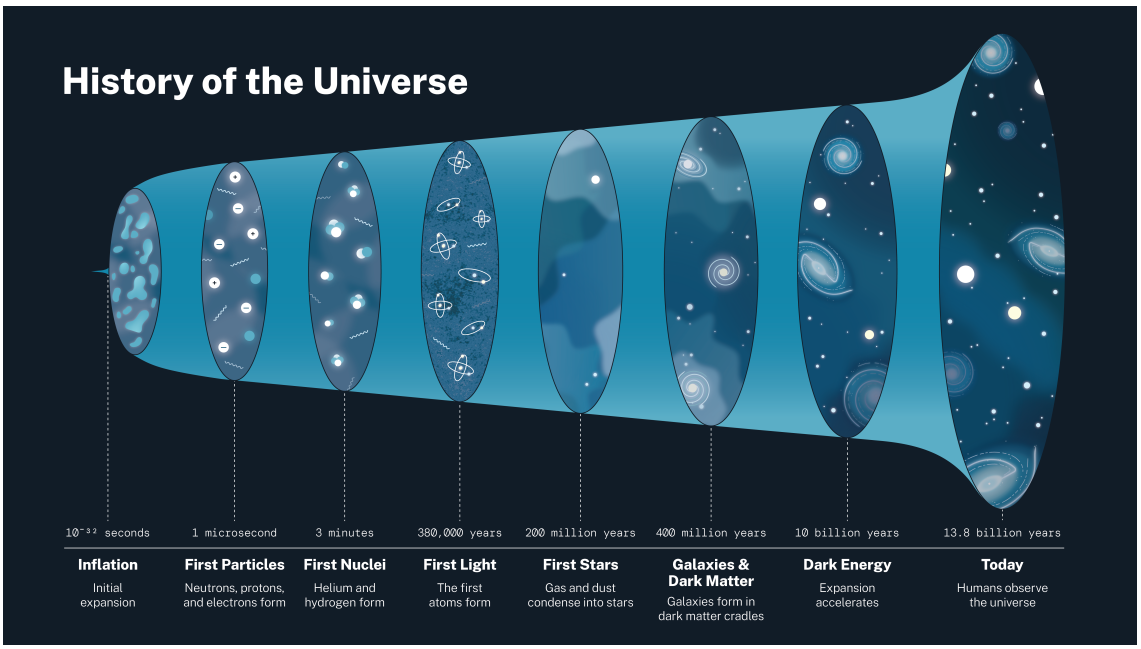

Figure 3: Sketch of the history of the universe, from the inflation period providing the initial expansion to the formation of current galaxies in the epoch of accelerated expansion of the universe. Although the first eras are completely hypothetical cases, since there is no observational evidence, they are important pieces to describe the history of the universe. Source `https://universe.nasa.gov/`.

Due to the difficulties that arise to carry out H_0 measurements, this constant can be parametrized by the scaled Hubble constant h, also known as *little* h, as follows $H_0 = h100\text{km s}^{-1}\text{Mpc}^{-1}$. Leaving h as a free cosmological parameter.

0.1 A brief introduction to the history of the universe

The evolution of the universe can be split into two main regimes, the early universe, and the late universe (see Fig. 3). The first one corresponds to the earliest stages of the universe, shortly after the Big Bang. It encompasses a period of rapid expansion, high temperatures, and the formation of fundamental particles and structures. Then, the late-universe stage refers to the current stage of evolution. Our understanding of these periods is based on theoretical models, observational data, and experiments.

- **The very early universe.** The earliest period of time in the history of the universe is the **Planck epoch**, beyond which the classical General Relativity regime does not apply. At this scale, both Quantum Mechanics and General Relativity are expected to play important roles. Following this epoch, the forces described by the Standard Model of Particles are assumed to be unified, this period corresponds to the **Grand unification era**. Once such a period finishes, it is believed that the strong force is separated from the other fundamental forces, but electromagnetic and weak interactions remain unified. For that reason, this era is known as the **electroweak era**. During this time the conservation of baryon number was violated, resulting in a asymmetry of matter and antimatter. This phenomenon, known as **baryogenesis**. Once the matter dominates over the antimatter in the universe, the next hypothetical epoch proposes a brief period of extremely rapid expansion of the early universe,

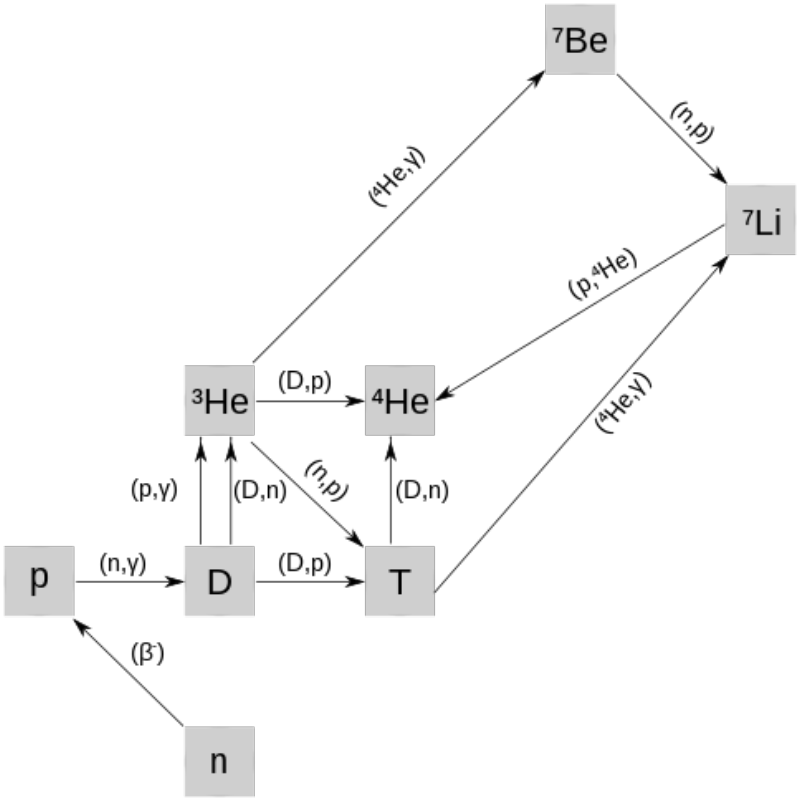

Figure 4: The nuclear chain reactions that played a crucial role in primordial nucleosynthesis involved the fusion of protons and neutrons to form light atomic nuclei. First, the deuterium is formed through the collision between protons. Then, the deuterium fuses with a proton to form Helium-3, which at the same time is capable to form Helium-4. The abundance of helium-4 (He-4) increases significantly during primordial nucleosynthesis. Additionally, a small amount of lithium-7 is produced through the fusion of helium-4 with a neutron. Source `https://commons.wikimedia.org/wiki/File:Main_nuclear_reaction_chains_for_Big_Bang_nucleosynthesis.svg`

inflation. This effect last until the energy density is transformed into normal matter and radiation, a process known as **reheating**.

- **Particle era.** After inflation finishes, the particle era started. In **Quark epoch** the universe was filled with a quark-gluon plasma. Collisions between particles produce baryons and mesons. After that, once the average energy of particle interactions had fallen below the binding energy of hadrons, the following period starts, **the Hadron epoch**. Here, quarks become confined within hadrons due to the strong nuclear force, resulting in the formation of hadrons including protons and neutrons. The formation of hadron/anti-hadrons pairs occurs but also the annihilation reactions, leaving a small residue of them. **The lepton era** immediately followed the hadron. Pairs of leptons and antileptons were created in large numbers, but as the Universe cooled, most leptons were annihilated In that period, the universe was dominated by photons, neutrinos, and electron-positrons pairs. An important aspect is the **neutrino decoupling** where neutrinos became *free-streaming* particles, meaning they ceased to interact with other particles.

- **Primordial Nucleosynthesis.** As the universe expands and cools, it becomes suitable to allow the fusion of protons and neutrons to form atomic nuclei. The primary elements

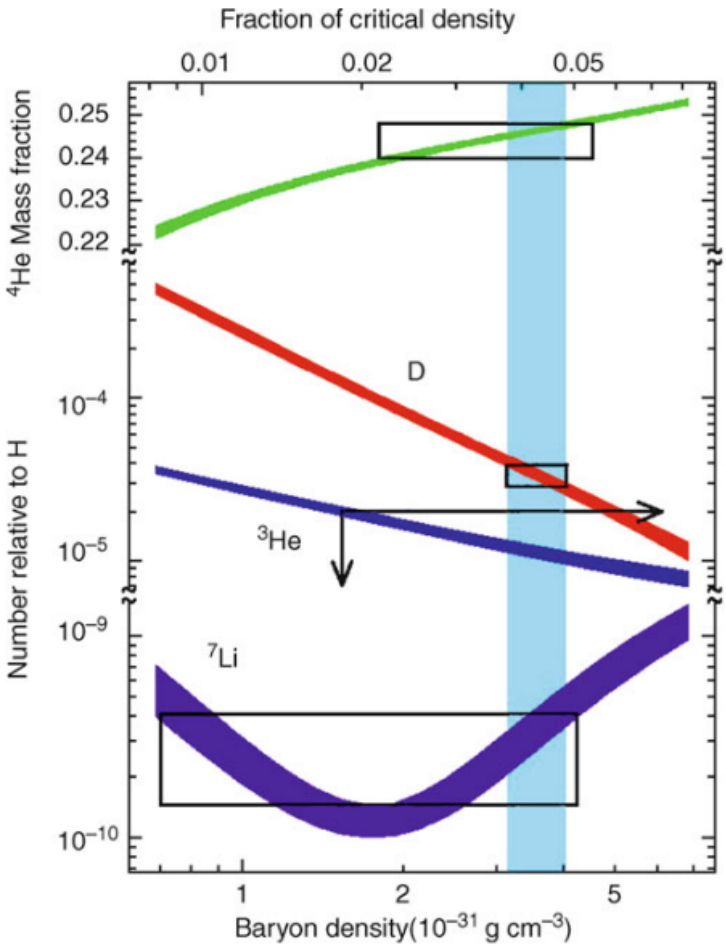

Figure 5: BBN prediction of the abundance of light elements in terms of the current baryon density. The rectangles mark the observed abundances. The vertical blue band corresponds to the value of Ω_b inferred from CMB. Source [32].

produced during nucleosynthesis were hydrogen-1 (protons) and helium-4, along with trace amounts of deuterium, helium-3, and lithium-7. Essentially all of the elements that are heavier than lithium were created much later, by stellar nucleosynthesis in evolving and exploding stars. The creation of new atomic nuclei from pre-existing nucleons (that is protons and neutrons) and nuclei as is shown in 4. The most important reactions are

$$p + e \quad \longleftrightarrow \quad n + \nu, \tag{5}$$

$$p + \bar{\nu} \quad \longleftrightarrow \quad n + e^+, \tag{6}$$

$$n \quad \rightarrow \quad p + e + \bar{\nu}. \tag{7}$$

The first two reactions maintain in equilibrium the proton-to-neutron ratio. After neutrino freeze-out equilibrium reactions become rare because the above reactions are based on weak interactions, the same as those that kept the neutrinos in chemical equilibrium. At the time of neutrino decoupling, we have $\frac{n_n}{n_p} \approx \frac{1}{3}$. When nucleosynthesis started, the simplest

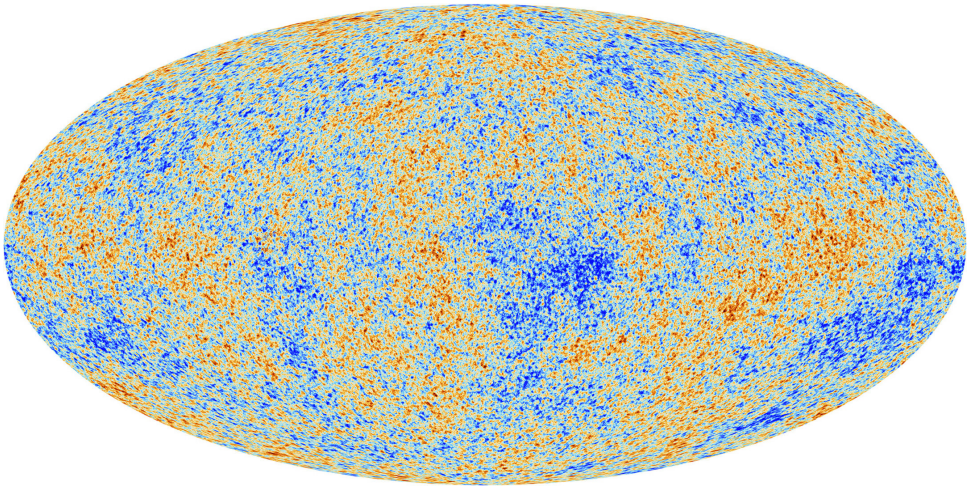

Figure 6: Heat map of the anisotropies in the CMB reported Planck. It show tiny temperature fluctuations that correspond to regions of slightly different densities. Source `https://www.esa.int/Science_Exploration/Space_Science/Planck`.

compound nucleus is the deuterium, whose reaction is described as

$$p + n \leftarrow D + \gamma. \tag{8}$$

The binding energy is $E_b = 2.225$MeV. When the temperature has decreased $k_B T \ll E_b$, the deuterium abundance becomes appreciable and for that moment, the fraction of neutrons has thus decayed, yielding the neutron-proton ratio $\frac{n_n}{n_p} \approx \frac{1}{7}$. After that, most of the neutrons become in deuterium. Once the deuterium density becomes appreciable, the formation of helium-4 started, whose binding energy is $E_h \sim 28$ MeV. At this moment, most of the deuterium is transformed into helium-4. However, due to the fact photons have energy greater than the binding energy of deuterium, this last was formed and immediately destroyed, this process is known as the *deuterium bottleneck*. Therefore, the formation of ^4He was delayed until the universe became cool enough for deuterium to survive. The ratio between the number density of helium-4 and the number of protons at that moment is $\frac{n_{He}}{n_n} = \frac{1}{2}$. The mass fraction of Helium-4, Y, can be expressed as follows

$$Y = \frac{4n_{He}}{4n_{he} + n_H} = \frac{2n_n}{n_p + n_n} = \frac{2(n_n/n_p)}{1 + (n_n/n_p)} \approx 0.25. \tag{9}$$

This expression means that about $\frac{1}{4}$ of the baryonic mass in the universe should be in the form of helium-4. This is a robust prediction of the Big Bang models, and it is in excellent agreement with observations [32]. At this moment, around 25% of the baryonic mass is in the form of helium and 75% is hydrogen with traces of D, helium-3 and lithium-7. Heavier nuclei cannot form because no stable nucleus of mass number 5 or 8 exists and thus no new, stable nuclei can be formed in collisions of two helium nuclei or of a proton with a helium nucleus.

- **Light elements abundance.** One important observational evidences that support the Standard Cosmological Model is the abundance of primordial elements. The $\frac{n_b}{n_\gamma}$ ratio is the key parameter determining the abundances of light elements after nucleosynthesis

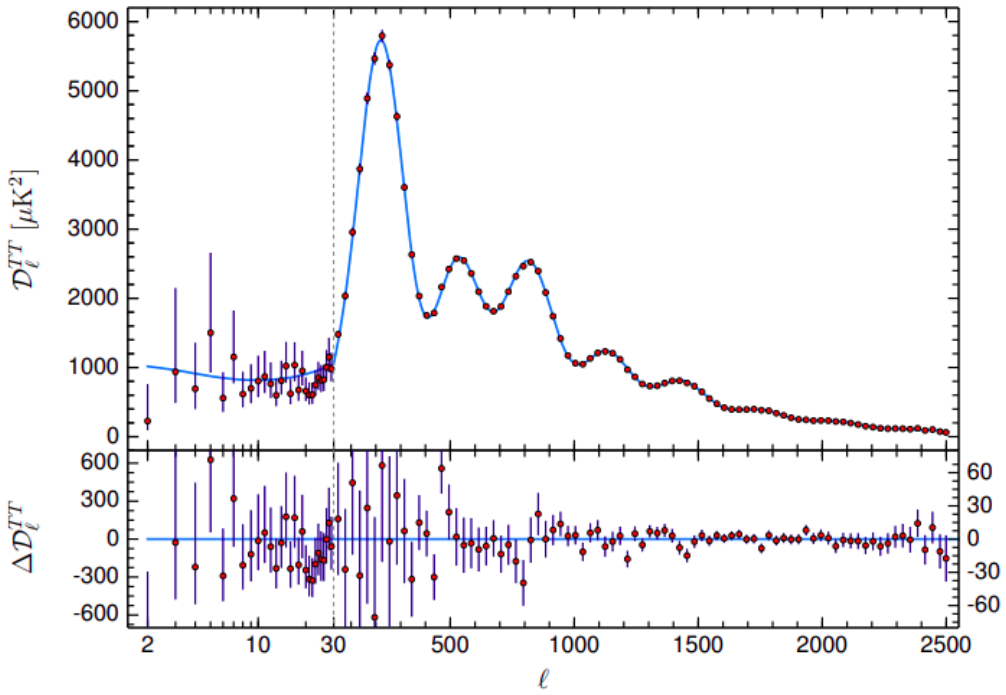

Figure 7: The CMB power spectrum reported by Planck. The green represents the best fit of the Standard Model of Cosmology. While the observations on small and intermediate angular scales agree extremely well with the model predictions, the fluctuations detected on large angular scales on the sky, between 90 and six degrees, are about 10 per cent weaker than the best fit of the model to Planck data. Source [1].

ends. Namely, the higher baryon-photon ratio is leads to a greater number of available baryons for nucleosynthesis, resulting in higher abundances of light elements.

From the measurements of the primordial elements it is possible to constrain the value of Ω_b. In fig. 5 the light elements abundances are shown as well as the regions of measurements. Notice, the baryon density lies well inside all the boxes.

- **Recombination.** At this moment, the universe consists of photons, protons, helium, and traces of other light elements and electrons. Once the universe had cooled enough, the atomic nuclei can capture electrons and form stable neutral atoms. The recombination of electrons and protons had a profound effect on photons in the early universe. Prior to recombination, photons were tightly coupled to the plasma through frequent scattering interactions with free electrons. However, as recombination completes, the number of free electrons significantly decreased. The end of recombination led to the decoupling of photons from matter, allowing them to travel freely through the universe. This is the moment when the universe become transparent leaving as remnant the Cosmic Microwave Background (CMB).

  - **The Cosmic Microwave Background.**
    This CMB radiation was predicted by the Big Bang theory and discovered by Penzias and Wilson in 1964, using an antenna temperature of 3K. Later on, the COBE satellite discovered that primordial temperature fluctuations of order $\frac{\Delta T}{T} = 10^{-5}$ [34] (see Fig. 6).

Theories of the formation of large-scale structure predict the existence of slight inhomogeneities in the distribution of matter in the early universe which underwent gravitational collapse to form galaxies, galaxy clusters, and superclusters. These matter density inhomogeneities lead to temperature anisotropies in the CMB due to regions with slightly higher matter density had a slightly stronger gravitational pull, causing photons to lose more energy (resulting in a cooler temperature), while regions with lower density had a weaker gravitational pull and photons gained more energy, giving a warmer temperature. The temperature anisotropy at a point (θ, ϕ) on the sky can be expressed in the basis of spherical harmonics in terms of multipole moments as

$$\frac{\Delta T}{T}(\theta, \phi) = \sum_{\ell,m} a_{\ell,m} Y_{\ell,m}(\theta, \phi), \tag{10}$$

where the coefficients can be written in terms of the multipole C_ℓ as $\langle a^*_{\ell m} a_{\ell' m'} \rangle \equiv C_\ell \delta_{\ell' \ell} \delta_{m' m}$ and $Y(\theta, \phi)$ term accounts for the fluctuations.

The monopole term essentially represents the average temperature of the CMB, and its temperature is related to the temperature of a blackbody radiator. The monopole term when $\ell = 0$ the $Y(\theta, \phi)$ gives, as a result, $Y(\theta, \phi)$ is reduced to 1. The average temperature around $T_\gamma = 2.275 + 0.0006$ K [17] and the specific intensity is given by

$$I_\nu = \frac{2h^3}{c^2} \frac{1}{\exp\{h\nu/k_B T\} - 1}. \tag{11}$$

The energy density is given by $\rho_\gamma = \frac{\pi^2}{15} T^4 \approx 4.64 \times 10^{-34} g \cdot \mathrm{cm}^{-3}$.

CMB dipole represents the largest anisotropy and corresponds to the first spherical harmonic $\ell = 1$. The dipole term in the CMB is caused by the motion of an observer on Earth with respect to the rest frame of the CMB. Finally, The variations in the CMB temperature maps at higher multipoles ($\ell \leq 2$) are interpreted as being mostly the result of perturbations in the density of the early Universe, manifesting themselves at the epoch of the last scattering of the CMB photons.

In fig 7 the power spectrum of the cosmic microwave background radiation temperature anisotropy in terms of the angular scale is shown made with data from Plack. The position of the first peak in the CMB power spectrum corresponds to a specific angular scale, around one degree, and represents the physical size of the *sound horizon* (r_s) at the time of recombination.The second and third peaks tell us about the amount of matter in the universe. Given the initial fluctuations in the universe, all matter would tend to gravitationally clump toward the higher temperature (higher density) fluctuations. The height of the third peak gives us a measure of how much dark matter there is compared to the total amount of light in the early universe.

- **The dark age.**

  Once the universe became transparent the universe was filled with neutral hydrogen gas. Without ionizing radiation, the gas clouds remained neutral and could not collapse under gravity to form stars. Meanwhile, the density fluctuations grew over time due to self-gravity. One of the significant events that marked the end of the Dark Age was the formation of the very first generation of stars, known as Population III stars. These hypothetical stars were composed mainly of primordial gases, such as hydrogen, helium, and trace amounts of lithium and beryllium. These population of stars would then produce the metals observed in Pop II stars and initiate the gradual increase in metallicity across subsequent generations of stars, giving rise to the next era.

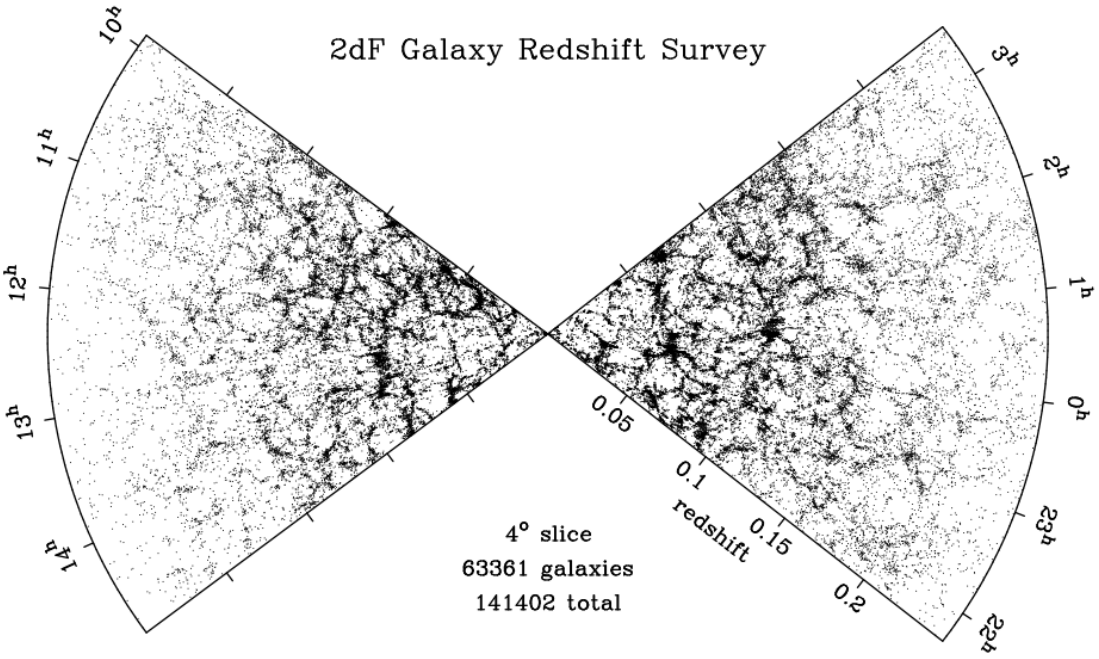

Figure 8: Galaxy distribution from the 2dfGRS survey with 141402 galaxies. In the radial direction, the redshift is plotted and the polar angle is the right ascension. Hubble's law states that the redshift of an object is directly proportional to its distance from us. Therefore, the map illustrates the three-dimensional distribution of galaxies, with our own galaxy positioned at the center of the image. Source [30].

- **Reionization.** This is the second phase transition of gas in the history of the universe. The energetic photons from these population III stars are now capable of ionizing hydrogen in their vicinity. Following the formation of population III stars, they will explode as supernova [32]. These powerful events result in the ejection of metals produced by these stars into the intergalactic medium (IGM). During this process, it is possible that the kinetic energy transferred by the supernovae to the halo exceeds its binding energy, resulting in the baryons blowing away from the halo, therefore, the star formation is prevented. However, since the universe is transparent for photons, they can travel long distances and destroy molecular hydrogen. In order for gas to undergo cooling in halos without molecular hydrogen, their virial temperature needs to exceed about 10^4K.Within this halos, efficient star formation can occur and the first proto-galaxies can form. These systems then ionize the interstellar medium and the reionization process is completed.

- **Large-scale structure formation.** Matter continues to draw together under the influence of gravity, to form galaxies. The stars from this time period, known as Population II stars, are formed early on in this process. More recently, the formation of population I stars occurs, those are young systems with the highest metallicity As galaxies form, they are not randomly distributed but tend to form clusters and superclusters interconnected through filamentary structures. These filaments, along with the dark matter halos and voids in between, make up the cosmic web—a vast network of structures spanning the universe as it is shown in Fig. 8 where the galaxy distribution from the 2dfGRS survey is displayed. Alternatively, cosmological and small-scale N-body simulations have been carried out in order to study

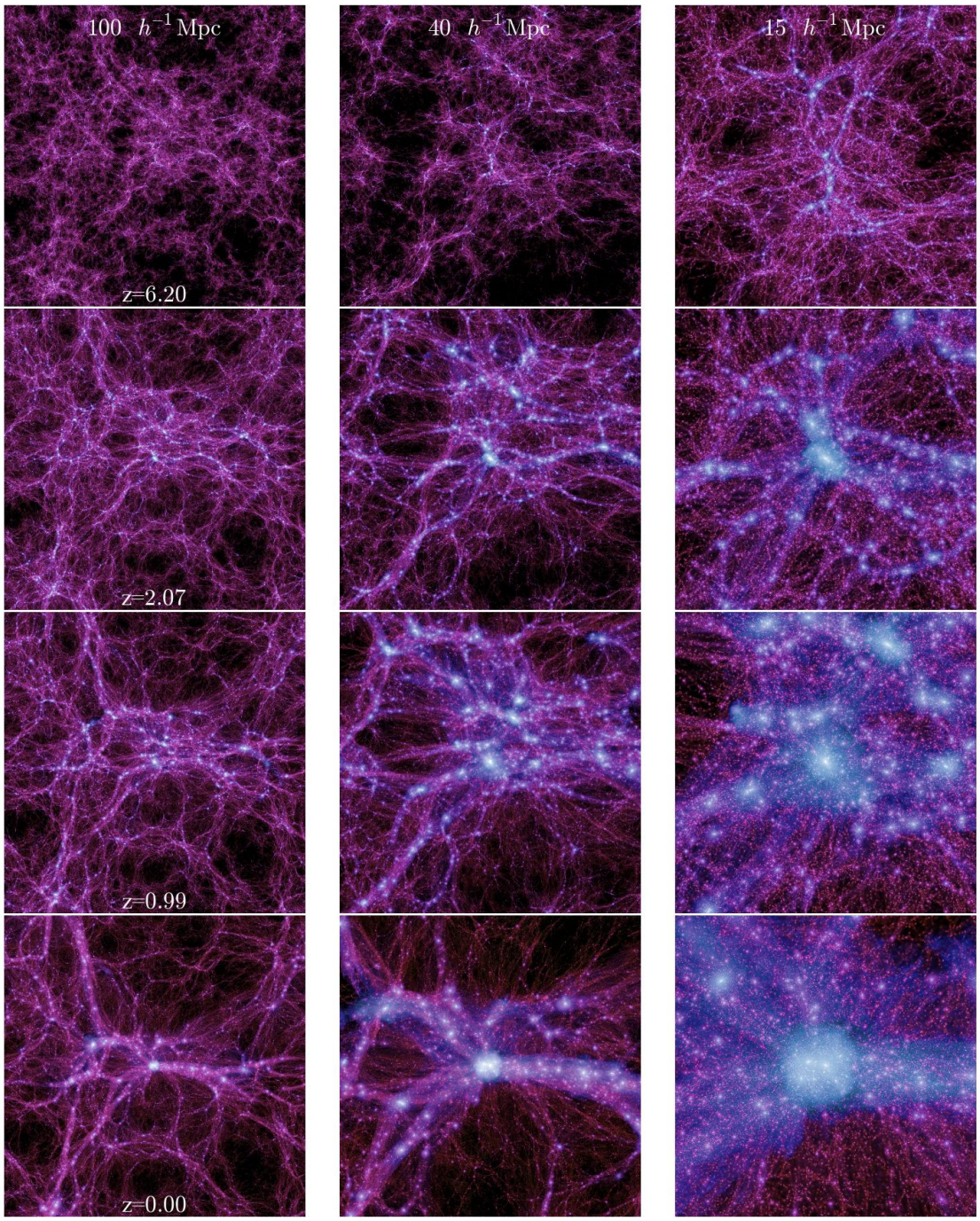

Figure 9: Evolution of structure formation from $z = 6.2$ to $z = 0$ at different scales performed by the Millennium simulation, one of the most famous simulations of all time, ushering in a new era of simulations . Here, it is possible to observe the cosmic net and the formation of clusters and superclusters. Taken from `https://wwwmpa.mpa-garching.mpg.de/`.

the structure formation and evolution. Fig. 9 shows the Millennium Simulation at different redshifts [35].

0.2 The Standard Model of Cosmology

0.2.1 Einsten's theory

The fundamental theory of modern canonical Cosmology is established upon the Einstein field equations: a set of non-linear coupled partial differential equations for the components of the metric, sourced by the components of the energy-momentum (EM) tensor, with the symmetries imposed by the Cosmological Principle. This is known as the General Relativity [15] and there exist three central premises for this theory. Firstly, the theory must be coordinate independent or *covariant*. This is the so-called *Principle of General Covariance* [26]. Secondly, the equation of motion must be made up of second-order terms in derivatives of the metric. And thirdly, the EM tensor must be covariantly conserved [38].

The field equations are derived from the Principle of *Least action* applied to the Einstein-Hilbert (EH) action by varying the metric $\delta g_{\mu\nu}$

$$\delta S = \delta S_{\text{E-H}} + \delta S_{\text{matter}} = \delta \int dx^4 \sqrt{-g} \left(\frac{c^4}{16\pi G} R + \mathcal{L}_{\text{matter}} \right) = 0, \tag{12}$$

where the Riccie scalar, R, gives the lagrangian density as follows

$$\mathcal{L}_{\text{GR}} = \sqrt{-g} R = \sqrt{-g} g^{\mu\nu} R_{\mu\nu}, \tag{13}$$

where, $g = \det(g_{\mu\nu})$.

The field equations, which describe the behavior of spacetime in the presence of matter and energy, can be expressed as follows

$$G_{\mu\nu} \equiv R_{\mu\nu} - \frac{1}{2} g_{\mu\nu} R + g_{\mu\nu} \Lambda = -\frac{8\pi G}{c^2} T_{\mu\nu}, \tag{14}$$

where $G_{\mu\nu}$ is known as the *Einstein tensor*. $T_{\mu\nu}$ is the EM tensor, which describes the properties of the content in the Universe, Λ is the cosmological constant, which appears in the right-handed side of the equation and can be absorbed into the EM tensor and be treated as another type of matter. In fact, the key principle of General Relativity states that gravity is an effect due to the curvature of spacetime which is generated by the content of matter.

The term $R_{\mu\nu}$ is known as the Ricci tensor and can be defined in terms of the Christoffel symbols

$$R_{\lambda\nu} = \Gamma^{\kappa}_{\lambda\nu,\kappa} - \Gamma^{\kappa}_{\lambda\kappa,\nu} + \Gamma^{\alpha}_{\lambda\nu} \Gamma^{\kappa}_{\kappa\alpha} - \Gamma^{\alpha}_{\lambda\kappa} \Gamma^{\kappa}_{\nu\alpha}, \tag{15}$$

with $\Gamma^{\lambda}_{\mu\nu} = \frac{1}{2} g^{\lambda\alpha} \Big(g_{\mu\alpha,\nu} + g_{\nu\alpha,\mu} - g_{\mu\nu,\alpha} \Big)$, here $g_{\lambda\alpha}$ is the covariant form of the metric. Usually, the field equations are expressed in the following short form

$$G^{\mu}_{\nu} = 8\pi G T^{\mu}_{\nu}. \tag{16}$$

The Einstein's tensor is conserved through the Bianchi equation, which implies the local conservation of the EM tensor

$$G^{\alpha}_{\nu;\alpha} = 0, \quad \Rightarrow \quad T^{\alpha}_{\nu;\alpha} = 0. \tag{17}$$

In literature, there have been reported different solutions to these equations. For instance, in order to describe the space around two blck-holes, it is considered a spherical system with a mass located in the coordinate origin, having in this way the Schwarzschild solution [33].

0.2.2 Geometry of spatially homogeneous and isotropic universes and the FLRW metric

A line element in a homogeneous and isotropic space is defined in terms of the space metric g_{ij}. In this case ds corresponds directly to the physical distance. In order to describe the space, different curvatures can be considered. A line element corresponding to a space that fulfills the characteristics of being isotropic, homogeneous and also encompassing different geometries is described as

$$ds^2 = a^2 \left[d\vec{x}^2 + K \frac{(\vec{x} \cdot d\vec{x})^2}{1 - K\vec{x}^2} \right], \tag{18}$$

being a, until now, a positive constant. The constant K determines whether the curvature (positive, negative, or zero) by means of the following labels

$$K = \begin{cases} +1, & \text{sphere} \\ -1, & \text{hyperboloid} \\ 0 & \text{Plane} \end{cases} \tag{19}$$

For the first case, we have a positive constant curvature, which corresponds to a closed spatial manifold. In the opposite case when K is negative, we have a hyperbolic space which is open. The simplest case is when the curvatures is zero, which means a plane Universe. Up to this point, only a space with curvature has been described. Nevertheless, it is necessary to consider the temporary part to describe the evolution of a Universe in the space-time. Let's define the Friedmann-Lemaitre-Robertson-Walker (FLRW) metric.

$$ds^2 = -c^2 dt^2 + a^2(t) \left(\frac{dr^2}{1 - K^2} + ar^2 d\theta^2 + r^2 \sin^2 \theta d\phi^2 \right), \tag{20}$$

$$= -c^2 dt^2 + a^2(t) \left(\frac{dr^2}{1 - Kr^2} + r^2 d\Omega^2 \right), \tag{21}$$

where $x^i \in (r, \theta, \phi)$ expressing in spherical coordinates and $d\Omega$ is the solid angle. One of the main properties about this metric is the symmetry, moreover the off-diagonal components equal zero. Additionally, the metric capable to describe a isotropic and homogeneous Universe is unique. [25]. This is the *Copernican Principle* . However, according to the *Cosmological Principle* such conditions are only met on large scales. At small scales, perturbations and their growth, due to the gravitational instability, must be considered.

Particularly, for a plane Universe, $K = 0$, the metric in Cartesian coordinates, by taking into account the Minkowski signatures and there the spatial components has a negative sign, can be written in the following form,

$$g_{\mu\nu} = \begin{pmatrix} -1 & 0 & 0 & 0 \\ 0 & a^2(t) & 0 & 0 \\ 0 & 0 & a^2(t) & 0 \\ 0 & 0 & 0 & a^2(t) \end{pmatrix}. \tag{22}$$

Therefore, a line element takes the form $ds^2 = -dt^2 + a^2(t)\delta_{ij} dx^i dx^j$, where δ_{ij} is the Kronecker delta.

0.2.3 Dynamics and Evolution of the Background Universe: The Friedmann equations

Now, a particular case for Einstein's equations for the case of a homogeneous and isotropic universe with curvature. Using the metric (18), the Ricci tensor and scalar can be expressed as

$$R^{\mu}_{\nu} = \text{diag}(R^0_0, R^i_j) = \text{diag}\left(-3\frac{\ddot{a}}{a}, \delta_{ij}\left[2\dot{a}^2 + \ddot{a}a + 2K\right]\right), \tag{23}$$

$$R = 6\left(\frac{\ddot{a}}{a} + \frac{\dot{a}^2}{a^2} + \frac{K}{a^2}\right). \tag{24}$$

By considering the the equation of field(14) and the form of the metric (20), the Einstein tensor can be written in terms of the purely temporary and purely spatial components

$$G^{\mu}_{\nu} = R^{\mu}_{\nu} - \frac{1}{2}\delta^{\mu}_{\nu}R. \tag{25}$$

In order to solve these equations, the right-handed side (16) must be specified first. To describe matter in the universe it is usual to assume a perfect fluid with energy density ρ and pressure P and hence, the EM tensor takes the form

$$T^{\mu}_{\nu} = Pg^{\mu}_{\nu} + (\rho + P)U^{\mu}U_{\nu}, \tag{26}$$

where $U^{\mu} = dx^{\mu}/\sqrt{-ds^2}$ is the 4-velocity of the fluid, which is usually expressed as $U^{\mu} = \text{diag}(1, v^i)$ for massive particles ans as $U^{\mu} = \text{diag}(1, 0, 0, 0)$ in the rest frame of the fluid particles. This assumption is not entirely general, but can be taken into account due to most of the components behaving as a perfect fluid at large scales. However, in the early Universe, it is necessary to consider interactions between these components and the particles from the Standard Model of Particle Physics. In contrast, in the intermediate regimen, we can only use the phase space distribution for individual particles belonging to some specific species.

By taking into account the eq. (26), Einstein's equation, with respect to the comoving rest frame, can be expressed as

$$G^0_0 = 3\frac{\dot{a}^2}{a} + 3\frac{K}{a^2} = 8\pi G\rho, \tag{27}$$

$$G^i_j = \delta_{ij}[2\dot{a}^2 + a\ddot{a}] - 3\delta_{ij}a^2\left(\frac{\ddot{a}}{a} + \frac{\dot{a}^2}{a^2} + \frac{K}{a^2}\right) = \delta_{ij}8\pi G \tag{28}$$

$$\Rightarrow \quad \frac{\ddot{a}}{a} + \frac{1}{2}\frac{\dot{a}^2}{a^2} = -4\pi G\rho P, \tag{29}$$

rearranging these terms we can obtain the Friedmann and acceleration equations, which describe a FLRW Universe

$$\left(\frac{\dot{a}}{a}\right)^2 = \frac{8\pi G}{3}\rho - \frac{K}{a^2}, \tag{30}$$

and

$$\frac{\ddot{a}}{a} = -\frac{4\pi G}{3}(\rho + 3P). \tag{31}$$

These equations can be combined to obtain the continuity equation which also directly follows from the EM conservation $T^{\alpha}_{0,\alpha} = 0$,

$$\dot{\rho} + 3\frac{\dot{a}}{a}(\rho + P) = 0. \tag{32}$$

0.2.4 Redshift and distances

Given two points in a curved space, the curve with a shorter length is known as a *Geodesic* [7]. Free particles in a curved space travel along these geodesics, which obey the following equation

$$\frac{d^2x^\mu}{ds^2} + \Gamma^\mu_{\alpha\beta}\frac{dx^\alpha}{ds}\frac{dx^\beta}{ds} = 0. \tag{33}$$

The massless particles travel through *null* geodesics, where $ds^2 = 0$, whereas the massive particles travel in *temporaloid* geodesics where the signature is $ds^2 > 0$, as long as there are no external forces. If the latter happens, the masive particles travel along the so-called *world lines*.

For the massless particles, whose 4-momentum can be described as $P^\mu \equiv \frac{dx^\mu}{ds}$, the components for the 4-momentum are $P^\mu = (E, p^i)$, where p^i is the comoving 3-momentum vector. By considering the 4-momentum magnitudes is zero [H.], it follows that

$$\begin{aligned} |P|^2 &= g_{\mu\nu}P^\mu P^\nu, & (34)\\ &= E^2 - a^2\delta_{ij}p^i p^j = 0, & (35)\\ \Rightarrow |p|^2 &= E^2 a^{-2}. & (36) \end{aligned}$$

The 0^{th} component of the geodesic equation (33) for a massless particles

$$\begin{aligned} 0 &= E\frac{dP^0}{dt} + \Gamma^0_{ij}p^i p_j, & (37)\\ &= E\frac{dE}{dt} + a\dot{a}|p|^2 \quad \Rightarrow \quad \frac{1}{E}\frac{dE}{dt} + \frac{\dot{a}}{a} = 0, & (38) \end{aligned}$$

which gives $E \propto \frac{1}{a}$. This means that when the universe expands, then $a \to \infty$, $E \to 0$, and the massless particles lose energy. For photons, the energy is expressed in terms of the wave function λ as $E = \lambda^{-1}$, which means the expansion in the Universe stretches the wavelength of photons $\lambda \propto a$, therefore the redshift is defined as

$$z \equiv \frac{\lambda_{\text{observer}} - \lambda_{\text{source}}}{\lambda_{\text{source}}} = \frac{a_{\text{observer}} - a_{\text{source}}}{a_{\text{source}}}, \tag{39}$$

and assuming we observe this photon today, when $a = 1$, then

$$a_{\text{source}} = \frac{1}{1+z}. \tag{40}$$

Now, about the distances, we can define the *comoving* distance which remains constant over time despite the expanding space (see fig. 1). In order to convert it to a physical distance, also known as *proper* distance, it is necessary to consider the scale factor. The proper distance represents the physical separation between two objects in the universe, accounting for the expansion of space as follows

$$r = \int_0^r d\tilde{r} = \int_{t_{\text{ini}}} \frac{dt}{a(t)} = \int_{a_{\text{init}}}^a \frac{da}{aH}. \tag{41}$$

Given that a is adimensional, we have $r \sim H^{-1}$, which defines the so-called *Huble scale* $r_H = H^{-1}$, Which corresponds to an estimate of the size of the universe at a given time, and the *Hubble time*. Additionally, taking into account the finiteness of the age of the universe, it can be deduced the maximum distance that light can have traveled from its starting point is finite as well. For this reason, we can define horizons. On one side, the *particle horizon* [3] is the farthest place from which the light could have traveled. On the other side, the *event horizon* [18] is a boundary beyond which events cannot affect an observer.

0.2.5 Evolution of the species in a FLRW universe

The EM tensor can contain information of different *species* such as relativistic matter, also known as radiation, non-relativistic matter, and the cosmological constant which described the dynamics in the universe, which can be absorbed in the tensor, as mentioned before.

In literature, there have been reported many works about the nature of the cosmological constant [8, 9, 28, 2, 24]. Usually, it is known as *Dark Energy* [10]. On one hand, different properties such as the equation of state varying in time has been attributed to it, this is known as *quintessence* [36]. On the other hand, it has been related to different modified gravity models.

Another fundamental ingredient contained in the energy-momentum tensor is the baryons. This type of matter corresponds to the visible structure in the Universe. In astronomy, baryonic matter should include protons, neutrons, and all objects composed of them. The composition and mechanisms involved in this type of matter have been highly explored at small and large scales.

The Friedmann's equations (30), (31) and (32) can be solved as long as the density $\rho_{\rm tot} = \sum_x \rho_x$ and the total pressure $P_{\rm tot} = \sum_x P_x$ are known. If we consider a flat universe, the Friedmann equation can be written as

$$\dot{\rho}_x + 3H\rho_x(1 + w_x) = 0, \tag{42}$$

where $\rho_{\rm crit}(a) = \dfrac{3H^2}{8\pi G}$ is the critical density, i.e. the density required for the universe to have a flat geometry on large scales. Also, $w_x = \dfrac{P_x}{\rho_x}$ represent the equation of state of each specie, assuming that they are barotropic fluids. Indeed, it is convenient to define the density parameter for a given specie as $\Omega_x(a) = \dfrac{\rho_x(a)}{\rho_{crit}(a)}$, which compared the actual density of the specie in the universe to the critical density. In fact, the following constriction over the matter, radiation, and cosmological constant density must be fulfilled

$$\Omega_m + \Omega_r + \Omega_\Lambda = 1. \tag{43}$$

In the present day, the density parameters meet the following expression [23]

$$\Omega_{r,0} < \Omega_{m,0} < \Omega_{\Lambda,0}, \tag{44}$$

where $\Omega_{x,0} = \Omega_x(a = 1)$. According to [1] the values for the parameter density at 68% confidence level are

$$\Omega_\Lambda = 0.6889 \pm 0.0056, \tag{45}$$

$$\Omega_m = 0.3111 \pm 0.0056, \tag{46}$$

$$\Omega_r = \Omega_\nu + \Omega_\gamma = 9.0513 \times 10^{-5}, \tag{47}$$

here, it has been considered that the radiation density has a contribution from both photons γ and neutrinos ν related by $\rho_\nu = N_{eff}\frac{7}{8}\left(\frac{4}{11}\right)^{4/3}\rho_\gamma$ [13], with $N_{\rm eff} = 3.046$ as the effective number of neutrino species.

For the radiation case, the equation of state is $w_r = \dfrac{1}{3}$, and the solution for (42) is

$$\rho_r(a) = \rho_{r,0}a^{-4}, \tag{48}$$

where $\rho_{x,0} = \rho_x(a = 1)$ represents the energy density of the specie x today.
For the matter, the equation of state is $w_m = 0$, then the solution is

$$\rho_m(a) = \rho_{m,0}a^{-3}. \tag{49}$$

Finally, for the cosmological constant, the equation of state is $w_\lambda = -1$. Defining the following parameters for the density $\rho_\Lambda = \dfrac{\Lambda}{8\pi G}$, the obtained solution is

$$\rho_\Lambda(a) = \rho_{\Lambda,0}a^{-3(1+w_\Lambda)} = \rho_{\Lambda,0}. \tag{50}$$

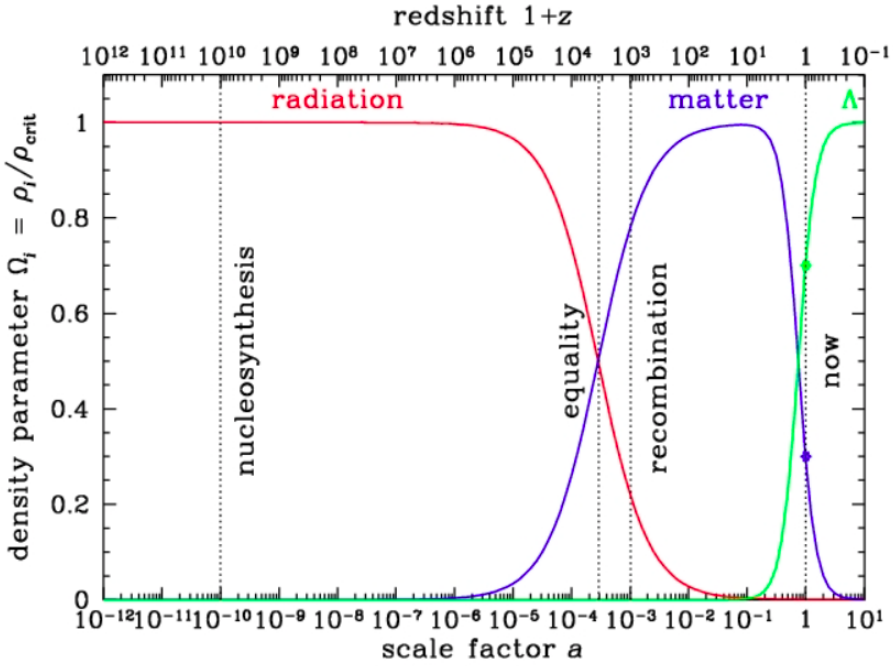

Figure 10: The cosmic evolution of the density parameters for matter, radiation, and cosmological constant. Ω_r is initially dominant but decreases as time increases passing through the equality radiation-matter era. Then, Ω_r becomes dominant after this epoch and after that, decreases. The Ω_Λ increases exponentially, being the dominant component today. Source `http://courses.atlas.illinois.edu/`.

0.2.6 Cosmic Evolution of the scale factor and the density parameters of species

Now if we consider the case when one of the species dominates $\rho_x \gg \rho_y$, then the total density can be approximated as $\rho_{\rm tot}(a) \sim \rho_x(a)$. In such a case, the Friedmann equation can be solved easily. Therefore, it is possible to identify different eras where one of the three species (matter, radiation, cosmological constant) dominates. In the beginning, radiation was dominant, but as the universe cooled and expanded, matter started to dominate, so it is possible to define an epoch of matter-radiation equality $\Omega_m(a_{\rm eq}) = \Omega_r(a_{\rm eq})$.

By considering the different eras, Friedmann's equation can be expressed as

$$H^2 = \frac{8\pi G}{3}\sum_x \rho_x(a) \tag{51}$$

$$= \frac{8\pi G}{3}\Big(\rho_{r,0}a^{-4} + \rho_{m,0}a^{-3} + \rho_\Lambda\Big), \tag{52}$$

where $H(a) = \dfrac{\dot{a}}{a}$ is known as the Hubble parameter. The last equation takes the form

$$H^2 = H_0^2\Big(\Omega_{r,0}a^{-4} + \Omega_{m,0}a^{-3} + \Omega_\Lambda\Big), \tag{53}$$

with $H_0 \sim 100h{\rm km}/s$. The Hubble parameter is dimensionless and has a value of $h = 0.7$ [21]. Fig. 10 shows the evolution of the density parameters as a function of the redshift considering radiation, matter, and cosmological constant Ω_r, Ω_m and Ω_Λ. There, we can see Ω_r drops as

time increases. Also, Ω_m increases until it reaches its maximum value and then decreases. In the meantime, Ω_Λ grows rapidly reaching its maximum value today. Below is the scale factor solution for some important epochs in the history of the universe.

- **Big Bang.** $a_{\rm init} \sim 0$.
- **Radiation.** When $\rho_r(a) \gg \rho_m(a) \quad \Rightarrow \quad \Omega_r(a) \gg \Omega_m(a)$.
  For a flat universe $K = 0$, the scale factor can be expressed as
  $$a_r(t) \sim (H_0^2 \Omega_{r,0})^{1/4} t^{1/2}. \tag{54}$$
  If the universe is considered with curvature, that is $K \neq 0$, then the solution takes the form
  $$a_r(t) = \sqrt{H_0^2 \Omega_{m,0} - K(t+t_0)^2}. \tag{55}$$
- **Matter.** When $\rho_m(a) \gg \rho_\Lambda(a) \quad \Rightarrow \quad \Omega_m(a) \gg \Omega_\Lambda(a)$.
  For a universe without curvature, the solution is
  $$a_m(t) \sim (H_0^2 \Omega_{m,0})^{1/3} t^{2/3}. \tag{56}$$
  If the universe is dominated by non-relativistic matter and cosmological constant, the solution is
  $$a(t) = \left[\sqrt{\frac{\Omega_{m,0}}{\Omega_{\Lambda,0}}} \sinh\left(\frac{3H_0}{2} \sqrt{\Omega_{\Lambda,0}} (t+t_0) \right) \right]. \tag{57}$$
- Λ **constant**. For this type of universe, the scale factor reads as
  $$a_\Lambda \sim \exp\{ t \sqrt{H_0^2 \Omega_\Lambda} \}. \tag{58}$$
- **Today.** $a_0 \sim 1$.

0.3 The problem of Dark Matter

0.3.1 Formation of the Relic abundance

In order to study the dark matter and the formation of relic abundance, it is convenient to consider that the only process in which the dark matter is involved is this annihilation $1+2 \leftrightarrow 3+4$. Here, the particle of interest is 1 and the processes allowed are the annihilation between 1 and 2 producing 3 and 4, and vice versa. The Boltzmann equation reads as [14]

$$a^{-3} \frac{d(n_1 a^3)}{dt} = n_1^{(0)} n_2^{(0)} \langle \sigma v \rangle \left\{ \frac{n_3 n_4}{n_3^{(0)} n_4^{(0)}} - \frac{n_1 n_2}{n_1^{(0)} n_2^{(0)}} \right\}, \tag{59}$$

where n_i is the number density of species i when an interaction process occurs, which in terms of the chemical potential reads as $n_i = e^{\mu_i/T} n_i^{(0)}$.

Here μ_i is the *chemical potential* defined as the rate of change of free energy of a thermodynamic system with respect to the change in the number of particles of the species that are added to the system. Also, T is the temperature of the system, and E_i is the energy for each species. The quantities $n_i^{(0)}$ are given by

$$n_i^{(0)} = \frac{g_i}{(2\pi^3)} \int d^3p e^{-E_i/T} = \begin{cases} g_i \left(\dfrac{m_i T}{2\pi} \right)^{3/2} e^{-m_i/T} & m_i \gg T \\ g_i \dfrac{T^3}{\pi^2} & m_i \ll T \end{cases} \tag{60}$$

and they correspond to the number of densities in the absence of chemical potential (when no process occurs). Here, g_i is the degeneration of the species

Now, the thermally averaged cross-section $\langle\sigma v\rangle$, corresponds to the average 4-momentum-phase-space of the amplitude of the process and can be computed using the theory of particle physics

$$\langle\sigma v\rangle \equiv \frac{1}{n_1^{(0)}n_2^{(0)}}\int\frac{d^3p_1}{(2\pi)^3 2E_2}\int\frac{d^3p_2}{(2\pi)^3 2E_3}\int\frac{d^3p_3}{(2\pi)^3 2E_4}\int\frac{d^3p_4}{(2\pi)^3 2E_4}e^{(E_1+E_2)/T} \tag{61}$$

$$\times(2\pi)^4\delta^3(p_1+p_2-p_3-p_4)\delta(E_1+E_2-E_3-E_4)|\mathcal{M}|^2. \tag{62}$$

From eq. (59), it is straightforward to notice that in the absence of interaction, the density for each specie times the scale factor cubed is conserved. This fact demonstrates the fundamental characteristic of the expanding universe: as the comoving grid expands, the volume occupied by a fixed number of particles increases proportionally to a^3. Therefore, the physical number density of these particles falls off as a^{-3}. This also implies that the particles are in *chemical equilibrium*, that is

$$\frac{n_3 n_4}{n_3^{(0)}n_4^{(0)}} = \frac{n_1 n_2}{n_1^{(0)}n_2^{(0)}}. \tag{63}$$

In the Dark matter scenario, by considering a heavy particle candidate X annihilating into two lights particle ℓ. These last components are assumed to be very tightly coupled to the cosmic plasma, so they can be considered to be in chemical and kinetic equilibrium, that is $n_\ell = n_\ell^{(0)}$. Therefore, the eq. (59) can be rewritten as

$$a^{-3}\frac{d(n_X a^3)}{dt} = \langle\sigma v\rangle\Big\{(n_X^{(0)})^2 - n_X^2\Big\}. \tag{64}$$

Defining $Y \equiv \dfrac{n_X}{T^3}$, the Boltzmann equation becomes $\dfrac{dY}{dT} = T^3\langle\sigma v\rangle\Big\{Y_{\rm EQ}^2 - Y^2\Big\}$, with $Y_{\rm EQ} \equiv \dfrac{n_X^{(0)}}{T^3}$. This quantity can be interpreted as the abundance of the specie with respect to the thermal bath.

Now, it is possible to describe the previous equation in terms of the mass m of the heavy particle, using the following definition $x \equiv \dfrac{m}{T}$. Then, the evolution equation is

$$\frac{dY}{dx} = -\frac{\lambda}{x^2}\Big\{Y^2 - Y_{\rm eq}^2\Big\}, \tag{65}$$

with $\lambda \equiv \dfrac{m^3\langle\sigma v\rangle}{H(m)}$. The previous expression has the form of the *Ricatti equation.*

Here, we can distinguish different cases, for high temperatures we have $x \ll 1$ we have the second case in the eq. (60) and the annihilation between particles is very efficient, $Y_{\rm eq} \approx Y$, that means Y is tracing its equilibrium value. Moreover, from eq. (64), the left hand side can be expressed as $\dfrac{dn_x}{dt} + 3Hn_x$, for the case when $Hn \ll \langle\sigma v\rangle n_X^2$, then the solution would be $n_x \propto a^{-3}$. This is equivalent to saying that DM particles do not annihilate anymore and their number density decreases only because the scale factor of the universe increases, and therefore the relic abundance of dark matter remains. The crossover happens when $\langle\sigma v\rangle \sim H$.

Freeze-out

In (65), When $x \gg 1$, the $Y_{\rm eq}$ becomes exponentially suppressed, this corresponds to the first case in eq. (60). Then, the equilibrium won't be maintained resulting in a freeze-out process. As mentioned before, if a massive particle species remained in thermal equilibrium until the present, its abundance, $n \sim (m_i T)^{3/2}e^{-m_i/T}$, would be negligible because of the exponential factor. If the interactions of the species freeze out at a temperature such that m/T is not much greater than 1, the species can have a significant relic abundance today [20]. It is important to assume that the

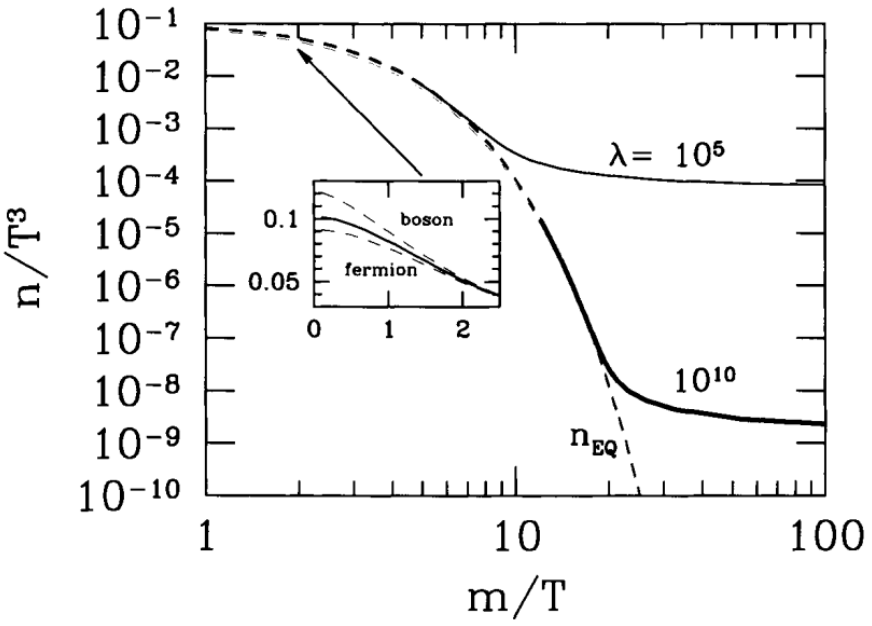

Figure 11: Abundance of massive cold particles as a function of the mass and the inverse of temperature. Here, both fermions and baryons are considered but the difference is only perceptible for high temperatures. We can also see that if the equilibrium is maintained, then $n_{\rm eq}$ drops exponentially. If the freeze-out occurs, it depends on the thermally averaged cross-section. These are considered cold relics since they freeze out at $m > T$. Even though the hot relic formation is not shown, it is important to note that this relic abundance is independent of when freeze-out occurs since the equilibrium curve is flat there. Source [14].

species is stable (or very long-lived compared to the age of the universe when their interactions freeze out). If freeze-out happens when the particles are still relativistic we call them *hot relics* if it occurs when they are non-relativistic we call them *cold relics*.

Fig. 11 shows the behavior of the abundance, or yield, as a function of $\frac{m}{T}$ for both massive fermions and bosons. There, we can see that the higher the value of λ, this means particles with larger cross-section σ, freeze out later, and this later freeze-out carries along with it a lower relic abundance. After freeze-out, the heavy particle density simply falls of as a^{-3}, as the universe expands.

The dark matter density can be expressed in terms of the mass of the heavy particle, x_f (the value of m/T at the moment of freeze out) and $\langle\sigma v\rangle$

$$\Omega_x = 0.3h^{-2}\left(\frac{x_f}{10}\right)\left(\frac{g_*(m)}{100}\right)^{1/2}\frac{10^{-39}\text{cm}^3 s^{-1}}{\langle\sigma v\rangle}. \tag{66}$$

The fact that this estimation yields a value close to one for cross sections around 10^{-39}cm^2 has been seen as a promising indication. It implies that there exist several theories that predict the existence of particles with such tiny cross-sections. Perhaps the most plausible candidate is a weakly interacting massive particle (WIMP), whose cross sections has been computed giving a value of that order.

0.3.2 Observational evidence

There is a substantial amount of observational evidence supporting the existence of dark matter, which is a fundamental piece of the Standard Cosmological model and the main component of total

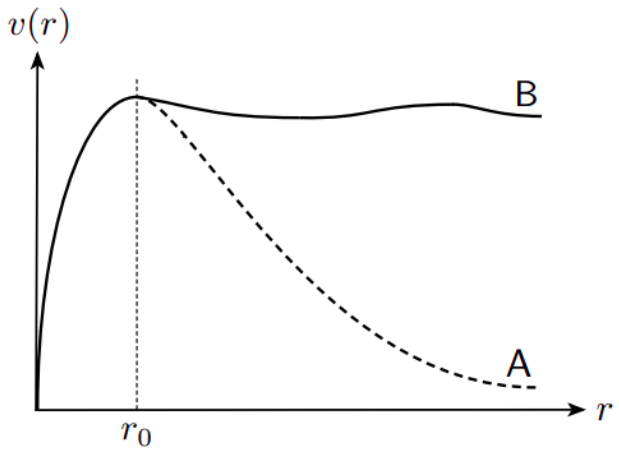

Figure 12: Representation scheme of a rotation curve derived from the Keplerian laws (A), the greater the radius, the less the velocity. The vertical dashed line that intersects the r-axis at r_0, represents the maximum speed, once that value has been reached, the curve begins to decrease. The line (B) represents an observed rotation curve, where the velocity remains approximately constant after reaching the maximum value. Source [4]

matter. This evidence can be found both at small and large scales and additionally, they can serve as consistency tests for extension models to the ΛCDM model, where a dark matter candidate with different CDM properties is considered.

The first two evidences have been mentioned before, as evidence of the Cosmological model, the large-scale structure formation, and the CMB (see section 0.1.

Galactic rotation curves

Galactic rotation curves provide strong evidence for the existence of dark matter. Indeed, the observed rotational velocities do not follow the expected pattern predicted by assuming visible matter alone, indicating the presence of an additional mass that cannot be accounted for by ordinary matter.

The first measurement of dark matter in the Galaxy was made by Jan Oort in 1932 [27], who concluded that visible stars near the sun could account for only about half the mass implied by the velocities of stars perpendicular to the disk of our Galaxy. In 1933, Fritz Zwicky [39] applied a similar dynamical argument to clusters of galaxies, noting that observed galaxies accounted for 10 or less of the mass needed to gravitationally bind clusters, given the large velocities of galaxies in a cluster. In fig. 12 the discrepancy between observations (labeled by B) and predictions from the Keplerian formalism (labeled by A) are shown. In fact, we observe that both curves match at the center, but for large radii, the difference between them is clearly noticeable, observations account for much more matter than luminous matter inferred from different methods, reaching a maximum value and remaining approximately constant thereafter. This missing matter is attributed to dark matter.

Gravitational lensing

It has been observed that the gravity of massive galaxy clusters, which contain dark matter, bends and distorts the light of more-distant galaxies located behind the cluster. This phenomenon is called *gravitational lensing* and can only be explained by General Relativity. The exact nature of this effect depends on the relative distance and position between the observer, lens, and light

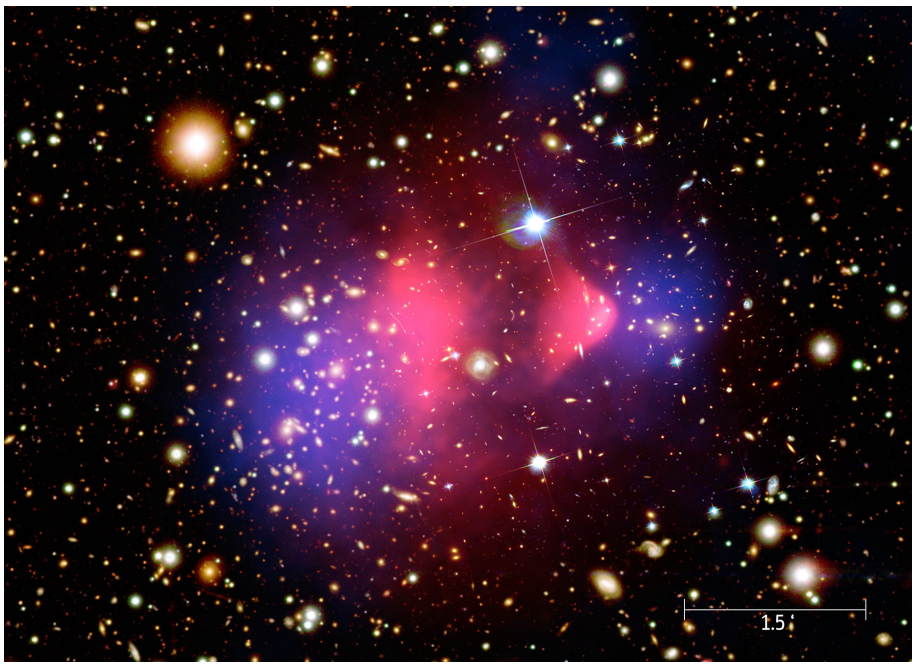

Figure 13: Image of the Bullet cluster using a Chandra X-ray image in pin, superimposed over a visible light image which shows the galaxies, with matter distribution calculated from gravitational lensing. This cluster shows a head-on collision where one of the galaxies has passed through the other, like a bullet. From gravitational lensing, the distortion of background images by mass in the cluster, reveals the mass of the cluster is dominated by dark matter which does not interact with the rest of the matter. Source `https://www.nasa.gov/mission_pages/chandra`.

source, the size of the lens, and the mass inside the lens.

In general relativity, the deflection angle of light in a gravitational field can be expressed as $\tilde{\alpha} = \dfrac{4GM}{c^2\xi}$, where M is the mass of the deflecting object, and ξ is an impact parameter. An for extended gravitational lens, the deflection can be written simply as a vector sum over point masses

$$\tilde{\alpha} = \sum_i \tilde{\alpha}_i = \sum_i \frac{4Gm_i}{c^2} \frac{\vec{\xi} - \vec{\xi}_i}{\left|\vec{\xi} - \vec{\xi}_i\right|^2}, \tag{67}$$

where $\vec{\xi}$ is the position of a light ray in the lens plane and $\vec{\xi}_i$ are the mass elements positions. In the continuum limit, this becomes an integral over the surface mass density. Also, if the deflection is small we can approximate the gravitational potential along the deflected trajectory by the potential along the undeflected trajectory

$$\tilde{\alpha}(\vec{\xi}) = \frac{4G}{c^2} \int d^2\xi' \Sigma(\vec{\xi}') \frac{\vec{\xi} - \vec{\xi}'}{\left|\vec{\xi} - \vec{\xi}'\right|^2}, \tag{68}$$

where the surface mass density is defined as $\Sigma(\vec{\xi}) \equiv \int dr_3 \rho(\xi_1, \xi_2, r_3)$, which is the mass density projected onto a plane perpendicular to the incoming ray.

Gravitational lensing effects are imprinted in all distant galaxies: their images are all slightly distorted as they are lensed by the massive structures in the Universe lying between us and them, this phenomenon is known as *weak lensing signal*. In some cases, the deflection is large enough

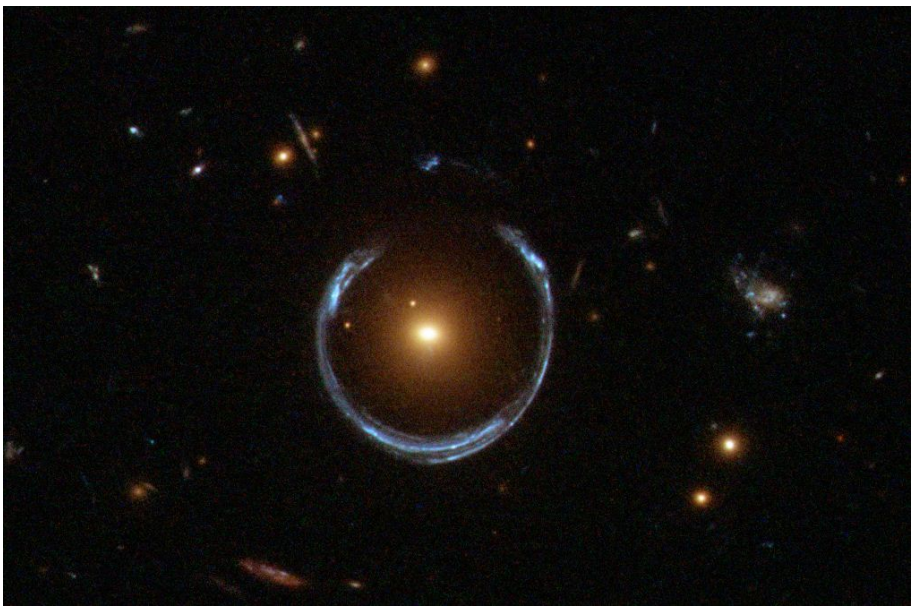

Figure 14: Strong lensing of a luminous red galaxy (LRG) as a consequence of a more distant blue galaxy. Here the formation of Einstein's ring is evident. Usually, light bending results in two discernible images of the distant galaxy, however, in this particular cluster, the alignment of the lensing objects is exceptionally precise, causing the background galaxy to be distorted into a horseshoe shape. This distortion takes the form of a nearly complete ring, creating a remarkable and captivating sight. Source.

that shows significant and easily observable distortions, such as the formation of multiple images, arcs, or even complete Einstein rings. This effect is known as *strong gravitational lensing* and it is often observed in systems where a massive object, such as a galaxy or a galaxy cluster, acts as the lens. In fig. 14 a strong lensing is shown and the Einstein rings are visible as well.

Bullet cluster

The bullet cluster also known as 1E $0657-56$ is a phenomenon that not only supports the existence of dark matter but also its properties and it is shown in Fig. 13. In the figure, on the right side of the cluster's center, one can observe a prominent and compact emission of X-rays, often referred to as the 'bullet.' Continuing further to the right, there is a noticeable arc-shaped discontinuity in the surface brightness. By examining the temperature distribution on both sides of the discontinuity, it can be deduced that it represents a shock front. In fact, the gas distribution on the right side resembles that of the air around a supersonic plane or bullet. Based on the intensity of the shock, it can be inferred that the bullet is moving at a velocity of approximately 3500 km/s as it travels through the intergalactic medium of the cluster [32]. The interpretation of this observation is a collision of two clusters, where the one less massive has passed, from the left to the right, through a more massive cluster.

0.3.3 Dark matter tensions

Despite the evidences that supports the contribution of dark matter in the standard cosmological model, there are some aspects that this theory cannot fully explain. These tensions arise from discrepancies between certain observations and predictions of the model.

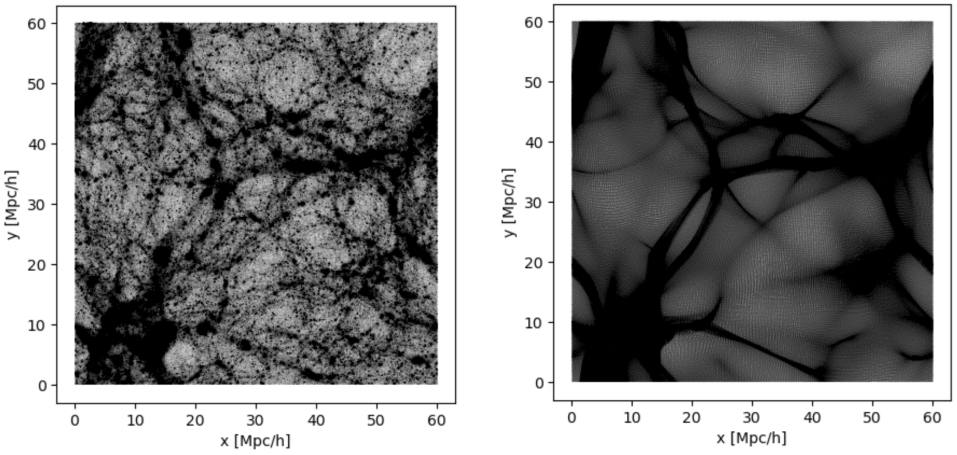

Figure 15: Snapshots in the xy-plane for two different models are displayed. Left: standard CDM and right a model with suppression at small scales. The difference in the substructure is very evident but the cosmic net at large scales is the same.

The missing satellite problem

This problem refers to a discrepancy between the predicted number of small dark matter substructures, or satellite galaxies, and the observed number of such satellites around larger galaxies like the Milky Way. In fact, on one hand, our galaxy is orbited by about fifty satellite galaxies. This astrophysical systems are often less luminous or fainter compared to the Milky Way. They have lower star formation rates and fewer massive, luminous stars. Some satellite galaxies may contain predominantly older stellar populations [22]. In addition, they are generally significantly smaller than the Milky Way itself showing lower masses and smaller physical sizes.

In order to handle this problem, in many extension models to the Standard Cosmological Model it has been considered a cut-off in the Matter Power Spectrum at a small scale, which implies that structure formation on small scales will also be suppressed. This cut-off is generated depending on the properties of the dark matter candidate, so it can have different origins in each model. In fig. 15 two snapshots are shown, on the left, standard CDM was used and on the right a model with a pronounced cut-off. Here, it is evident the structure formation at large scales follows the same geometry.

The core-cusp problem

Another of the famous problems in modern Cosmology is the *core-cusp problem*. Such a problem refers to a discrepancy between the inferred dark matter density profiles of spheroidal dwarfs, irregular galaxies, and some galaxies of low surface brightness (LSB) and the density profiles predicted by cosmological N-body simulations. The cosmological simulations produce satellite galaxies of high dark matter density, whereas the observed rotation curves of such galaxies are more varied, and generally suggest less-concentrated volumes of dark matter.

In literature, there have been presented different possible solutions to the core-cusp problem. One possible solution is that baryonic matter affects the density profile of dark matter. Feedback mechanisms, such as stellar winds, supernovae, and active galactic nuclei, can expel gas and energy from the central regions of galaxies, leading to the creation of a core. These processes may redistribute the dark matter and flatten the density profile [11]. Alternatively, the properties of dark matter candidates different from CDM may influence the shape of the density profile. For instance, as it was mentioned before, in WDM the high thermal velocities in the early universe prevent the particles from collapsing into small-scale structures as efficiently as CDM particles. This results in

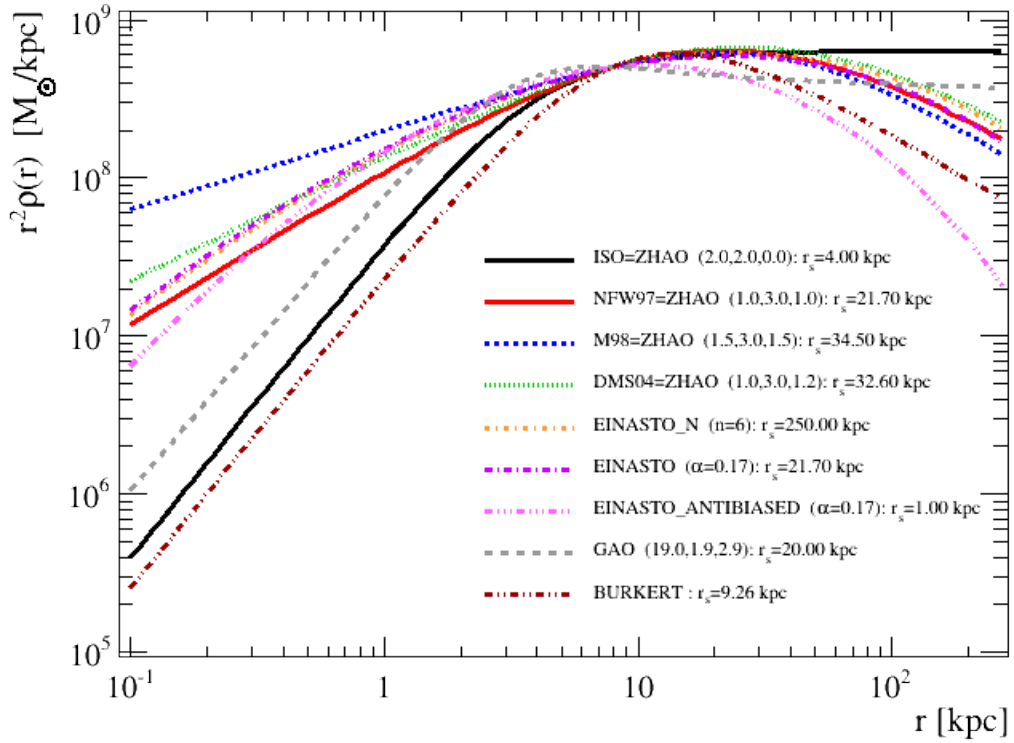

Figure 16: Different density profiles as a function of the radius. In red we see the typical NFW profile, we can observe that at radii close to zero the density is higher compared to other profiles that are rather flat, such as the Isothermal (black line), Einasto (orange and purple lines), Burkert (brown line). In all cases, the closer the radius is to zero, the greater the central density will be. Source `http://clumpy.gitlab.io/`.

a suppression of power on small scales, smoothing out density fluctuations. In SFDM, the central region of each dark matter halo gives rise to a core where no additional structure formation occurs, and the FDM field is in its ground state. This model describes a gravitationally bound object as having two distinct components. The inner part, characterized by the dominance of quantum pressure, is referred to as the core.

Too-big-to-fail **problem**

CDM simulations predict that the most massive subhalos within dark matter halos should host dwarf galaxies with significant luminosity and stellar mass. This conclusion can be obtained from two approaches, from baryon with simulations and from dark matter-only simulations implemented with semi-analytical models. In both cases, baryon physics is implemented. However, the observed satellite galaxies in the Local Group tend to be less luminous, and with older stellar populations

Various proposed solutions have been explored to address this issue, for instance, baryonic processes. The most massive subhalos can experience feedback effects, such as the expulsion of gas and the heating of the surrounding medium, due to processes like supernova explosions and stellar winds. These feedback mechanisms can suppress star formation within these subhalos. Since the implementation of baryon physics in the simulations is a work in progress, it is possible that these processes have not been fully studied yet.

0.4 Goals and outline of the thesis

As mentioned throughout this chapter, the standard cosmological model has successfully predicted a wide range of observations and phenomena in the universe, starting from the big bang theory as well as from an expanding universe and having CDM as one of the main ingredients. Additionally, CDM has shown good matching in large-scale structure formation, but it also has several small-scale tensions, which opens the door to new physics involving extension models. Throughout the last decades, different dark matter candidates have been proposed, showing different properties and, in one way or another, offering different solutions to these problems. With the use of numerical simulations and adequate comparison with the observations, the parameters of these models have been constrained so that they work in an adequate range. Constant research and adaptation to specific problems of these new theories contribute to the construction of knowledge in order to find concrete solutions to these issues.

The main goal of this thesis is to study the properties of dark matter in different astrophysical systems by considering different approaches, cosmological simulations, simulations at small scales, and observations. The study focuses on understanding the nature of dark matter, the distribution of the populations of halos, as well as the genealogical history of each one of them, its influence on the formation and evolution of large-scale structures in the universe as well as the agglomerations of small groups. Moreover, it seeks to understand the dynamic and structural effects that occur during halo mergers and how these processes are delimited by the nature of dark matter, and the way they impact the evolution of single and multiple configurations. This study has been performed using different dark matter models, namely CDM, GDM, and SFDM, as they each offer different alternatives to dark matter tensions in the standard cosmological model.

Particularly, in the study of cosmological simulations, one of the main objectives is the analysis of the formation and evolution of Hickson Compact Groups in GDM models. In order to understand how the nature of the dark matter model affects their spatial distribution, the total count at $z = 0$, the mechanisms of clustering as well as the kinematic and luminous properties. For this purpose, these agglomerations are attractive systems for study, because they are considered to be dominated by dark matter and also present different kinematic properties from other similar groups, such as a longer crossing time and high-velocity dispersion. Then, they represent alternative systems to those commonly studied, such as the spheroidal dwarfs of the local group.

Additionally, at small scales, the aim is to study how dark matter influences the dynamics of galaxy collisions and mergers, namely the virialization process, the shape of the density profile of the configurations, tidal disruption, and gravitational interaction. For that reason, the evolution of different assemblies has been explored, such as the single equilibrium configuration, boosted configuration, binary systems, and configurations embedded in an external potential well. For this study, two models have been compared, the first is CDM, which is part of the standard cosmological model, and the second one is SFDM, having an origin of a different nature than the former.

Finally, the last objective, but not least, is to research the relationship between baryonic and dark matter. Since at the observational level, the characteristics of dark matter are inferred from the baryon dynamics. This part of the work has been divided into two main parts. The first consists of the implementation of machine learning algorithms trained from synthetic galaxy catalogs, derived from N-body simulations, to predict some scaling relationships between stellar mass and magnitudes, bulge-disk relation, and halo abundance matching. Since the neural network only learns information available during training, it avoids having to consider additional information from baryon physics. Therefore, there would be an alternative to observational methods or theoretical models that are often complicated and have a large number of free parameters. The second part is related to the reconstruction of the rotation curves of the galaxies observed in MaNGA, where the bulge-disk decomposition has been carried out and the contribution that dark matter has in the total curve has been considered. the exploration of the different shapes of the density profiles in the observations gives guidelines as to how the simulated profiles should be, and therefore what the properties of the dark matter that generate them should be.

Cosmological simulations offer the advantage of being able to study the evolution of structures from the initial conditions, taken at high redshifts, up to the present day. For this reason, it is possible to trace the history of each halo in $z = 0$, the mergers in which it was involved, and its parents, and descendants. Moreover, it is possible to analyze the evolution of astrophysical systems, such as groups of galaxies, and the interaction they have with the environment that surrounds them. Thus, cosmological simulations can also be used to establish initial conditions for simulations of small-scale halo or galaxy collisions. On the other hand, small-scale simulations allow us to explore in detail the processes of tidal forces, virtualization, and the characteristics of density profiles. however, the main disadvantage of numerical simulations is usually related to boundary problems, resolution, and computational cost. In addition to that, the conditions of the dark matter candidate must be imposed. For observations, data processing can be complicated and some baryon physics considerations must be made. It is important to mention that there is a strong restriction in the limit of the observation instruments, so we can only study structures from a certain luminosity threshold and close to us. As can be seen, all the approaches discussed show advantages and disadvantages. However, studying them together brings us closer to understanding the nature and properties of dark matter.

Finally, is planned to study how the internal and external slopes of the adjusted density profile for Zhao and for SFDM change, that is, the values of their parameters for galaxies isolated or embedded in dense environments. This is with the intention of studying the dependence on the density profile, but also to have a broader context to create more realistic initial conditions.

This work is divided into four main parts. The first part is composed of an introduction and Chapter 1, where it is shown the Standard Cosmology starting from the formalism of general relativity and later the theory of perturbations at a linear and non-linear level. The second part deals with the GDM model and corresponds to Chapter 2. First, the free parameters which describe the theory are introduced, as well as the effect they produce on the power spectrum and therefore in the Halo and Stellar Mass Functions. Finally, the mechanisms of formation and evolution of Hickson Compact Groups are presented, the differences, between their kinematic and luminous properties, and the prevalence of these clusters today. In Chapter 3, small-scale simulations are shown, where different assemblies of configurations are studied using two different models, CDM and SFDM. First, the SFDM theory is introduced, followed by the presentation of algorithms to solve the Schrodinger-Poisson system. Then the stability of the halos in CDM and their evolution are shown. Likewise, the comparison of both models and the effects that dark matter has on the kinematics and stability of the different configurations are analyzed. Then, the fourth part corresponds to Chapter 4. First, different machine learning algorithms are presented to estimate the mass of galactic components such as disks, bulges, and dark matter halo. In addition, some scale relationships inferred from neural networks are shown as well as the comparison with observed galaxies in SDSS. Then, a study focused on the observations is carried out, particularly the rotation curves built from stellar velocity maps taking into account the baryonic components and the contribution of the halo, in order to study the different density profiles shown in nature.

Bibliography

[1] Aghanim, N., Akrami, Y., Ashdown, M., Aumont, J., Baccigalupi, C., Ballardini, M., Banday, A., Barreiro, R., Bartolo, N., Basak, S., et al. (2020). Planck 2018 results-vi. cosmological parameters. *Astronomy & Astrophysics*, 641:A6.

[2] Amendola, L. et al. (2013). Cosmology and fundamental physics with the Euclid satellite. *Living Rev. Rel.*, 16:6.

[3] Anderson, P. R. (1984). Effects of quantum fields on singularities and particle horizons in the early universe. ii. *Physical Review D*, 29(4):615.

[4] Araujo, A., Ló pez, D. F., and Pereira, J. G. (2019). De sitter-invariant special relativity and galaxy rotation curves. *Gravitation and Cosmology*, 25(2):157–163.

[5] Bergmann, P. G. (1976). *Introduction to the Theory of Relativity*. Courier Corporation.

[6] Boesgaard, A. M. and Steigman, G. (1985). Big bang nucleosynthesis: theories and observations. *Annual Review of Astronomy and Astrophysics*, 23(1):319–378.

[7] Busemann, H. (2012). *The geometry of geodesics*. Courier Corporation.

[8] Carroll, S. M. (2001). The Cosmological constant. *Living Rev. Rel.*, 4:1.

[9] Carroll, S. M. (2003). Why is the universe accelerating? *eConf*, C0307282:TTH09.

[10] Copeland, E. J., Sami, M., and Tsujikawa, S. (2006). Dynamics of dark energy. *International Journal of Modern Physics D*, 15(11):1753–1935.

[11] De Blok, W. (2010). The core-cusp problem. *Advances in Astronomy*, 2010.

[12] Dicke, R. H., Peebles, P. J. E., Roll, P. G., and Wilkinson, D. T. (1965). Cosmic black-body radiation. *Astrophysical Journal, vol. 142, p. 414-419*, 142:414–419.

[13] Dodelson, S. (2003). *Modern Cosmology*. Academic Press, Elsevier Science.

[14] Dodelson, S. and Schmidt, F. (2020). *Modern cosmology*. Academic press.

[15] Einstein, A. and Minkowski, H. (1920). The foundation of the generalised theory of relativity. *On a Heuristic Point of View about the Creation and Conversion of Light*, 1:22.

[16] Fixsen, D. (2009a). The temperature of the cosmic microwave background. *The Astrophysical Journal*, 707(2):916.

[17] Fixsen, D. J. (2009b). THE TEMPERATURE OF THE COSMIC MICROWAVE BACKGROUND. *The Astrophysical Journal*, 707(2):916–920.

[18] Gibbons, G. W. and Hawking, S. W. (1977). Cosmological event horizons, thermodynamics, and particle creation. *Physical Review D*, 15(10):2738.

[H.] H., P. Cosmology Lecture Notes, Part I: The Unperturbed Universe. University of Cambridge,.

[20] Kolb, E. W. and Turner, M. S. (1981). The early universe. *Nature*, 294(5841):521–526.

[21] Komatsu, E., Smith, K., Dunkley, J., Bennett, C., Gold, B., Hinshaw, G., Jarosik, N., Larson, D., Nolta, M., Page, L., Spergel, D., Halpern, M., Hill, R., Kogut, A., Limon, M., Meyer, S., Odegard, N., Tucker, G., Weiland, J., Wollack, E., and Wright, E. (2011). Seven-year Wilkinson Microwave Anisotropy Probe (WMAP) Observations: Cosmological Interpretation. *Astrophysical Journal*, 192(2):18.

[22] Koposov, S., Belokurov, V., Evans, N., Hewett, P., Irwin, M., Gilmore, G., Zucker, D., Rix, H.-W., Fellhauer, M., Bell, E., et al. (2008). The luminosity function of the milky way satellites. *The Astrophysical Journal*, 686(1):279.

[23] Larson, D., Dunkley, J., Hinshaw, G., Komatsu, E., Nolta, M., Bennett, C., Gold, B., Halpern, M., Hill, R., Jarosik, N., Kogut, A., Limon, M., Meyer, S., Odegard, N., Page, L., Smith, K., Spergel, D., Tucker, G., Weiland, J., Wollack, E., and Wright, E. (2011). Seven-year Wilkinson Microwave Anisotropy Probe (WMAP) Observations: Power Spectra and WMAP-derived Parameters. *Astrophysical Journal*, 192(2):16.

[24] Li, M., Li, X.-D., Wang, S., and Wang, Y. (2013). Dark Energy: A Brief Review. *Front. Phys. (Beijing)*, 8:828–846.

[25] McVittie, G. C. (1965). *General Relativity and Cosmology*. Urbana, University of Illinois Press.

[26] Norton, J. D. (1993). General covariance and the foundations of general relativity: eight decades of dispute. *Reports on Progress in Physics*, 56(7):791.

[27] Oort, J. H. (1950). The structure of the cloud of comets surrounding the solar system and a hypothesis concerning its origin. *Bulletin of the Astronomical Institutes of the Netherlands*, 11:91–110.

[28] Padmanabhan, T. (2008). Dark energy and gravity. *Gen. Rel. Grav.*, 40:529–564.

[29] Pauli, W. (2013). *Theory of relativity*. Courier Corporation.

[30] Peacock, J. A., Cole, S., Norberg, P., Baugh, C. M., Bland-Hawthorn, J., Bridges, T., Cannon, R. D., Colless, M., Collins, C., Couch, W., Dalton, G., Deeley, K., Propris, R. D., Driver, S. P., Efstathiou, G., Ellis, R. S., Frenk, C. S., Glazebrook, K., Jackson, C., Lahav, O., Lewis, I., Lumsden, S., Maddox, S., Percival, W. J., Peterson, B. A., Price, I., Sutherland, W., and Taylor, K. (2001). A measurement of the cosmological mass density from clustering in the 2df galaxy redshift survey. *Nature*, 410(6825):169–173.

[31] Riess, A. G., Casertano, S., Yuan, W., Bowers, J. B., Macri, L., Zinn, J. C., and Scolnic, D. (2021). Cosmic Distances Calibrated to 1% Precision with Gaia EDR3 Parallaxes and Hubble Space Telescope Photometry of 75 Milky Way Cepheids Confirm Tension with ΛCDM. *Astrophysical Journal Letters*, 908(1):L6.

[32] Schneider, P. (2006). *Extragalactic Astronomy and Cosmology*. Springer Berlin Heidelberg, Berlin, Heidelberg.

[33] Schwarzschild, K. (1916). On the gravitational field of a mass point according to Einstein's theory. *Sitzungsber. Preuss. Akad. Wiss. Berlin (Math. Phys.)*, 1916:189–196.

[34] Smoot, G. F., Bennett, C. L., Kogut, A., Wright, E., Aymon, J., Boggess, N., Cheng, E., De Amici, G., Gulkis, S., Hauser, M., et al. (1992). Structure in the cobe differential microwave radiometer first-year maps. *Astrophysical Journal, Part 2-Letters (ISSN 0004-637X), vol. 396, no. 1, Sept. 1, 1992, p. L1-L5. Research supported by NASA.*, 396:L1–L5.

[35] Springel, V., Frenk, C. S., and White, S. D. M. (2006). The large-scale structure of the universe. *Nature*, 440(7088):1137–1144.

[36] Tsujikawa, S. (2013). Quintessence: a review. *Classical and Quantum Gravity*, 30(21):214003.

[37] Wald, R. M. (2010). *General relativity*. University of Chicago press.

[38] Weinberg, S. (1972). *Gravitation and Cosmology: Principles and Applications of the General Theory of Relativity*. John Wiley and Sons, New York.

[39] Zwicky, F. (1933). The redshift of extragalactic nebulae. *Helvetica Physica Acta*, 6:110–127.

Chapter 1

Cosmological perturbations theory and structure formation

1.1 Linear Theory

Up to this moment, we have seen that the field equations can be solved when the FLRW metric is considered (20) with a source given by the energy-momentum tensor of a perfect fluid. Now, the spatial dependence on both sides of the equation will be introduced. In order to get the solution for these types of equations, the implementation of numeric methods is necessary. Also, it is possible to implement the Perturbations Theory, which consists of the implementation of small perturbations to the homogeneous solutions.

In order to study the linear theory, let's consider a perturbed line element

$$ds^2 = a^2\Big\{-(1-2\Psi)d\tau^2 - 2\vec{\nabla}_i\eta d\tau dx^i + \Big[(1+\frac{1}{3}h)\gamma_{ij} + D_{ij}\nu\Big]dx^i dx^j\Big\}, \tag{1.1}$$

where $D_{ij} = \vec{\nabla}_i\vec{\nabla}_j - \frac{1}{3}\gamma_{ij}\nabla^2$ is the differential traceless operator while the $\vec{\nabla}$ is the covariant derivative. Additionally, $a(\tau)$ is the scale factor in conformal time $\tau = \int dt/a(t)$, here γ_{ij} is the spatial metric. The perturbed metric has four scalar modes Ψ, h, η y ν.

It is also possible to define a metric for the line element. The most common are the synchronous gauge and the Newtonian gauge. In some cases, it is easy to manipulate the mathematical terms using the first one, with $\eta = \Psi = 0$. Now, for the Newtonian gauge, the perturbations are directly related to the physical quantities, in this case, $\nu = \eta = 0$. The Newtonian potential can be identified as $\phi = -\dfrac{h}{6}$.

For the Newtonian gauge, the line element can be written as

$$ds^2 = a^2(\tau)\left[-(1+2\psi)d\tau^2 + (1-2\phi)dx^i dx^j\right]. \tag{1.2}$$

The 4-vectors in this case can be expressed as $x^\mu \in (t, r, \theta, \phi)$, where the spatial components meet the relation $\vec{x} = a(t)\vec{r}$, being $\vec{r}$ comoving.

1.1.1 Perturbations Theory

In the same way that the line element has been perturbed, Einstein's equations (16) can be also perturbed. Therefore the perturbations become time and spatial-dependent. For that reason, both sides of the equations need to be perturbed, the part corresponding to the Einstein tensor and the part related to the energy-momentum tensor.

$$G^0_{\mu\nu} + \delta G_{\mu\nu} \quad = \quad 8\pi G(T^0_{\mu\nu} + \delta T_{\mu\nu}). \tag{1.3}$$

The temporal components of the Einstein tensor (25) can be expressed as follows

$$\begin{aligned} G_0^{0(0)} &= \frac{3}{a^2}H^2, \\ G_i^{0(0)} &= 0, \\ G_j^{i(0)} &= \frac{1}{a^2}(H^2 + 2\dot{H})\delta^i_j. \end{aligned} \tag{1.4}$$

Additionally, after several algebraic operations, the components at first order can be written as

$$\begin{aligned} \delta G^0_0 &= \frac{2}{a^2}\Big[\nabla^2\phi + 3H(\dot{\phi} + H\psi)\Big], \\ \delta G^0_i &= \frac{2}{a^2}(\dot{\phi} + H\psi)_{,i}, \\ \delta G^i_j &= -\frac{2}{a^2}\Big[\Big((H^2 + 2\dot{H})\psi + \ddot{\phi} + 2H\dot{\phi} + H\dot{\psi} + \frac{1}{2}\nabla^2(\psi - \phi\Big)\delta^i_j - \frac{1}{2}(\psi - \phi)D_{,ij}\Big]. \end{aligned} \tag{1.5}$$

Now, solving Einstein's equations in either of the two gauges, it is more convenient if the Fourier space k is considered. Therefore, the temporal-temporal, temporal-spatial, and spatial-spatial components from the field equations are

$$\begin{aligned} k^2\phi + 3H(\dot{\phi} + H\psi) &= 4\pi G a^2 \delta T^0_0, \\ k^2(\dot{\phi} + H\psi) &= 4\pi G a^2 (\bar{\rho} + \bar{P})\Theta, \\ \ddot{\phi} + H(\dot{\psi} + 2\dot{\phi}) + \left(2\frac{\ddot{a}}{a} - \frac{\dot{a}^2}{a^2}\right)\psi + \frac{k^2}{3}(\phi - \psi) &= \frac{4\pi}{3} G a^2 \delta T^i_i, \\ k^2(\phi - \psi) &= 12\pi G a^2 (\bar{\rho} + \bar{P})\sigma, \end{aligned} \tag{1.6}$$

where $(\bar{\rho} + \bar{P})\Theta \equiv ik^i \delta T^0_j$, for this case this results in $\Theta = ik^i v_j$.

Moreover, the 4-velocity can also be perturbed. The perturbed component is expressed as

$$U^\mu = a^{-1}\delta^\mu_0 + \delta U^\mu. \tag{1.7}$$

Since the following condition $g_{\mu\nu}U^\mu U^\nu = 1$ must be met, we obtain $\delta u^0 = -a^{-1}\phi$, which means,

$$u^0 = a^{-1}(1 - \phi), \quad u^i = \delta u^i. \tag{1.8}$$

With the above information, it is possible to calculate the components of the energy-momentum tensor. However, also the source of the field equations can be written in terms of the pressure and density, with their respective perturbations $\delta\rho = \rho - \bar{\rho}$, $\delta P = P - \bar{P}$, which must be of the same order as the perturbations of the metric. The temporal, spatial, and temporal-spatial components are shown below

$$\begin{aligned} T^0_0 &= (\rho + P)U^0 U_0 - P = (\rho + P)U^0 g_{0\mu} U^\mu - P \\ &= (\rho + P)a^{-1}(1 - \phi) g_{00} U^0 - P \\ &= (\rho + P)a^{-1}(1 - \phi)a^2(1 + 2\phi)a^{-1}(1 - \phi) - P \\ &= (\rho + P)a^{-1}(1 - \phi)a(1 + \phi) - P = \rho \\ &= \bar{\rho} + \delta\rho \end{aligned} \tag{1.9}$$

$$\begin{aligned} T^0_i &= (\rho + P)U^0 U_i = (\rho + P)a^{-1}(1 - \phi) g_{i\mu} U^\mu \\ &= (\rho + P)a^{-1}(1 - \phi) g_{ij} U^{ij} \\ &= (\rho + P)a^{-1}(1 - \phi)\Big[- a^2\Big((1 - 2\phi)\delta_{ij} + 2E_{ij}\Big)\delta u^j\Big] \\ &= (\rho + P)a(1 - \phi)\delta U^i = -(\rho + P)a\delta U^i \\ &= -(\bar{\rho} + \bar{P})a\delta U^i \end{aligned} \tag{1.10}$$

$$T^i_j = (\rho + P)U^i U_j - P\delta^i_j = (\rho + P)\delta U^i \delta U_j - P\delta^i_j = -P\delta^i_j \tag{1.11}$$

where $\bar{\rho}$ and $\bar{P}$ represent the energy density and the background pressure, respectively.
Now, the conservation of the energy-momentum tensor is a consequence of the field equations. Therefore, it must be fulfilled $T^\nu_{\mu;\nu} = 0$, which it is translated into

$$T^\nu_{\mu,\nu} = T^\nu_{\mu\nu} + \Gamma^\nu_{\lambda\nu} T^\lambda_\mu - \Gamma^\lambda_{\mu\nu} T^\nu_\lambda = 0. \tag{1.12}$$

The zero components of the last expression is the energy conservation

$$T^\nu_{0;\nu} = T^\nu_{0,\nu} + \Gamma^\nu_{\lambda\nu} T^\lambda_0 - \Gamma^\lambda_{0\nu} T^\nu_\lambda, \tag{1.13}$$

together with (1.9), (1.10),(1.11) and after some algebraic steps we obtain (42), where $\omega = \frac{P}{\rho}$ is the equation of state. Now, if we only consider the terms in first order, we can get the equation that involves the evolution of the perturbation in the density, compared to the background density

$$\dot{\delta} = -(1+\omega)(\Theta - 3\dot{\phi}) - 3H\left(\frac{\delta P}{\delta \rho} - \omega\right)\delta, \tag{1.14}$$

being

$$\delta \equiv \frac{\delta \rho}{\bar{\rho}} \tag{1.15}$$

the density contrast.
The spatial components, at the same time, can express the conservation of the momentum $T^{\nu}_{i;\nu} = T^{\nu}_{i,\nu} + \Gamma^{\nu}_{\lambda\nu}T^{\lambda}_{i} - \Gamma^{\lambda}_{i\nu}T^{\nu}_{\nu}$, after several operations and by expressing the terms in the Fourier space, we have

$$\dot{\Theta} = -H(1-3\omega)\Theta - \frac{\dot{\omega}}{1+\omega}\Theta + \frac{\delta P/\delta\rho}{1+\omega}k^2\delta - k^2\sigma + k^2\psi. \tag{1.16}$$

For the primordial perturbations, there is a relation between δP and $\delta\rho$ in terms of the sound of the speed, $\delta P = c_s^2\delta\rho$, where the adiabatic sound of the speed can be expressed as

$$c_s^2 = \frac{\bar{P}}{\bar{\rho}} = \omega\frac{\dot{p}}{p}\left(\frac{\dot{\rho}}{\rho}\right)^{-1} = -\omega\frac{\dot{P}}{p}\left(\frac{\dot{a}}{a}\right)^{-1}\frac{1}{3(1+\omega)}. \tag{1.17}$$

The previous equations are also valid for a fluid that is not coupled with other species, so they should be modified if the individual components interact with other from a different fluid. For completeness, the analogous expressions obtained in the synchronous gauge are shown, where the line element is defined as

$$ds^2 = a^2(\tau)(-d\tau^2 + (\delta_{ij} + h_{ij})dx^i dx^j), \tag{1.18}$$

then, the equations for the perturbations are

$$\begin{aligned}\dot{\delta} &= -(1+\omega)\left(\Theta + \frac{\dot{h}}{2}\right) - 3\frac{\dot{a}}{a}\left(\frac{\delta P}{\delta\rho} - \omega\right)\delta, \\ \dot{\Theta} &= -\frac{\dot{a}}{a}(1-3\omega)\Theta - \frac{\dot{\omega}}{1+\omega}\Theta + \frac{\delta P/\delta\rho}{1+\omega}k^2\delta - k^2\sigma.\end{aligned} \tag{1.19}$$

1.2 The Boltzmann equation

Until now, an energy-momentum tensor has been used for a perfect fluid. Nevertheless, this only applies to certain types of fluids and in certain situations. In general, to describe other types of fluids you need to know more properties than just density and pressure. In this case, dark matter and baryons can be described as a non-relativistic fluid. However, photons and neutrinos require a relativistic treatment in their phase space function. Also, the fluids are not isolated but can have interactions.

The components of the differential Boltzmann equation describing the evolution of the phase space distribution is

$$\frac{df}{dt} = \frac{\partial f}{\partial \tau} + \frac{dx^i}{d\tau}\frac{\partial f}{\partial x^i} + \frac{dq}{d\tau}\frac{\partial f}{\partial q} + \frac{dn^i}{d\tau}\frac{\partial f}{\partial n^i} = \left(\frac{\partial f}{\partial \tau}\right)_{\text{collision}} \tag{1.20}$$

where the term on the right-hand side refers to collisions.

1.2.1 Boltzmann equation for non-relativistic matter

In this case, we are dealing with massive particles, so the 4-momentum squared is expressed as $\mathrm{P}^2 = g_{\mu\nu}P^\mu P^\nu = -m^2$. Therefore, the following relationship between energy and momentum p given by $p^2 = g_{ij}P^iP^j$ is fulfilled,

$$E \equiv \sqrt{p^2 + m^2}. \tag{1.21}$$

Now, by using the metric and the previous energy relation, we can derive the components of the 4-momentum

$$P^0 = E(1-\Psi), \tag{1.22}$$

$$P_i = \frac{\mathcal{P}}{a}(1-\Phi)\hat{P}_i. \tag{1.23}$$

Once the previous expressions are obtained, the Boltzmann equation can be written. Observing the expression for the 4-moment eq. (1.10), it is convenient to use E as one of the dependent variables for the distribution function, so eq. (1.24) would be rewritten as

$$\frac{df}{dt} = \frac{\partial f}{\partial t} + \frac{\partial f}{\partial x^i}\frac{dx^i}{dt} + \frac{\partial f}{\partial E}\frac{dE}{dt} + \frac{\partial f}{\partial \hat{P}^i}\frac{d\hat{P}^i}{dt}. \tag{1.24}$$

The last term on the right-hand side corresponds to the product of two first-order terms, so it can be neglected. In turn, the second term on the same side can be rewritten using the equations (1.11), (1.22), and (1.23) as

$$\frac{\partial f}{\partial x^i}\frac{dx^i}{dt} = \frac{\mathcal{P}}{E}(1-\Phi-\Psi)\frac{\hat{P}^i}{a}\frac{\partial f}{\partial x^i}, \tag{1.25}$$

where the term $\dfrac{\partial f}{\partial x^i}$ is to first order, so the potentials can be neglected, leaving as

$$\frac{\partial f}{\partial x^i}\frac{dx^i}{dt} = \frac{\mathcal{P}}{E}\frac{\hat{P}^i}{a}\frac{\partial f}{\partial x^i}. \tag{1.26}$$

Regarding the part dependent on energy, it is convenient to consider the equations of the geodesic given by

$$\frac{dP^\mu}{dt} + \Gamma^\mu_{\alpha\beta}P^\alpha P^\beta = 0, \quad \Rightarrow \underbrace{\frac{dt}{d\lambda}}_{\equiv P^0}\frac{dP^0}{dt} = -\Gamma^0_{\alpha\beta}P^\alpha P^\beta. \tag{1.27}$$

Therefore, the equation of the geodesic for the first component can be written as

$$E(1-\Psi)[\dot{E}(1-\Psi) - E\dot{\Psi}] = -\Gamma^0_{\alpha\beta}P^\alpha P^\beta. \tag{1.28}$$

From (1.2) we have the following relations $g_{00,0} = -2\Psi_{,0}, g_{00,k} = -2\Psi_{,k}, g_{ij,0}\delta_{ij} = \Big(2a\dot{a}(1+2\Phi) + 2a^2\Phi_{,0}\Big), g^{00} = -(1-2\Psi)$, where $A_{,i}$ denotes $\dfrac{dA}{dx^i}$.
Now, in this case, the Christoffel symbols that appear in the second term of the geodesic equation (1.27), can be expressed as a function of scalar perturbations to the metric, as shown below

$$\begin{aligned} P^\alpha P^\beta \Gamma^0_{\alpha\beta} &= -\frac{(1-2\Psi)}{2}\Bigg[-2\Psi_{,0}E^2(1-2\Psi) - 4\Psi_{,k}E(1-\Psi)\frac{\mathcal{P}}{a}(1-\Phi)\hat{P}_k \\ &\quad -2[a\dot{a}(1+2\Phi) + a^2\Phi_{,0}]\delta_{ij}\left(\frac{\mathcal{P}^2}{a^2}(1-2\Phi)\hat{P}^i\hat{P}^j\right)\Bigg] \\ &\underbrace{=}_{\theta(1)} (1-2\Psi)\left[\Psi_{,0}E^2 + 2\Psi_{,k}E\frac{\mathcal{P}}{a}\hat{P}_k + \mathcal{P}^2(H+\Phi_{,0})\right], \end{aligned} \tag{1.29}$$

By introducing this expression on the right-hand side of Eq. (1.28) we have

$$E(1-\Psi)\Big[\dot{E}(1-\Psi)-E\dot{\Psi}] \quad = \quad -(1-2\Psi)\Big[\Psi_{,0}E^2+2\Psi_{,k}E\frac{\mathcal{P}}{a}\hat{P}_k+\frac{\mathcal{P}^2}{E}(H+\Phi_{,0})\Big].$$

resulting in

$$\frac{\dot{E}}{E} \quad = \quad -\frac{\mathcal{P}}{E}\frac{\hat{P}_k}{a}\Psi_{,k}-\frac{\mathcal{P}^2}{E^2}(H+\Phi_{,0}). \tag{1.30}$$

Finally, applying eqs. (1.26) and (1.30) in eq. (1.24) we have the Boltzmann equation for the case of first-order massive particles

$$\frac{\partial f}{\partial t}+\frac{\mathcal{P}}{E}\frac{\hat{P}_k}{a}\frac{\partial f}{\partial x^k}-\frac{\partial f}{\partial E}\left(\frac{\mathcal{P}^2}{E}H+\frac{\mathcal{P}^2}{E}\frac{\partial\Phi}{\partial t}+\frac{\hat{P}_k\mathcal{P}}{a}\frac{\partial\Psi}{\partial x^k}\right)=0. \tag{1.31}$$

Multiplying both sides of Eq. (1.31) by a volume of phase space and integrating, we get

$$\frac{\partial}{\partial t}\int\frac{d^3\mathrm{p}}{(2\pi)^3}f_{\rm dm}+\frac{1}{a}\frac{\partial}{\partial x^i}\int\frac{d^3\mathrm{p}}{2\pi)^3}f_{\rm dm}\frac{\mathrm{p}\hat{p}^i}{E}-\left[H+\frac{\partial\Phi}{\partial t}\right]\int\frac{d^3\mathrm{p}}{(2\pi)^3}\frac{\partial f_{\rm dm}}{\partial E}\frac{\mathrm{p}^2}{E} \tag{1.32}$$

$$-\frac{1}{a}\frac{\partial\Psi}{\partial x^i}\int\frac{d^3p}{(2\pi)^3}\frac{\partial f_{\rm dm}}{\partial E}\hat{P}^i\mathrm{P}=0. \tag{1.33}$$

Also taking into account that the density of dark matter and the velocity are expressed as

$$n_{\rm dm}=\int\frac{d^3p}{(2\pi)^3}f_{\rm dm},\quad v^i\equiv\frac{1}{n_{\rm dm}}\int\frac{d^3p}{(2\pi)^3}f_{\rm dm}\frac{\mathrm{p}\hat{P}^i}{E}, \tag{1.34}$$

Therefore, the Boltzmann equation can be derived into the continuity equation

$$\frac{\partial n_{\rm dm}}{\partial t}+\frac{1}{a}\frac{\partial(n_{\rm dm}v^i)}{\partial x^i}+3\left[\frac{\dot{a}}{a}+\frac{\partial\Phi}{\partial t}\right]n_{\rm dm}=0. \tag{1.35}$$

If we consider the contribution to zero order of the previous equation, the same result is obtained as in Eq. (49) that represented the solution to the Friedmann equation (42) for the case of massive particles

$$\frac{\partial n_{\rm dm}}{\partial t}+3\frac{\dot{a}}{a}n_{\rm dm}^{(0)}=0 \quad \Rightarrow \quad n_{\rm dm}^{(0)}\propto a^{-3}. \tag{1.36}$$

On the contrary, when considering first-order terms, a perturbation is made on the dark matter density given by $n_{\rm dm}=n_{\rm dm}^{(0)}[1+\delta(\vec{x},t)]$, where the perturbation corresponds precisely to the density contrast $\delta\rho/\rho$. So the first-order equation is expressed as

$$\frac{\partial\delta}{\partial t}+\frac{1}{a}\frac{\partial v^i}{\partial x^i}+3\frac{\partial\Phi}{\partial t}=0. \tag{1.37}$$

It is important to note that both new variables have been introduced into this dark matter regime ρ and $\vec{v}$. Therefore two additional equations will be needed to describe dark matter in this case. The first one corresponds to Eq. (1.37). To find the second one, consider Eq. (1.31), multiplying by the factor $d^3\mathrm{p}(\mathrm{p}/E)\hat{P}^j/(2\pi)^3$ and integrated. The equation for the first moment is

$$0 \quad = \quad \frac{\partial}{\partial t}\int\frac{d^3\mathrm{p}}{(2\pi)^3}f_{\rm dm}\frac{\mathrm{p}\hat{P}^j}{E}+\frac{1}{a}\frac{\partial}{\partial x^i}\int\frac{d^3\mathrm{p}}{(2\pi)^3}f_{\rm dm}\frac{\mathrm{p}^2\hat{p}^i\hat{p}^j}{E^2} \tag{1.38}$$

$$-\left[\frac{\dot{a}}{a}+\frac{\partial\Phi}{\partial t}\right]\int\frac{d^3\mathrm{p}}{(2\pi)^3}\frac{\partial f_{\rm dm}}{\partial E}\frac{\mathrm{p}^3\hat{P}^j}{E^2}-\frac{1}{a}\frac{\partial\Psi}{\partial x^i}\int\frac{d^3\mathrm{p}}{(2\pi)^3}\frac{\partial f_{\rm dm}}{\partial E}\frac{\hat{p}^i\hat{p}^j\mathrm{p}^2}{E}. \tag{1.39}$$

The first term is directly related to the density and velocity of dark matter, while the second can be neglected as it is of second order. The other terms must be treated integrating by parts and after some algebraic steps the following expression is obtained for the first moment of eq. of Boltzmann

$$\frac{\partial(n_{\rm dm}v^j)}{\partial t} + 4\frac{\dot{a}}{a}n_{\rm dm}v^j + \frac{n_{\rm dm}}{a}\frac{\partial\Psi}{\partial x^j} = 0. \tag{1.40}$$

By using the relation (1.36), one has that the first order equation is

$$\frac{\partial v^j}{\partial t} + \frac{\dot{a}}{a}v^j + \frac{1}{a}\frac{\partial\Psi}{\partial x^j} = 0. \tag{1.41}$$

The equations (1.37), (1.41) are the equations that govern the evolution of the density contrast and velocity of the dark matter. It is important to note that in the previous calculations terms of equal or higher order to p/E have been neglected since we are considering that dark matter cools. However, if one wants to deal with dark matter whose mass is very small, such as massive neutrinos, then these terms must be taken into account.

Since dark matter is studied in this work, the procedure to obtain the corresponding Boltzmann equation has been broken down in this subsection, as well as the evolution of the perturbations. For completeness, the analogous equations for the different species will be shown below. The reader may refer to the following references [6, 14] for further details regarding the procedures.

1.2.2 Cold Dark Matter

The equations (1.37) and (1.41) can be written in conformal time and expressed in Fourier space, resulting in [14]:

$$\dot{\delta}_{\rm dm} = -\theta_c + 3\dot{\phi}, \tag{1.42}$$

$$\dot{\theta}_{\rm dm} = -\frac{\dot{a}}{a}\theta_c + k^2\psi, \tag{1.43}$$

where the relation $\theta = ik^i v_j$ has been considered. These same expressions can be obtained directly from the set of equations (1.14) and (1.16) that describe the evolution of perturbations in an uncoupled fluid in the Newtonian gauge. When considering a perfect non-collisional fluid, as is the case of cold dark matter, then the pressure and viscosity are equal to zero, which results in Eqs. (1.42).

For completeness, this result is also shown in the synchronous metric

$$\dot{\delta}_c = -\frac{1}{2}\dot{h}. \tag{1.44}$$

1.2.3 Massless neutrinos

In this case, there is a barotropic relationship that can be inferred from the components of the energy-momentum tensor $\rho_\nu = 3P_\nu = -T^0_0 = T^i_i$.For this case, the Boltzmann equation reduces to the case of massless particles,

$$F_\nu(\vec{k},\hat{n},\tau) = \sum_{l=0}^{\infty}(-i)^l(2l+1)F_{\nu l}(\vec{k},\tau)P_l(\hat{k}\cdot\hat{n}), \tag{1.45}$$

where $F_{\nu l} = j_l(kr)$ given by the Bessel functions.

The evolution of the Boltzmann equation in the Newtonian gauge is expressed as

$$\frac{\partial F_\nu}{\partial\tau} + ik\mu F_\nu = 4(\dot{\phi} - ik\mu\psi). \tag{1.46}$$

Finally, the set of equations governing the evolution of the phase space distribution function for massless neutrinos in the Newtonian gauge are [14]

$$\dot{\delta}_\nu = -\frac{4}{3}\theta_\nu + 4\dot{\phi}, \tag{1.47}$$

$$\dot{\theta}_\nu = k^2\left(\frac{1}{4}\delta_\nu - \sigma_\nu\right) + k^2\psi, \tag{1.48}$$

$$\dot{F}_{\nu l} = \frac{k}{2l+1}\Big(lF_{\nu(l-1)} - (l+1)F_{\nu(l+1)}\Big], \quad l \geq 2. \tag{1.49}$$

For the synchronous gauge

$$\dot{\delta}_\nu = -\frac{4}{3}\theta_\nu - \frac{2}{3}h, \tag{1.50}$$

$$\dot{\theta}_\nu = k^2\left(\frac{1}{4}\delta_\nu - \sigma_\nu\right) \tag{1.51}$$

$$\dot{F}_{\nu 2} = 2\dot{\sigma}_\nu, \tag{1.52}$$

$$\dot{F}_{\nu l} = \frac{k}{2l+1}\Big(lF_{\nu(l-1)} - (l+1)F_{\nu(l+1)}\Big], \quad l \geq 3. \tag{1.53}$$

1.2.4 Photons

Before recombination, photons and baryons interact via Compton scattering. The linear collision operators for this effect are [14]

$$\left(\frac{\partial F_\gamma}{\partial \tau}\right)_C = an_e\sigma_T\Big[-F_\gamma + F_{\gamma 0} + 4\vec{n}\cdot\vec{v}_e - \frac{1}{2}(F_{\gamma 2} + G_{\gamma 0} + G_{\gamma 2})P_2\Big], \tag{1.54}$$

$$\left(\frac{\partial G_\gamma}{\partial \tau}\right)_C = an_e\sigma_T\Big[-G_\gamma + \frac{1}{2}(F_{\gamma 2} + G_{\gamma 0} + G_{\gamma 2})(1 - P_2)\Big], \tag{1.55}$$

where n_e y $\vec{v}_e$ are the average density and speed of the electrons. Additionally, $F_\gamma(\vec{k}, \hat{n}, \tau)$ is the summed total phase space density over all polarizations, whereas $G_\gamma(\vec{k}, \hat{n}, \tau)$ is the difference of the polarized components. Therefore the equations that govern the dynamics of photons is

$$\dot{\delta}_\gamma = -\frac{4}{3}\theta_\gamma + 4\dot{\phi}, \tag{1.56}$$

$$\dot{\theta}_\gamma = k^2\left(\frac{1}{4}\delta_\gamma - \sigma_\gamma\right) + k^2\psi + an_e\sigma_T(\theta_b - \theta_\gamma), \tag{1.57}$$

$$\dot{F}_{\gamma 2} = \frac{8}{15}\theta_\gamma - \frac{3}{5}kF_{\gamma 3} + \frac{4}{15}\dot{h} + \frac{8}{5}\dot{\eta} - \frac{9}{5}an_e\sigma_T\sigma_\gamma + \frac{1}{10}an_e\sigma_T(G_{\gamma 0} + G_{\gamma 2}), \tag{1.58}$$

$$\dot{F}_{\gamma l} = \frac{k}{2l+1}\Big[lF_{\gamma(l-1)} - (l+1)F_{\gamma(l+1)}\Big] - an_e\sigma_T F_{\gamma l}, \tag{1.59}$$

$$\dot{G}_{\gamma l} = \frac{k}{2l+1}\Big[lG_{\gamma(l-1)} - (l+1)G_{\gamma(l+1)}\Big] + an_e\sigma_T\left[-G_{\gamma l} + \frac{1}{2}(F_{\gamma 2} + G_{\gamma 0} + G_{\gamma 2})\left(\delta_{l0} + \frac{\delta l2}{5}\right)\right], \tag{1.60}$$

where γ and b refer to photons and baryons, respectively.

In the synchronous metric we have

$$\dot{\delta}_\gamma = -\frac{4}{3}\theta_\gamma - \frac{2}{3}\dot{h}, \tag{1.61}$$

$$\dot{\theta}_\gamma = k^2\left(\frac{1}{4}\delta_\gamma - \sigma_\gamma\right) + an_e\sigma_T(\theta_b - \theta_\gamma), \tag{1.62}$$

$$\dot{F}_{\gamma 2} = \frac{8}{15}\theta_\gamma - \frac{3}{5}kF_{\gamma 3} - \frac{9}{5}an_e\sigma_T\sigma_\gamma + \frac{1}{10}an_e\sigma_T(G_{\gamma 0} + G_{\gamma 2}), \tag{1.63}$$

$$\dot{F}_{\gamma l} = \frac{k}{2l+1}\Big[lF_{\gamma(l-1)} - (l+1)F_{\gamma(l+1)}\Big] - an_e\sigma_T F_{\gamma l}, \tag{1.64}$$

$$\dot{G}_{\gamma l} = \frac{k}{2l+1}\Big[lG_{\gamma(l-1)} - (l+1)G_{\gamma(l+1)}\Big] + an_e\sigma_T\left[-G_{\gamma l} + \frac{1}{2}(F_{\gamma 2} + G_{\gamma 0} + G_{\gamma 2})\left(\delta_{l0} + \frac{\delta l2}{5}\right)\right], \tag{1.65}$$

1.2.5 Baryons

In the case of baryons, they can be described in the same way as a non-relativistic fluid, so the following relations are fulfilled $\delta P_b/\delta\rho_b = c_s^2 = w$. The perturbation equations in the Newtonian gauge are [14]

$$\dot{\delta}_b = -\theta_b + 3\dot{\phi}, \tag{1.66}$$

$$\dot{\theta}_b = -\frac{\dot{a}}{a}\theta_b + c_s^2k^2\delta_b + \frac{4\bar{\rho}}{3\bar{\rho}_b}an_e\sigma_T(\theta_\gamma\theta_b) + k^2\psi. \tag{1.67}$$

In the synchronous metric the expression is as follows

$$\dot{\delta}_b = -\theta_b - \frac{1}{2}\dot{h}, \tag{1.68}$$

$$\dot{\theta}_b = -\frac{\dot{a}}{a}\theta_b + c_s^2k^2\delta_b + \frac{4\bar{\rho}}{3\bar{\rho}_b}an_e\sigma_T(\theta_\gamma\theta_b). \tag{1.69}$$

The speed of sound is defined as

$$c_s^2 = \frac{\dot{P}_b}{\dot{\rho}_b} = \frac{k_BT_b}{\mu}\left(1 - \frac{1}{3}\frac{dlnT_b}{lna}\right) \tag{1.70}$$

1.3 Matter Power Spectrum

The power spectrum describes the density contrast δ as a function of the scale k through a two-point correlation function. If the perturbations are generated by a particular inflation model, then the power spectrum contains the complete statistical information of the entire model.

The dimensionless power spectrum is expressed as

$$\Delta^2(k) = \Delta^2(k_0)\left(\frac{k}{k_0}\right)^{n_s(k_0)-1}, \tag{1.71}$$

where $n_s - 1 \equiv \dfrac{d\ln P^2}{d\ln k}$ is the spectral index and k_0. According to observational measurements, the spectral index is very close to 1[12]. If S is considered a scalar variable, the power spectrum would be denoted by

$$\langle S(\vec{k},\tau)S(\vec{k'},\tau) = \frac{2\pi^2}{k^3}\delta_D(\vec{k} - \vec{k'})P_s(k), \tag{1.72}$$

where δ_D corresponds to the Dirac delta function. This expression is defined over homogeneity and statistical isotropy. Therefore, the scale-dependent power spectrum of matter that describes the perturbations can be written in its dimensionless version as

$$\Delta_\delta(\tau, k) \equiv \frac{k^3 P(\tau, k)}{2\pi^2} \propto k^4. \tag{1.73}$$

In the epoch of dominant matter, the power spectrum can also be written in terms of the primordial spectrum and the growth factor

$$P(t, k) = D_+^2 P_0(k), \tag{1.74}$$

where $P_0(k)$ denotes the primordial power spectrum and is usually described through the Zeldovich prescription $P_0(k) = Ak_s^n$, being A is a normalization constant. Additionally, the growth factor describes the amplitude through a simple differential equation in terms of the densities of the cosmological model

$$D_+(a) \propto \frac{H(a)}{H_0} \int_0^a \frac{da'}{\left[\Omega_m/a' + \Omega_\Lambda a'^2 - (\Omega_m + \Omega_\Lambda)\right]^{3/2}}. \tag{1.75}$$

1.3.1 Transfer function

Sometimes, perturbations with different wave numbers evolved differently in the very early Universe. This modifies the matter power spectrum from the power law form given above. The transfer functions $T(k)$ encodes the information on the evolution of the density perturbation $\delta(k)$, and the matter power spectrum reads

$$P_0(k) = Ak^n T^2(K). \tag{1.76}$$

The transfer function can be computed for any cosmological model if the matter content of the universe is specified. In particular, it depends on the nature of dark matter.

1.4 Evolution of non-linear structures

Linear perturbation theory has a limited range of applicability; in particular, the evolution of structures like clusters of galaxies cannot be treated within the framework of linear perturbation theory. Although numerical methods are required to study the evolution of matter, there are some cases where the description of non-linear evolution for the distribution of mass in the universe can be done analytically.

1.4.1 Spherical collapse

The spherical collapse model is possibly the simplest to study the evolution of nonlinear structures. For this, an Einstein-de-Sitter-type universe is considered, that is, a spatially flat universe with the dominant matter. In fact, the equations of motion that describe the size of the sphere are identical to the Friedmann equations that describe the cosmic expansion of the universe, but with an effective matter density Ω'_m.

$$\frac{1}{a}\frac{da}{dt} = H_0\left(\Omega'_m a^{-3} + (1 - \Omega'_m)a^{-2}\right)^{1/2}. \tag{1.77}$$

According to the theory of relativity, the evolution of this spherical overdensity will be independent of the background evolution. Considering a spherical region in an expanding universe with a density given by

$$\rho(t) = [1 + \delta(t)]\bar{\rho(t)}, \tag{1.78}$$

where δ is the density contrast (1.15). Furthermore, it is assumed that the density is constant inside the sphere. The density perturbations for small times are assumed to be small, so the linear theory applies and, therefore, one has $\delta(t) \propto D_+(t)$, as long as $\delta \ll 1$.

The parametric solutions for Eq. (1.77), in conformal time are [10]

$$R(\theta) = A(1-\cos\theta), \tag{1.79}$$
$$t(\theta) = B(1-\sin\theta), \tag{1.80}$$

where $\theta = H_0\tau(\Omega'_m - 1)^{1/2}$. Also, $A = r_0\Omega'_m/2(\Omega'_m - 1)$, $B = H_0^{-1}\Omega'_m/2(\Omega'_m - 1)^{3/2}$.

Let's also consider that R is the initial comoving radius of the overdensity, again, as long as it holds that $\delta \ll 1$. The mass inside this sphere is

$$M = \frac{4\pi}{3}R^3\rho_0(1+\delta_i) \sim \frac{4\pi}{3}R^3\rho_0. \tag{1.81}$$

The sphere will expand slower than the universe outside, allowing the density contrast to grow even larger. If the initial density is large enough, then the expansion will continue until it reaches the maximum physical radius when $\theta = \pi$, $R = 2A$, and $t = B\pi$. After which the spherical collapse will happen at a time $t_{\rm col} = 2B$, just when $\theta = 2\pi$.

Virialization process

The sphere will not collapse to a single point unless the density is perfectly homogeneous and the particles inside move in perfectly radial orbits. However, in reality, there are small gravitational fluctuations that deflect particles from their trajectories. These particles will disperse the collapsing particles, causing the inhomogeneities to amplify. As a consequence, the virialization process is known as *violent relaxation*, which happens in a time as short as the collapse itself. The system get virialized when the following relation fulfill $\theta_{\rm vir} = \dfrac{2\pi}{3}$, when overdensity takes the form

$$\Delta_{\rm vir} = \frac{\rho(2\pi/3)}{\bar{\rho}(2\pi)}, \tag{1.82}$$

when $t_{\rm vir} = t_{\rm col}(\theta = 2\pi)$.

1.4.2 *The halo model*

The halo model is an analytical model that describes the distribution of dark matter. It is based on the spherical collapse model, where matter collapses as spherically symmetrical objects. This model also predicts the final state as a virialized halo given an initial perturbation. In the simplest form of the halo model, it is assumed that all dark matter is contained within so-called *halos of dark matter*, which collapse into larger and larger halos. In general, the halo model is a way to account for nonlinear structure growth.

One parameter that is usually considered is the *variance* smoothed matter density field, $\sigma(R)$. This variance is defined in function of the comoving distance R, which is defined by the size of a function *top-hat window*

$$W(x) = \frac{3\Big(sin(x) - x\cos(x)\Big)}{x^3}. \tag{1.83}$$

Then, the root mean square of the Gaussian field fluctuations, described through the power spectrum in the dominant matter epoch, is expressed as shown below

$$\sigma^2(R) = \int P(k, z=0)|W(Rk)|^2\frac{k^3}{2\pi}d\ln k, \tag{1.84}$$

where $P(k, z)$ is the matter power spectrum discussed in section 1.3.

In order to associate particular halos to particular values of $\sigma(R)$, we need to connect the size of the *window* function R, with the mass of the halo M. For this, it must be considered that R is the comoving region that contains the amount of matter associated with the halo. Being a comoving region, it will always contain the same amount of matter as it expands,

$$R(M) = \left(\frac{3M}{4\pi\rho_{m,0}}\right)^{1/3}, \tag{1.85}$$

where $\rho_{m,0} = \Omega_{m,0}\rho_{\mathrm{crit},0}$. The halo count can be scaled with observations in a defined region of $8Mpc/h$. Therefore, the power spectrum as well as the mass function can be scaled through the analytical normalization of σ. The very specific value of $8Mpc/h$ is used since the value of the associated variance σ_8 is close to unity [1]. This parameter is crucial in Cosmology since they have a great influence on the growth of fluctuations in the early universe.

Mass functions

The numbers of halos in the high-redshift Universe are critical for determining the numbers of stars and galaxies at high redshift, for understanding reionization, and for guiding observational campaigns designed to search for the first stars and galaxies. The mass function describes the distribution of the dark matter halos. Specifically, it gives the number density of dark matter halos per mass interval. The evolution of mass function is highly sensitive to cosmology because matter density controls the rate at which structure grows.

The differential halo mass function, or halo mass function [26] for short, dn/dM, is defined as the number of halos of mass M per unit volume per unit interval in M. A general mathematical form for the mass function is [19, 23, 11]

$$\frac{dn}{dM} = f(\sigma)\frac{\rho_m}{M}\frac{d\ln\sigma^{-1}}{dM}, \tag{1.86}$$

where $\rho_m = \rho_{\mathrm{crit}}\Omega_m$ is the mean matter density and $f(\sigma)$ is known as the *halo multiplicity function*. Such a function depends on how halos are defined. In 1.1 we can see a compilation of different fitting functions. All of them have been derived empirically and contrasted with observations. Implicitly, the mass function depends on the linear matter power spectrum $P(k)$ in order to map from M to σ. In fig. 1.2, the mass function for some of the fitting functions in Fig. 1.1. We can observe these functions are similar within the range shown, all of them have been plotted at $z = 0$.

1.5 Numerical simulations of structure formation

The cosmic structure has formed as a result of the gravitational amplification of primordial density fluctuations together with the action of other physical processes (adiabatic gas dynamics, radiative cooling, photoionization, recombination, and radiative transfer). These complex nonlinear processes, acting over a wide range of length scales (from kiloparsecs to tens of megaparsecs), make this a difficult problem for computation. During the last two decades, significant progress has been made in developing numerical methods and statistical tools for analyzing simulations and data.

1.5.1 The Gadget code

In this work, we will use the Gadget-4 (**GA**laxies with **D**ark matter and **G**as int**E**rac**T**) code, which is a massively parallel code for $N-$body/hydrodynamical cosmological simulation. It can be applied to a variety of different types of simulations. The code can be used for plain Newtonian dynamics or for cosmological integration in arbitrary cosmologies, both with or without boundary conditions.

Table 1: Compilation of Fitting Functions

Ref.	Fitting Function $f(\sigma)$	Mass Range	Redshift Range	Cosmology Fitted
Press and Schechter (1974)	$f_{\rm PS}(\sigma) = \sqrt{\frac{2}{\pi}}\frac{\delta_c}{\sigma}\exp\left[-\frac{\delta_c^2}{2\sigma^2}\right]$	–	–	–
Sheth et al. (2001)	$f_{\rm ST}(\sigma) = A\sqrt{\frac{2a}{\pi}}\left[1+\left(\frac{\sigma^2}{a\delta_c^2}\right)^p\right]\frac{\delta_c}{\sigma}\exp\left[-\frac{a\delta_c^2}{2\sigma^2}\right]$, $A = 0.3222$, $a = 0.707$, $p = 0.3$.	–	–	Einstein-de Sitter
Jenkins et al. (2001)	$f_{\rm J}(\sigma) = 0.315\exp\left[\lvert\ln\sigma^{-1}+0.61\rvert^{3.8}\right]$	$-1.2 < \ln\sigma^{-1} < 1.05$	$0-5$	τCDM, ΛCDM
Reed et al. (2003)	$f_{\rm R03}(\sigma) = f_{ST}(\sigma)\exp\left[\frac{-0.7}{\sigma\cosh(2\sigma)^5}\right]$	$-1.7 < \ln\sigma^{-1} < 0.9$	$0-15$	$\Omega_M = 0.3$, $\Omega_\Lambda = 0.7$
Warren et al. (2006)	$f_{\rm W}(\sigma) = 0.7234\left(\sigma^{-1.625}+0.2538\right)\exp\left[\frac{-1.1982}{\sigma^2}\right]$	$10^{10}{\rm M}_\odot < M < 10^{15}{\rm M}_\odot$	0	ΛCDM: WMAP1
Reed et al. (2007)	$f_{\rm R07}(\sigma) = \nu\exp\left[-\frac{ca\frac{\delta_c^2}{\sigma^2}}{2}-\frac{0.03\left(\frac{\delta_c}{\sigma}\right)^{0.6}}{(n_{\rm eff}+3)^2}\right]$ $\times A\sqrt{\frac{2a}{\pi}}\left[1+\left(\frac{1}{\frac{\delta_c^2}{\sigma^2}a}\right)^p+0.6G_1(\sigma)+0.4G_2(\sigma)\right]$ $n_{\rm eff} = 6\frac{d\log\sigma^{-1}}{d\log M}-3$, $G_1(\sigma) = \exp\left[-\frac{\ln(\sigma^{-1}-0.4)^2}{0.72}\right]$, $G_2(\sigma) = \exp\left[-\frac{\ln(\sigma^{-1}-0.75)^2}{0.08}\right]$	$-1.7 < \ln\sigma^{-1} < 0.9$	$0-30$	ΛCDM: WMAP1
Tinker and Kravtsov (2008)	$f_{\rm T}(\sigma,z) = A\left(\left(\frac{b}{\sigma}\right)^a+1\right)\exp\left[-\frac{c}{\sigma^2}\right]$, $A = 0.186\,(1+z)^{-0.14}$, $a = 1.47\,(1+z)^{-0.06}$, $b = 2.57\,(1+z)^{-\alpha}$, $c = 1.19$, $\alpha = \exp\left[-\left(\frac{0.75}{\ln(\Delta_{vir}/75)}\right)^{1.2}\right]$	$-0.6 < \ln\sigma^{-1} < 0.4$	$0-2.5$	ΛCDM: WMAP1, WMAP3+
Crocce et al. (2010)	$f_{\rm Cr}(\sigma) = A\left(\sigma^{-a}+b\right)\exp\left[-\frac{c}{\sigma^2}\right]$, $A = 0.58\,(1+z)^{-0.13}$, $a = 1.37\,(1+z)^{-0.15}$, $b = 0.3\,(1+z)^{-0.084}$, $c = 1.036\,(1+z)^{-0.024}$	$10^{10.5}{\rm M}_\odot < M < 10^{15.5}{\rm M}_\odot$	$0-2$	$(\Omega_M, \Omega_\Lambda, n, h, \sigma_8) = (0.25, 0.75, 0.95, 0.7, 0.8)$
Courtin et al. (2010)	$f_{\rm Co}(\sigma) = f_{\rm ST}(\sigma)$, $A = 0.348$, $a = 0.695$, $p = 0.1$	$-0.8 < \ln\sigma^{-1} < 0.7$	0	ΛCDM: WMAP5
Bhattacharya et al. (2011)	$f_{\rm B}(\sigma,z) = A\sqrt{\frac{2}{\pi}}\exp\left[-\frac{a\delta_c^2}{2\sigma^2}\right]\left[1+\left(a\frac{\delta_c^2}{\sigma^2}\right)^{-p}\right]\left(\frac{\delta_c^2}{\sigma^2}\sqrt{a}\right)^q$, $A = 0.333\,(1+z)^{-0.11}$, $a = 0.788\,(1+z)^{-0.01}$, $p = 0.807$, $q = 1.795$	$10^{11.8}{\rm M}_\odot < M < 10^{15.5}{\rm M}_\odot$	$0-2$	wCDM+
Angulo et al. (2012)	$f_{\rm A}(\sigma) = A\left[\left(\frac{b}{\sigma}\right)^a+1\right]\exp\left[-\frac{c}{\sigma^2}\right]$, $(A,a,b,c) = (0.201, 1.7, 2.08, 1.172)$ or $(A,a,b,c)_{\rm SUB} = (0.265, 1.9, 1.675, 1.4)$	$10^{8}{\rm M}_\odot < M < 10^{16}{\rm M}_\odot$	0	ΛCDM: WMAP1
Watson et al. (2013)	$f_{\rm WFOF}(\sigma,z) = f_{\rm T}(\sigma,z)$, $A = 0.282$, $a = 1.406$, $b = 2.163$, $c = 1.21$	$-0.55 < \ln\sigma^{-1} < 1.31$	$0-30$	ΛCDM: WMAP5
Watson et al. (2013)	$f_{\rm WSO}(\sigma,z) = \Gamma(\Delta,\sigma,z)f_{\rm T}(\sigma,z)$, $(A,a,b,c)_{z=0} = (0.194, 2.267, 1.805, 1.287)$, $(A,a,b,c)_{z>6} = (0.563, 874, 3.810, 1.453)$, $(A,a,b,c)_{0<z<6} =$ $\Omega_M(z)\times(1.907(1+z)^{-3.216}+0.074,$ $3.136(1+z)^{-3.058}+2.349,$ $5.907\times(1+z)^{-3.599}+2.344,\ 1.318)$, $\Gamma(\Delta,\sigma,z) = C(\Delta)\left(\frac{\Delta}{178}\right)^{d(z)}\exp\left[\frac{p\left(1-\frac{\Delta}{178}\right)}{\sigma^q}\right]$, $C(\Delta) = 0.947\exp\left[0.023\left(\frac{\Delta}{178}-1\right)\right]$, $d(z) = -0.456\Omega_M(z)-0.139$, $p = 0.072$, $q = 2.130$.	$-0.55 < \ln\sigma^{-1} < 1.05$ $(z=0)$, $-0.06 < \ln\sigma^{-1} < 1.024$ $(z>0)$	$0-30$	ΛCDM: WMAP5

Figure 1.1: Different analytic halo mass functions from Press and Schechter in 1974 to Watson in 2013. The mass range where these expressions are valid is also shown, as well as the redshift. Source: [16]

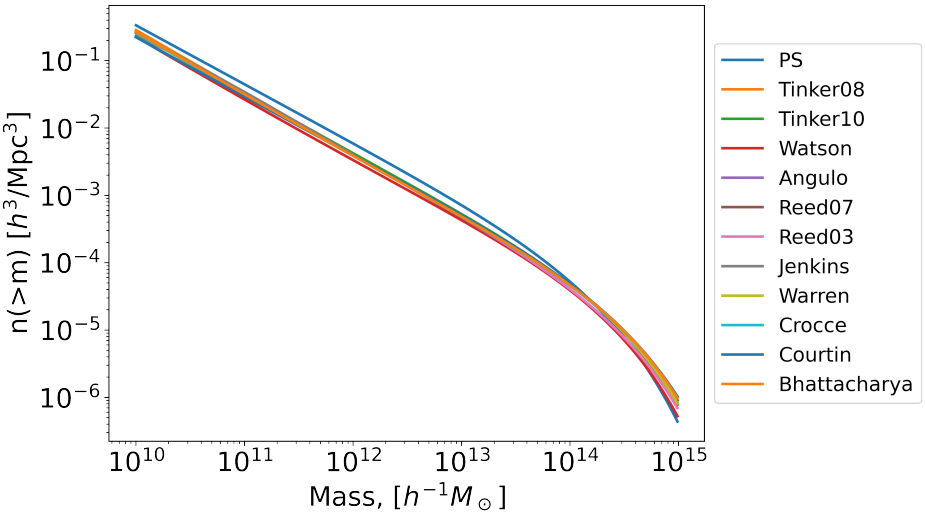

Figure 1.2: Halo mass function for some empirical functions. Here, we observe the number of halos per unit of mass, per unit of volume. The plots were constructed using the halo mass function calculator [16].

In this chapter, we have seen a simplified description of the evolution of density perturbations in the universe. In order to solve the equation (1.3), several assumptions have to be considered and they are restricted to the simplest systems, treating a density perturbation as a single, highly symmetrical object that collapses. Additionally, the collapsing matter is non-relativistic ($\rho \ll P$), and that collapse is only possible on sub-horizon scales ($k \ll aH$). This means that in ΛCDM we can restrict to Newtonian perturbation equations. Therefore, we have to consider the collisionless Boltzmann equation (1.24)

$$\frac{df}{dt} = \frac{\partial f}{\partial t} + \mathbf{v}\frac{\partial f}{\partial \mathbf{x}} - \frac{\partial \Phi}{\partial \mathbf{r}}\frac{\partial f}{\partial \mathbf{v}}, \tag{1.87}$$

and the non-relativistic version of the Poisson equation, expressed in terms of comoving coordinates

$$\nabla^2\Phi(\mathbf{r},t) = 4\pi G \int f(\mathbf{r},\mathbf{v},t)d\mathbf{v}. \tag{1.88}$$

The dynamics of any group of collisionless particles interacting only through gravity can be described by the following Hamiltonian expression

$$H = \sum_i \frac{\mathbf{p}_i^2}{2m_i a(t)^2} + \frac{1}{2}\sum_{ij}\frac{m_i m_j \varphi(\mathbf{x}_i - \mathbf{x}_j)}{a(t)}, \tag{1.89}$$

where $H = H(p_1, \dots p_N, x_1, \dots, x_n, t)$ are comoving coordinates vectors, and the corresponding canonical momenta are given by $p_i = a^2 m_i \dot{x}_i$. The explicit time dependence of the Hamiltonian arises from the evolution $a(t)$ of the scale factor, which is given by the Friedman-Lemaitre model [21]. The Newtonian potential is a sum over the discretized potentials

$$\phi(\mathbf{x}) = \sum_i^N m_i \varphi(\mathbf{x} - \mathbf{x}_i). \tag{1.90}$$

The explicit time dependence of Hamiltonian arises from the evolution $a(t)$ of the scale factor, which is given by the Friedman-Lemaitre model.

If we assume periodic boundary conditions for a cube of size L^3 the interaction potential $\varphi(x)$ is the solution of

$$\nabla^2\varphi(\mathbf{x}) = 4\pi G\left[-\frac{1}{L^3} + \sum_n \tilde{\delta}(\mathbf{x} - nL)\right], \tag{1.91}$$

where the sum over $n = (n_1, n_2, n_3)$ extends over all integer triplets. Note that the mean density is substracted here, so the solution corresponds to the *peculiar potential*, where the dynamics of the system is governed by $\nabla^2\phi(\mathbf{x}) = 4\pi G|\rho(\mathbf{x}) - \bar{\rho}|$. For the discretized particle system, the peculiar potential is defined as [21]

$$\phi(\mathbf{x}) = \sum_i m_i\varphi(\mathbf{x} - \mathbf{x}_i). \tag{1.92}$$

The single particle density distribution function $\tilde{\delta}(\mathbf{x})$ is the Dirac δ-function convolved with a normalized gravitational softening kernel of comoving scale ϵ. In the Gadget code, the kernel function used is $\tilde{\delta}(\mathbf{x}) = W(|\mathbf{x}|, 2.8\epsilon)$, where $W(r)$ is given by

$$W(r,h) = \frac{8}{\pi h^3}\begin{cases} 1 - 6\left(\frac{r}{h}\right)^2 + 6\left(\frac{r}{h}\right)^3, & 0 \le \frac{r}{h} \le \frac{1}{2}, \\ 2\left(1 - \frac{r}{h}\right)^3, & \frac{1}{2} \le \frac{r}{h} \le 1, \\ 0 & \frac{r}{h} > 1. \end{cases} \tag{1.93}$$

For this choice, the Newtonian potential of a point mass at zero in non-periodic space is $-Gm/\epsilon$, the same as for a Plummer *sphere* of size ϵ. The function $\epsilon(r)$ describes a gravitational softening law, which can be expressed

$$\epsilon(r;\epsilon_0) = -\frac{2.8\epsilon_0}{W(r/2.8\epsilon_0)} - r. \tag{1.94}$$

Softened potential in periodic system

The gravitational potential $\Phi(\mathbf{x})$ produced by N particles with masses m_j at coordinates $\mathbf{x}_j$ in a domain $L_x \times L_y \times L_z$ that is periodically replicated in all three directions, is given by

$$\Phi(\mathbf{x}) = -\sum_{j=1}^{N}\sum_{n=-\infty}^{\infty}\left[\frac{m_j}{|\mathbf{x}_j - \mathbf{x} + \mathbf{q}_n| + \epsilon(|\mathbf{x}_j| - \mathbf{x} + \mathbf{q}_n)} - m_j\varphi_n(\mathbf{x})\right], \tag{1.95}$$

here $\mathbf{q}_n$ denotes periodic displacement vectors given by $\mathbf{q}_n = (n_xL_x, n_yL_y, n_zL_z)$, where $\mathbf{n} = (n_x, n_y, n_z)$ are integer triplets and the sum over N extends over all these triplets.

Gadget uses the Ewald method [7] to compute long-range interactions in periodic systems. Ewald summation is a special case of the Poisson summation formula, replacing the summation of interaction in real space with an equivalent summation in Fourier space. In this method, the long-range interaction is divided into two parts, a short-range contribution, and a long-range contribution

$$\Phi(\mathbf{r}) \equiv \phi_{\rm sr}(\mathbf{r}) + \phi_{\rm lr}(\mathbf{r}), \tag{1.96}$$

where the labels sr and lr stand for short and large interactions, respectively. This technique can be applied instead of the conventional method, which demands a high computational cost, as the direct summation for all particles.

Tree algorithm

The standard tree algorithm implemented in Gadget is based on the classic published in [3]. In such a method, the force of individual particles on an individual particle from nearby particles is, on average, computed as a direct sum. The influence of remote particles is included by performing multipole expansions of clusters or cells containing many particles, truncated at a fixed, relatively low order. The force on a particle is then obtained from expansions.

All particles are mapped onto a finely resolved space Peano-Hilbert curve. The gravitational potential generated by the points inside a node is

$$\Phi(\mathbf{x}) = -G \sum_{j \in \text{node}} m_j g(\mathbf{x}_j - \mathbf{x}), \tag{1.97}$$

where $g(\mathbf{x}) = g(-\mathbf{x})$ is the Green's functions of the interaction, then $g(\mathbf{x}) = 1$ for the Newtonian case, and as the equation (1.95) for the periodic case. The center of mass of the points, denoted by s, in the node for a Taylor expansion of the potential around this point is

$$\Phi(x) = -G \sum_{n=0}^{p} \frac{1}{n!} \mathbf{Q}_n \cdot \mathbf{D}_n(\mathbf{s} - \mathbf{x}) + \mathcal{O}(\theta^{p+1}), \tag{1.98}$$

with θ being the characteristic angular extension under which the particle group is sen. The Cartesian multiple moments are defined as follows

$$\mathbf{Q}_n \equiv \sum_{j \in \text{node}} m_j (\mathbf{x}_j - \mathbf{s})^{(n)}, \tag{1.99}$$

and derivative tensors

$$\mathbf{D}_n = \nabla^{(n)} g(\mathbf{x}) \tag{1.100}$$

The notation $\mathbf{x}^{(n)}$ refers to the n-th outer product of the vector with itself. The Gadget-4 code supports $p = 1, 2, 3, 4, 5$. The acceleration exerted on a test mass at location $\mathbf{x}$ can be written as

$$\mathbf{a}(\mathbf{x}) = -\nabla\Phi(\mathbf{x}) = -G \sum_{n=0}^{p-1} \frac{1}{n!} \mathbf{Q}_n \cdot \mathbf{D}_{n+1}(\mathbf{s} - \mathbf{x}) + \mathcal{O}(\theta^p). \tag{1.101}$$

The basic structure of the hierarchical algorithm can be summarized as follows. At each step, the system is organized into cells. For each particle, the force computation begins at the top of the hierarchy (i.e. at low spatial resolution) and the size of the current cell l is compared to the distance to the particle d

$$\frac{l}{r} \leq \theta_c, \tag{1.102}$$

where θ_c is a fixed tolerance parameter [3], then the internal structure of the cell is ignored and the force on the particle is computed using the corresponding truncated expansion. Otherwise, the cell is subdivided into components and the criterion is applied recursively to each unit. Here, θ is a function of the maximum angular size of a cluster of cells. This "angle" controls the relative amplitude of successive terms in the multipole expansion. In principle, the hierarchical tree method offers a significant reduction in computational cost compared to other techniques.

TreePM method

An alternative method to the pure tree algorithm is the Particle-Mesh method, which combines the PM method on large scales with a tree code to handle particle-particle interactions at small separations. A PM code adds the construct of a regular grid to the distribution of particles. The density field represented by particles is interpolated onto grid points and the Poisson equation is

solved in Fourier space. Particles do not interact directly with each other but only through a mean field. The density field is constructed using a kernel to split the mass of the particles to the grid cells around the particle position.

In this case, the real-space sum over the nearest periodic images, that is $\mathbf{q} = 0$, resulting in a total short-potential range

$$\phi_{\rm sr}(\mathbf{x}) = \sum_j m_j \left\{ \frac{-1}{|\mathbf{r}_j| + \epsilon(|\mathbf{r}_j|)} + \frac{1}{|\mathbf{r}_j|} + \frac{\pi}{\alpha^2 V} - \frac{\mathrm{ercf}(\alpha|\mathbf{r}_j|)}{|\mathbf{r}_j|} \right\}, \tag{1.103}$$

where $\mathbf{r}_j = |\mathbf{x} - \mathbf{x}_j + \mathbf{q}^*|$ denotes the nearest periodic distance of j to the reference point. In real space, the sum gives a long-range potential of the form

$$\phi_{\rm lr} = \sum_{j=1}^{N} m_j \frac{4\pi}{V} \sum_{k\neq 0} \frac{\exp\left[-|\mathbf{k}|^2/(4\alpha^2)\right]}{|\mathbf{k}|^2} \cos[\mathbf{k}\cdot(\mathbf{x} - \mathbf{x}_j)], \tag{1.104}$$

which can be computed through Fourier methods. In this case, the TreePM method corresponds to a special case of the Ewald summation technique, whose terms are directly those which appear in eq. (1.96). The short-range term, in principle, can be computed by using the tree algorithm. This decomposition can make the TreePM method faster than ordinary tree algorithms.

1.6 Different types of dark matter

1.6.1 Warm Dark Matter

The hot dark matter (HDM) scenario for structure formation consists of particles that travel with ultrarelativistic velocities. However, this idea failed because the particle speeds were to high and erased perturbations up to tens of megaparsec scales. Within this theory, structure formation was *top-down* with galaxies forming only through fragmentation of *pancakes* and at redshifts too low to be compatible with observations. As an alternative to the eminent problem derived from HDM, the Warm Dark Matter (WDM) model emerges. It consists of HDM cooled down. Neutrinos decouple when the temperature of the primordial soup $T \sim 1$ MeV and $a \sim 10^{-10}$ and become non-relativistic when $T_h \sim m_h/3k_b$, where k_B is the Boltzmann constant.

The*free-streaming* scale is given by

$$k_{\rm fs} = \sqrt{4\pi G\bar{\rho}}\frac{a}{v_{\rm x,median}}, \tag{1.105}$$

$$= \sqrt{\frac{3}{2a}} H_0 \frac{1}{v_{\rm x,median}}. \tag{1.106}$$

Here, $v_x = 1$ when the particles are relativistic. Otherwise, $v_x = \dfrac{3k_B T_{0,x}}{am_x}$. Therefore, $k_{fs} \to \infty$ when $a \to 1$ and $T \to 0$.

One of the most important features printed in the linear matter power spectrum is the suppression by dark matter free-streaming, $k_{\rm fs}$. The distribution of velocities of the dark matter suppresses gravitational clustering and erases cosmological perturbation at scales below the WDM free-streaming length, resulting in a cut-off in the power spectrum. The cut-off in the matter power spectrum can be described by a transfer function $T^2(k)$

$$T_{\rm wdm}(k) = \left(1 + (\alpha k)^{2\nu}\right)^{-5/\nu}, \tag{1.107}$$

then, the matter power spectrum for the WDM candidate can be written in terms of that function for the CDM model and $T_{\rm wdm}$ mentioned above, as follows

$$P_{\rm wdm}(k) = P_{\rm cdm}(k) T^2_{\rm wdm}(k). \tag{1.108}$$

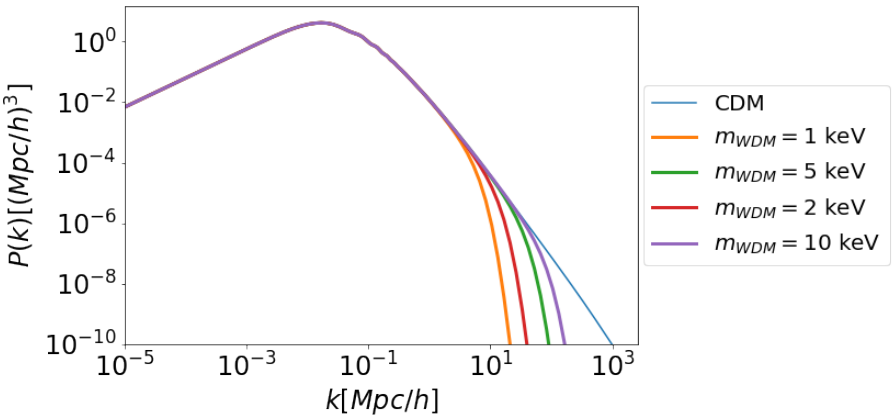

Figure 1.3: Linear matter power spectra, at z=0, for four different WDM models, where the masses of the particle have been varied between 1keV and 10keV. All of them produce a cut-off as scales around 10 Mpc/h. The curves were constructed following the eq. (1.108).

The transfer function depends of the α parameter which regulates the cut-off with respect to the CDM fiducial model. In fact, α is known as the scale break parameter, defined in terms of the cosmological parameters, that is

$$\alpha = 0.049 \left(\frac{m_{\rm wdm}}{1{\rm keV}}\right)^{-1.11} \left(\frac{\Omega_{\rm wdm}}{0.25}\right)^{0.11} \left(\frac{7}{0.7}\right)^{1.22}. \tag{1.109}$$

The value for ν is fixed. In [25] the value reported is $\nu = 1.12$, while in [5] they report $\nu = 1.2$. Additionally, the linear power spectrum $P_{\rm WDM}(k)$ must be normalised t ensure that σ_8^2 at $k = 1/8h{\rm Mpc}^{-1}$ [2]. It can also be defined as the free-streaming length of thermal relic warm dark matter particles in terms of the cosmological information from WDM [27]

$$\lambda_{\rm fs} \sim 0.11 \left[\frac{\Omega_{\rm wdm} h^2}{0.15}\right]^{1/3} \left[\frac{m_{\rm wdm}}{\rm keV}\right]^{-4/3} {\rm Mpc}, \tag{1.110}$$

which is related to the free-streaming scale

$$k_{\rm fs} = 5{\rm Mpc} \left(\frac{m_{\rm wdm}}{\rm keV}\right) \left(\frac{T_\nu}{T_{\rm wdm}}\right). \tag{1.111}$$

The exact value of the cutoff scale in the linear matter power spectrum depends on the specific WDM particle mass and the cosmological parameters of the model. In Fig. 1.3 the linear matter power spectra for four different WDM models and the standard CDM are shown. The lightest WDM particles cause a very prominent cut-off at scales around 8 kpc/h. Indeed, the larger the mass the cut-off becomes less prominent.

1.6.2 Generalized Dark Matter

GDM represents a general fluid described using a purely phenomenological approach to constrain the DM properties in the linear regime.

In the standard regime, CDM is considered a collisionless and pressureless fluid. Its energy-momentum tensor is given entirely by its density and velocity of the fluid $u^\mu = dx^\mu/\sqrt{-ds^2}$ [14],

$$T_{\mu\nu} = \rho u_\mu u_\nu. \tag{1.112}$$

In contrast, for a perfect fluid of energy density and pressure P, the energy-momentum tensor has the form

$$T^{\mu}_{\nu} = Pg^{\mu}_{\nu} + (\rho + P)u^{\mu}u_{\nu}, \tag{1.113}$$

where the pressure P and energy density ρ of a perfect fluid at a given point are defined to be the pressure and energy density measured by a comoving observer at rest with the fluid at the instant of measurements.

The GDM parametrization adds pressure P and anisotropic stress $\Sigma_{\mu\nu}$ respect to the CDM expression, that is [22]

$$T_{\mu\nu} = (\rho + P)u_{\mu}u_{\nu} + Pg_{\mu\nu} + \Sigma_{\mu\nu}. \tag{1.114}$$

The pressure and density perturbations are divided into background quantities (which will be denoted by an overbar up to now: $\bar{\rho}$ and $\bar{P}$) and perturbed quantities as usual. The last two terms of eq. (1.114) are controlled by the equation of state w and the sound speed c_s^2 (pressure perturbation) and the viscosity $c^2_{\rm vis}$ (anisotropic stress). The equation of state related to the background quantities in the usual way $w = \dfrac{\bar{\rho}}{\bar{P}}$, and the additional perturbations are governed by some closure equation to define completely the system.

GDM is able to reproduce other well-known models. If playing CDM is required, then $(w, c^2_{\rm s}, c^2_{\rm vis}) \to (0, 0, 0)$, for HDM $(w, c^2_{\rm s}, c^2_{\rm vis}) \to (1/3, 1/3, 1/3)$ whereas for SFDM it must be considered $(w, c^2_{\rm s}, c^2_{\rm vis}) \to (\omega, 1, 0)$ [9].

In Fig. 1.4 shows the different variations of each of the parameters in the range between 1×10^{-6} and $w = 1\times10^{-2}$. The first panel corresponds to the variation for w, there, the difference between each power spectra is barely noticeable. We can observe that w changes the expansion history of the universe for a fixed Ω_m. For this reason, the curves before the pivot scale are slightly lower than the fiducial model when w is positive, beyond this scale, the GDM power spectra are higher than the fiducial. When w is negative as it is shown in 1.4 (b) the opposite happens, showing a subtle cut-off at small scales. Moreover, we can observe that both c_s^2 and $c^2_{\rm vis}$ can cause a decay in the gravitational potential power spectrum, but in different ways. The decay scale can be written in terms of the free parameters [13]

$$k^{-1}_{\rm dec}(\eta) \approx \eta\sqrt{c_s^2 + \frac{8}{15}c^2_{\rm vis}}, \tag{1.115}$$

that is, such a scale depends on the combination of both parameters. On one hand, when c_s^2 is sufficiently large, then it causes oscillations in density perturbation, below the Jeans equation. On the other hand, if $c_{\rm vis^2}$ is dominant, damps the perturbation without oscillations.

The GDM model will be explored in greater detail in the next section, where different cases of the free parameters will be studied.

1.6.3 Scalar Field Dark Matter

Now we will study a model that has become popular in recent decades. Scalar Field Dark Matter is a theoretical model that proposes dark matter as a scalar field rather than a traditional particle. In this model, dark matter is described by a fundamental scalar field ϕ. This model proposes that galactic halos form by Bose-Einstein condensation of a scalar field whose boson has an ultra-light mass of the order of $m \sim 10^{-22}$eV. From this mass, it follows that the critical temperature of condensation $T_c \sim \dfrac{1}{m^{5/3}} \sim$ TeV, therefore, they form Bose-Einstein Condensates (BEC) drops very early in the Universe. In addition, the Compton length associated to this boson is $\lambda_c = \dfrac{2\pi\hbar}{m}$, which depends on the mass of the bosonic particle, therefore the size is about $\sim$ kpc, which corresponds to the dark halo-size of typical galaxies [15].

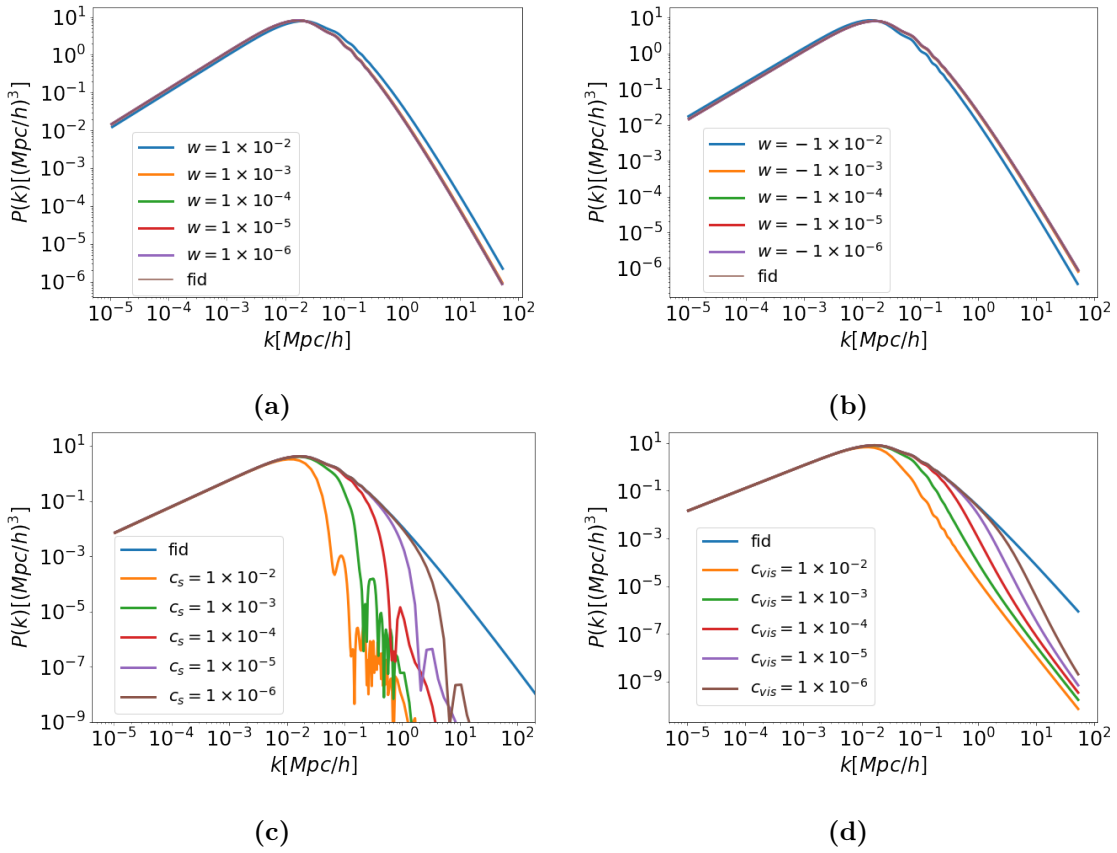

Figure 1.4: Linear matter power spectrum at $z = 70$ obtained by varying in defined ranges each of the free parameters of GDM. While a parameter varies, the other values remain fixed and equal to zero, then we can observe the variation of the parameters by themselves. In all cases, the smaller the parameter value, the less prominent the cut-off will be with respect to the fiducial value.

In the relativistic regime, the equation of motion for the scalar field is the Klein-Gordon equation $\partial_\mu \partial^\mu \phi - \partial_\phi V = 0$, whereas the non-relativistic regime leads to a Schrödinger-type equation for a wave function ψ.

In the linear perturbation regime, the scalar field should follow the structure formation of the standard CDM paradigm at large scales. The Lagrangian corresponding to the scalar field is

$$\mathcal{L}_\phi = -\sqrt{g}\left[\frac{1}{2}(\partial\phi)^2 + V(\phi)\right], \quad g = \det(g_{\mu\nu}). \tag{1.116}$$

Therefore, the Klein-Gordon equation in a homogeneous and isotropic spacetime with null curvature is

$$\ddot{\phi} + 3H\dot{\phi} + m^2\phi = 0. \tag{1.117}$$

There are two main stages in the evolution of the scalar field, an overdamped one with $H \gg m_a$ that results in $\phi \simeq$ const.. The other one is characterized by rapid oscillations of the field around the minimum of the potential, which is triggered once $H \ll m$ during which $\phi \sim a^{-3/2}$.

When considering the perturbed synchronous metric in (1.18), the linearly perturbed KG equation in Fourier space reads [24]

$$\ddot{\varphi} = -3H\dot{\varphi} - \left(\frac{k^2}{a^2} + m^2\right)\varphi - \frac{1}{2}\dot{\phi}\dot{\tilde{h}}, \tag{1.118}$$

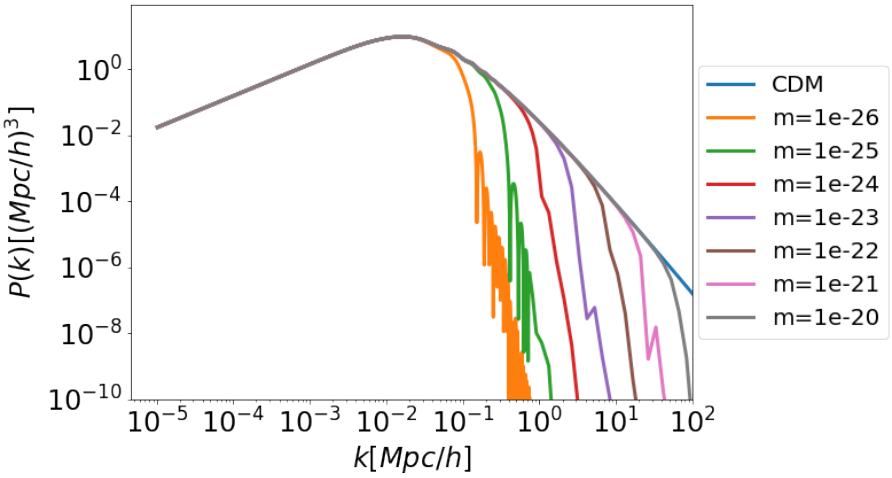

Figure 1.5: Matter power spectrum at $z = 70$ for the SFDM model. The lines were constructed using a range of mass between $m = 1 \times 10^{-26}$ and $m = 1 \times 10^{-20}$. The smaller the mass, the more pronounced the cut-off, in addition, the oscillations increase.

where $\phi(t, k) = \phi(t) + \varphi(t, k)$, being φ a small field perturbation and $\bar{h} = h^l_l$ is the trace of the spatial perturbations in the metric. At the same time, the perturbations over the density $\delta\rho_\phi$, pressure δP_ϕ and velocity divergence Θ_ϕ are the following

$$\delta\phi_\phi = \dot{\phi}\dot{\varphi} + \partial_\phi V\phi, \tag{1.119}$$

$$\delta P_\phi = \dot{\phi}\dot{\varphi} - \partial_\phi V\varphi, \tag{1.120}$$

$$(\rho_\phi + P_\phi)\Theta_\phi = \frac{k^2}{a}\dot{\phi}\varphi. \tag{1.121}$$

The true behavior of scalar field perturbations is actually more complex and numerical solutions are needed. In literature there exist different approaches to handle that problem.

In fig. 1.5 the matter power spectrum for different masses are shown, although the observations favor the $m = 1 \times 10^{-23}$ and $m = 1 \times 10^{-22}$ values.The curves were generated using the code [1], where the polar form of the KG equation is solved. The plots are shown at redshift $z = 70$, in the same way as fig. 1.4 for the GDM model. In chapter 3 the SFDM model at small scales will be further discussed through the implementation of different numerical methods.

1.7 Dark matter halos properties

1.7.1 Navarro Frenk White density profile

This profile has been constructed from N-body simulations through the study of hierarchical clusters in the universe. In [17] found that there is a universal profile, independent of the halo mass, the initial density fluctuation spectrum, and values of the cosmological parameters. In that work, they used simulations to study the formation of CDM halos with masses spanning about 4 orders of magnitude, ranging from dwarf galaxy halos to those rich galaxy clusters, and found that the profile can be well described by a steep slope at small radii following the formula

$$\rho(r) = \frac{\rho_{\rm crit}}{\left(\frac{r}{r_s}\right)\left(1 + \frac{r}{r_s}\right)^2}, \tag{1.122}$$

[1] https://github.com/lurena-lopez/class.FreeSF

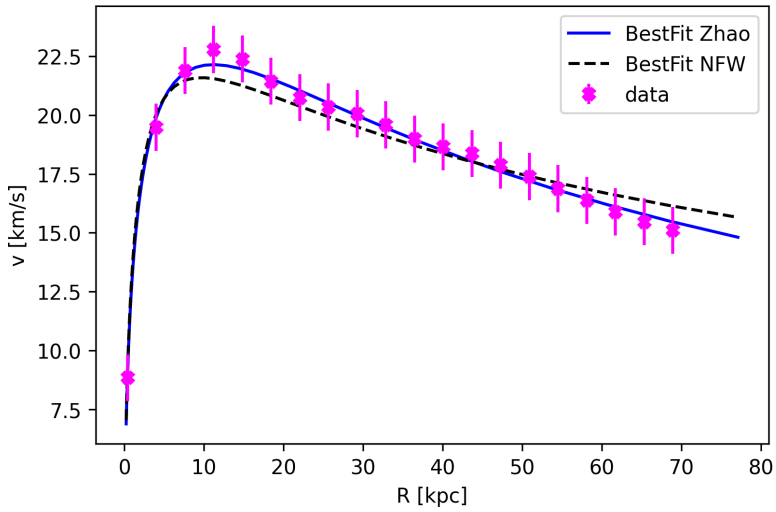

Figure 1.6: Rotation curve for a random halo taken from a cosmological simulation (purple dots). The best fit considering the Zhao profile (solid line) and the NFW one (dashed line) are also shown. The cosmological parameters considered for the simulation were $\Omega_m = 0.25$, $\Omega_b = 0.05$, the box size $L = 100\text{Mpc}/h$ and the number of particles $N_{\text{part}} = 512^3$ for CDM model.

where $\rho_{\text{crit}} = \dfrac{3H^2}{8\pi G}$ is the critical density and r_s is a scale radius. Here it is shown explicitly what has been mentioned in previous chapters, simulations favor cuspy density profiles for dark matter halos. That is, the density of the halo decreases smoothly from the center toward the outer region. This central cusp has important implications for the formation and evolution of galaxies, as it affects the distribution of baryonic matter (ordinary matter) and the potential wells in which galaxies form.

1.7.2 Zhao profile

A general expression to describe many dark matter profiles may involve more parameters to parameterize the inner and outer slopes. The Zhao profile corresponds to a family of models proposed in [28]. It is an alternative to the commonly used NFW profile and it incorporates three extra parameters (α, β, γ) to describe the inner and outer slopes.

The general expression is

$$\rho(r|r_s, \rho_s, \alpha, \beta, \gamma) = \frac{\rho_s}{\left(\frac{r}{r_s}\right)^{\gamma}\left[1 + \left(\frac{r}{r_s}\right)^{\alpha}\right]^{\frac{\beta-\gamma}{\alpha}}}, \tag{1.123}$$

where r_s is the scale radius, ρ_s is the density normalization $\rho(r_s)$, α is the logarithmic transition slope, which controls the sharpness of the transition between the inner and outer slopes, β is the outer logarithmic slope and γ is the inner logarithmic slope.

There are some special cases of the Zhao profile when there are specific parameters. For example, when $(\alpha, \beta, \gamma) = (2, 2, 0)$ the modified isothermal profile it is reproduced. Moreover, if $(\alpha, \beta, \gamma) = (1, 3, 1)$ then we have the NFW profile. Additionally, when $(\alpha, \beta, \gamma) = (1.5, 3, 1.5)$ then, we have the Moore profile. In general, when $\gamma = 1$ or above, we have a cuspy profile, in fact, there is a divergence when $r = 0$. On the contrary, if $\gamma = 0$, it is rather a flattened profile.

As a way to illustrate the difference between both profiles and their rotation curves, Fig. 1.6 shows a rotation curve derived from cosmological simulations (purple dots). Additionally, the best

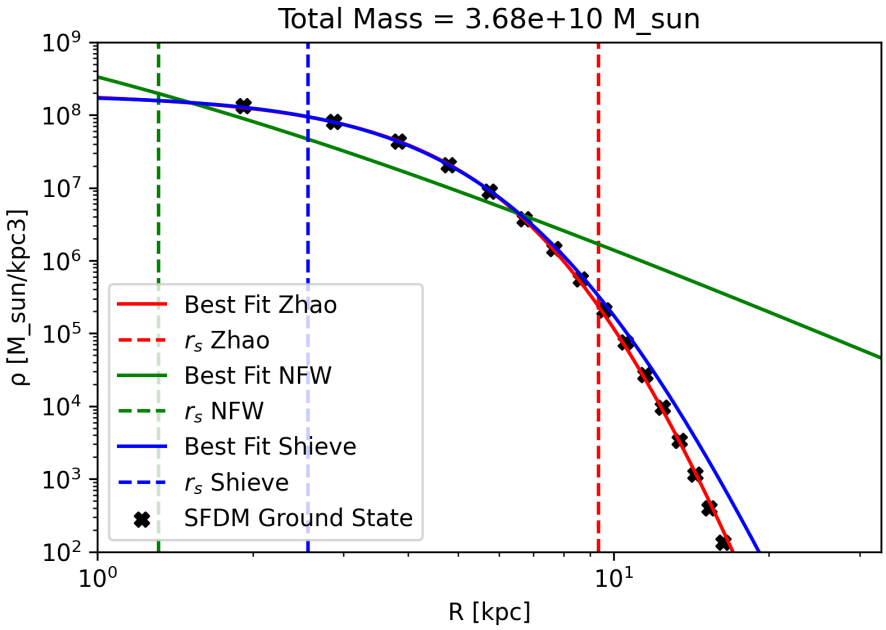

Figure 1.7: The soliton profile obtained from the solution (1.128), corresponding to the ground state. The best fit for Zhao and NFW profiles are also shown. The Zhao profile has the parameters $r_s = 8.876$, $\log(\rho_s) = 8.303$,$\alpha = 1.979$, $\beta = 17.503$ and $\gamma = 7.117 \times 10^{-6}$.

fit for both Zhao (solid line) and NFW (dashed lines) profiles are shown. Since the Zhao profile has more parameters to adjust the slopes, has the best fit. On the contrary, the NFW one fits well in the central region but not the tail.

1.7.3 Soliton profile

Another of the profiles that will be studied in this section is the soliton profile. The soliton corresponds to the ground state of the self-gravity time-independent Schrödinger-Poisson system.

The field approach to the formation of structure within the SFDM paradigm refers to the solutions obtained from the Schrödinger-Poisson (SP) system, represented by the equations

$$i\hbar\frac{\partial\psi}{\partial t} = -\frac{\hbar^2}{2m}\nabla^2\psi + m\Phi\psi, \tag{1.124}$$

$$\nabla^2\Phi = 4\pi G\rho, \tag{1.125}$$

where $\rho = |\psi|^2$. Here ψ is the wave function that represents the boson particles in their ground state and ϕ is the Newtonian gravitational potential. Sometimes, a self-interaction term in the SP system is considered, then it would become the Gross-Pitaeevski-Poisson system [8, 18].

The SN system can be solved to obtain non-singular self-gravitating configurations. The equilibrium configurations reads as follows $\psi(t,x) = e^{-i\omega t}\varphi(r)$. The set of eqs. (1.124) become the following system of ordinary differential equation

$$i\frac{\partial\psi}{\partial t} = -\frac{1}{2r}\frac{\partial^2}{\partial r^2}(r\psi) + \Phi\psi, \tag{1.126}$$

$$\frac{\partial^2}{\partial r^2}(r\Phi) = r\psi\psi^*, \tag{1.127}$$

where $r = \sqrt{x^2 + z^2}$ is the spherical radial coordinate. In [4] the following conditions are considered: at the origin $\phi(0) = \partial_x \phi(0) = 0$ and isolation $\phi(x \to \infty) = 0$, the system becomes an eigenvalue problem where the frequency of the wave functions is the eigenvalue. The system to be solved reads

$$\frac{\partial^2}{\partial r^2}(r\Phi) = 2r(U - \omega)\varphi \tag{1.128}$$

$$\frac{\partial^2}{\partial r^2}(r\Phi) = r\varphi^2. \tag{1.129}$$

The soliton corresponds to the solution of the system (1.128). The profile is defined as $\rho = |\phi|^2$. One of the main features of the soliton profile is the flattened shape that has in the central region. Fig. 1.7 shows that the soliton profile corresponds to the ground state (black crosses) and is the best fit for both the Zhao (red solid line) and NFW (green solid line) profiles. We can see that Zhao's profile fits well in the central region. However, the NFW is not capable of properly reproducing any of the regions, due to the cuspy form close to zero.

Additionally, in [20] derived an empirical density profile for dark matter halos, consisting of a soliton-like core and an NFW density halo dominant at large radii. They used high-resolution cosmological simulations based on the dynamics of SFDM in the Newtonian limit, governed by the SP system (1.124). Such a profile can be approximated by

$$\rho_{\rm SFDM} = \Theta(r_\epsilon - r)\rho_{\rm sol}(r) + \Theta(r - r_\epsilon)\rho_{\rm NFW}(r), \tag{1.130}$$

where Θ is a step function, r_ϵ is the transition radius where the density changes from the soliton profile

$$\rho_{\rm sol}(r) = \frac{\rho_c}{\left[1 + 0.091\left(\frac{r}{r_c}\right)^2\right]^8}, \tag{1.131}$$

to the NFW profile

$$\rho_{\rm NFW} = \frac{\rho_s}{\left(\frac{r}{r_s}\right)\left(1 + \frac{r}{r_s}\right)^2}. \tag{1.132}$$

Then, $\rho_c = 1.9\left(\frac{m}{10^{-23}\text{eV}}\right)^{-2}\left(\frac{r_c}{\text{kpc}}\right)^{-4} M_\odot \text{pc}^{-3}$ is the central soliton density and r_c the half-light radius of the soliton-like region.

Bibliography

[1] Amendola, L. and Tsujikawa, S. (2010). *Dark energy: theory and observations*. Cambridge University Press.

[2] Bardeen, W. A. (1985). Gauge anomalies, gravitational anomalies, and superstrings. Technical report, Fermi National Accelerator Lab.

[3] Barnes, J. and Hut, P. (1986). A hierarchical O(N log N) force-calculation algorithm. *Nature*, 324(6096):446–449.

[4] Bernal, A. and Guzman, F. S. (2006). Scalar field dark matter: Nonspherical collapse and late-time behavior. *Physical Review D*, 74(6):063504.

[5] Bode, P., Ostriker, J. P., and Turok, N. (2001). Halo formation in warm dark matter models. *The Astrophysical Journal*, 556(1):93–107.

[6] Dodelson, S. (2003). *Modern Cosmology*. Academic Press, Elsevier Science.

[7] Ewald, P. P. (1921). Die Berechnung optischer und elektrostatischer Gitterpotentiale. *Annalen der Physik*, 369(3):253–287.

[8] Gross, E. P. (1961). Structure of a quantized vortex in boson systems. *Il Nuovo Cimento (1955-1965)*, 20(3):454–477.

[9] Hu, W. (1998). Structure formation with generalized dark matter. *The Astrophysical Journal*, 506(2):485–494.

[10] Hu, W. (2018). Cmb tutorials.

[11] Jenkins, A., Frenk, C. S., White, S. D. M., Colberg, J. M., Cole, S., Evrard, A. E., Couchman, H. M. P., and Yoshida, N. (2001). The mass function of dark matter haloes. *Monthly Notices of the Royal Astronomical Society*, 321(2):372–384.

[12] Komatsu, E., Smith, K., Dunkley, J., Bennett, C., Gold, B., Hinshaw, G., Jarosik, N., Larson, D., Nolta, M., Page, L., Spergel, D., Halpern, M., Hill, R., Kogut, A., Limon, M., Meyer, S., Odegard, N., Tucker, G., Weiland, J., Wollack, E., and Wright, E. (2011). Seven-year Wilkinson Microwave Anisotropy Probe (WMAP) Observations: Cosmological Interpretation. *Astrophysical Journal*, 192(2):18.

[13] Kopp, M., Skordis, C., and Thomas, D. B. (2016). Extensive investigation of the generalized dark matter model. *Physical Review D*, 94(4).

[14] Ma, C.-P. and Bertschinger, E. (1995). Cosmological perturbation theory in the synchronous and conformal newtonian gauges. *The Astrophysical Journal*, 455:7.

[15] Magañ a, J. and Matos, T. (2012). A brief review of the scalar field dark matter model. *Journal of Physics: Conference Series*, 378:012012.

[16] Murray, S. G., Power, C., and Robotham, A. S. (2013). Hmfcalc: An online tool for calculating dark matter halo mass functions. *Astronomy and Computing*, 3:23.

[17] Navarro, J. F., Frenk, C. S., and White, S. D. M. (1997). A universal density profile from hierarchical clustering. *The Astrophysical Journal*, 490(2):493–508.

[18] Pitaevskii, L. P. (1961). Vortex lines in an imperfect bose gas. *Sov. Phys. JETP*, 13(2):451–454.

[19] Press, W. H. and Schechter, P. (1974). Formation of Galaxies and Clusters of Galaxies by Self-Similar Gravitational Condensation. *Apj*, 187:425–438.

[20] Schive, H.-Y., Chiueh, T., and Broadhurst, T. (2014). Cosmic structure as the quantum interference of a coherent dark wave. *Nature Physics*, 10(7):496–499.

[21] Springel, V. (2005). The cosmological simulation code gadget-2. *Monthly Notices of the Royal Astronomical Society*, 364(4):1105–1134.

[22] Thomas, D. B., Kopp, M., and Markovič , K. (2019). Using large-scale structure data and a halo model to constrain generalized dark matter. *Monthly Notices of the Royal Astronomical Society*, 490(1):813–831.

[23] Tinker, J., Kravtsov, A. V., Klypin, A., Abazajian, K., Warren, M., Yepes, G., Gottlöber, S., and Holz, D. E. (2008). Toward a halo mass function for precision cosmology: The limits of universality. *The Astrophysical Journal*, 688(2):709.

[24] Urena-López, L. A. (2019). Brief review on scalar field dark matter models. *Frontiers in Astronomy and Space Sciences*, 6:47.

[25] Viel, M., Lesgourgues, J., Haehnelt, M. G., Matarrese, S., and Riotto, A. (2005). Constraining warm dark matter candidates including sterile neutrinos and light gravitinos with WMAP and the lyman-alpha forest. *Physical Review D*, 71(6).

[26] White, M. (2002). The mass function. *The Astrophysical Journal Supplement Series*, 143(2):241.

[27] Zentner, A. R. and Bullock, J. S. (2003). Halo substructure and the power spectrum. *The Astrophysical Journal*, 598(1):49.

[28] Zhao, H. (1996). Analytical models for galactic nuclei. *Monthly Notices of the Royal Astronomical Society*, 278(2):488–496.

Chapter 2

Study of the properties of dark matter as a non-perfect fluid: GDM model

This chapter corresponds to the publication [19]. Here, the family of GDM models will be studied, as well as the theory of linear perturbations associated. In addition, an analysis will be performed by considering three different free functions which govern the dynamics of the Bardeen gravitational potential, particularly in the Power Spectrum. The combination of these parameters, namely $c^2_{\rm vis}$ and $c^2_{\rm s}$ induces the decay of the gravitational potential once either the decay scale or the Jeans scale are reached. This implies a natural cut-off in the power spectrum at small scales compared to the CDM model. Subsequently, cosmological dark matter-only simulations will be carried out by considering the initial conditions with the primordial power spectrum generated from the GDM prescription. For the simulations, three specific scenarios of the GDM model have been considered, whose free parameters are very close to the CDM value. Afterwards, the stellar population of halos will be computed at different times of the simulation and finally, galaxy catalogs will be created through the use of semi-empirical models, taking into account the history of each of the halos at $z = 0$.. All of the above, in order to study Hickson Compact Groups of galaxies in the three scenarios of GDM with CDM.

2.1 The Generalized Dark Matter model

2.1.1 Equations of the perturbations

The GDM model is a phenomenological description of a fluid with pressure P_g and stress tensor Σ_g. The description presented below is only valid for a universe with a Friedman-Robertson-Walker (FRW) metric.

The perturbed metric of linear order is

$$ds^2 = a^2\bigg(-(1+2\Psi)d\tau^2 - 2\vec{\nabla}_i\zeta d\tau dx^i + \left[\left(1+\frac{1}{3}h\right)\gamma_{ij} + D_{ij}v\right]dx^i dx^j\bigg) \tag{2.1}$$

where Ψ, ζ, h y ν are the scalar perturbations to the metric. The scale factor $a(\tau)$ is written in terms of the conformal time as $\tau = \int dt/a(t)$. Furthermore, γ_{ij} is the metric of three-dimensional curved space with curvature κ and $\vec{\nabla}_i$ is the covariant derivative of $\gamma_{[}ij]$. At the same time, $D_{ij} = \vec{\nabla}_i\vec{\nabla}_j - \frac{1}{3}\gamma_{ij}\vec{\nabla}^2$, is the traceless derivative operator [17, 14].

Within this context, the EM tensor for GDM corresponds to (1.114). The velocity components of the fluid can be parameterized as

$$u_0 = -a(1+\Psi), \quad u_i = -a\vec{\nabla}_i\theta, \tag{2.2}$$

where Θ is the scalar perturbation of the velocity of the fluid. Furthermore, perturbations on density and pressure can be described as

$$\rho = \bar{\rho}(1+\Psi), \quad P = \rho(\omega + \Pi) \tag{2.3}$$

where $\Pi = \dfrac{\delta P}{\bar{\rho}}$ is the normalized perturbation on the pressure. In addition, the background pressure and density are defined as follows$\bar{\rho} = \sum_I \bar{\rho}_I$ y $\bar{P} = \sum_I \bar{P}_I$ for the i-th component.

With the previous information, the temporal, spatial, and temporal-spatial components of the moment energy tensor are written as

$$\begin{aligned} T^0_0 &= -\bar{\rho}(1+\delta), \\ T^0_i &= -(\bar{\rho}+\bar{P})\vec{\nabla}_i\theta, \\ T^i_0 &= (\bar{\rho}+\bar{P})\vec{\nabla}^i(\theta-\zeta), \\ T^i_j &= \bar{\rho}(\omega+\Pi)\delta^i_j + (\bar{\rho}+\bar{P})D^i_j\Sigma. \end{aligned} \tag{2.4}$$

It is worth mentioning that in an FRW universe, it is true that $\bar{\Sigma}_{\mu\nu} = 0$, therefore the stress tensor is only present at the perturbation level through the scalar mode Σ, as observed in the last equation referring to the spatial components [14].

Now, the conservation of the energy-momentum tensor $\nabla_\mu T^\mu_{\mu\nu} = 0$, which can be rewritten as

$$T^\nu_{\mu,\nu} = T^\nu_{\mu\nu} + \Gamma^\nu_{\lambda\nu} T^\lambda_\mu - \Gamma^\lambda_{\mu\nu} T^\nu_\lambda. \tag{2.5}$$

The temporal component of(2.5) corresponds to the conservation of energy and by considering the set of equations (2.4), the corresponding conservation law for an FRW-type universe is obtained, which turns out to be the same as that derived from a perfect fluid for CDM,

$$\frac{\dot{\bar{\rho}}_I}{\bar{\rho}_I} = -3(1 + w_I)\frac{\dot{a}}{a} \tag{2.6}$$

where $w_I \equiv \dfrac{\bar{P}_I}{\bar{\rho}_I}$. Furthermore, the adiabatic speed of sound is defined as

$$c^2_{al} \equiv \frac{\dot{\bar{P}}_I}{\dot{\bar{\rho}}_I} = w_I - \frac{\dot{w}_I}{3H(1 + w_1)}, \tag{2.7}$$

with $H = \dfrac{\dot{a}}{a}$. For the case where w_I is time-independent, it can be noted that $c_{al} = w_l$. It is important to make a distinction between the GDM equation of state, where the subscript $I = g$ (which for simplicity will be denoted as w), from the background equation of state $w_{\text{tot}} = \bar{P}/\bar{\rho}$. Thus, we see that the adiabatic velocity is completely determined by $w(a)$.

In first order, the equation that describes the evolution of the density contrast is obtained, also known as the equation of continuity in Fourier space.

$$\dot{\delta}_I = 3H(w_I\delta_I - \Pi_I) - (1 + w_I)\left[\frac{k^2}{a}(\theta_I - \zeta) + \frac{1}{2}\dot{h}\right] \tag{2.8}$$

where $\delta \equiv \dfrac{\delta\rho}{\bar{\rho}}$ the density contrast [18].

On the other hand, considering the spatial components of (2.5), the conservation of momentum is obtained. In first order the Euler equation is derived

$$a\dot{\theta}_I = -(1 - 3c^2_a)aH\theta_I + \frac{\Pi_I}{1 + w_I} - \frac{2}{3}k^2\Sigma_I + \Psi, \tag{2.9}$$

which determines the evolution of the scalar perturbation on velocity.

As mentioned above, the last two terms for P and $\Sigma_{\mu\nu}$ are the ones that make the difference with respect to the expression for a perfect fluid, where they are equal to zero. However, the equations of perturbation theory (2.8) y (2.9) do not completely determine these quantities, but must be expressed in terms of the metric and other variables of the fluid. For example, through the microscopic theory of the distribution function that satisfies the Boltzmann equation. Therefore, two additional equations, called closure, are required to complete the system.

$$\Pi_g = c^2_a\delta_g + 3(1 + w_I)(c^2_s - c^2_a)aH\theta_g \tag{2.10}$$

$$\dot{\Sigma}_g = -3H\Sigma_g + \frac{4}{1 + w_I}c^2_{vis}\left(\frac{\theta_g}{a} - \frac{1}{2}\dot{v}\right) \tag{2.11}$$

The first equation corresponds to the perturbation on the pressure $\Pi_g = \dfrac{P_g - \bar{P}_g}{\bar{\rho}_g}$. The second to the evolution of the scalar part of the stress tensor. The system of equations that fully describes the evolution of GDM perturbations is composed of (2.8),(2.9), (2.10) y (2.11). Here it is clearly

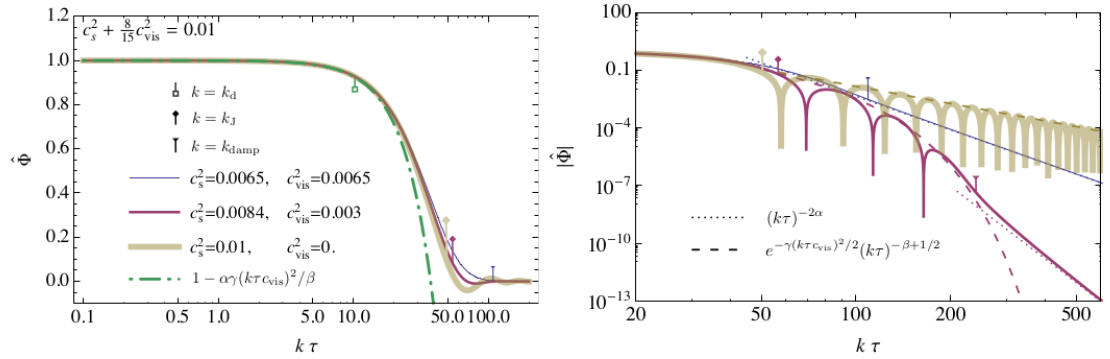

Figure 2.1: The lines show the different solutions to $\hat{\Phi}$ for specific values of the free functions. It is evident that once the decay scale is reached the potential decays due to the combination of $c_{\rm vis}^2$ and $c_{\rm s}^2$. The right panel shows the decay in detail. The dashed lines show the envelope described by (2.19), while the dotted lines show the asymptotic behavior of the over-damped regime. Source: [17]

observed that the free function$c_{\rm s}^2$ controls the perturbation on pressure Π, whereas $c_{\rm vis}^2$ controls the evolution of Σ. Moreover, the equation of state $w = \bar{\rho}/\bar{P}$ relates the density and pressure of the fluid. Therefore, different values for the free functions give rise to different solutions for the equations[15].

2.1.2 Dynamics of gauge-invariant potentials

Up to this moment, no particular metric has been defined, but it is easy to get any of the two standard metrics assuming:

- **synchronous** $\zeta = \Psi = 0$
- **Newtonian** $v = \zeta = 0$ y $\Phi = \eta = \dfrac{h}{6}$

It is now convenient to define gauge-invariant variables, such as Bardeen potentials

$$\hat{\Phi} \equiv \eta + H\left(\frac{1}{2}\dot{\nu} + \zeta\right) \quad \hat{\Psi} \equiv \Psi - \frac{1}{a}\partial_\tau\left[a\left(\frac{1}{2}\dot{\nu} + \zeta\right)\right] \tag{2.12}$$

Finally, a third quantity is defined that is useful when performing algebraic operations.

$$R \equiv \hat{\Phi} + \frac{2}{3}\frac{\hat{\Phi} + H\hat{\Psi}}{(1+\omega)H} \tag{2.13}$$

The dynamics of these potentials are determined in terms of the free functions at different moments in the evolution of the universe, which includes the growth of primordial fluctuations. Returning to Einstein's equations and choosing the effective algebraic expression for the scalar part of the stress tensor as it appears in [17]

$$\Sigma_g = \frac{4}{(1+w)H}\frac{c_{vis}^2}{5}(\theta_g - \zeta - \frac{1}{2}\dot{\nu}) \tag{2.14}$$

We obtain a harmonic oscillator-type equation for one of the Bardeen potentials $\hat{\Phi}$

$$\begin{aligned}\hat{\Phi''} \quad &+ \left(\frac{k}{H}\right)^2\left[\left[c_s^2 + \frac{8c_{vis}^2(1+3c_s^2)}{15(1+w)}\right]\hat{\Phi} + \frac{8c_v vis^2}{15(1+w)}\hat{\Phi'}\right) \\ &+ \left[1 + \frac{3}{2}(1+w) + \frac{12}{5}c_{vis}^2\right]\hat{\Phi'} = 0\end{aligned} \tag{2.15}$$

The general solution for the expression (2.15) looks like $\hat{\Phi} = A_0 M(\alpha, \beta, -\gamma k^2 \tau^2 c_{vis}^2)$.

In order to observe the behavior of the above solution, we will consider several different scenarios, which will be briefly explained below.

- **Case 1:** $c_{\mathbf{s}} k\tau \ll 1, \quad c_{\mathbf{vis}} k\tau \ll 1$
  The solution of the potential is
  $$\hat{\Phi} \sim 1 - \frac{\gamma\alpha c_{\rm vis}^2}{\beta} k^2\tau^2, \tag{2.16}$$
  so that if values much smaller than one of the free functions are considered, the potential can only decay. Indeed, the scale from which the potential begins to decay is
  $$k_d^{-1} \equiv \tau\sqrt{c_{\rm s}^2 + \frac{8}{15}c_{\rm vis}^2}, \tag{2.17}$$
  In the above expression, it is considered $|w|, c_{\rm s}^2, c_{\rm vis}^2 \ll 1$. The behavior of the potential once the decay scale is reached is clearly observed in the left panel of Fig 2.1, where $k_d\tau \sim 10$.

- **Caso 2:** $c_{\mathbf{vis}}^2 = 0$
  The exact solution reads as
  $$\hat{\Phi} = \frac{A_1 J_n(c_{\rm s^2} k\tau)}{(c_{\rm s}^2 k\tau)^n}, \quad n = \frac{2+3w}{2(1+3w)}, \tag{2.18}$$
  where A_1 is the normalization constant and J_n is the Bessel function of order n. The solution envelope is almost constant outside the Jeans scale and decays in the form $\tau^{-n-1/2}$, as shown in the right panel of Fig. 2.1.

  Once the Jeans scale is reached, the potential oscillates with a frequency of $c_{\rm s}k$. It is important to note that in this case, once the decay scale is reached, the oscillations never stop.

- **Case 3:** $c_{\mathbf{vis}} \ll c_{\mathbf{s}}^2, \quad c_{\mathbf{vis}} k\tau \ll 1$
  The approximate solution for the potential, in this case, turns out to be
  $$\hat{\Phi} \sim \frac{A_2 \exp\{-\gamma c_{\rm vis}^2 k^2\tau^2/2\}}{(c_{\rm eff} k\tau)^{\beta-1}} J_{\beta-1}(c_{\rm eff} k\tau) \tag{2.19}$$
  where A_2 is the normalization constant. This solution oscillates with a frequency of $c_{\rm eff}k$ where the effective speed of sound is expressed as $c_{\rm eff}^2 \sim c_{\rm s}^2 - \frac{2}{5}c_{\rm vis}^2$. From this it is possible to estimate the Jeans scale, where the main parameter to determine the acoustic regime is just $c_{\rm eff}^2$, it is also assumed that the values of the free functions are very close to zero and positive definite
  $$k_J^{-1} \equiv \frac{2c_{\rm eff}\tau}{\sqrt{105}} \sim 0.2 c_{\rm eff}\tau \tag{2.20}$$

- **Case 4:** $c_{\mathbf{vis}}^2/c_{\mathbf{s}}^2 \geq 1, \quad k \geq k_+$

  This is the damping regime, that is, where the potential decays without any oscillation. The scale where this happens again is rewritten in terms of the free parameters
  $$k_{\rm damp}^{-1}(\tau) = \frac{0.18 c_{\rm vis}^2}{\sqrt{1 + \frac{15c_{\rm s}^2}{8c_{\rm vis}^2}}}, \tag{2.21}$$
  The above expression is valid for $c_{\rm vis}^2 \ll c_{\rm s}^2$ and $c_{\rm vis}^2 \gg c_{\rm s}^2$. The exact solution for this case is $\hat{\Phi} \sim A_3 (c_{\rm vis}^2 k\tau)^{-2\alpha}$, for some normalization constant A_3. This behavior is represented by the dotted lines in the right panel of Fig. 2.1, once $k_{\rm damp} \sim 250$ is reached.

Model	w	c_s^2	c_{vis}^2
GDM I	-1×10^{-6}	1×10^{-7}	1×10^{-7}
GDM II	-1×10^{-6}	1×10^{-7}	1×10^{-6}
GDM III	6×10^{-4}	1.92×10^{-6}	1.1×10^{-7}

Table 2.1: Values of the free parameters of each model. These values were selected to be close to CDM and, therefore, to be able to neglect the collisional effects at small scales.

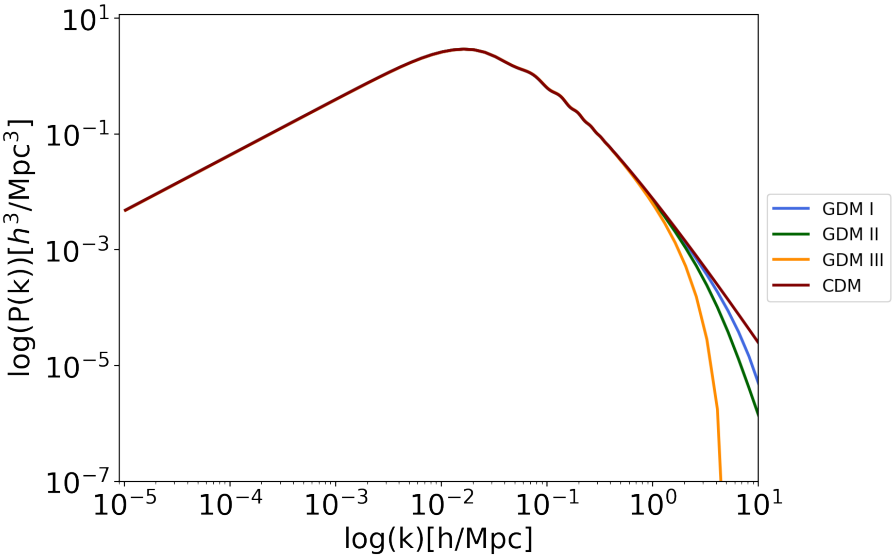

Figure 2.2: Matter Power Spectra for CDM and three different scenarios for GDM at z=127. Results are identical until $k = 1$, from this value, the GDM models start to show a cut-off in accordance with the c_{vis}^2, c_s^2 and w parameters, remaining in scenarios near CDM.

2.2 Structure formation in GDM scenarios

In order to study the change in structure formation in the different scenarios, N-body cosmological simulations have been carried out. For this, we must select specific values of the free parameters. the way in which these parameters were selected has been randomly, however, the condition was imposed that these parameters be close to the value of CDM, that is $(c_s^2, c_{vis}^2, w) = (0, 0, 0)$. With this we look for the cut in the power spectrum to be very subtle.

2.2.1 Matter Power Spectrum

Three different scenarios have been considered for GDM which are shown in Table 2.1, These values for the parameters are based on the constraints given in Fig. 2.3 mentioned in the first part of this chapter. It is worth mentioning that w can take positive and negative values, although the observations are more inclined towards negative values.

The power spectrum was generated by solving the linear equations of the perturbations using

Likelihood	Model	$10^2 w$		$10^6 c_s^2$ (upper bound)		$10^6 c_{\rm vis}^2$ (upper bound)	
(PPS+...)	(Λ-GDM+...)	95%	99%	95%	99%	95%	99%
		$-0.040^{+0.473}_{-0.468}$	$-0.040^{+0.700}_{-0.701}$	3.31	6.31	5.70	11.3
+ Lens		$0.066^{+0.434}_{-0.427}$	$0.066^{+0.654}_{-0.642}$	1.92	3.44	3.27	5.99
+ Lens + BAO		$0.074^{+0.111}_{-0.110}$	$0.074^{+0.164}_{-0.163}$	1.91	3.21	3.30	6.06

Figure 2.3: Constraints on the free parameters obtained by considering a GDM model with a cosmological constant (ΛGDM). Source: [34]

the Boltzmann GDM-class code [1] which is a modified version of the CLASS code [2] [15]. Fig. 2.2 shows the power spectrum obtained for the different models at $z = 127$, where it is evident that GDM I is less viscous than GDM II, which at the same time is *colder* ($c_{\rm s}$ is smaller)and more viscous than GDM III. In the last model, the potential decays earlier causing a more pronounced cut-off. Although the differences between the parameters of GDM I and GDM II are minimal, around $k = 1$, GDM I shows a less pronounced cut-off than the subsequent model. In all cases, the difference becomes visible from $k \geq 1$. Before this value, which corresponds to large scales, the Power Spectrum for all models is identical, which is to be expected, since CDM has good predictions at these scales. Notice that these cut-off at small scales are much less pronounced than those shown in Fig. 1.4.

2.2.2 Cosmological parameters and initial conditions

In order to create the initial conditions for the simulation we use the N-GenIC code [3] [31, 1], which constructs an initial N-body distribution of the distribution of density perturbations prescribed by a given power spectrum. The simulations were performed in the Gadget2 code [4] [30]. Since $c_{\rm vis}^2$ and $c_{\rm c}^2$ in our GDM fluid have very small values, we perform simulations considering as an approximation that the collisional effects between N-bodies at small scales are negligible. Basically, I am interested in studying the effects produced by the cutoff of the primordial Power Spectrum (due to the free path of linear perturbations) on the formation of nonlinear structures.

The cosmological parameters used in the simulations are the same for all runs associated with GDM I, GDM II, GDMIII and CDM, as shown in Table 2.2. All the simulations have the same box size and start at the same time, which makes it possible to compare the structures formed at late times. The value of σ_8 varies in each model because the Power Spectra are different. For the softening length ϵ, introduced in eq. 1.95, a commonly used form was taken into account, this is

$$\epsilon = \left(\frac{V}{N_{\rm tot}} \right)^{1/3} \tag{2.22}$$

V is the volume of the box, $V = L^3$ [41] and $N_{\rm tot} = 512^3$ particles. In fact, the selection of these parameters is of the utmost importance and depends entirely on the astrophysical system to be studied as well as on the available computational resources. In appendix A Some of the conditions that both the size of the box and the tabulated power spectrum must meet are shown so that the theory remains within the linear regime.

The snapshots of the simulations at $z = 0$ projected in the xy plane are shown in Fig. 2.6, where the library Pylians3[5] was used to make these figures. As expected, for all GDM cases there

[1] https://github.com/s-ilic/gdm_class_public
[2] https://lesgourg.github.io/class_public/class.html
[3] https://www.h-its.org/2014/11/05/ngenic-code/
[4] https://wwwmpa.mpa-garching.mpg.de/gadget/
[5] https://pylians3.readthedocs.io/en/master/index.html

Model	σ_8	z	L[Mpc/h]	ϵ[kpc]
GDM I	0.81	127	100	1
GDM II	0.75	127	100	1
GDM III	0.65	127	100	1
CDM	0.84	127	100	1

Table 2.2: Cosmological parameters for each model. The box size, initial z, and number of particles are the same, so the softening length will be the same. The value of σ_8 varies in each model depending on the power spectrum.

is an evident lack of structure at small scales compared to CDM, this is a direct consequence of the cut-off present in Fig. 2.2 Additionally, at large scales, the structure follows the same shape as it is shown in the right panels in all figures. Fig. 2.6 (d) shows a very sharp filament structure, very similar to what has been reported in WDM simulations (see for example [22]).

2.2.3 Halo Mass Function

Halo identification

Once the simulation has been carried out, the dark matter halos in each snapshot can be identified, in order to further study the structure of the different GDM scenarios. In order to identify the population of halos in cosmological simulations we use the Rockstar code [6] [5] which determines the over-densities of matter using the following steps

- The simulation volume is divided into 3D Friends-of-Friends groups.
- In each group, the positions and velocities of particles are normalized by the group's position and velocity dispersion, creating an inherent phase-space distance metric given by

$$d(p_1, p_2) = \left(\frac{|\vec{x}_1 - \vec{x}_2|^2}{\sigma_x^2} + \frac{|\vec{v}_1 - \vec{v}_2|^2}{\sigma_v^2} \right)^{1/2}, \tag{2.23}$$

  where σ_x and σ_y are the particle position and velocity dispersion for a given FOF group.
- An adaptive phase-space linking length is selected to ensure that 70% of the particles within the group are interconnected in subgroups. This process is repeated for each subgroup: renormalization, a new linking length, and a new level of substructure are calculated.
- After identifying all levels of substructure, seed halos are positioned at the lowest substructure levels. In the scenario where a parent group contains only one seed halo, all particles within the group are allocated to that specific seed halo. However, if the parent group contains multiple seed halos, the particles in the group are assigned to the closest seed halo in phase space. In this case, the phase-space metric is set by the seed halo properties, so that the distance between a halo h and a particle p is defined as

$$d(p_1, p_2) = \left(\frac{|\vec{x}_h - \vec{x}_p|^2}{r_{\rm dyn,vir}^2} + \frac{|\vec{v}_h - \vec{v}_p|^2}{\sigma_v^2} \right)^{1/2}, \tag{2.24}$$

[6] `https://bitbucket.org/gfcstanford/rockstar`

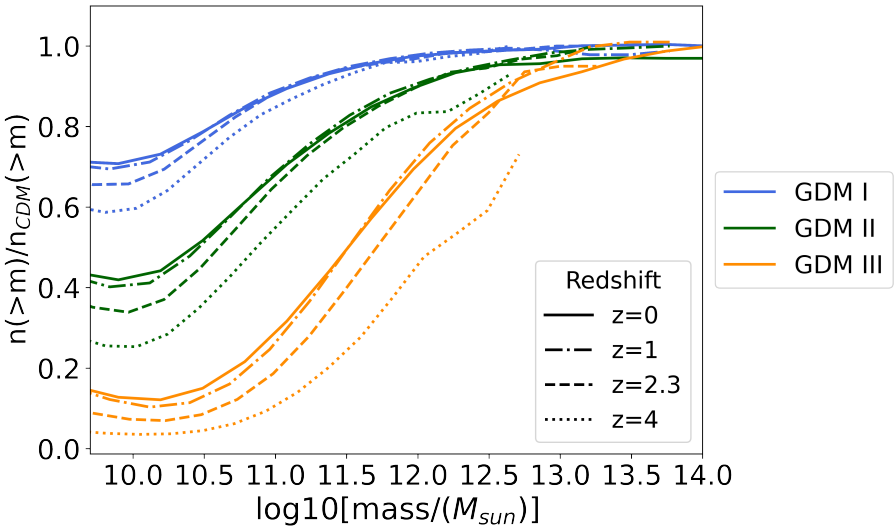

Figure 2.4: Relative percentage change of halo mass function associated with the 3 different GDM models with respect to CDM at different redshifts. The X-axis range falls within the resolution limits of the simulation, around 10^9 $M_\odot/h$ and at the upper limit 10^{14} $M_\odot/h$. The halo mass function for the GDM models shows a cut-off according to Fig. 2.2. For large redshifts, the large-scale structure is suppressed identically in all models. Additionally, the medium-scale structure is less suppressed for models with smaller c_s, compared to those at $z = 0$.

where

$$r_{\rm dyn,vir} = \frac{v_{\rm max}}{\sqrt{\frac{4}{3}\pi G \rho_{\rm vir}}}, \tag{2.25}$$

being σ_v the seed halo's current velocity dispersion and $v_{\rm max}$ the maximum circular velocity.

- Once the particles have been allocated to halos, any unbound particles are eliminated, and various halo properties such as positions, velocities, and other relevant attributes are computed. The $v_{\rm max}$ is computed directly from

$$v_{\rm max} = \sqrt{\frac{GM(r)}{r}}. \tag{2.26}$$

The scale radius R_s, in this case, has been computed by dividing the halo particles into radial equal-mass bins and directly fitting an NFW profile (1.122).

The halo mass is considered the sum of all particles without counting the substructure.

To quantify dark matter in different structures at various redshifts and compare them with CDM predictions, we calculated the halo mass function (HMF) for each model at different times. The results, shown in Fig. 2.4, reveal several observations. Firstly, the number density of halos in all models coincides with large masses, indicating adherence to the CDM structure formation on a large scale. Secondly, the power spectrum cutoff for GDM I, II, and III aligns with Figure 2.4, as expected since the power spectrum determines initial conditions. Lastly, for higher redshifts, the count of small and medium-sized halos decreases with increasing z. However, there is a significant discrepancy in the count of the largest structures, as these massive halos form closer to z approaching zero. This pattern aligns with the small-big structure behavior observed in CDM models.

Merger trees

The history of each halo, involving the progenitors and descendants, the collisions and mergers, also known as *merger trees*, is necessary to estimate the content of baryons and their properties. For this, a complete tracing of the halos must be done, towards larger z, where the formation of structure begins. Fig 2.5 shows a sketch of a halos history at $z = 0$. The red dots represent the most massive progenitors and therefore contribute to a greater extent to the mass of the final halo. the size of the dots is related to their mass, in such a way that smaller dots have smaller masses. halos with masses less than $10^8 M_{\odot/h}$ are not drawn. Some branches do not start from initial conditions either because the first parent was formed later or because the initial mass of the halo at $z = 127$ was very small. We used the Consistent-trees code [7] [6] to generate the merger trees following the below prescription

- First, the halo descendants are identified by tracking the particles that compose it.
- The positions and velocities of all halos are gravitationally evolved backward in time during the current timestep to determine their most probable positions at the previous timestep. The force between two halos is considered as $F_{1\to 2} = \dfrac{GM_1M_1}{r^2}$, where r is the distance between halo centers. The mass of each halo can be computed by considering an NFW profile for the halo, then

$$M_{\rm NFW}(r, r_s, \rho_0) = 4\pi\rho_0 \int_0^r \frac{r_s}{r}\left(1+\frac{r}{r_s}\right)^{-2} r^2 dr \tag{2.27}$$

$$= 4\pi\rho_0 r_s^3 \left[\ln\left(1+\frac{r}{r_s}\right) - \frac{r}{r+r_s}\right]. \tag{2.28}$$

  Now, here the substructure plays an important role. It is observed that as subhalos approach the center of the host, their gravitational influence on the bulk motion of the host gradually decreases. This decrease occurs because of the overlapping mass distributions between the subhalos and the host [5]. Additionally, subhalos are often much smaller than their host, then it is viable to introduce a softening length ϵ of the virial radius, similar to that used for cosmological simulations. Thus, the full-force equations becomes

$$F_{1\to 2} = \frac{GM_{\rm NFW}(r, r_s,)M_{vir,2}}{r^2 + (\epsilon r_{\rm vir,2})^2} \tag{2.29}$$

- Using the predicted progenitor halos from the previous step, the connections to spurious descendants can be cut off. The spurious halos can arise due to various reasons, including numerical noise and limitations in the analysis methods.
- In cases where the previous step has identified a good match, links are established for halos with probable progenitors at the previous timestep.
- If there are halos in the current timestep without probable progenitors, a new halo is created at the previous timestep. The position and velocity of this new halo are determined based on the evolution described in the previous step. However, any such halos generated in previous rounds will be removed if they have lacked genuine progenitors for multiple consecutive timesteps.
- For halos in previous timesteps that do not have any descendants, it is assumed that a merger took place with the halo exerting the strongest tidal field on it during the previous timestep. However, if a halo without a descendant is located too far away from other halos to experience a substantial tidal field, it is considered a statistical fluctuation and subsequently removed from the tree and catalogs.

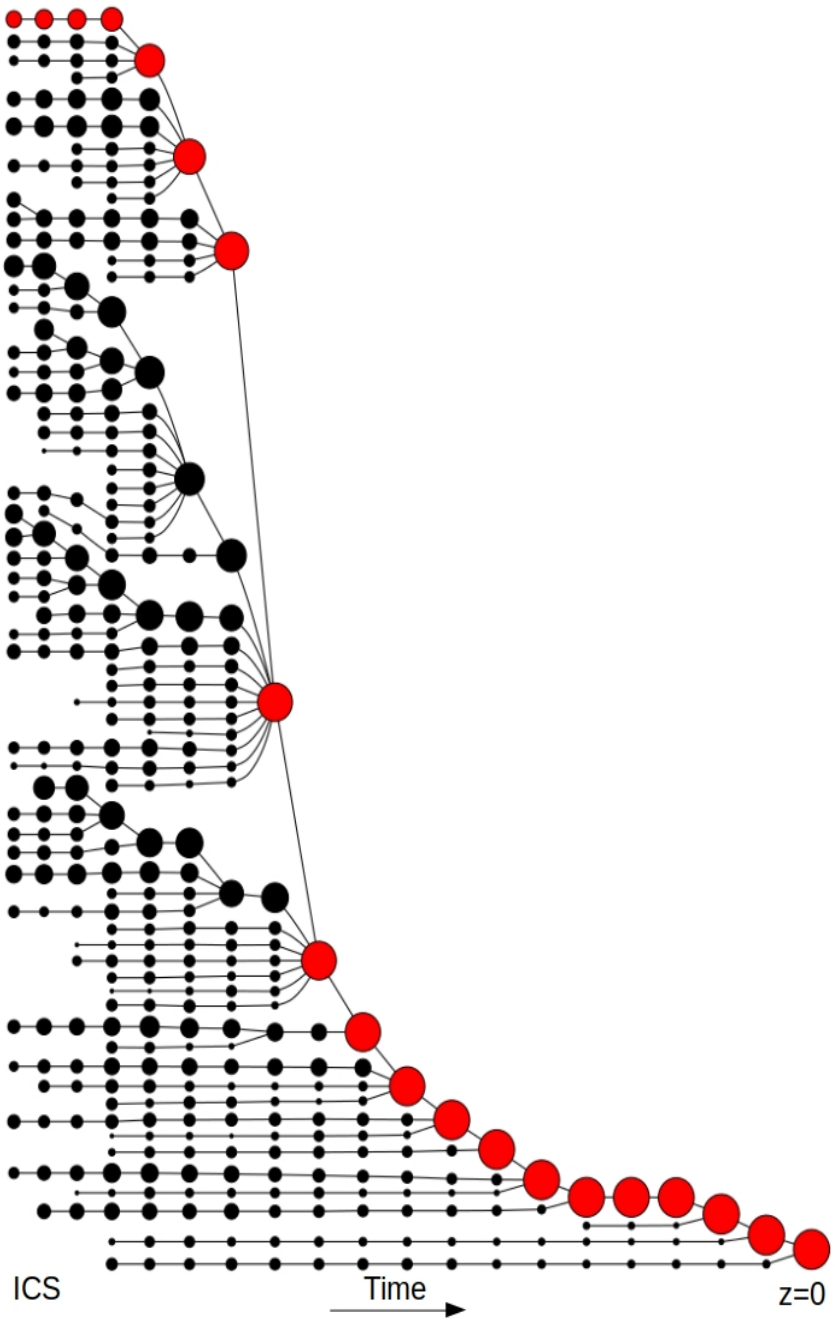

Figure 2.5: Sketch of the family tree of a halo at $z = 0$. the initial conditions are on the left, so time grows to the right until today. The red dots correspond to massive halos that coincide with the start of a new ramification. Halos whose mass is less than 10^8 are not drawn, so there is little contribution from the substructure.

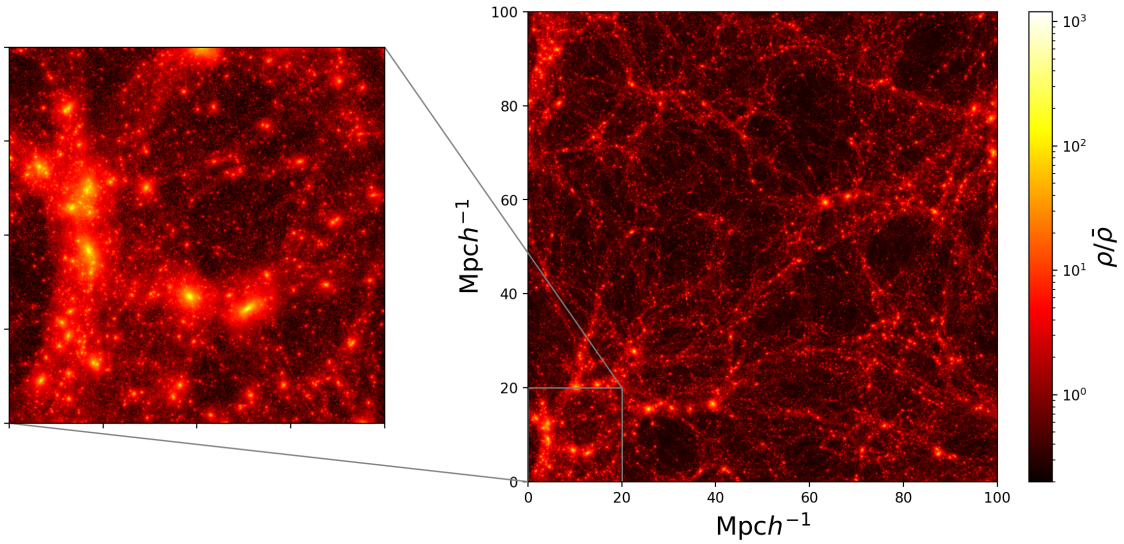

(a)

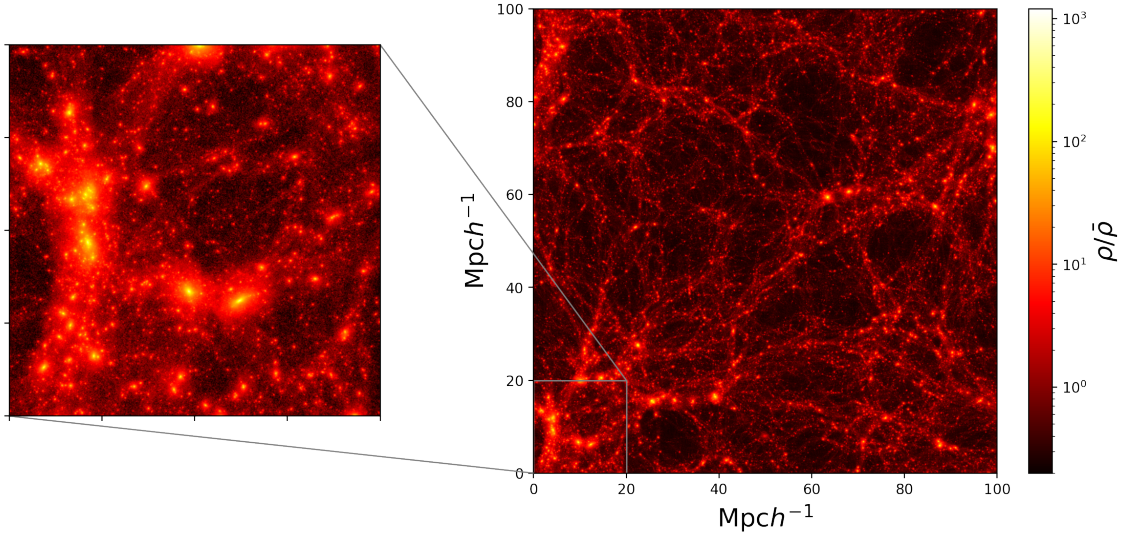

(b)

Figure 2.6: Projections in the XY plane of the simulations for CDM (a), GDM I (b), GDM II (c) and GDM III (d) for $Z \in [0, 50]\text{Mpc}/h$. In the left panels, we show an amplified region to observe the differences between models at small scales. For large scales, the structure formation seems very similar. In the high-density regions is clear how CDM has more substructure than the other models. GDM III is the model with the least structure formation and also the voids (i.e. the regions where the contrast has a negative value) are more evident.

[7] `https://bitbucket.org/pbehroozi/consistent-trees`

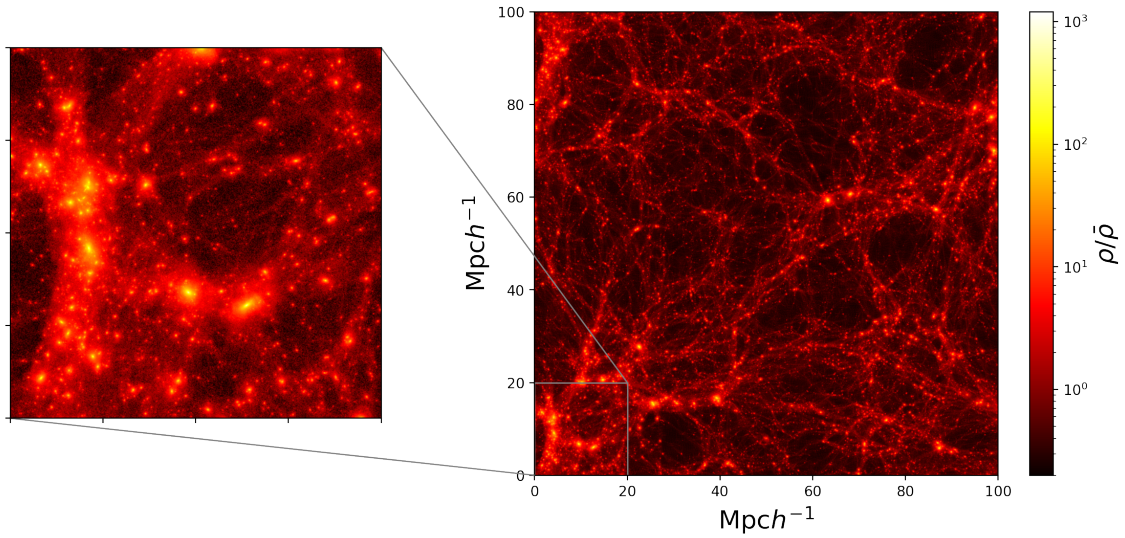

(c)

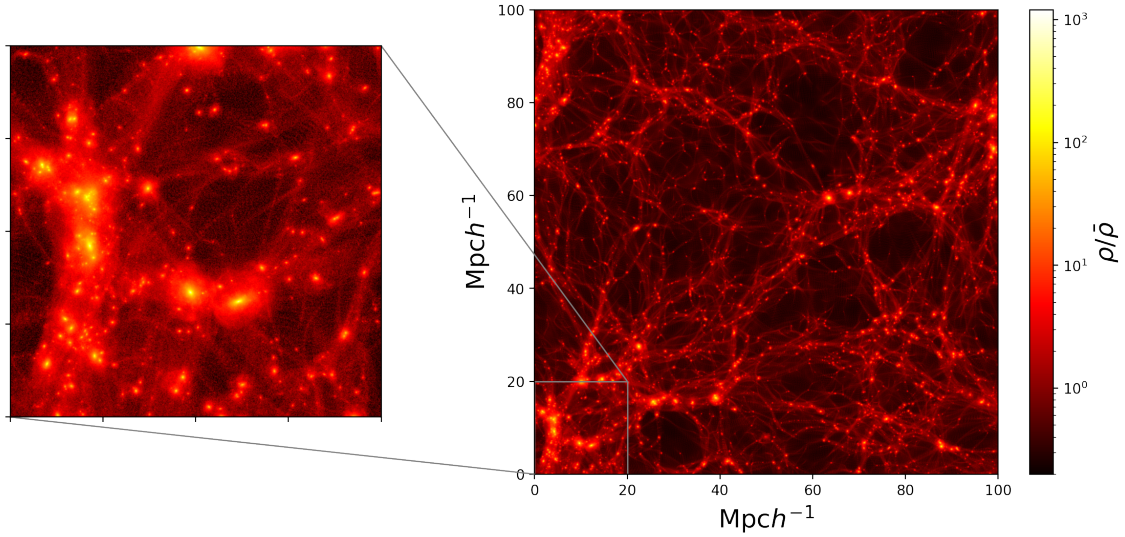

(d)

Figure 2.6: previous figure continued

Galaxy catalogs

Constructing galaxy catalogs from dark matter-only simulations is useful for describing galaxy populations in conjunction with halo dynamics. Various simulations have been reported in the literature where this method is used [31, 16, 33, 24]. In both models, the halo catalogs obtained at different times are considered and the history of each of them is reconstructed, from $z = 0$ to the initial condition.

The Universemachine code[8] [4] has been used to create the galaxy catalogs through semi-empirical models. In this case, it is usual to parameterize the potential of the halo through

[8] `https://bitbucket.org/pbehroozi/universemachine`

the maximum circular velocity $V_{\max} = \sqrt{G\frac{M(R}{R}}$, because it gives better results when treating clusters of galaxies [38]. In this case, the maximum peak is considered as a function of the redshift $v_{\rm Mpeak} \sim v_{\max}(z_{\rm Mpeak})$. To do this, the main steps are shown below

- A ratio is chosen between the SFR-$v_{\max}$ and $f_{\rm quenched}(v_{\rm vmax})$ from the parameter space, this determines the probability distribution of the SFR for each $v_{\max}$ of each halo in a given redshift. That is, a relationship must be established between star formation (or its suppression) as a function of the maximum circular velocity as it is expressed in the function [4]
$$P(\mathrm{SFR}|v_{M\mathrm{peak}}, z) = f_Q G(\mathrm{SFR}_Q, \sigma_Q) + (1 - f_Q)G(\mathrm{SFR}_{\mathrm{SF}}, \sigma_{\mathrm{SF}}), \tag{2.30}$$
here $v_{M\mathrm{peak}}$ is the $v_{\max}$ at the redshift of peak halo mass, $\Delta v_{\max}$ is the logarithmic growth in $v_{\max}$ over the past dynamical time, $G(\mu, \sigma)$ is a log-normal distribution with median μ and scater σ, f_Q is the graction of quenched galaxies. Also, SFR_{SF} and SFR_Q are the median SFR for star-forming and quenched galaxies.

- Then these probability distributions are mapped in time for each halo, in such a way that halos at early times have a small SFR and vice versa, in order to establish an evolution in the SFR and the quenched-fraction.

- Subsequently, the SFRs are integrated along the *merger-trees* to infer the growth of the galaxies through the collisions and mergers of the halos, from the initial conditions to $z = 0$.

- Using this, it is possible to predict the observables as the mass functions and compare them with the observational data and calculate the errors and deviations. This process is repeated until the desired results are obtained.

2.2.4 Stellar mass function

The Stellar Mass Function (SMF) is shown in Fig 2.7 together with the stellar mass functions reported in Table 1 of [23]. In this work, the authors analyzed the measurements of the stellar masses of a group of galaxies observed with the Spitzer telescope with redshifts $z = 0$ and $z = 4$.

The stellar mass functions for the models described in this work have been plotted in the redshifts closest to those available in the snapshots of our simulations to the mean value reported in the observations. Furthermore, the functions are shown in the [23] mass ranges. As we can see in Fig. 2.7, the GDM III prediction is very far from most observations in all cases. In turn, the CDM prediction for the number density of galaxies for masses less than $10^{10} M_\odot/h$ is overestimated for all redshifts. In some cases, the number densities of large-scale features observed are much higher than those reported by the models. This is the range where also the error bars for the observations increase.

2.3 Study of astrophysical systems in GDM scenarios: Hickson Compact Groups

2.3.1 Compact groups of galaxies

Compact groups are small isolated agglomerations containing between 4 to 7 galaxies located in a compact region in the sky. They were originally classified by Paul Hickson in 1984, and include 100 groups characterized by their redshift, positions, and magnitudes. It is worth noticing that the properties of the clusters are strongly related to the criteria used to classify them. Various classifications and treatments for compact groups have been reported in the literature. The discovery of compact clusters begins with Stefan [32] and Seyfert (1948) [28]. In 1957, Shakbazyan

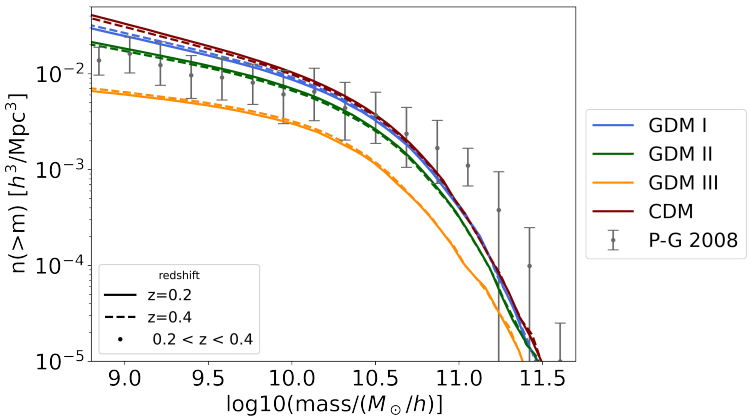

(a)

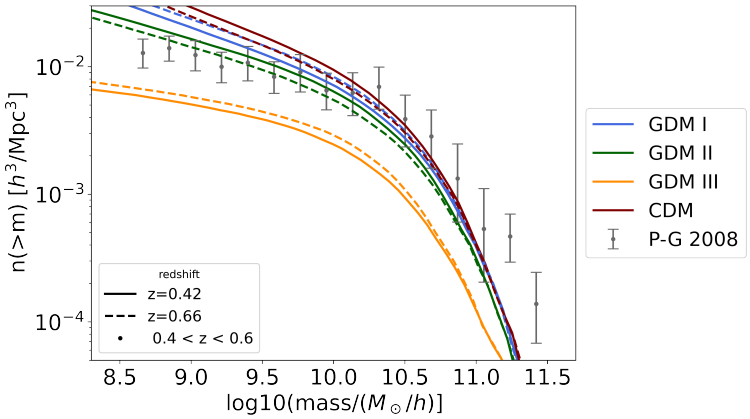

(b)

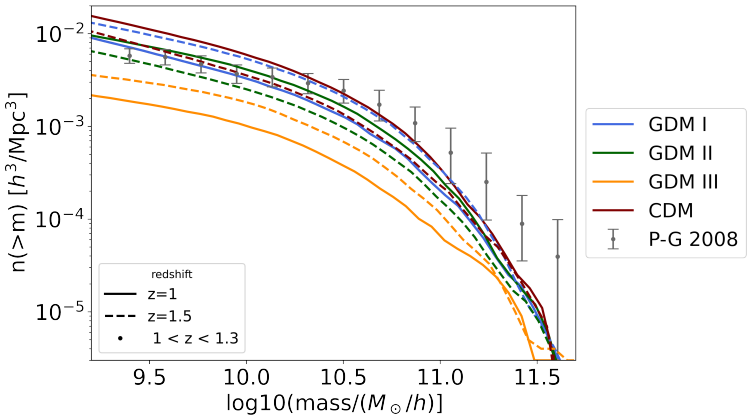

(c)

Figure 2.7: Stellar mass functions for the three GDM scenarios and the standard CDM scenario at different redshifts in the range (0.2). Also shown is the stellar mass function for the sample of galaxies observed by Spitzer reported in [23]

Figure 2.8: Stephan's Quintet, corresponding to HCG 92, was originally classified with five galaxy members, but only four of them are bound gravitationally. In fact, the NGC 7320 (at upper left) is actually a foreground galaxy, not a real group member. Source `https://www.nasa.gov/`.

created a catalog of clusters, allowing more members of HCGs [29]. Rose then continued building HCG catalogs, requiring a minimum of 3 members and a minimum magnitude of 17.5 [27]. Later on, Hickson introduced criteria based on galaxy magnitudes, redshift, and spatial distribution for HCGs. He used a compactness criterion with average surface brightness and an isolation criterion to avoid including cluster centers [13]. Fig. 2.8 shows the most famous HCG, the number 92 also known as the Stephan's Quintet.

HCGs are dark matter-rich clusters, crucial for studying intergalactic-level dark matter dynamics. Measurement of redshifts revealed discordant galaxies, whose redshifts differ significantly from the rest, possibly due to projection effects. Notably, even without accounting for discordant galaxies, the velocity dispersion of HCGs exceeds expectations based on their visible mass [12]. This suggests a shorter crossing time scale compared to the Hubble time. Some compact groups are part of larger, sparsely populated groups called *loose groups*. Approximately 70% of HCGs are located within loose groups or filaments according to a study reported in [26].

The existence of HCGs

Given the information above, HCGs persist only for a fraction of the Hubble time [2] so their current existence is an open question. The literature presents two possible solutions. The first suggests a mechanism that facilitates frequent replacement of compact groups, compensating for losses through individual galaxy mergers. Field galaxies occasionally joining the groups would maintain a constant number of members [25, 21, 40]. The second option involves a high formation rate of these clusters, allowing for their continued existence despite ongoing merger processes. One proposal suggests that HCGs can form within collapsing loose groups[37, 27, 35].

Studies of compact groups have also been carried out at the cosmological level. In [20] a simulated catalog was used to investigate the spatial properties of compact groups, they found

that about 30% of galaxy agglomerations correspond to dense physical systems and more than half of such groups contain an individual dark matter halo in common. Additionally, in [9] the compact groups were identified using a 2D selection criterion, and the fraction of physically dense groups was determined using the maximum physical separation between galaxies, concluding that more than 60% of them have 3D distances less than $200h^{-1}$kpc and between 59% and 76% have physical distances less than $100h^{-1}$Mpc. Later, in [8], a statistical study of the spatial distribution of compact groups in the universe was carried out, finding that only 27% of them can be considered subsystems of larger structures. Also, 70% of the embedded structures are physically compact in 3D. Finally, in [39] the prevalence of HCGs in 3D was studied, they used a selection criterion that results in a population of groups at $z < 0.03$ with a number density consistent with the observations.

2.3.2 HCG classification criteria

In 1982, Paul Hickson built a catalog of 100 compact groups, which he called HCG, based on the following classification criteria involving a number of members, compactness defined in terms of the magnitude of individual galaxies, and isolation in terms of the angle size. The original classification includes only three criteria and the catalog contains information on both the members and the group in general. The classification reads as follows:

- Population: $N \geq 4$,
- Isolation: $\theta_N \leq 3\theta_G$,
- Compactness: $\bar{\mu}_G < 26$,

where N is the total number of galaxies within 3 mags below the brightest member. This criterion allows the selection of galaxies with similar masses in order to avoid very massive members and their satellites. Also, $\bar{\mu}_G$ is the average of the total magnitude of these galaxies per arcsecond^2 within the smallest circle (with angular diameter given by θ_G) which contains the geometric centers. Finally, θ_N is the angular diameter of the largest concentric circle which must not contain external galaxies within the [11] magnitude range.

In some works, such as [3] or [36], the minimum number of members is $N \geq 3$, as was done in the catalog of Rose [27]. In this chapter we mainly focus on the study of the standard criteria $N = 4$, however, we also consider the case of triplets when classifying and counting HCGs for completeness.

On the other hand, additional considerations have been made, such as in [9], where a limit has been imposed for the magnitude in the red band (*R-band*), of the brightest galaxy,

$$R_{\text{brightest}} \leq 14.44(\text{flux limit}). \tag{2.31}$$

This equation corresponds to a limit for the flux which depends on the measurement technique.

Additionally, some restrictions over the velocities of the members were imposed, such as

$$|v_i - \tilde{v}| \leq 1000 \text{ km s}^{-1},$$

where v_i is the radial velocity for the i-th members and $\overline{v}$ is the average of radial velocity for the whole group [9, 39, 8]. This last condition is a filter to rule out *fly-by* galaxies, that is, those galaxies which do not belong to the group (that can be found along the line of sight) and therefore are not dynamically linked to the group. This criterion was added later in the subsequent works of Hickson [13].

2.3.3 Classification algorithms for simulated galaxy catalogs

Given that the selection criteria to identify HCGS is described in terms of the observed quantities, that is projected distances and magnitudes of the member galaxies. However, when talking about cosmological simulations, the information obtained corresponds to the physical distance between galaxies and their mass. The adaptation of the algorithm to identify compact groups in simulations is shown below.

1) **Compactness** The original catalog describes this point using the surface brightness of the group. In this work, we consider the average projected distance between members instead. Once a relationship between compactness and physical distance has been assigned, the compactness will be described through the 3D information. For more details see Section 2.3.3. This point is crucial for the identification of compact groups, since precisely what differentiates HCGs from other types of astrophysical systems is the very small portion they occupy in the sky. Therefore, correctly determining this criterion is of the most important for an adequate classification.

2) **Isolation**: This condition has been imposed in a very similar way to the original catalog. A shell whose radius is 3 times the radius of the grouping ($r_{\rm shell} = 3r_{\rm group}$) was built. Subsequently, the ratio of the density within the shell to the density in the group is calculated. A candidate is considered isolated if said amount is very close to zero. The condition is

$$\frac{\rho_{\rm shell}}{\rho_{\rm group}} < 10^{-4}. \tag{2.32}$$

   2a) **Boundary:** The simulations are carried out in a box of finite size, therefore boundary conditions must be imposed. Clusters located very close to any of the boundaries are eliminated, that is, those that fulfill $x_i - r_{\rm shell} < 0$ or $x_i + r_{\rm shell} >$L, where L is the size of the box and x_i the Cartesian coordinates of the candidates for HCGs. These agglomerations are eliminated because they could easily meet the isolation condition due to a portion of the shell being outside the boundary.

3) **Dwarf mass limit** Since we do not want a member galaxy to be a dwarf, we impose a mass limit given by $M_{\rm dwarf} = 2 \times 10^9 M_{\rm sun}/h$, in order to avoid them, as is done in [39]. This point also reinforces the condition that avoids incorrectly classifying dominant galaxies and their satellites.

4) **Membership** The criterion that rules *fly-by* galaxies is applied directly, as described above. $|v - \bar{v}| < 1000{\rm km}/s$,

5) **Mass-Ratio** This condition is imposed to have galaxies with comparable masses. It is assumed that the galaxy with the greatest luminosity corresponds to the galaxy with the dominant mass [39]. The comparison is made by choosing the three most massive galaxies in the group, which must fulfill

$$\frac{M_2 + M_3}{M_1} > 0.1, \tag{2.33}$$

   where M_1, M_2 y M_3 are labels for the first, second, and third most massive galaxies, respectively.

6) **Minimum number of members** Once the previous steps have been applied, the total number of members of the HCG candidates must be verified, since members can be removed with the filters. As mentioned above, two cases are considered, the first where the minimum number of members is $N \geq 4$, as in the original catalog, and the second where triplets of $N \geq 3$ galaxies are allowed (see section 2.3.2).

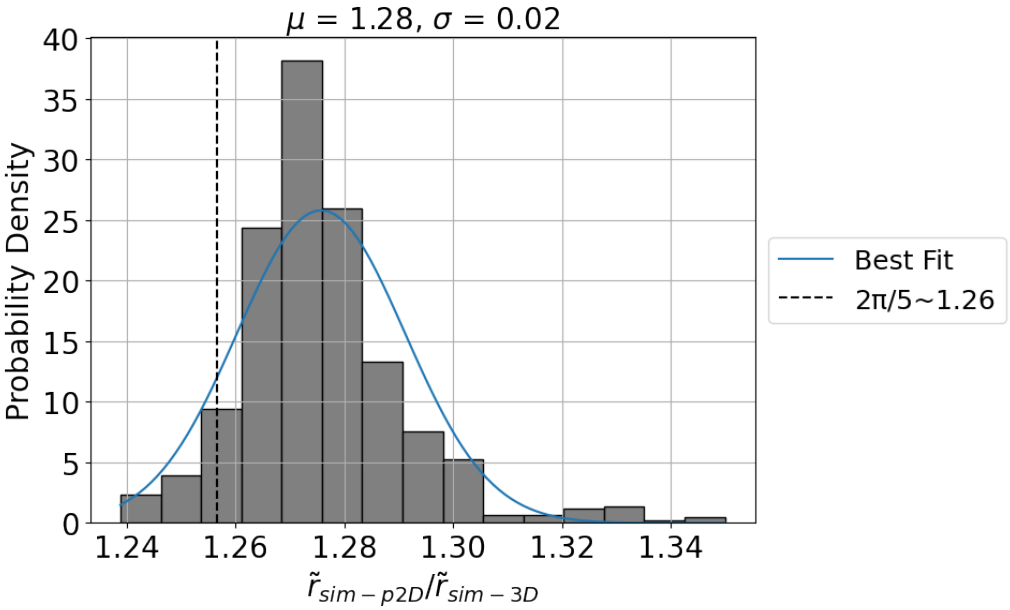

Figure 2.9: The relationship between the mean 3D separation, and the projected mean distance for all simulations using the clusters found for different $\epsilon \in [10, 120]$ kpc/h, considering only results with at least 10 clusters by simulation. The dotted lines correspond to the value obtained in [39]

Implementation of the classification algorithm

Before working with the classification algorithm, it is necessary to agglomerate the data. To do this, we use the DBSCAN algorithm [10]. For further explanation about this method please see B. The HCG classification was applied to the galaxy catalogs derived from simulations shown in Table 2.2. In the simulations, a wide range of distances between members (ϵ) $[10, 120]$ kpc/h was explored, with a minimum number of members set at $N = 3$ and $N = 4$. The DBSCAN algorithm was employed to identify galaxy clusters, and subsequently, the criteria 2) to 5) listed above were applied.

In order to find a relationship between the projected and the physical distance, we first project the separation $\tilde{r}_{\text{sim-p2D}}$ between the members of the agglomerations identified by DBSCAN onto the 8 faces of the box of the simulation. Then, we calculate the physical distance between the neighbors $\tilde{r}_{\text{sim-3D}}$. This helps us to compute the relationship between the two distances $\tilde{r}_{\text{sim-p2D}}/\tilde{r}_{\text{sim-3D}}$. The results are shown in Fig. 2.9, where all the data from all the models were taken into account. The mean value is

$$\mu_{\text{sim}} = 1.28 \pm 0.03 \tag{2.34}$$

within a confidence level of 2σ. It is interesting to note that this value is very close to the value reported in [39], where a Monte Carlo-type simulation was implemented to estimate that the relationship between the separation and the physical distance between galaxies is approximately $2\pi/5 \sim 1.26$.

For observations, the mean separation between members of HCGs reported is around 39kpc/h, therefore, making use of the relationship above, the corresponding physical spacing between members is

$$\tilde{r}_{\text{obs-3D}} = 49.78 \pm 1.26 \text{ kpc}/h. \tag{2.35}$$

This value is one that completely determines the criterion of Compactness 1). That is, the epsilon associated with DBSCAN must be such that the average separation between members is within the interval of $\tilde{r}_{\text{obs-3D}}$.

The relationship between ϵ and the mean 3D separation of the simulated data $\tilde{r}_{\text{sim-3D}}$ is shown in Fig. 2.10 for both scenarios N=4 (6a) and N=3 (7b) for the different models in Table 2.2. The blue band delimits the values of $\tilde{r}_{\text{obs-3D}}$. The agglomerations whose separation is within the blue band are considered Hickson Compact Groups according to the criteria originally imposed by Hickson. In both cases, the value of ϵ that fits the observational region is different for each model within a range $(65, 85)$ kpc$/h$.

The average physical separation increases with ϵ, but there are intervals where the slope approaches zero. These intervals are more common in models with higher structure suppression, especially models similar to GDM III. They are also more frequent for $N = 4$, indicating that triplet clusters are easier to form than those with $N = 4$.

2.3.4 Spatial properties of simulated HCGs

Once a relationship between the DBSCAN distance measure and the physical mean separation has been determined, we can now consider the latter for the subsequent analysis of the spatial properties of the groups. In Fig. 2.11 the number of Hickson groups is shown as a function of the mean separation for both cases $N = 4$ (a) and $N = 3$ (b). It is observed that for $N = 4$ the number of HCGs for GDM I is the largest for $r_{\text{sim-3D}}$ within $(40, \sim 74)$ kpc$/h$, while the count for CDM within the same range is slightly lower, followed by GDM II and GDM III. In contrast, the crossover scale for GDM II and CDM corresponds to $r_{\text{sim-3D}} \sim 43 - 48$ kpc$/h$, therefore, below this point for GDM II, a larger number of HCGs are found compared to CDM, this behavior means that GDM models can predict a larger number of HCGs even when the substructure is initially suppressed.

The situation for $N = 3$ is slightly different. First, in Fig.2.11 (b) we observe that it is more likely to find clusters with triplets. Second, the count for CDM is the largest in the entire interval. Although GDM I is very close to CDM within the range $(40, 50)$ kpc$/h$, therefore the GDM models would intersect CDM on a much smaller scale than in the previous case.

2.3.5 Host halos

According to N-body simulations, as some dark matter halos of individual galaxies merge, larger common halos can be created [2, 7]. Actually, dark matter of HCGs is distributed mainly in the intergalactic medium, and studies about the kinematics of HCGs environment, indicate that dark matter is mainly placed around the optical galaxies and not inside them [12].

In this work, by considering the mock catalogs for different models, we identified the host halos and their embedded substructure. We found that 88 percent of the HCGs in CDM are embedded in a host halo and the galaxy associated with that central halo also belongs to the group. The remaining 12 percent HCGs are embedded in a host halo, however, its corresponding central halo galaxy is not a member. For the GDM I model, 98 percent HCGs have a common halo, while for GDM II and GDM III 96 and 83 percent respectively. In addition, the structure within the host halos is not necessarily part of the HCGs, that is, in some cases, there are other halos and their associated galaxies that belong to the environment rather than the group.

2.3.6 On the relevance of the different filters when identifying HCGs

In Fig. 2.12 we present a sequence of counts of clusters classified by DBSCAN after applying different filters in the selection criteria (each filter is associated with a different color) for different models. DBSCAN selects the initial number of clusters by applying the compactness criterion, either for $N = 4$ (a) or $N = 3$ (c). Similarly, panels b) and d) show counts of galaxies for $N = 4$ and $N = 3$ respectively. The red bar corresponds to the initial number of galaxies/clusters which naturally decreases as successive filters are applied.

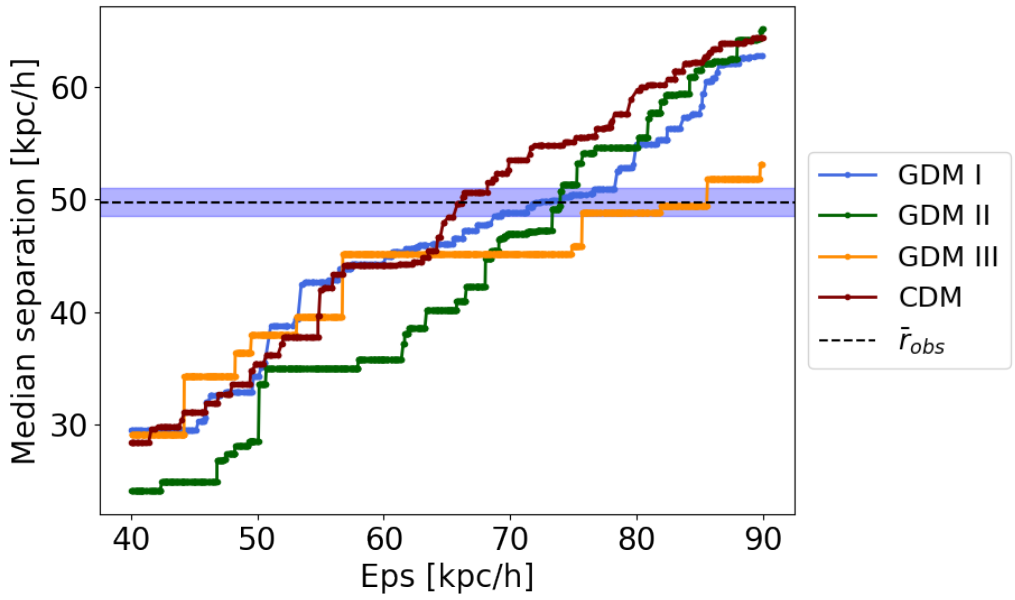

(a)

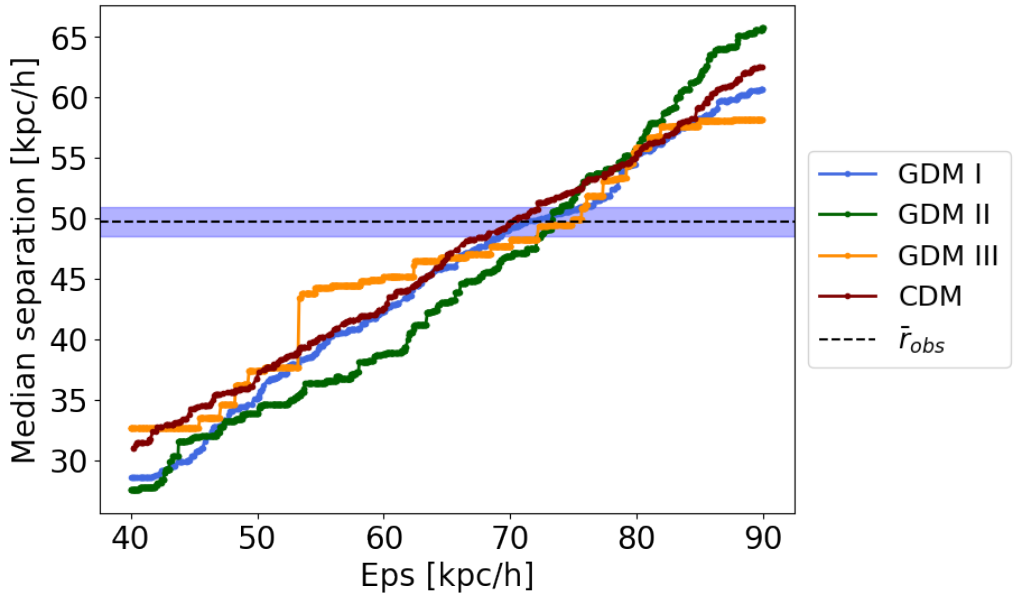

(b)

Figure 2.10: Results of the DBSCAN algorithm and the subsequent application of the filter to identify HCGs for $N_{\min} = 4$ (a) and $N_{\min} = 3$ (b), the observational results are considered within $r_{\text{obs}} = 39 \pm 2$ kpc. The parameter space is plotted in a region near the observational band in both cases.

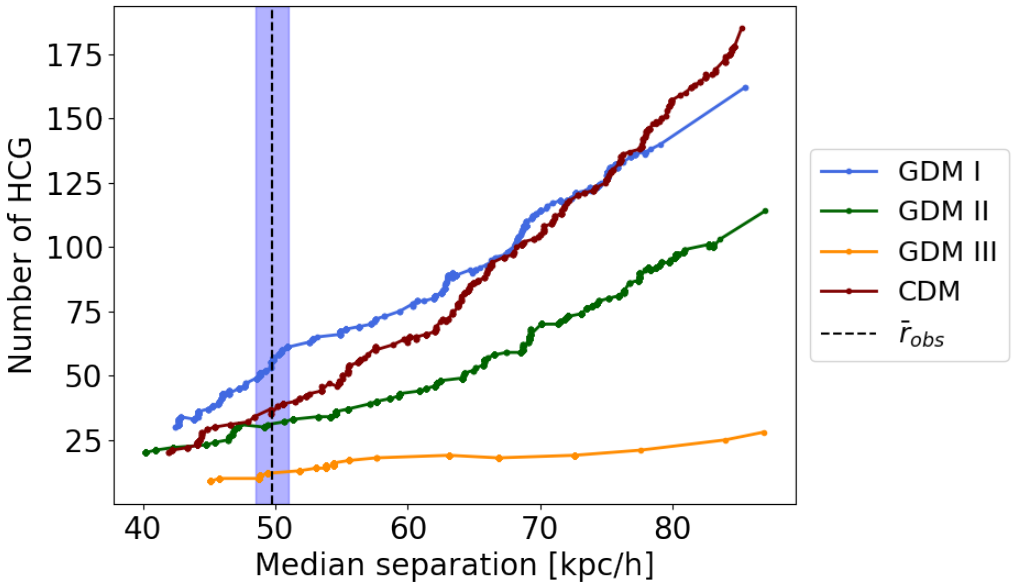

(a)

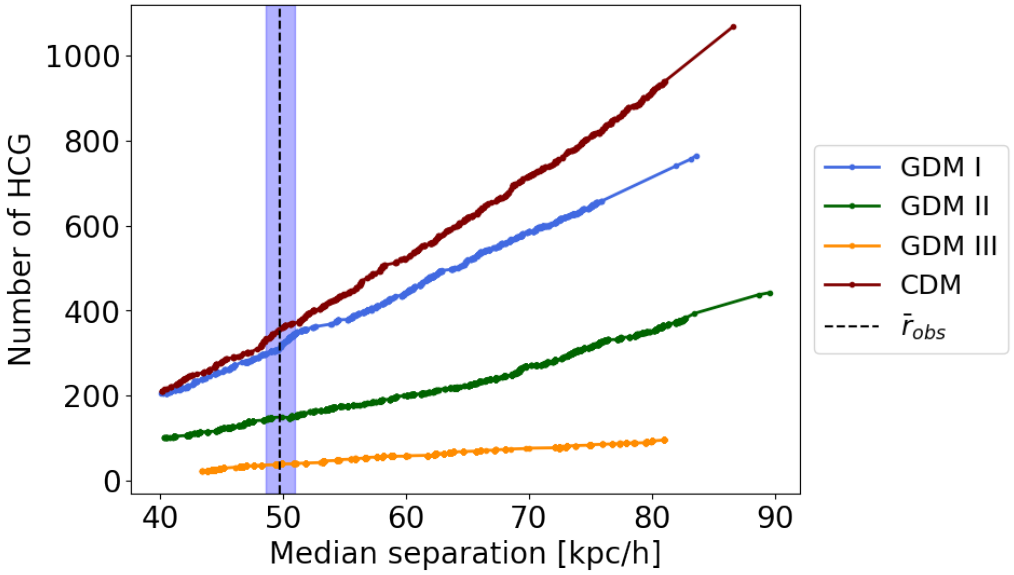

(b)

Figure 2.11: Results of the DBSCAN algorithm and the subsequent application of the filter to identify HCGs in the simulations. Here the physical distance is shown against the number of candidates for HCGs. In (a) for $N = 4$, GDM I shows the highest cluster count for mean spacing below 70 kpc/h, for separation greater than this, CDM starts to dominate. In the same way, a crossover for the count of GDM II and CDM close to the blue band of the observations is shown. Here, GDM II and GDM III remain below the CDM count throughout the interval.

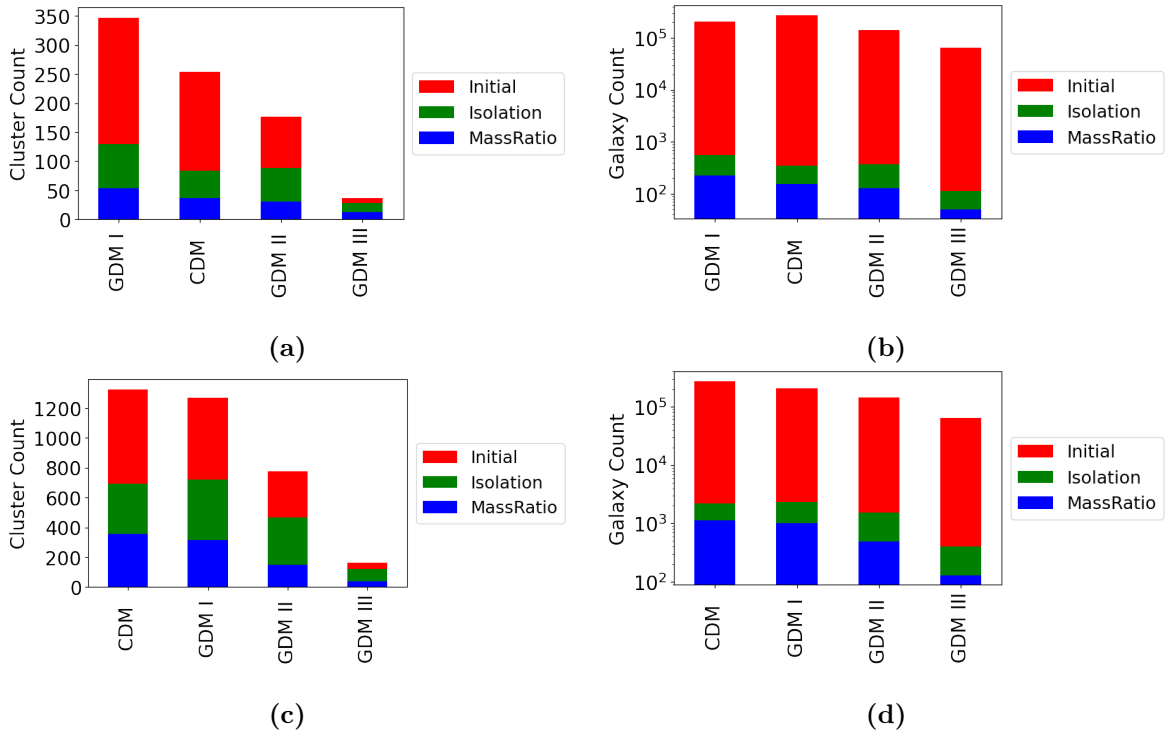

Figure 2.12: Evolution of the algorithm of classification considering the prevalence of the HCGs for N=4 (a) and N=3 (b). The full bar represents the total data set identified by DBSCAN (galaxies or clusters, respectively) in each model. The other blue and green bars represented the portion of data that survive their respective filter.

For $N = 4$, GDM I simulations had the most clusters, while CDM had the highest number of galaxy members overall. In contrast, for $N = 3$, CDM had slightly more clusters than GDM I. GDM III had the fewest clusters and galaxies for both $N = 3$ and $N = 4$, indicating a significant lack of small structures. In fact, GDM I has the most groups, followed by CDM, GDM II, and GDM III after applying the isolation filter. CDM faces challenges in meeting the isolation criterion due to abundant structures at smaller scales. GDM III is less affected by the criterion, having fewer clusters. This hierarchical trend persists with subsequent filters for $N = 4$, while the dwarf limit and fly-by restriction have minimal impact on galaxy counts and are not shown in Fig. 2.12.

Afterward, the mass-ratio criterion is applied. According to the blue bars (Fig. 2.12 (a) and (c)), the more pronounced cut-off in the initial power spectrum for a given model, the more clusters are ruled out by this filter. For instance, in GDM III simulations, where small structures are scarce, the probability of cluster formation is lower compared to other scenarios. Additionally, clusters in GDM III are dominated by the most massive galaxies, while CDM allows galaxies with significantly different masses to cluster together. Fig. 2.13 , panel a) shows that, on average, GDM III and GDM II have the most massive HCGs members with masses s of $3 \times 10^{13} M_{\odot}$ and $4 \times 10^{12} M_{\odot}$ respectively (see Fig. 2.13 b)). In contrast, for CDM, the mean value is $2 \times 10^{12} M_{\odot}$ and there is no significant contribution of galaxies with masses higher than $1 \times 10^{13} M_{\odot}$. CDM allows the clustering of galaxies with large mass differences, while GDM III favors clusters with similar-mass galaxies, resulting in HCGs dominated by massive galaxies.

Finally, the last boundary filter does not produce any effect physically relevant, however, its purpose is to reduce counting errors similar to the Min-halos constraint works.

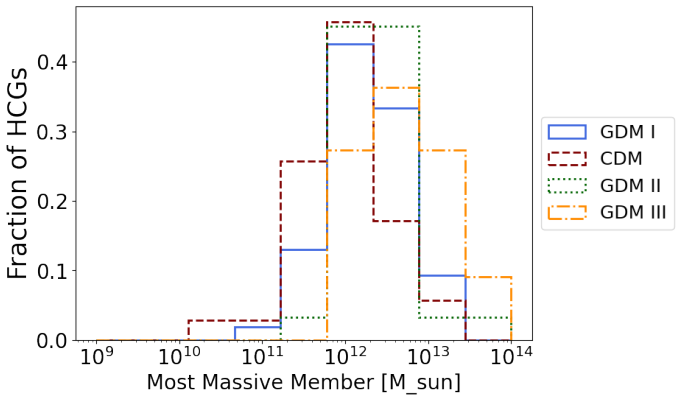

(a)

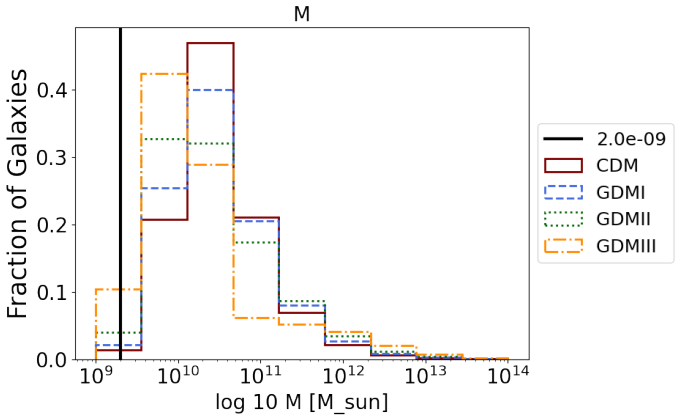

(b)

Figure 2.13: (a) Histograms of the mass of the largest HCGs members for the N=4 sample. As expected the distribution of masses in GDM III simulations is shifted to large values since a small substructure is seldom compared to CDM, therefore, it is more likely to find large galaxies than small ones. (b) Histograms of the virial masses of galaxy-sized halos within the mock catalogs for different models. The black vertical line corresponds to the dwarf limit.

2.3.7 Comparison with observations

In Fig. 2.14 we show the comparison between observed HCGs properties and those for the simulated data in general, only for $N = 4$ case. Fig. 2.14 (a) shows 2D distributions in the HCG mass-density ($M_{\rm vir} - \rho_g$) plane for different models and observations. In there, we observe overlapping regions in all cases. The mean value of HCGs mass within CDM, GDM I, II, and III simulations are $2 \times 10^{12} M_\odot$, $3 \times 10^{12} M_\odot$, $4 \times 10^{12} M_\odot$ and $3 \times 10^{13} M_\odot$ respectively, while the mean value for the observations is $2 \times 10^{12} M_\odot$. Discrepancies between mass distributions between models can be understood by virtue of the properties of the galaxy mass distributions in mock catalogs (as explained in the last section in Fig. 2.13) which result from different clustering mechanisms occurring in different models (see Section 2.3.6). In addition, the mean HGC density shown in Fig 2.14, in all cases is close to $1 \times 10^{16} M_\odot /$ Mpc^3. Likewise, in (b) and (c) we show the distributions for different HGC samples in the density-crossing ($\rho_g - t_c$) time and density-velocity dispersion ($\rho_g - \sigma_v$) planes, respectively.

It is well known in the literature that the crossing time of a group corresponds to a rough

measure of the dynamical stability of such a system and can be defined as follows [13]

$$t_c = \frac{4}{\pi}\frac{R}{\sigma_v}, \tag{2.36}$$

where R is the median projected separation between members and σ_v is the mean total velocity dispersion of the group. In (b) we observe that the distributions for HCG in simulations partially match those of observed HCGs. Values of the cross-time below $3 \times 10^{-1} H_0^{-1}$ are not consistent with those in all simulations, but only values above that threshold. In other words, these observed groups with small t_c cannot be reproduced in any simulation considered here. A similar situation is evident in (c) where the velocity dispersion distribution for observed HCGs is much higher than those for HGC in simulations. More precisely, the mean values for the velocity dispersion in CDM, GDM I, GDM II, and GDM III distributions are 69.9, 73.2, 68.6, and 89.7 km/s respectively. On the other side, the same quantity for the observational HCGs is 344 km/s.

On the other hand, the parameter space velocity dispersion-crossing time is shown in 2.14 (d). According to the previous comments we can see the discrepancies between the velocity dispersion. Since t_c closely depends on the dynamics in HCGs, it is linked to the kinematics in such systems. Therefore, the existing tension for the velocity dispersion between observations and simulations is intimately related to that for the crossing time.

The HCG distribution in the mass-crossing time and mass-velocity dispersion planes shown in panels (e) and (f) of Figs. 2.14 respectively. For the mass, there are regions where the distributions for observations and simulations match. However, in the last panel (f), distributions for observations and models are disjoint but we can identify some points lying inside the simulated regions.

Another interesting fact is the correlations between different observables. some of them are more prominent than others, for example, panel (d) clearly shows that there exists a linear scaling relation between the crossing time and the velocity dispersion either in models or observations. In contrast in panel (f) a similar correlation can be noticed between the virial mass and the velocity dispersion, and the slopes corresponding to models and observations are pretty similar. Despite the discrepancy between estimates of the velocity dispersion in observations and simulations, it is interesting that the $M_{\rm vir} - \sigma_v$ scaling relation is similar in both cases.

2.3.8 Time Evolution of simulated HCGs

In order to obtain the HCGs counts along the time for different models we applied directly the algorithm of classification to our mock catalogs at different values of the scale factor corresponding to scale factors from a=0.14 to a=1. The results are shown in Fig, 2.15 for N=4 (a) and N=3 (b). This plot shows that a maximum number of HCG is achieved at a_{max} right before a=1. Our estimate for a_{max} is close to the mean value corresponding to the observational HCGs sample represented by a dashed line. In both cases, the curve for the number of HCGs remains almost flat between a=0.2 and a=0.6, except for GDM III, which has the maximum value around a=0.3. After that, the number of groups starts to grow more efficiently within all the models, except for GDM III, whose counts remain around the same small value over time. Another interesting feature of the time series of the counts is the existence of a local maximum at $a = 0.7$ which arises just after the onset of the growing epoch at a=0.6. For some models (such as GDM II) the number of HCG at that point is comparable to the absolute maximum at a_{max}. This brings new questions motivating future works regarding HCGs evolution indeed.

2.4 Conclusions

The main result of this work, is the study of some properties of populations of HCG in catalogues generated from N-body simulations with different initial seeds prescribed according to the linear

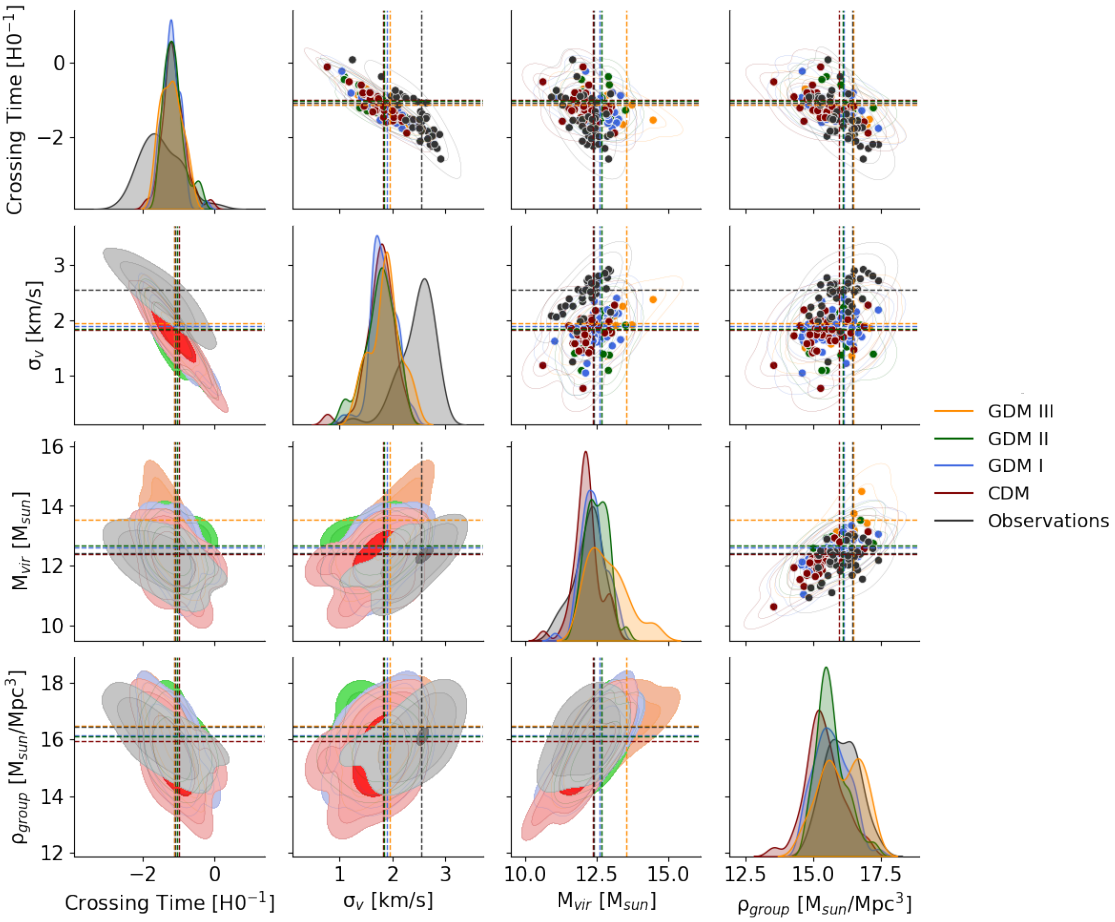

Figure 2.14: Comparison between observational and simulated data. We present the parameter space between virial mass, density, crossing time, and velocity dispersion in a matrix plot, with their respective histograms in the diagonal. We used kernel density estimation in the triangular-lower component with 1, 2, and 3-σ confidence levels in the contours, whereas in the triangular-upper component, we show the raw data.

matter power spectrum of three GDM models. Within this theoretical framework, the dark matter corresponds to a general fluid with non-vanishing sound speed, viscosity and equation of state. The GDM models chosen in this work have fixed and sufficiently small values of those free functions Consequently, dark matter linear perturbations free-stream giving rise to a cut-off in the matter power spectrum at small scales. Basically, an important goal of this work is to study the structure formation within these scenarios considering initial conditions with a lack of small substructure and its impact on counts and physical properties of populations of HCGs.

A second important result was the implementation of an algorithm to identify HCGs in our mock catalogues by accommodating the original Hickson compactness criterion (which uses projected separations between members) in terms of actual 3D physical separations available in mock catalogues. Specifically, we establish the compactness criterion by determining the ratio between physical and projected distances between members, namely 1.28. A very similar value was reported in [39] estimated using a different method. Afterwards, by monitoring the impact of different filters onto counts of clusters we identified the most relevant corresponding to the isolation condition and the mass-ratio relation. The former mainly affects counts within models with a larger amount

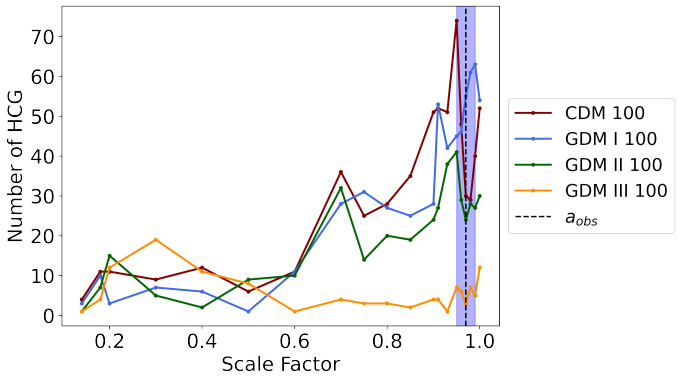

(a)

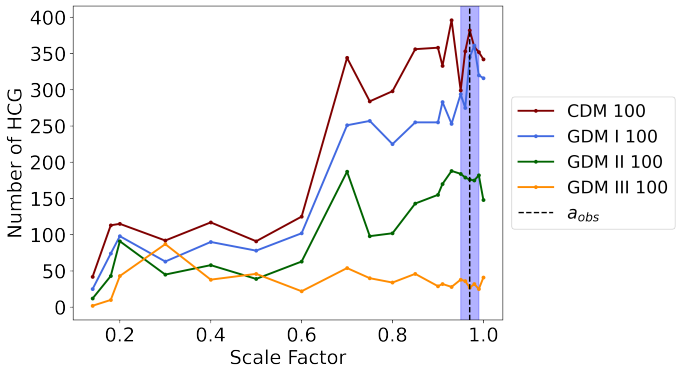

(b)

Figure 2.15: Time series of the number of HCGs through time for $N = 4$ (a) and $N = 3$ (b) in different GDM scenarios. The number of groups remains almost constant and very similar between models for a while ($a \in (0.2, 0.6)$). After this point, the HCG number increases significantly for CDM, GDM I, and GDM II. The maximum value is reached at $a \sim 0.97$ in the three cases. On the other hand, GDM III seems to reach its maximum at $a \sim 0.3$. The blue band and the central dashed line represent the median redshift of the observational sample and its uncertainty respectively.

of substructure which prevents isolation of structures. Besides, the mass-ratio condition mainly affects counts of models with less amount of substructure since in that case galaxy clusters are less likely to form given that massive galaxies are numerous. The main relevance of this criterion is that there are different galaxy clustering mechanisms in different models, in this work we identified self agglomeration (mainly for CDM) and clustering induced by a falling into a dominant gravitational potential well (as in GDM III).

Finally, in order to track the time evolution of counts of HCG in different populations, we applied the algorithm of classification to clustering in the mock catalogues from $z = 0$ to $z = 6$. The time series of the counts present an absolute maximum for CDM, GDM I and GDM II, whose value is quite similar to that reported for observed HCG and occurs at around the same redshift. A remarkable feature of the time series for such models is that it remains flat for a while before starting to significantly grow until reaching the absolute maximum close to $z = 0$. In contrast, counts for HCGs in GDM III remain small and similar to the initial value. In general, this model shows the most notable differences in all tests here reported. In the future, we aim to carry out a more complete study of the evolution of groups and it would include the evolution of each member over time, as well as the study of their environment.

Bibliography

[1] Angulo, R. E., Springel, V., White, S. D. M., Jenkins, A., Baugh, C. M., and Frenk, C. S. (2012). Scaling relations for galaxy clusters in the Millennium-XXL simulation. *mnras*, 426(3):2046–2062.

[2] Barnes, J. (1984). N-body studies of compact groups of galaxies dominated by dark matter. *Monthly Notices of the Royal Astronomical Society*, 208(4):873–885.

[3] Barton, E., Geller, M., Ramella, M., Marzke, R. O., and da Costa, L. N. (1996). Compact Group selection From Redshift Surveys. *Aj*, 112:871.

[4] Behroozi, P., Wechsler, R. H., Hearin, A. P., and Conroy, C. (2019). UniverseMachine: The correlation between galaxy growth and dark matter halo assembly from z = 0-10. *Monthly Notices of the Royal Astronomical Society*, 488(3):3143–3194.

[5] Behroozi, P. S., Wechsler, R. H., and Wu, H.-Y. (2012a). THE ROCKSTAR PHASE-SPACE TEMPORAL HALO FINDER AND THE VELOCITY OFFSETS OF CLUSTER CORES. *The Astrophysical Journal*, 762(2):109.

[6] Behroozi, P. S., Wechsler, R. H., Wu, H.-Y., Busha, M. T., Klypin, A. A., and Primack, J. R. (2012b). GRAVITATIONALLY CONSISTENT HALO CATALOGS AND MERGER TREES FOR PRECISION COSMOLOGY. *The Astrophysical Journal*, 763(1):18.

[7] Bode, P. W., Cohn, H. N., and Lugger, P. M. (1993). Simulations of Compact Groups of Galaxies: The Effect of the Dark Matter Distribution. *The Astrophysical Journal*, 416:17.

[8] Díaz-Giménez, Eugenia and Zandivarez, Ariel (2015). Where are compact groups in the local universe? *A&A*, 578:A61.

[9] Díaz-Giménez, E. and Mamon, G. A. (2010). Compact groups from the Millennium Simulations – I. Their nature and the completeness of the Hickson sample. *Monthly Notices of the Royal Astronomical Society*, 409(3):1227–1243.

[10] Ester, M., Kriegel, H.-P., Sander, J., and Xu, X. (1996). A density-based algorithm for discovering clusters in large spatial databases with noise. In *Proceedings of the Second International Conference on Knowledge Discovery and Data Mining*, KDD'96, page 226–231. AAAI Press.

[11] Hickson, P. (1982). Systematic properties of compact groups of galaxies. *The Astrophysical Journal*, 255:382–391.

[12] Hickson, P. (1997). Compact groups of galaxies. *Annual Review of Astronomy and Astrophysics*, 35(1):357–388.

[13] Hickson, P., Mendes de Oliveira, C., Huchra, J. P., and Palumbo, G. G. (1992). Dynamical Properties of Compact Groups of Galaxies. *The Astrophysical Journal*, 399:353.

[14] Hu, W. (1998). Structure formation with generalized dark matter. *The Astrophysical Journal*, 506(2):485–494.

[15] Ilić, S., Kopp, M., Skordis, C., and Thomas, D. B. (2021). Dark matter properties through cosmic history. *Phys. Rev. D*, 104:043520.

[16] Klypin, A. A., Trujillo-Gomez, S., and Primack, J. (2011). Dark Matter Halos in the Standard Cosmological Model: Results from the Bolshoi Simulation. *The Astrophysical Journal*, 740(2):102.

[17] Kopp, M., Skordis, C., and Thomas, D. B. (2016). Extensive investigation of the generalized dark matter model. *Phys. Rev. D*, 94:043512.

[18] Kopp, M., Skordis, C., Thomas, D. B., and Ilić, S. (2018). Dark matter equation of state through cosmic history. *Physical Review Letters*, 120(22).

[19] López-Sánchez, J. N., Munive-Villa, E., Avilez-López, A., and Martínez-Bravo, O. M. (2022). Compact groups in gdm cosmological simulations. *Monthly Notices of the Royal Astronomical Society*, 515(3):3199–3211.

[20] McConnachie, A. W., Ellison, S. L., and Patton, D. R. (2008). Compact groups in theory and practice – I. The spatial properties of compact groups. *Monthly Notices of the Royal Astronomical Society*, 387(3):1281–1290.

[21] Moore, B., Ghigna, S., Governato, F., Lake, G., Quinn, T., Stadel, J., and Tozzi, P. (1999). Dark matter substructure within galactic halos. *The Astrophysical Journal*, 524(1):L19–L22.

[22] Paduroiu, S. (2022). Warm dark matter in simulations. *Universe*, 8(2):76.

[23] Pérez-González, P. G., Rieke, G. H., Villar, V., Barro, G., Blaylock, M., Egami, E., Gallego, J., de Paz, A. G., Pascual, S., Zamorano, J., and Donley, J. L. (2008). The stellar mass assembly of galaxies fromz= 0 toz= 4: Analysis of a sample selected in the rest-frame near-infrared withSpitzer. *The Astrophysical Journal*, 675(1):234–261.

[24] Prada, F., Klypin, A. A., Cuesta, A. J., Betancort-Rijo, J. E., and Primack, J. (2012). Halo concentrations in the standard Lambda cold dark matter cosmology. *Monthly Notices of the Royal Astronomical Society*, 423(4):3018–3030.

[25] Ramella, M., Diaferio, A., Geller, M. J., and Huchra, J. P. (1994). The Birthplace of Compact Groups of Galaxies. *The Astrophysical Journal*, 107:1623.

[26] Rood, H. J. and Struble, M. F. (1994). Spatial coincidence between a number of hickson compact groups and loose groups or clusters. *Publications of the Astronomical Society of the Pacific*, 106(698):413–416.

[27] Rose, J. A. (1977). A survey of compact groups of galaxies. *Apj*, 211:311–318.

[28] Seyfert, C. K. (1948). Five thousand external galaxies and a new dense group. *Aj*, 53:203.

[29] Shakhbazyan, R. K. (1973). Compact groups of compact galaxies. *Astrofizika*, 9:495–501.

[30] Springel, V. (2005). The cosmological simulation code gadget-2. *Monthly Notices of the Royal Astronomical Society*, 364(4):1105–1134.

[31] Springel, V., White, S. D. M., Jenkins, A., Frenk, C. S., Yoshida, N., Gao, L., Navarro, J., Thacker, R., Croton, D., Helly, J., Peacock, J. A., Cole, S., Thomas, P., Couchman, H., Evrard, A., Colberg, J., and Pearce, F. (2005). Simulations of the formation, evolution and clustering of galaxies and quasars. *Nature*, 435(7042):629–636.

[32] Stephan, P. M. E. (1877). Nébuleuses nouvelles découvertes et observées à l'Observatoire de Marseille. *Monthly Notices of the Royal Astronomical Society*, 37(6):334–339.

[33] Teyssier, R., Pires, S., Prunet, S., Aubert, D., Pichon, C., Amara, A., Benabed, K., Colombi, S., Refregier, A., and Starck, J.-L. (2009). Full-sky weak-lensing simulation with 70 billion particles. *A&A*, 497(2):335–341.

[34] Thomas, D. B., Kopp, M. I., and Markovivc, K. (2019). Using large scale structure data and a halo model to constrain Generalised Dark Matter. *Monthly Notices of the Royal Astronomical Society*, 830(2):155.

[35] Tovmassian, H. M. and Chavushyan, V. H. (2000). Compact groups: Local groups? *The Astronomical Journal*, 119(4):1687–1690.

[36] Tzanavaris, P., Hornschemeier, A. E., Gallagher, S. C., Johnson, K. E., Gronwall, C., Immler, S., Reines, A. E., Hoversten, E., and Charlton, J. C. (2010). Ultraviolet+Infrared Star Formation Rates: Hickson Compact Groups with Swift and Spitzer. *The Astrophysical Journal*, 716(1):556–573.

[37] Vennik, J., Richter, G. M., and Longo, G. (1993). The neighbourhoods of the nearest hickson groups. *Astronomische Nachrichten: A Journal on all Fields of Astronomy*, 314(6):393–397.

[38] Wechsler, R. H. and Tinker, J. L. (2018). The connection between galaxies and their dark matter halos. *Annual Review of Astronomy and Astrophysics*, 56(1):435–487.

[39] Wiens, C. D., Wenger, T. V., Tzanavaris, P., Johnson, K. E., Gallagher, S. C., and Xiao, L. (2019). The occurrence of compact groups of galaxies through cosmic time. *The Astrophysical Journal*, 873(2):124.

[40] Zepf, S. E. (1993). The Frequency of Mergers in Compact Groups. *Apj*, 407:448.

[41] Zhang, T., Liao, S., Li, M., and Gao, L. (2019). The optimal gravitational softening length for cosmological N-body simulations. *Mon. Not. Roy. Astron. Soc.*, 487(1):1227–1232.

Chapter 3

Small-scale system dynamics: SFDM and CDM

In the previous chapter, we have studied the properties of some astrophysical systems from cosmological simulations. Essentially, the cut-off produced at small scales given by the linear power spectrum in the initial conditions has been explored. In this chapter, we are going to study the dynamics of systems at small scales in two different models, CDM and SFDM. At small scales, the effects derived from the characteristics of each dark matter candidate become highly relevant. In addition, different processes can be studied such as halo formation and growth, halo mergers and interactions, tidal disruption, internal dynamics, and the contribution from the environment.

This chapter corresponds to the publication [10]. In the first part, we will study the Schrödinger-Poisson system and the methods used to evolve the system will be discussed. Some examples will also be shown that prove the numerical performance and precision of the code. The second part of the chapter is dedicated to the study of CDM at small scales, where the Jeans equation to stabilize dark matter halos will be studied. Finally, a comparison between both models will be made using simple examples, in order to explore the differences between both models.

3.1 Scalar Field Dark Matter at small scales

The possibility of scalar fields as dark matter has gained great interest in the community during the last decade due to its interesting phenomenological implications. Particularly, scalar field theories describing ultralight axion-like particles with masses around 10^{-22}eV have turned appealing owing to their lack of small-scale problems, such as the missing satellites problem and the halo core-cusp problem, because of the large de Broglie length of such light particle of the order of kiloparsecs. Particularly interesting is that the accumulation of bosons assembles macroscopic coherent states corresponding to a Bose-Einstein condensate that may play the role of dark matter halos as described in recent reviews [7, 6, Lee, 15]

The analysis of the model includes the study of the evolution and formation of structures, which needs the use of large-scale numerical simulations. The regime where this analysis happens is that in which the dynamic of the bosonic gas is ruled by the Gross-Pitaevskii-Poisson (GPP) system, where the parameter order obeys the Gross-Pitaevskii equation for the Bose gas subject to the gravitational potential sourced by the boson cloud itself. This analysis includes studies of structure formation and formation of universal density profiles.

The Scalar Field Dark Matter paradigm assumes dark matter is a spin-0 ultra-light scalar field with masses around $m \sim 10^{-22}\text{eV}/c^2$ and positive self-interactions. Due to the ultra-light boson mass, the SFDM could form Bose–Einstein condensates (BEC) in the very early Universe, which is interpreted as dark matter halos. Additionally, most of these works assume the SFDM is at zero temperature, implying the SFDM ultra-light bosons occupy the ground state only.

The Gross-Pitaevskii-Poisson system is appropriate as a description of a structure made of BEC-DM, where both gravitational and velocity fields are small enough that they can be treated in the Newtonian regime. This set of equations in an expanding universe takes the form

$$i\hbar\left(\frac{\partial}{\partial t}+\frac{3}{2}H\right)\psi = \left(-\frac{\hbar^2}{2ma^2}\nabla^2+\frac{g}{m}|\psi|^2+m\Phi\right)\psi \tag{3.1}$$

$$\nabla^2\Phi = 4\pi G a^2(\rho-\rho_b), \tag{3.2}$$

with $\rho = |\psi|^2$ is the mass density of the scalar field and $\rho_b = \rho_b(a=0)a^{-3}$ is the homogeneous background value. Additionally, the cubic term $|\psi|^2\psi$ is considered as the self-interaction term, here g is known as the coupling constant defined as $g = 4\pi\hbar^2\frac{a_s}{m}$, where a_s is the scattering length. If $g > 0$ the interaction is repulsive, on the contrary, it is attractive.

Additionally, for the case of small scales, this means that a can be approximated to today's value ($a = 1$), so the set of equations (3.1) can be applied to study the evolution of single configurations, collisions or mergers between two or more configurations. For the special case when $g = 0$, the equation reduces to the Schrödinger-Poisson system, eq. (1.124).

3.1.1 Time evolution

There are different numerical methods to solve the Schrödinger-Poisson system in d dimensions reported in the literature [16, 5, 3, 12]. In this case, the method reported in [10] has been used (see appendix C. The Schrödinger equation is a time-dependent linear partial parabolic differential equation. For that reason, it is necessary to discretize the time domain, by means of one of the most common methods: explicit, implicit, or semi-implicit [13]. These methods can be described by the following expression

$$(\mathbb{1} - \theta\Delta t\mathbb{M})\, u^{n+1} = (\mathbb{1} + (1-\theta)\Delta t\mathbb{M})\, u^{n}, \tag{3.3}$$

where M represents the right-hand side of the equation 1.124, which depends on the spatial part, Δt is the time step,u is the solution in the timestep n and θ is the parameter which determines the method used, that is

$$\theta = 0 \qquad \text{Explicit,} \tag{3.4}$$
$$\theta = 1 \qquad \text{Implicit,} \tag{3.5}$$
$$\theta = \frac{1}{2} \qquad \text{Semi-implicit.} \tag{3.6}$$

Particularly, for this type of equation it has been found that the semi-implicit method, known as **Cranck-Nicholson scheme** [2], is the most adequate to evolve the system over time, since it is unconditionally stable. On the other hand, there are different methods to discretize the space, such as finite difference, finite element or spectral methods [11]. In this work, the finite difference method has been used, which discretizes the domain of the problem into a grid and replaces the derivatives in the differential equations with finite difference approximations

$$\partial_x fi \approx \frac{fi+1 - f_{i-1}}{2h_x}, \tag{3.7}$$
$$\partial_{xx} fi \approx \frac{fi+1 - 2f + f_{i-1}}{h_x^2}, \tag{3.8}$$
$$\partial_{xy} fi \approx \frac{fi+1, j+1 - f_{i-1,j+1} - f_{i+1,j-1} + f_{i-1,j-1}}{4h_x h_y}. \tag{3.9}$$

For the Schrödinger equation at the points of the logical domain, $(\xi_i, \eta_j, \kappa_k, t^n)$ and $(\xi_i, \eta_j, \kappa_k, t^{n+1})$, where the wave function evaluated at each time step is written as $\psi^n_{i,j,k}$ and $\psi^{n+1}_{i,j,k}$ respectively and these values are related as follows

$$(\mathbb{1} + \mathbb{M})\psi^{n+1}_{i,j,k} = (\mathbb{1} - \mathbb{M})\psi^{n}_{i,j,k}, \tag{3.10}$$

where Δt is time resolution, $\mathbb{M} = \frac{i}{2}\hat{H}\Delta t$ and H is the Hamiltonian discrete operator defined on the logical domain Ω_L.

Now, the Poisson equation is an elliptical partial differential equation. Analogously to the previous example, the space is discretized using finite differences, which implies a system of linear equations with an equivalent matrix $\mathcal{A}\boldsymbol{u} = \boldsymbol{b}$, such that $\mathcal{A}$ has the size of $N^d \times N^d$, which is valid for a mesh with N points along each axis, equally separated by a spatial step h. That is, if $d = 3$, then $h_x = h_y = h_z$. In general, solving this type of system directly is computationally expensive. For instance, for $N = 100$ and $d = 3$, the size of the associated matrix would be 1000000×1000000. Furthermore, these systems cannot be efficiently solved using direct methods such as Gauss-Jordan or by inverting the matrix associated with the system $\mathcal{A}$. In order to solve this system it is possible to implement iterative methods such as Jacobi, SOR, Multigrid, etc. Additionally, it is convenient to implement the use of a sparse matrix. In this case, we have used the **Minimum Residual method**, taking advantage of the fact that the representative matrix

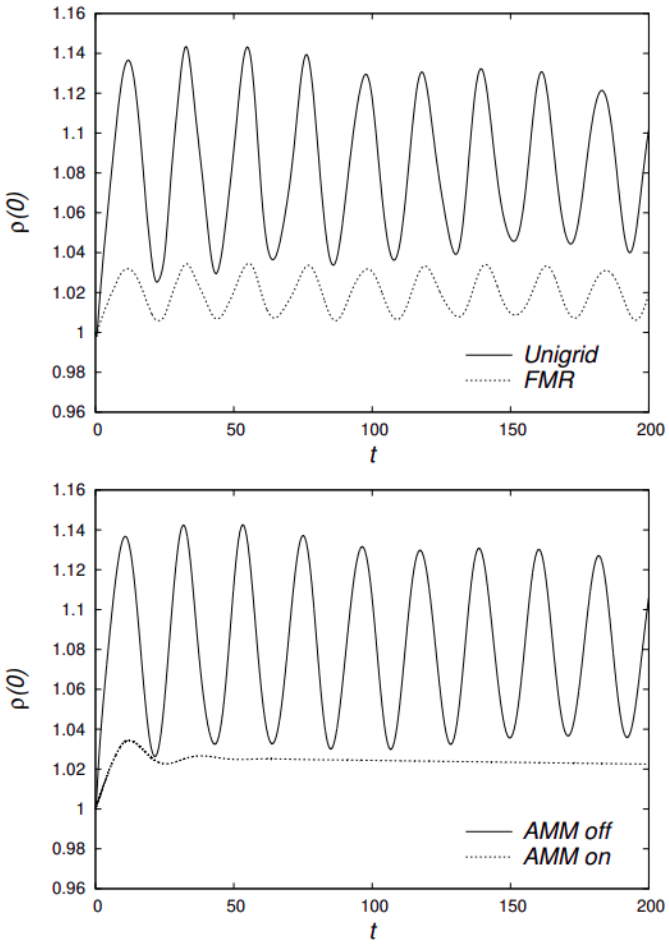

Figure 3.1: Central density as a function of time for an equilibrium configuration using the xBEC code in unigrid and FMR modes, using the ADI evolution methods (top). Results were obtained using the AMM method in off and on modes (bottom).

of the system is highly symmetric. This method minimizes the residual to find the solution of the system. First, it is necessary to give an initial guess x_k for the solution vector and then compute the residual as

$$r_k = |\boldsymbol{b} - \mathcal{A}\boldsymbol{x}_k|. \tag{3.11}$$

Then, the solution vector is updated by adding a correction term to the current solution, $\boldsymbol{x}_{k+1} = \boldsymbol{x}_k + \boldsymbol{d}_k$. The choice of the correction term $\boldsymbol{d}_k$ depends on the specific iterative technique used. Indeed, such term is chosen to minimize the norm of the residual in eq. (3.11). The iteration process continues until a convergence criterion is met or a maximum number of iterations is reached.

A detailed description of the methods to solve the Schrödinger-Poisson system can be found in [10]. Below some examples of simulations with different assemblies of configurations will be shown.

Evolution of an equilibrium configuration

As a first problem, we consider the evolution of a ground state stationary spherical configuration. The numerical domain is set to the box $[-20, 20]^3$. For comparison, the control code xBEC is used in unigrid FMR mode and for comparison, the AMM code is set in the equivalent off (on)

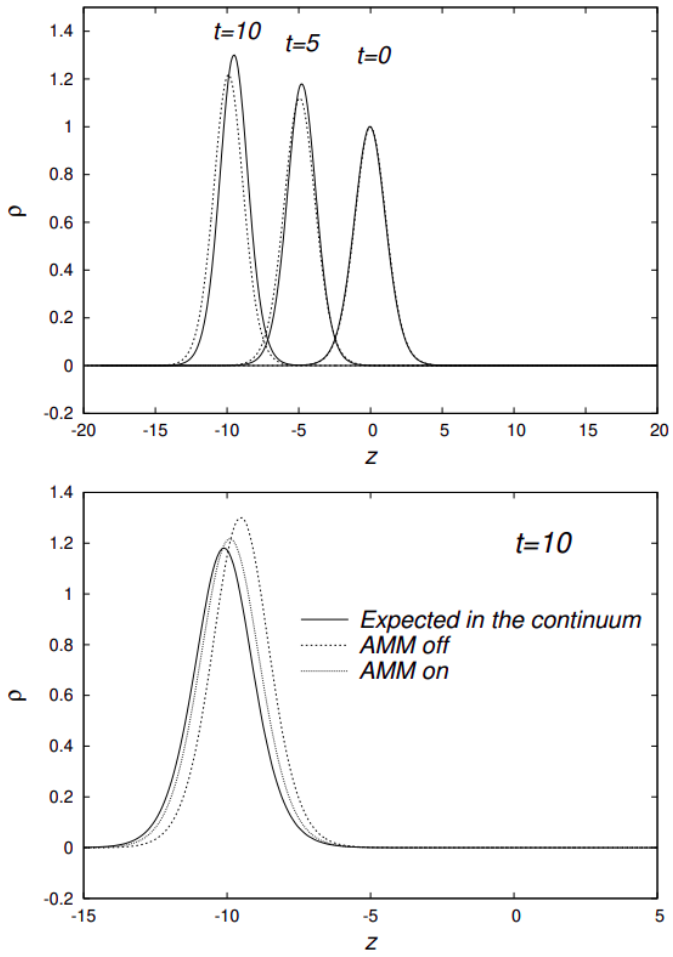

Figure 3.2: Snapshots of density for the boosted configuration with $v_z = -1$ at time $t = 0, 5, 10$ simulated with AMM in off and on modes. (Bottom) We show a zoom-in of the solution at time $t = 10$ and the estimated solution in the continuum limit calculated with a Richardson extrapolation with the xBEC code.

mode. Physically, because the initial configuration is stationary in the continuum, it is expected that the density $|\psi|^2$ remain time-independent during the evolution. Nevertheless, finite differences approximation and time integration introduce permanent truncation errors that perturb the wave function. The effect is that the configuration oscillates, in fact with specific mode frequencies (see e.g. [4]), whose amplitude should converge to zero when increasing resolution. The results using the xBEC code in unigrid and FMR modes appear in the first panel of Figure 3.1. This figure shows that the amplitude of density oscillation reduces by a factor of four when doubling resolution, indicating second-order convergence. On the other hand, the results for the AMM code in on (off) modes appear in the second panel and shows also a similar convergent behavior. In the case of the AMM method, precise convergence is not expected since the resolution is not exactly double, but gradually increasing resolutions that depend on the domain coordinates Also notice that the oscillations are damped in the case of AMM-on mode, which is due to the spatially dependent resolution, that produces space-dependent discretization errors different in each part of the domain.

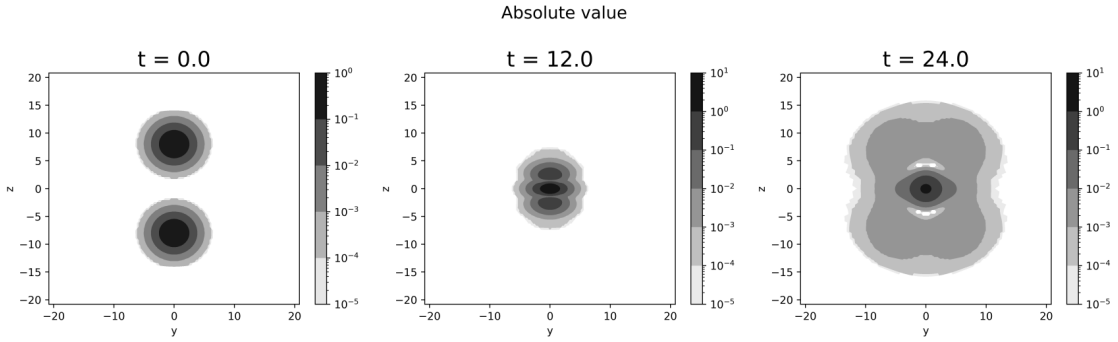

Figure 3.3: Projections of the density at three different times during the merger of the binary configurations on the yz-plane.

Evolution of a boosted equilibrium configuration

The code needs to show the ability to simulate moving configurations. This is why a second test involves a boosted equilibrium configuration. The setup consists in redefining the wave function of an equilibrium configuration $\psi_{\rm eq}(\boldsymbol{x}, 0) \to e^{-iv_z}\psi_{\rm eq}(\boldsymbol{x}, 0)$, which produces the configuration to move along the z direction with velocity v_z.

For illustration, we use $v_z = -1$ and the configuration located initially at the coordinate origin. In Figure 6 we show snapshots of the density $|\psi|^2$ projected along the $z-$axis using the AMM code in off and on modes. In order to know about the effects of refinement within the AMM code, we look closer at the snapshot at time $t = 0$ and compare the results using the AMM-off and AMM-on modes with the expected solution in the continuum also in Figure 3.2. The AMM-off uses a constant resolution $\Delta_{xyz} = 0.4$ whereas the AMM-on uses a transformation that covers the range of resolutions from $\Delta_{xyz} = 0.4$ far from the blob to $\Delta_{xyz} = 0.2$ around the maximum density. The solution in the continuum is calculated as the Richardson extrapolation of solutions obtained with the xBEC in unigrid mode with resolutions $\Delta_{xyz} = 0.2, 0.1$. The results show convergence toward the solution in the continuum when using the AMM-on mode.

3.1.2 Evolution of a binary configuration

For the next step, we show the solution of the SP system for the frontal collision of two equal mass equilibrium configurations with head-on velocity $v_z = \pm 0.5$ launched from initial positions $z0 = \pm 8$ along the z-axis. This case with $E < 0$ corresponds to a merger where the two initial configurations fuse and form a final single blob. In Fig. 3.3 we show some snapshots of the projected density on the yz-plane. In Fig. 3.4 we show some diagnostics, including the time series of the central density of the system and the virialization function $2K + W$. Also shown is a convergence test of the density at two times. For this, we generated three runs with a different resolution with xBEC and produced the Richardson extrapolated solution to the continuum. The plots show that in the solutions using AMM-off with uniform resolution 0.4 and AMM-on with resolution from 0.4 to 0.2, the numerical solutions converge to the expected in the continuum.

3.1.3 Embedded SP configurations inside a Soliton Halo

The primary objective of this section is to demonstrate the utilization of our AMM code in simulating the evolution of a subhalo. This subhalo possesses the density profile of an equilibrium configuration and resides within the gravitational potential of a host halo whose gravitational potential dominates and eventually disrupts the subhalo. By considering this specific case, our main aim is to explore a straightforward scenario reminiscent of SFDM halos that exist within

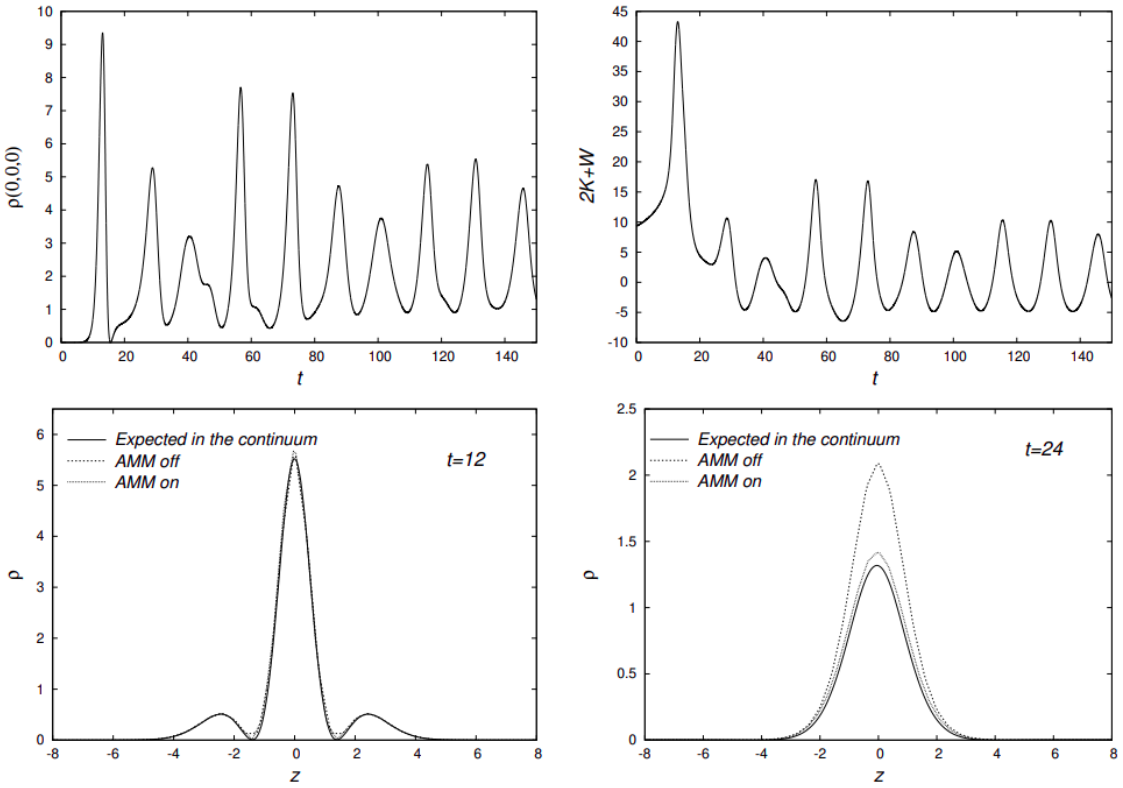

Figure 3.4: The central value of the density and virialization function as a function of time for the head-on merger of two equilibrium configurations using the AMM method. At the bottom, we show the density using AMM-off and AMM-on converging to the expected solution at the continuum at two snapshots along the z-axis.

highly interacting astrophysical environments. In Problem C, we conducted simulations involving a initially stationary configuration, which gravitationally interacts with a larger configuration featuring a fixed core-like density profile. Such simulations hold promise for investigating highly interacting galactic systems, including groups and clusters of galaxies, which have been relatively scarce or absent within alternative scenarios to CDM, such as the SFDM model. The complexity of phenomena observed in these systems is considerable, therefore it is necessary the employment of sophisticated numerical and physical methods in order to obtain a reasonably accurate depiction of their dynamics and evolution. To achieve this goal, we consider the host galaxy halo to be spherically shaped, with a soliton density profile obtained from cosmological simulations, as prescribed below [17]

$$\rho_c(r) = \frac{0.019\left(\frac{m}{10^{-22}\mathrm{eV}}\right)^{-2}\left(\frac{r_c}{\mathrm{kpc}}\right)^{-4}}{\left[1+0.091\left(\frac{r}{r_c}\right)^2\right]^8}, \tag{3.12}$$

where

$$r_c = 1.6\left(\frac{m}{10^{-22}\mathrm{eV}}\right)^{-1}\left(\frac{M_{\mathrm{vir}}}{10^9 M_\odot}\right)^{-1/3}\mathrm{kpc}, \tag{3.13}$$

corresponding to a core size of approximately 2 kpc. This density distribution sources a - gravitational potential Vbg that is kept fixed during the evolution.

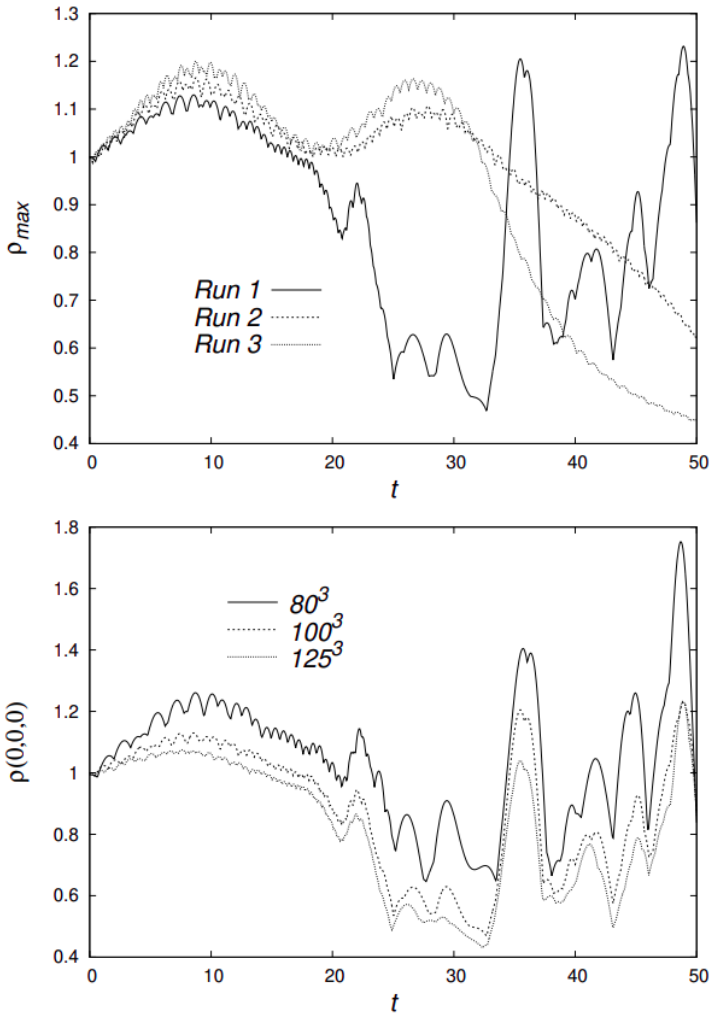

Figure 3.5: (Top) Maximum of the subhalo density $|\psi|^2$ as a function of time, for different initial conditions. (Bottom) Self-convergent behavior of the maximum density for Run 1 using three resolutions with resolution factor $1.25 = 125/100 = 100/80$.

The host halo produces a fixed gravitational potential that is plugged into the Schr¨odinger equation. This potential arises from solving the Poisson equation $\rho_c(r)$ in (3.12) at the initial time and plays the role of a gravitational trap that confines the substructure into a bound region. In our case of study, we consider a mass of the host halo that is larger than the mass of the subhalo by a factor of two. Since it is of interest to study the disruption effect suffered by the subhalo due to the interaction with the host, we set the initial conditions such that the center of the host halo stays fixed at the origin of coordinates, whereas the subhalo configuration is initially centered at $\vec{x}(0) = (0, 10, 0)$ in code units (corresponding to $\vec{x}(0) = (0, 19, 2, 0)$kpc, using $v \sim 10\text{km}/s$ as the average velocity of boson in the condensate [7] in order to calculate the de Broglie length), with initial velocity $\vec{v}(0) = (0, 0, -v_0)$. The initial velocity magnitude v_0 is the only parameter that is varied in the three different simulations. In order to set the values of v_0 we take as reference the value $v_{\text{ref}} = \sqrt{\dfrac{M_c(r)}{r}}$ and $M_c(r) = \int_0^r \rho_c(r')r'^2 dr'$. The idea is that with this initial velocity the trajectory of the center of the subhalo corresponds to a nearly circular orbit on the yz-plane.

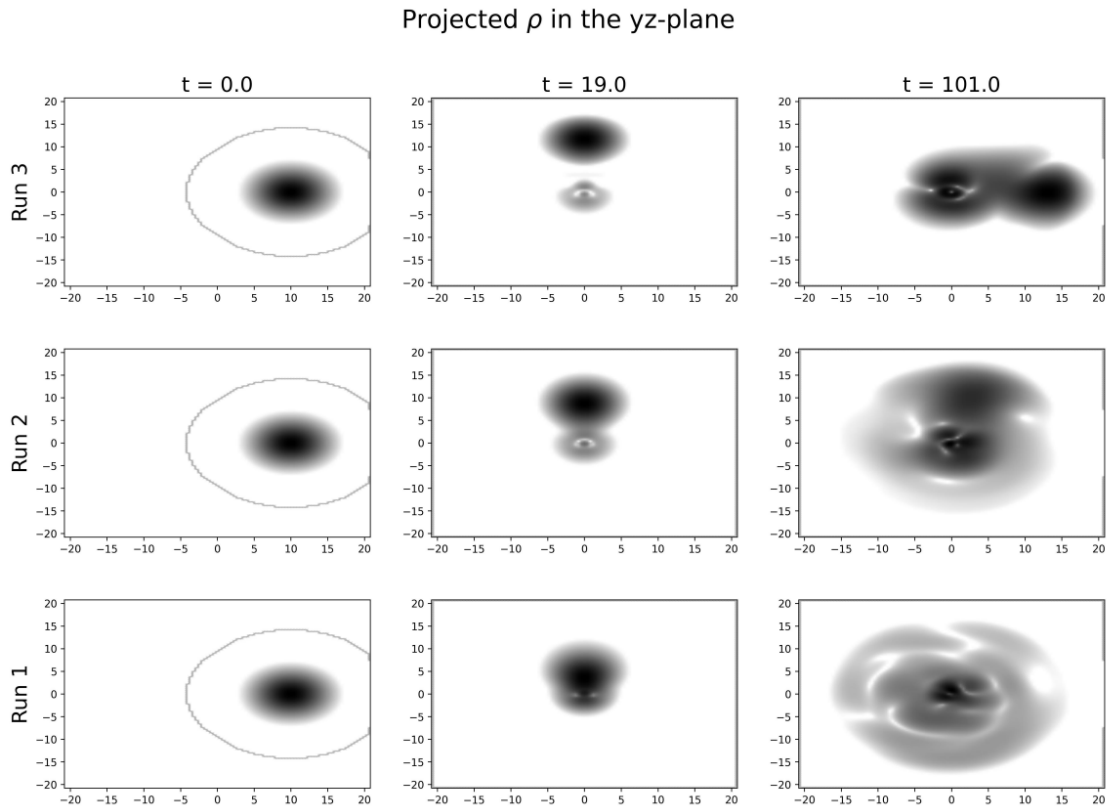

Figure 3.6: Snapshots of the subhalo density projected on the yz-plane at times $t = 0, 19, 101$ from left to right in different simulations. For reference, the center of the host galaxy lies at the coordinate origin.

The three runs correspond to different values of the initial velocity of the subhalo defined as follows:

- Run 1. $v_0 = v_{\rm ref} - 0.2 \approx 0.4$. In this case, it is expected that the gravitational force dominates over the centripetal force.
- Run 2. $v_0 = v_{\rm ref} \approx 0.6$. The subhalo would move in a nearly circular trajectory. Due to tidal effects, the spherical shape would be destroyed and part of the mass of the subhalo would be torn apart whereas the other part would be accreted towards the center of the potential.
- Run 3. $v_0 = v_{\rm ref} + 0.2 \approx 0.8$. The subhalo would tend to escape from the host potential and eventually, its mass will be lost through the boundaries.

The domain for all our simulations is given by a cubic box with edges placed at $[-20.8, 20.8]^3$ which is discretized into a mesh containing $N = 104^3$ points. Fig. 3.5 10 shows the maximum density of the subhalo , for Runs 1, 2, and 3 as a function of time. Also in that figure, we show the self-convergent behavior for Run 1 of the maximum of density, using three runs with successive resolutions with resolution factors of 1.25.

We considered the time series of the maximum density of the subhalo as an indicator of the extent of deformation of the subhalo. The behavior of density maximum indicates that the subhalo tends to remain closer to the initial value as the angular momentum is bigger and also oscillates with a larger amplitude. In conclusion, the larger the angular momentum is, the more deformed

results of the subhalo. Finally, in Fig. 3.5 we illustrate the evolution of the subhalo density for the three runs, projected on the yz-plane. Interestingly, as clearly can be seen in snapshots shown in Fig. 3.6, we can distinguish two possible fates of the subhalo, for run 1 since the angular momentum is sufficiently small, a significantly large fraction of the mass remains as a bounded configuration infalling towards the host center, while the rest of the initial mass is ripped away from the subhalo and either scatters around the host potential well or gets away from it. In conclusion, in the last scenario, the disruption effect on the subhalo results in deformation and a reduction in mass. In contrast, in the other side limit, simulated in run 3, the subhalo holds large enough angular momentum to dissolve the subhalo, and part of its mass is kidnapped by the host and the other fraction runs away from it.

3.2 CDM at small scales

3.2.1 Halo stability

The collisionless Boltzmann equation

For modeling a collisionless system such a galaxy or a halo, we can use the Boltzmann equation, where the six-dimensional phase-space distribution function is the probability of finding a particle or star in the volume $d^3\mathbf{x}d^3\mathbf{v}$ around the position $\mathbf{x}$ and velocity $\mathbf{v}$ at time t. From eq. (1.20), we can write the the collisionless Boltzmann equation,

$$\frac{\partial f}{\partial t} + \dot{\mathbf{x}} \cdot \frac{\partial f}{\partial \mathbf{x}} + \dot{\mathbf{p}} \cdot \frac{\partial f}{\partial \mathbf{p}} = 0. \tag{3.14}$$

This equation can be written in different forms depending on the context, in this case, it is convenient to use the Hamiltonian expression, that is

$$0 = \frac{\partial f}{\partial t} + \frac{\partial f}{\partial \mathbf{x}} \cdot \frac{\partial H}{\partial \mathbf{p}} - \frac{\partial f}{\partial \mathbf{p}} \cdot \frac{\partial H}{\partial \mathbf{x}}. \tag{3.15}$$

Due to the characteristics of the system we desire to describe, the Hamiltonian in spherical coordinates for a particle in a gravitational potential can be written as

$$H = \frac{1}{2}\left(p_r^2 + \frac{p_\theta^2}{r^2} + \frac{p_\phi^2}{r^2 \sin^2\theta}\right) + \Phi. \tag{3.16}$$

Combining both eq. (3.15) and eq. (3.16) and after some algebraic expressions

$$\frac{\partial f}{\partial t} \quad + p_r \frac{\partial f}{\partial r} + \frac{p_\theta}{r^2}\frac{\partial f}{\partial \theta} + \frac{p_\phi}{r^2 \sin^2\theta}\frac{\partial f}{\partial \phi} - \left(\frac{\partial \Phi}{\partial r} - \frac{p_\theta^2}{r^3} - \frac{p_\phi^2}{r^3 \sin^2\theta}\right)\frac{\partial f}{\partial p_r} \tag{3.17}$$

$$- \left(\frac{\partial \Phi}{\partial \theta} - \frac{p_\phi^2 \cos\theta}{r^2 \sin^3\theta}\right)\frac{\partial f}{\partial p_\theta} - \frac{\partial \Phi}{\partial \phi}\frac{\partial f}{\partial p_\phi} = 0. \tag{3.18}$$

Here, the canonical momenta are given by

$$p_r = \dot{r} = v_r \tag{3.19}$$

$$p_\theta = r^2\dot{\theta} = r v_\theta \tag{3.20}$$

$$p_\phi = r^2 \sin^2\theta \dot{\phi} = r \sin\theta v_\phi. \tag{3.21}$$

Taking into account the previous information and after many simplifications, the eq. (3.17) in spherical coordinates can be expressed in terms of the canonical momenta, as follows becomes

$$p_r \frac{\partial f}{\partial r} + \frac{p_\theta}{r^2}\frac{\partial f}{\partial \theta} - \left(\frac{d\Phi}{dr} - \frac{p_\theta^2}{r^3} - \frac{p_\phi^2}{r^3 \sin^2\theta}\right)\frac{\partial f}{\partial p_r} + \frac{p_\phi^2 \cos\theta}{r^2 \sin^3}\frac{\partial f}{\partial p_\theta} = 0. \tag{3.22}$$

After integrating overall momenta and applying some theorems to simplify several terms, the expression Boltzmann equation for a collisionless system in spherical coordinates [1]

$$\frac{\partial}{\partial r}(r^2 \sin\theta \rho \overline{p_r^2}) + \frac{\partial}{\partial \theta}(\sin\theta \rho \overline{p_r p_\theta}) + r^2 \sin\theta \rho \left(\frac{d\Phi}{dr} - \frac{\overline{p_\theta^2}}{r^3} - \frac{\overline{p_\phi^2}}{r^3 \sin^2\theta} \right) = 0. \tag{3.23}$$

the last equation can be fully simplified as follows

$$\frac{d(\rho \overline{v_r^2})}{dr} + \rho \left(\frac{\Phi}{dr} + \frac{2\overline{v_r^2} - \overline{v_\theta^2} - \overline{v_\phi}^2}{r} \right) = 0. \tag{3.24}$$

Jeans equation

Here, it is convenient to introduce the anisotropy parameters in terms of the radial and tangential velocity dispersion σ_r^2 and σ_t^2. here $\sigma_r^2 = \langle v_r^2 \rangle$ is the radial dispersion. The tangential velocity reads as $\sigma_t^2 = \sigma_\theta^2 + \sigma_\phi^2$

$$\beta = 1 - \frac{\sigma_\theta^2 + \sigma_\phi^2}{2\sigma_r^2} = 1 - \frac{\overline{v_\theta^2} + \overline{v_\phi^2}}{2\overline{v_r^2}} \tag{3.25}$$

This parameter is directly related to the orbits of motion given by the particles of the system. Due to spherical symmetry being assumed, then $\sigma_\theta = \sigma_\phi$. If the distribution is isotropic, then $\beta = 0$. If the orbits exhibit a preference for radial motions, that implies $\beta > 0$, while for $\beta < 0$ the preference is tangential.

In terms of the anisotropy parameter, the eq. (3.24) becomes the known spherically symmetric Jeans equation, in this case, for the second radial velocity moment [18]

$$\frac{\partial(\rho \overline{\sigma_r^2})}{\partial r} + 2\frac{\beta}{2}\rho \overline{v_r^2} + \rho \frac{\partial \Phi}{\partial r} = 0, \tag{3.26}$$

If we assume symmetry, then $\sigma_\theta = \sigma_\phi$. Since various considerations about the symmetry of the system are assumed, once β is determined, the eq. 3.26 reduces to a ordinary differential equation for $\rho\sigma_r^2$. The simplest case is when $\beta = 0$, then eq. (3.26) becomes an ordinary differential equation for $\rho\overline{\sigma_r^2}$ which can be directly integrated with the boundary condition $\lim_{r\to}\overline{\sigma_r^2} = 0$ as

$$\overline{v_r^2}(r) = \frac{1}{\rho(r)} \int_r^\infty dr' \rho(r') \frac{d\Phi}{dr'}. \tag{3.27}$$

The quantity ρ corresponds to the density profile and from now on it will be considered as Zhao's profile (1.123) within the CDM model because it is capable of modeling different slopes in different regions as a function of radius. That is, it can reproduce both flat and cuspy profiles. The treatment to solve Jean's equation to model a halo that follows the density profile is carried out by using a modified version of the GalIC code [18]. In this version, the Zhao profile has been implemented, in such a way that the free parameters α, β, and γ, and of course r_s and ρ_s, are taken as input.

The total mass of the halo system then is computed in terms of the density profile

$$M(r) = 4\pi \int_0^r \rho(r') r'^2 dr'. \tag{3.28}$$

Fig. 3.7 shows the temporal evolution of the density profile of a simulated halo, from $t = 0$ to $t = 1.4 \times 10^9$yr. The stable halo was constructed using the modified version of GalIC and the simulations were carried out in the Gadget 4 code [14]. In the figure, we can see the halo is stable enough during the simulated range. For the outer part of the halo, near $r = 1 \times 10^3$ the density fluctuations start to get larger, but the density value has already decayed by at least four orders.

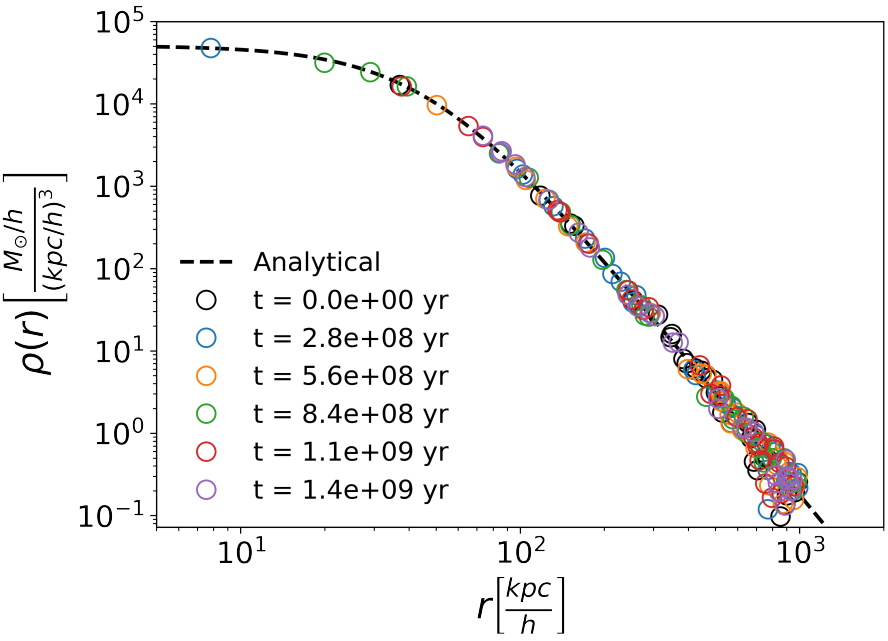

Figure 3.7: time-evolved dark matter halo density profile. we can see that the profile is quite stable up to 1.4 Gyr. The differences begin to become noticeable around $r = 500\text{kpc}/h$, where the density has decreased by at least five orders of magnitude.

3.3 Comparison between CDM and SFDM

3.3.1 Coarse-graining method

The Vlasov equation describes a self-gravitating and non-collisional system. A popular way of approximating the solution to the Vlasov equation is by determining the nonlinear evolution of CDM, which can be done with N-body simulations or, in other words, a usual way to define CDM is through a phase space $f = f(\boldsymbol{x}, \boldsymbol{u})$, such that it is a solution of the Vlasov equation

$$\frac{\partial f}{\partial t} = -\frac{\mathbf{u}}{a^2} \cdot \boldsymbol{\nabla}_x f + \boldsymbol{\nabla}_x \Phi \cdot \boldsymbol{\nabla}_u f \tag{3.29}$$

$$\Delta\Phi = \frac{4\pi G \rho_0}{a} \left(\int d^3u f - 1 \right), \tag{3.30}$$

This is the collisionless Boltzmann equation with a long-range gravitational force $\boldsymbol{\nabla}_x \Phi$

In order to compare the results, we must calculate the coarse-grained phase space f of both the CDM and SFDM configurations. The coarse-grained function is shown below [8]

$$\bar{f}(t, \vec{x}, \vec{u}) = \int \frac{d^3x' d^3u'}{(2\pi\sigma_x\sigma_u)^3} \exp\left\{ -\frac{(x-x')^2}{2\sigma_x^2} - \frac{(u-u')^2}{2\sigma_u^2} \right\} f(t, \vec{x}', \vec{u}') \tag{3.31}$$

$$= \exp\left\{ \frac{\sigma_x^2}{2}\Delta_x + \frac{\sigma_u^2}{2}\Delta_u \right\} \{f\}, \tag{3.32}$$

and it is obtained from f through a convolution with a Gaussian with widths σ_x and σ_u.

The moments $\overline{M}^{(n)}$ of $\bar{f}$ are expressed in terms of the moments of f, that is, in terms of $M^{(n)}$

$$\bar{M}^{(0)} = \exp\left\{\frac{\sigma_x^2}{2}\Delta_x\right\}\{M^{(0)}\}, \tag{3.33}$$

$$\bar{M}_i^{(1)} = \exp\left\{\frac{\sigma_x^2}{2}\Delta_x\right\}\{M_i^{(1)}\}, \tag{3.34}$$

$$\bar{M}_{ij}^{(2)} = \exp\left\{\frac{\sigma_x^2}{2}\Delta_x\right\}\{M_{ij}^{(2)}\} + \sigma_u^2\bar{M}^{(0)}\delta_{ij}, \tag{3.35}$$

here, the moments are given in terms of the distribution function as $M_{i_1,\ldots,i_2}(\boldsymbol{x}) \equiv \int d^3u u_i \ldots u_{i_n} f(\boldsymbol{x},\boldsymbol{u})$, and can be derived in terms of the generating function

$$M^{(n)}_{i_1\ldots i_n}(\boldsymbol{x}) \equiv \int d^3u u_{i_1}\ldots u_{i_n} f(\boldsymbol{x},\boldsymbol{u}). \tag{3.36}$$

The first three moments represent the $n(t,\vec{x})$ is the density, $u_i(t,\vec{x})$ is the velocity of the fluid and Σ_{ij} is the mass-weighted velocity dispersion and are given by

$$M^{(0)} = n \tag{3.37}$$

$$M_i^{(1)} = nu_i \tag{3.38}$$

$$M_{ij}^{(2)} = nu_iu_j + n\Sigma_{ij}. \tag{3.39}$$

Next, we will study two specific cases that will be helpful when comparing different simulations

CDM case

For the particular case when CDM is considered, the coarse-grained function can be expressed as follows

$$\bar{f}_c(t,\boldsymbol{x},\boldsymbol{u}) = \frac{1}{(2\pi)^3\sigma_x^3\sigma_u^3}\int d^3q \exp\left\{-\frac{|\boldsymbol{x}-\boldsymbol{X}(t,\boldsymbol{q})|}{2\sigma_x^2}\right\}\exp\left\{-\frac{|\underline{,}u-\boldsymbol{u}(t,\boldsymbol{q})|}{2\sigma_u^2}\right\}, \tag{3.40}$$

and the moments are expressed in terms of the lagrangian coordinates $\boldsymbol{x}$, therefore $X(t,\boldsymbol{q})$ and $U(t,\boldsymbol{q})$ are the positions and velocities of the particles

$$\bar{M}^{c(0)} = \frac{1}{(2\pi)^3\sigma_x^3\sigma_u^3}\int d^3q \exp\left\{-\frac{|\boldsymbol{x}-\boldsymbol{X}(t,\boldsymbol{q})|}{2\sigma_x^2}\right\} \tag{3.41}$$

$$\bar{M}_i^{c(0)} = \frac{1}{(2\pi)^3\sigma_x^3\sigma_u^3}\int d^3q \exp\left\{-\frac{|\boldsymbol{x}-\boldsymbol{X}(t,\boldsymbol{q})|}{2\sigma_x^2}\right\}U_i(t,\boldsymbol{q}) \tag{3.42}$$

$$\bar{M}_{ij}^{c(0)} = \frac{1}{(2\pi)^3\sigma_x^3\sigma_u^3}\int d^3q \exp\left\{-\frac{|\boldsymbol{x}-\boldsymbol{X}(t,\boldsymbol{q})|}{2\sigma_x^2}\right\}U_i(t,\boldsymbol{q})U_j(t,\boldsymbol{q}) + \sigma_u^2\overline{M}^{c(0)}\delta_{ij}, \tag{3.43}$$

N-body case

Particularly, for the case of N-body, the first moment of $\bar{f}$ can be expressed in a discrete way with a summation by means of the transformation $\int d^3q = \frac{m}{\rho_0}\sum_I$ as

$$\bar{n}(\boldsymbol{x}) = \frac{m}{\rho_0}\frac{1}{(2\pi)^{3/2}\sigma_x^3}\sum_I \exp\left\{-\frac{|\boldsymbol{x}-\boldsymbol{X}(\boldsymbol{q})|^2}{2\sigma_x^2}\right\}. \tag{3.44}$$

Schrödinger-method

The non-relativistic Schrödinger-Poisson system in a ΛCDM universe with scale factor a reads

$$i\tilde{\hbar}\frac{\partial\psi}{\partial t} = -\frac{\tilde{\hbar}^2}{2a^2}\boldsymbol{\nabla}\psi + \Phi\psi \tag{3.45}$$

$$\boldsymbol{\nabla}^2\Phi = \frac{4\pi G\rho_0}{a}(|\psi|^2 - 1), \tag{3.46}$$

where $\tilde{\hbar} \equiv \dfrac{\hbar}{m}$.

It is convenient to obtain the Husimi representation ψ_H of the wave function ψ, which depends explicitly on the positions $\boldsymbol{x}$ and velocities $\boldsymbol{v}$ as follows [8]

$$\psi_H(t, \boldsymbol{x}, \boldsymbol{u}) \equiv \int d^d x' K_H(\boldsymbol{x}, \boldsymbol{x'}, \boldsymbol{u})\psi(t, \boldsymbol{u}), \tag{3.47}$$

where

$$K_H(\boldsymbol{x}, \boldsymbol{u}) \equiv \frac{\exp\left[-\dfrac{(\boldsymbol{x}-\boldsymbol{x}')^2}{4\sigma} - m\dfrac{i}{\tilde{\hbar}}\boldsymbol{u}\cdot\boldsymbol{x}'\right]}{(2\pi\tilde{\hbar})^{d/2}(2\pi\sigma_x^2)^{d/4}}. \tag{3.48}$$

analogously to the previous process, the coarse-grained moments can be computed using the transformation eq. (3.31), that is in terms of the moments for ψ, that is $M^{W(0)}$. The moments can be expressed as follows

$$M^{H(0)} = \exp\left\{\frac{\sigma_x^2}{2}\Delta\right\}\{M^{W(0)}\} \equiv n^H, \tag{3.49}$$

$$M_i^{H(1)} = \exp\left\{\frac{\sigma_x^2}{2}\Delta\right\}\{M_i^{W(1)}\} \equiv n^H u_i^H, \tag{3.50}$$

$$M_{ij}^{H} = \exp\left\{\frac{\sigma_x^2}{2}\Delta\right\}\{M_{ij}^{W(2)}\} + \sigma_u^2 M^{H(0)}\delta_{ij} \equiv n^H u_i^H u_j^H + n^H\Sigma_{ij}^H. \tag{3.51}$$

3.3.2 Boosted configuration

As a first example, we have a boosted configuration. The SFDM initial conditions were created as described in 3.1.1 but now we have $v_x = 10$ km/s. The mass of the boson is 5×10^{-23}. The configuration was positioned at 20 and the evolution time was $t = 7.49$ Gyr. For CDM, the density distribution was created by fitting Zhao profile (1.123) with the soliton derived from the solution of the Schrödinger-Poisson system with spherical symmetry (1.128). The best params are $r_s = 8.54$, $\log\rho_s = 8.79$, $\alpha = 1.87$, $\beta = 38.6$ and $\gamma = 0$. Fig. 3.8 shows three snapshots at different times of the evolution of the boosted configuration. The left panel corresponds to CDM and the right one to SFDM.

3.3.3 Binary Collision

Central collision 1

In this case, there are two configurations located at 6 kpc and −6 kpc from the origin. The initial velocity for the configuration on the left is $v_x = 10$ km/s and $v_x = -10$ km/s for the right one. Fig. 3.9 shows the behavior of this collision. In both cases, the configurations merge and produce tidal disruption. However, this effect is much more pronounced in the SFDM case. In fact, we can see interference patterns once the collision starts.

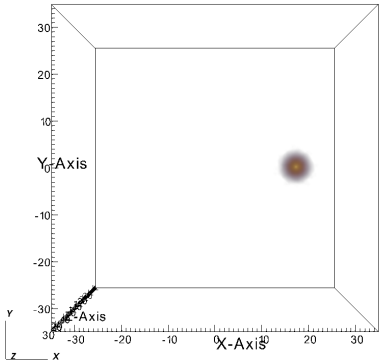

(a)

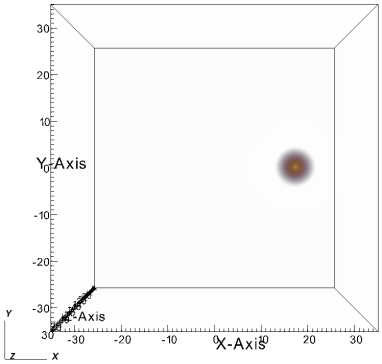

(b)

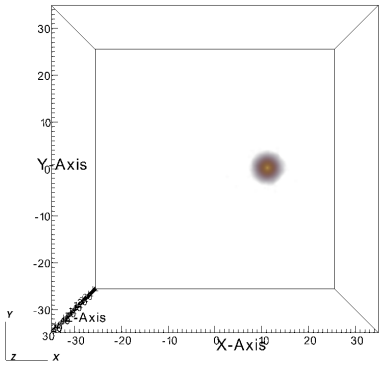

(c)

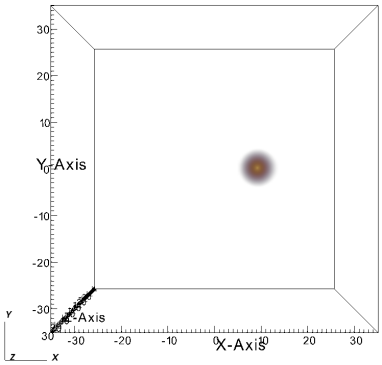

(d)

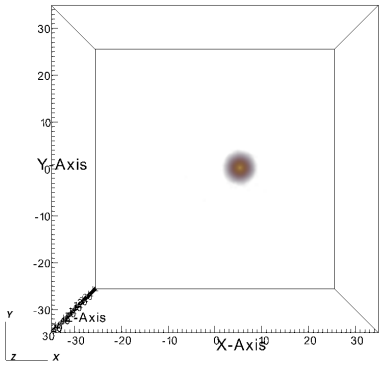

(c)

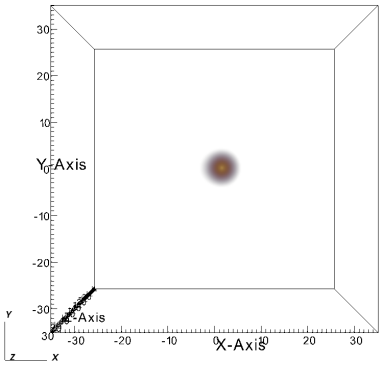

(d)

Figure 3.8: Snapshots projected in the xy-plane for the boosted configuration at three different times. The left panel corresponds to CDM and the right panel to SFDM.

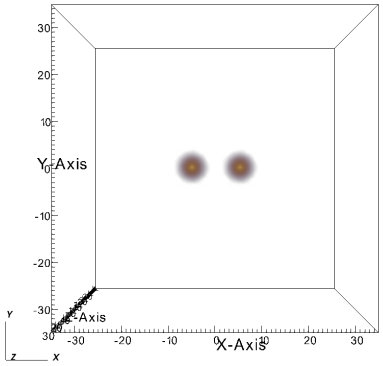

(a)

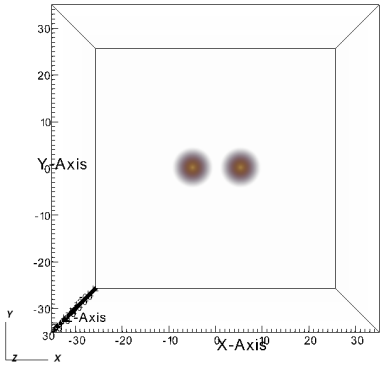

(b)

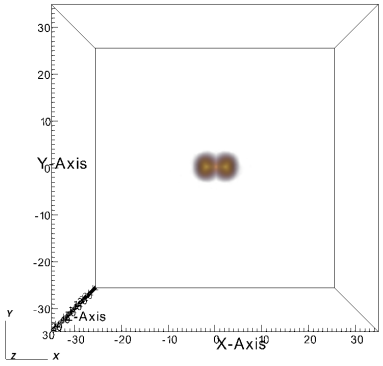

(c)

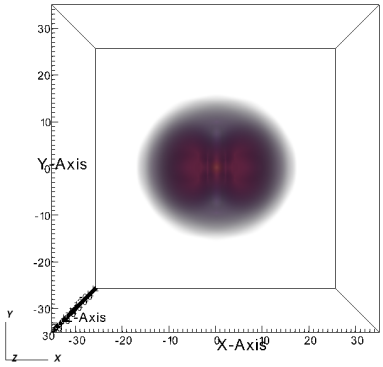

(d)

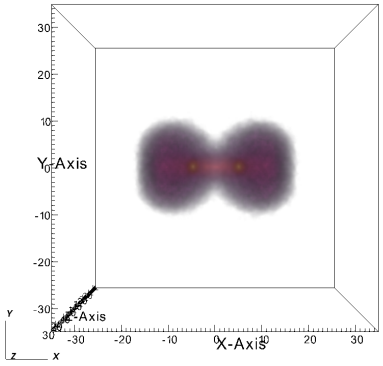

(c)

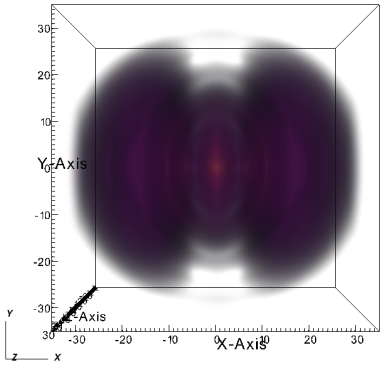

(d)

Figure 3.9: Snapshots projected in the xy-plane for collision 1 at three different times. The left panel corresponds to CDM and the right panel to SFDM.

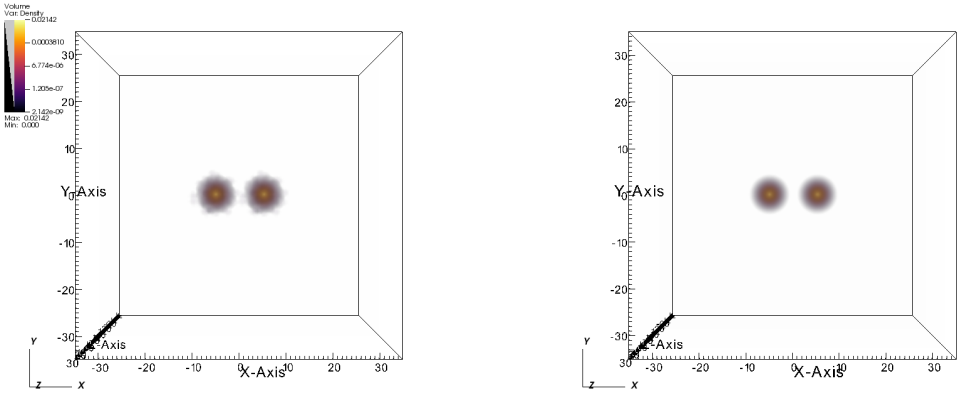

(a) **(b)**

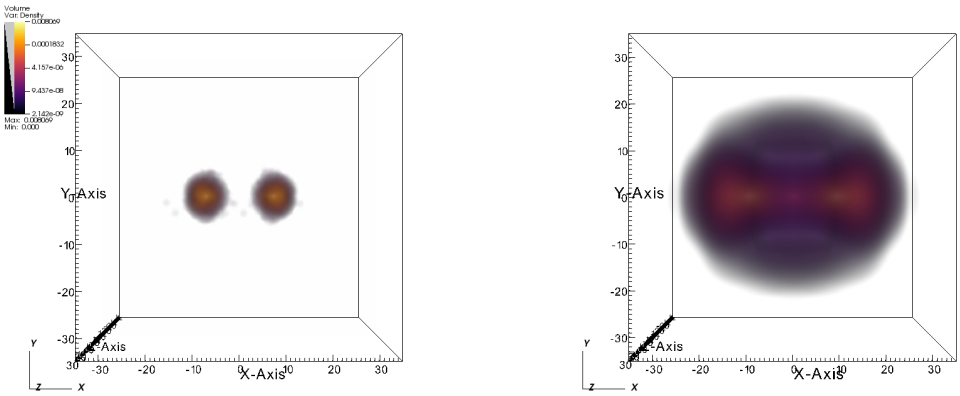

(c) **(d)**

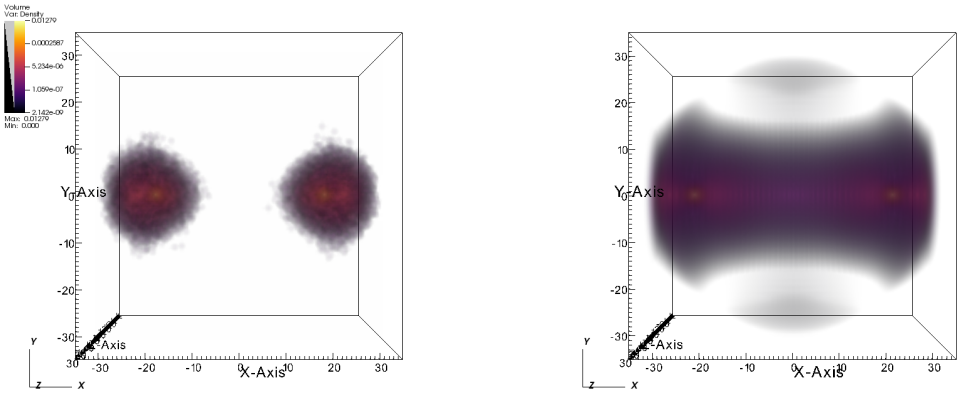

(c) **(d)**

Figure 3.10: Snapshots projected in the xy-plane for collision 2 at three different times. Left panel corresponds to CDM and the right panel to SFDM.

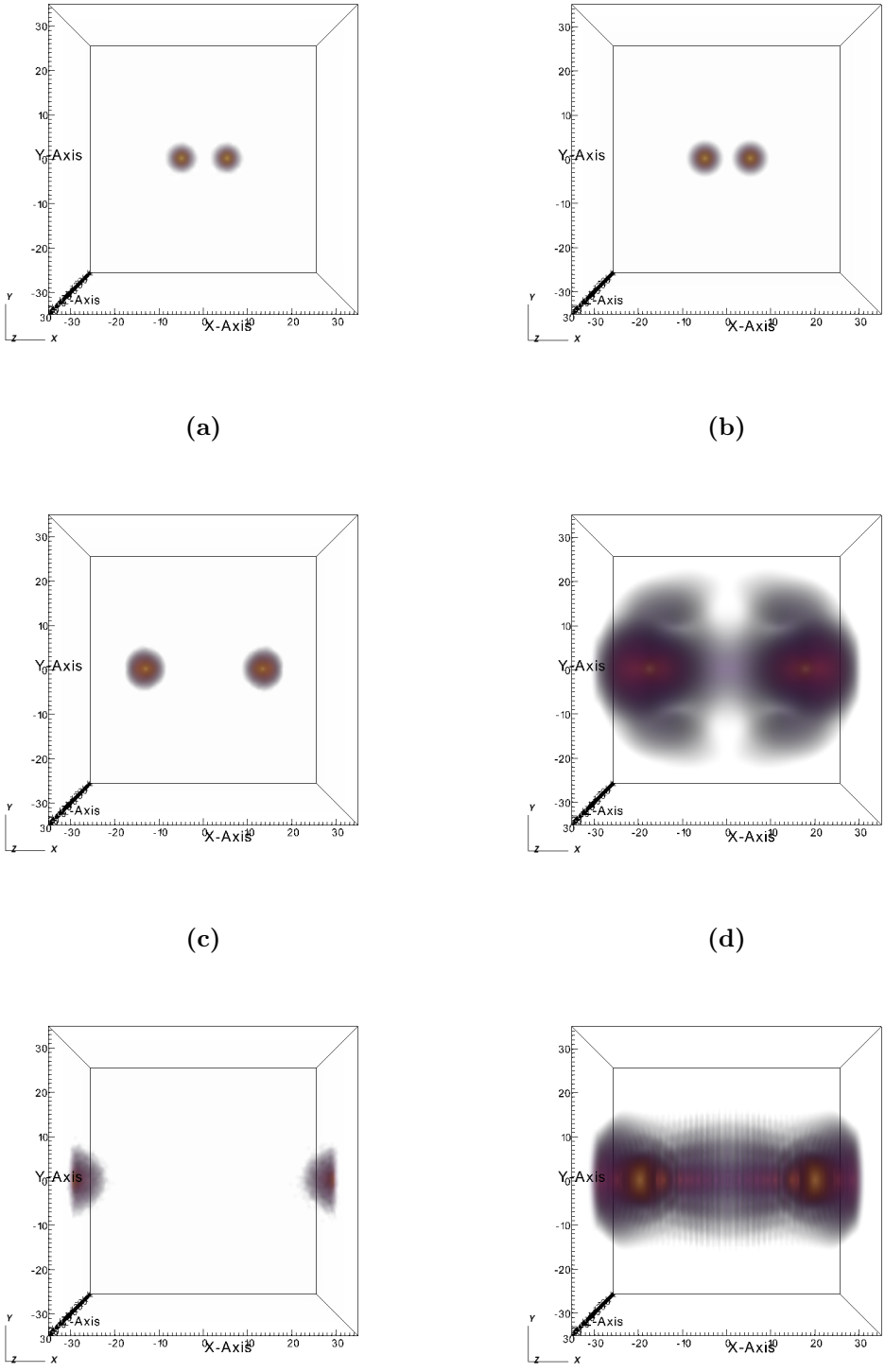

(a) **(b)**

(c) **(d)**

(c) **(d)**

Figure 3.11: Snapshots projected in the xy-plane for collision 3 at three different times. The left panel corresponds to CDM and the right panel to SFDM.

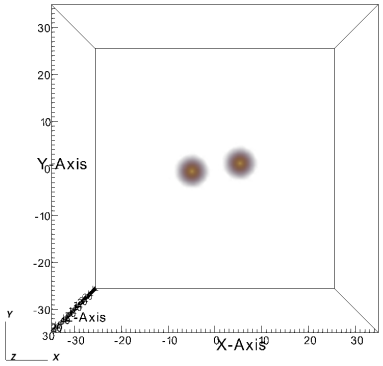

(a)

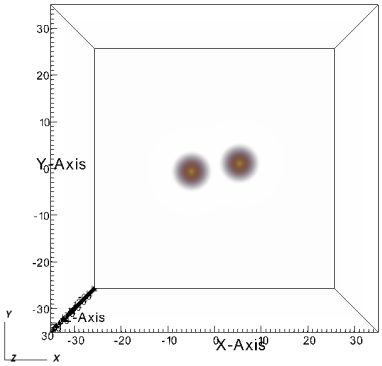

(b)

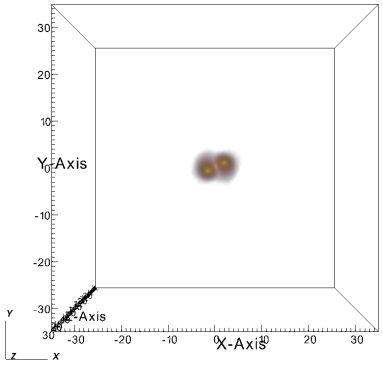

(c)

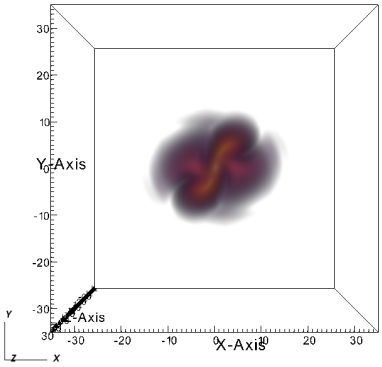

(d)

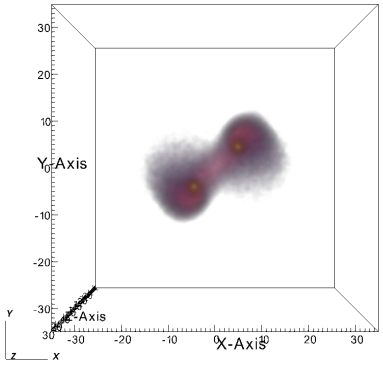

(c)

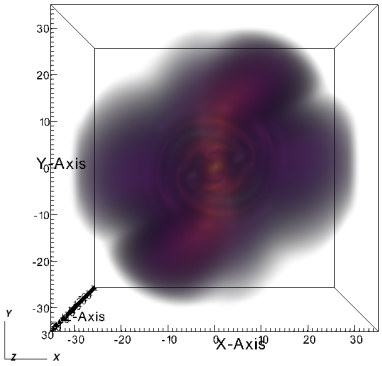

(d)

Figure 3.12: Snapshots projected in the xy-plane for the collision off, at three different times. The left panel corresponds to CDM and the right panel to SFDM.

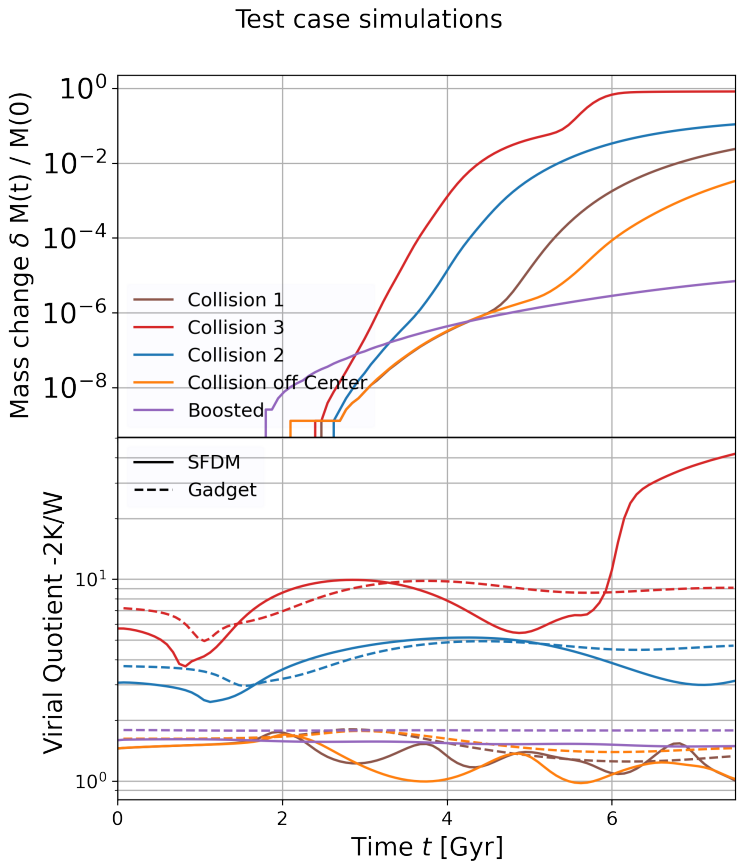

Figure 3.13: Top panel: Change of the total mass of the system in the SFDM model as a function of time. This effect is due to the implementation of the sponge potential. Systems with more violent collisions tend to lose mass quickly. Bottom panel: Virial coefficient for each of the configurations. assemblies. The solid lines correspond to the SFDM model, while the dotted lines to CDM. The most virialized systems are the boosted configuration and the off-center collision.

Central collision 2

This case is similar to the previous one but using $v_x = 20$ km/s. Fig. 3.10 shows the results, here CDM halos manage to pass through each other but are much more disturbed than in the previous case. For SFDM the halos manage to move away from each other, creating a flattened shape.

Central collision 3

The velocities here are considered as $v_x = 30$ km/s. Here the initial velocity of the halo is high enough that it makes both halos pass by. For CDM, the halos after colliding are slightly disturbed but for SFDM, the halos are noticeably disturbed, taking a *bullet* shape after the collision, and of course, forming interference patterns as shown in Fig. 3.11.

Off-center collision

In this case, the configurations have the same position in x, but now there is also an offset in y. The particle on the left is positioned at $y = -1$ kpc with velocity $v_x = 10$ km/s, while the one on

the right is at $y = 1$ kpc with $v_x = -10$ km/s. Fig. 3.12 shows the snapshots for this case, as in the previous cases, the configurations for SFDM are highly disrupted.

change for all of the cases considered. For scalar field dark matter, periodic boundaries were implemented and it was also considered a sponge potential, which is a numerical technique used to absorb or dampen outgoing waves, effectively preventing them from reflecting back into the domain. This effect causes loss of mass since part of it is absorbed. Fig. 3.13 upper panel shows the mass change for all examples seen. We can see that collision 3 loses mass faster since it is a more violent shock and the tidal forces reach the boundary faster. Then we have collisions 2 and 1. The boosted configuration is the one that loses fewer particles since it gently approaches the boundary. Additionally, in the bottom panel the virial energy term $-\frac{2k}{W}$ is displayed, according to the virial theorem, the closer this value is to 1, the more virialized the system will be. Again, the boosted configuration and the off-center collision are closest to 1.

3.4 Conclusions and perspectives

In this chapter, small-scale simulations have been studied considering two dark matter models, CDM and SFDM. We have constructed a code using the Adaptive Moving Mesh method to solve the Schrödinger-Poisson system. For the problems presented it has been shown the ability of the method code to provide the adaptability of the numerical resolution to desired high-density regions in the physical domain. In fact, the method can handle scenarios involving the dynamics of dark matter configurations. Particularly, the problem of a configuration embedded in a soliton Halo was presented. This problem brings up some insights for studying highly interacting galactic systems such as groups and clusters of galaxies. The main achievement was to track the evolution of the configuration playing the role of a galactic-sized SFDM-subhalo suffering a disrupting effect produces by the gravity of a host halo.

In the second part of the chapter, small-scale simulations of different simple assemblies of configurations were performed with two types of dark matter, CDM and SFDM. The initial conditions were created in a similar way, using the same positions and giving the same initial velocities. For CDM the density distribution, a fit of the soliton profile was performed using the Zhao profile, to find the values α,β, and γ that best describe it. In all cases, SFDM shows more violent collisions forming strong interference patterns.

This work is still in progress, it is planned to compare different cases and analyze how the density profiles change in this type of simulation for both models when the configurations are isolated or embedded in dense environments. On the other hand, it is planned to analyze different types of rotation curves and density profiles in order to find the most suitable boson mass value. Likewise, it is planned to build the density profile that parameterizes different rotation curves of observations. For this, the boson mass must be adjusted and, in addition to the soliton term, an NFW term must be considered (see eq.(1.130)) in order to draw different types of profiles.

The main goal of this research is to carry out simulations of different Hickson compact groups will be carried out, whose initial conditions will be created with the information from the cosmological simulations. This will allow us to study the crossing and the virialization process of these agglomerations, as well as the behavior of the velocity dispersion of the group.

Bibliography

[1] Binney, J. and Tremaine, S. (2011). *Galactic dynamics*, volume 20. Princeton university press.

[2] Crank, J. and Nicolson, P. (1947). A practical method for numerical evaluation of solutions of partial differential equations of the heat-conduction type. In *Mathematical proceedings of the Cambridge philosophical society*, volume 43, pages 50–67. Cambridge University Press.

[3] Edwards, F., Kendall, E., Hotchkiss, S., and Easther, R. (2018). Pyultralight: a pseudo-spectral solver for ultralight dark matter dynamics. *Journal of Cosmology and Astroparticle Physics*, 2018(10):027.

[4] Guzmán, F. (2019). Oscillation modes of ultralight bec dark matter cores. *Physical Review D*, 99(8):083513.

[5] Guzman, F. S. and Urena-Lopez, L. A. (2004). Evolution of the schrödinger-newton system for a self-gravitating scalar field. *Physical Review D*, 69(12):124033.

[6] Hui, L. (2021). Wave dark matter. arxiv e-prints, page. *arXiv preprint arXiv:2101.11735*, 2101.

[7] Hui, L., Ostriker, J. P., Tremaine, S., and Witten, E. (2017). Ultralight scalars as cosmological dark matter. *Physical Review D*, 95(4):043541.

[8] Kopp, M., Vattis, K., and Skordis, C. (2017). Solving the Vlasov equation in two spatial dimensions with the Schrödinger method. *Phys. Rev. D*, 96(12):123532.

[Lee] Lee, J. Epj web conf. 168, 06005 (2018). *arXiv preprint arXiv:1704.05057*.

[10] Munive-Villa, E., López-Sánchez, J. N., Avilez-López, A. A., and Guzmán, F. (2022). Solving the schrödinger-poisson system using the coordinate adaptive moving mesh method. *Physical Review D*, 105(8):083521.

[11] Press, W. H., Teukolsky, S. A., Vetterling, W. T., and Flannery, B. P. (2007). *Numerical recipes 3rd edition: The art of scientific computing*. Cambridge university press.

[12] Schwabe, B., Gosenca, M., Behrens, C., Niemeyer, J. C., and Easther, R. (2020). Simulating mixed fuzzy and cold dark matter. *Physical Review D*, 102(8):083518.

[13] Shapira, Y. (2012). *Solving Pdes in C++: Numerical methods in a unified Object-oriented Approach*, volume 9. SIAM.

[14] Springel, V., Pakmor, R., Zier, O., and Reinecke, M. (2021). Simulating cosmic structure formation with the gadget-4 code. *Monthly Notices of the Royal Astronomical Society*, 506(2):2871–2949.

[15] Suá rez, A., Robles, V. H., and Matos, T. (2013). A review on the scalar field/bose-einstein condensate dark matter model. In *Astrophysics and Space Science Proceedings*, pages 107–142. Springer International Publishing.

[16] Trellakis, A., Galick, A., Pacelli, A., and Ravaioli, U. (1997). Iteration scheme for the solution of the two-dimensional schrödinger-poisson equations in quantum structures. *Journal of Applied Physics*, 81(12):7880–7884.

[17] Yavetz, T. D., Li, X., and Hui, L. (2022). Construction of wave dark matter halos: Numerical algorithm and analytical constraints. *Physical Review D*, 105(2):023512.

[18] Yurin, D. and Springel, V. (2014). An iterative method for the construction of n-body galaxy models in collisionless equilibrium. *Monthly Notices of the Royal Astronomical Society*, 444(1):62–79.

Chapter 4

Study of galactic systems and their DM properties

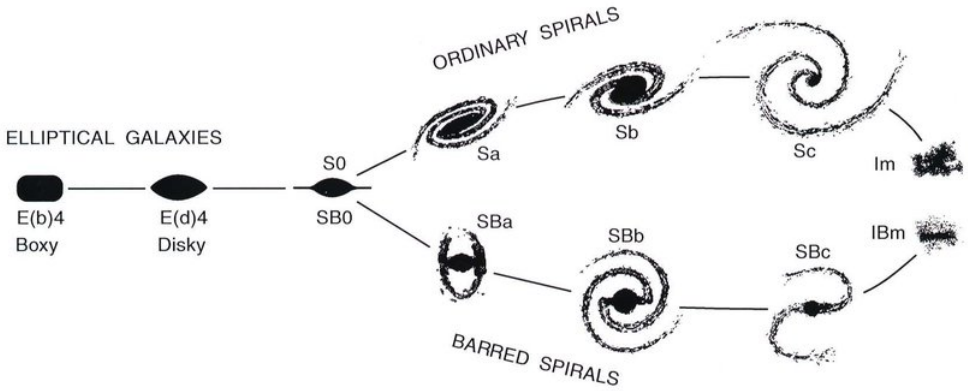

Figure 4.1: Hubble tuning fork diagram, is a system for classifying and categorizing galaxies based on their morphological features observed in optical wavelengths. First, we have elliptical galaxies which are elongated or spherical systems. Then, the spiral galaxies appear. The main feature of these types is the disk structure which is divided into two subcategories: normal and barred spirals. Finally, the irregular galaxies do not conform to well-defined structures, exhibiting irregular shapes. Although it was initially believed that this diagram would represent evolutionary information, there is no direct relation to the individual history of each galaxy. Source [4].

In this chapter, we will study the dynamics of the galactic components, at observational and simulation levels. We also present some of the most important scale relations derive phenomenologically. Additionally, a compendium of the most commonly used machine learning algorithms will be presented and used to estimate the mass of the galactic components. Finally, the performance of each algorithm will be tested against Mendel's catalog, which is derived from the SDSS information. Moreover, some scale relations involving baryons and dark matter will be explored in both observations and simulations.

4.0.1 Bulge-disk decomposition

Galaxies contain many components which contribute in different ways to the total dynamics of the system. Nevertheless, at the observational level, we receive light from the entire galaxy as a whole, therefore, there are different methods to separate each of these components, involving analyzing various properties and characteristics of a galaxy. The most common methods used are photometry, spectroscopy, and structural analysis. Particularly, the bulge-disk decomposition is hard to perform since it depends on the data quality, the complexity of the galaxy's structure, and the method employed.

One of the most popular corresponds to the morphological classification proposed by Edwin Hubble [1] consisting of four types of galaxies, elliptical, spiral, barred spiral, and irregular. In Fig. 4.1 the Hubble classification is shown. Another scheme is the isophotal radius measurement [2], that is, the size attributed to a galaxy component corresponding to a particular level of surface brightness. Additionally, a way to characterize the light distribution independent of the light profile is through concentration, defined by the ratio of two radii, each one containing a fixed fraction of the total galaxy luminosity [3].

Another technique for reconstructing visible mass components in galaxies is to use standardized fitting functions. Surface brightness profiles provide information about how the brightness of a galaxy changes as a function of distance from its center. The bulge component typically exhibits a steeper brightness profile compared to the disk component. Ideally, such functions are constructed from physical principles governing galactic formation and evolution. Unfortunately,

given the complexity of the physics behind these processes, these models tend to be complicated and have a large number of parameters, therefore, the commonly used functions are derived empirically or phenomenologically. For instance, the disk components are well-fitted by an exponential law. Additionally, for the elliptical galaxies and the bulges in the spiral ones, the elements typically considered are the Hubble law [1], the King's model [5], and the de Vaucouleurs's law [6]. Nevertheless, in some cases, the bulges associated with late-type galaxies are best fitted by exponential laws [7, 8].

Furthermore, spectroscopic methods have been used to single out these galactic components, for example in [9]. These methods involve studying the light emitted by galaxies at different wavelengths and extracting information about their structural components. Basically, when the light profile of the galaxy at each wavelength in the spectrum is considered, it is possible to fit the bulge and disk light profiles to the distribution in a similar way to the photometric bulge-disk decomposition, which corresponds to the one-dimensional case [10].

4.0.2 Scale relations

Scale relations provide valuable insights into the formation, evolution, and physical processes operating within galaxies, providing important constraints for theoretical models. Such relations are derived from large observational surveys of galaxies and have been established through extensive statistical analyses at the phenomenological level. Some of the most important scale relations will be explained below.

- **Sersic's law.** The Séric profile corresponds to a generalization of the de Vaucouleurs's profile and describes how the intensity I of a galaxy varies as a function of the distance R from its center.

$$I(R) = I_e \exp\left\{-b_n\left[\left(\frac{R}{R_e}\right)^{1/n} - 1\right]\right\}, \tag{4.1}$$

  where b_n is approximately $2n - \frac{1}{3}$ for $n > 8$. The smaller the value of n, the less centrally concentrated the profile is, and the shallower (steeper) the logarithmic slope at small (large) radii. Most galaxies are fit by Sérsic profiles with indices in the range $1/2 < n < 10$. This general case can also fit the surface of brightness distribution for lenticular galaxies and in some cases, it can also model disk galaxies. From eq. (4.1) the surface brightness profile can be derived

$$\mu(R) = \mu_e + \frac{2.5 b_n}{\ln(10)}\left[\left(\frac{R}{R_e}\right)^{1/n} - 1\right], \tag{4.2}$$

  In Fig. 4.2 the brightness surface profile is shown for different values of the parameter n.

- **Exponential profile.** The exponential surface brightness profile is a mathematical model commonly used to describe the light distribution in disk-like structures, such as spiral galaxies and galactic disks. It provides a simple and effective description of the surface brightness as a function of radial distance from the center of the structure. The expression is as simple as

$$I(R) = I_0 \exp\left(-\frac{R}{h}\right), \tag{4.3}$$

  where $I(R)$ is the surface brightness at a given radius, I_0 is central surface brightness, and h is the scale length. This profile is commonly observed in the outer regions of spiral galaxies, where the disk dominates the light distribution. It is often used to describe the stellar distribution in galactic disks, where the stars are distributed in a thin, rotating disk-like structure. Sometimes, some late-type bulges are also well-fitted by this law.

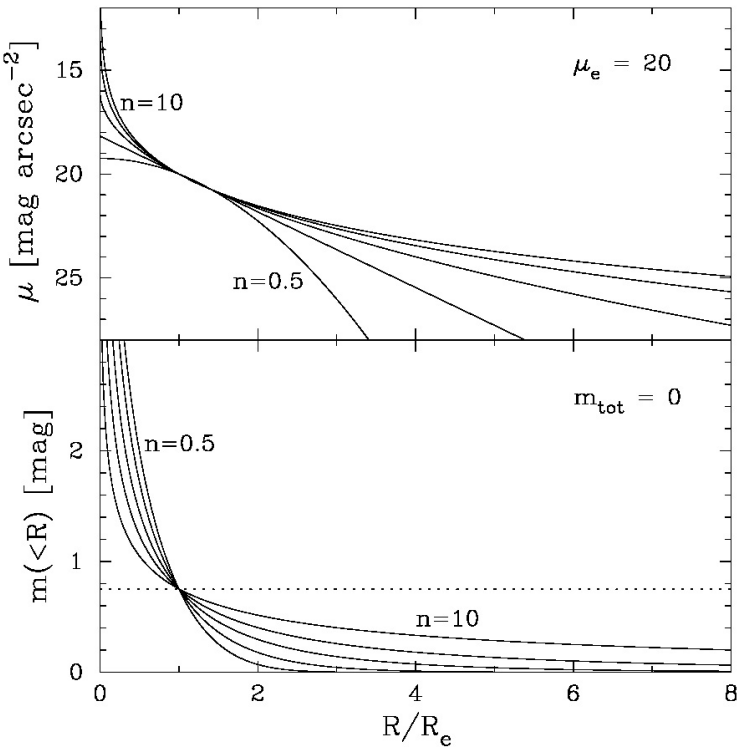

Figure 4.2: The Sersic profile plotted for different values of n, from $n = 1$ to $n = 10$.. The smaller the value of n, the more flattened the light profile will be, when n grows, the profile becomes steeper. The Sersic aperture magnitude profile is also shown in the bottom panel.

- **Tully-Fisher relation.** There is an expression that relates the maximum rotation velocity of spirals and their luminosity known as the Tully-Fisher relation described through the equation

$$L \propto v_{\max}^{\alpha}, \tag{4.4}$$

here is the power-law index, that is the slope, $\alpha \sim 4$. An important fact is that the larger the wavelength of the filter in which the luminosity is measured, the smaller the dispersion of the Tully–Fisher relation. Indeed, the α parameters increase as a function of the wavelength of the filter. That is, the relation is steeper for red galaxies, which correspond to the more luminous or massive systems. Because of this close correlation, the luminosity of spirals can be estimated quite precisely by measuring the rotational velocity. The determination of the (maximum) rotational velocity is independent of the galaxy's distance.

If the rotation curves have a flat behavior in the outer part, as usually observed, that implies the total mass can be written as $M = \dfrac{v_{\max}^2 R}{G}$, being R the distance from the center of the galaxy in the range of the flat part, then $V_{\rm rot} \approx V_{\max}$. Due to the fact, it is not possible to obtain the total mass of a spiral galaxy because of the extent of the dark halo, it is better to estimate the **mass-to-light ratio** γ, that is a quotient between the total mass of a given volume and its luminosity. This accounts for the dark matter as well. Fig. 4.3 shows the Tully-Fisher relation for two different types of spiral galaxies.

- **Faber-Jackson relation.** This relation is an empirical correlation observed between the luminosity L (or absolute magnitude) and the velocity dispersion of stars σ_0 in the center of

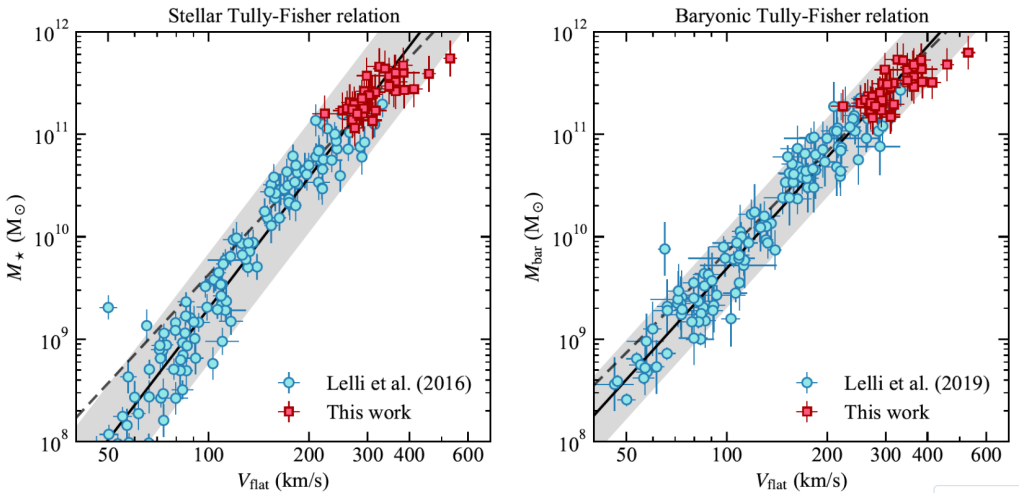

Figure 4.3: Tully-Fisher relations for massive spiral galaxies. The stellar Tully-Fisher relation (left) and the baryonic Tully-Fisher relation (right) are shown. As expected, the more massive the galaxy the higher the maximum rotation velocity. Depending on the type of spiral galaxy will be the slope. Source [11].

elliptical galaxies and it is expressed as follows

$$L \propto \sigma_0^4, \quad \text{or} \quad \log(\sigma) = -0.1 M_B + \text{const.}, \tag{4.5}$$

The Faber-Jackson relation implies that larger and more massive elliptical galaxies have higher velocity dispersion and therefore greater stellar velocity dispersion. This correlation suggests a connection between the gravitational potential of the galaxy and the motion of its stars.

- **The fundamental plane.** There also exists a relation between dynamics and luminosity for early-type elliptical or lenticular galaxies, where the velocity dispersion for those systems is lower than that of the Faber-Jackson relation, and it is known as the fundamental plane. It is usually expressed as a relationship between the effective radius, average surface brightness and central velocity dispersion of the galaxies. In fact, it is called *plane*, because any of the three parameters may be estimated from the other two, as together they describe a plane

$$\log R_e = 0.34 \langle \mu \rangle_e + 1.4 \log \sigma_0 + \text{const.}, \tag{4.6}$$

where $\langle \mu \rangle_e$ is the average surface brightness within R_e measured in mag/arcsec^2. Fig. 4.4 shows different projections of the plane relation, including the Faber-Jackson one.

4.0.3 Simulation framework

Alternatively, numerical simulations have played an important role in exploring in detail predictions of galaxy formation and dynamics within the standard ΛCDM prescription. Particularly, for identifying structural components of the galactic systems, the most popular approach is semi-analytical models, where a highly simplified description of the baryonic physics is combined with Monte-Carlo methods in order to reconstruct merging history trees [13].

Disk Formation

To explain the disk formation first it has to be considered that galaxies form at the center of dark halos and obtain stars from the interstellar medium and by accretion of the satellite galaxies. In

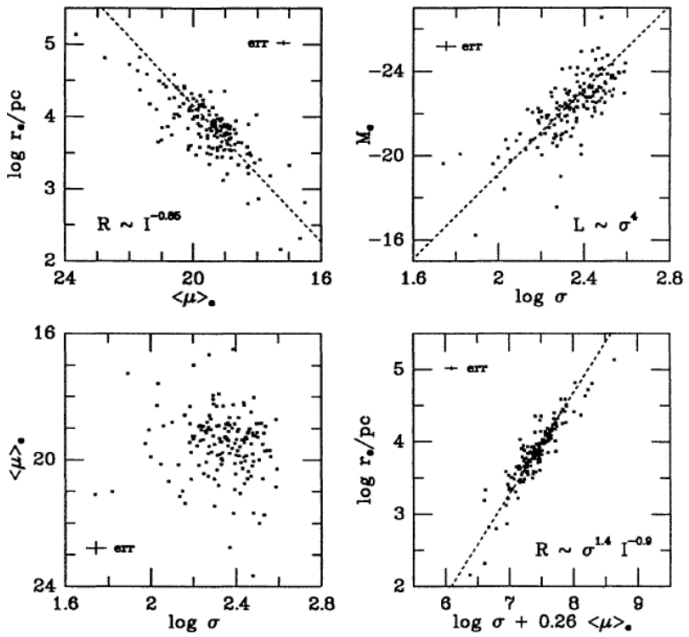

Figure 4.4: Projections of the fundamental plane onto different two-parameter planes. Upper left: the relation between radius and mean surface brightness within the effective radius. Upper right: Faber–Jackson relation. Lower left: the relation between mean surface brightness and velocity dispersion shows the fundamental plane viewed from above. Lower right: the fundamental plane viewed from the side linear relation between radius and a combination of surface brightness and velocity dispersion. Source [12].

literature, the fitting function used to describe the fraction of baryons in a halo depends on mass and redshifts

$$f_b(z, M_{\rm vir}) = f_b^{\rm cos}\left(1 + (2^{\alpha/3} - 1)\left[\frac{M_{\rm vir}}{M_F(z)}\right]\right)^{-3/\alpha}, \tag{4.7}$$

where $f_b^{\rm cos} = 17\%$ is the universal baryon fraction, and $\alpha = 2$ is used. The infalling material is expected to be diffuse gas, composed of primarily hydrogen and helium, along with traces of other elements. The gas gradually falls into the potential wells of the dark matter halos. As the gas accretes, it can cool and condense due to radiative cooling processes. The cooled gas can accumulate in the central regions of the dark matter halo. In [14] the cooling process involves two main quantities, the cooling time and the cooling radius in the hot halo, calculated as follows

$$t_{\rm cool} = \frac{3\mu m_H k_B T_{\rm vir}}{2\rho_{\rm hot}\Lambda(T_{\rm hot}, Z_{\rm hot})}, \quad r_{\rm cool} = \left[\frac{t_{\rm dyn,h} m_{\rm hot}\Lambda(T_{\rm hot}, Z_{\rm hot})}{6\pi\mu m_H k_B T_{\rm vir} R_{\rm vir}}\right]^{1/2}, \tag{4.8}$$

where μm_H is the mean particle mass, $\rho_{\rm hot}$ is the hot gas density at radius r, $\Lambda(T_{\rm hot}, Z_{\rm hot})$ is the temperature-metallicity-dependent cooling function [15], $Z_{\rm hot}$ is the metallicity of the hot gas and $T_{\rm dyn,h}$ is the dynamical time.

The infalling gas carries angular momentum, which plays a crucial role in the formation of a disk structure. Commonly, it is assumed that the angular momentum of the disk is the same as that of the dark matter halo. Angular momentum conservation causes the gas to settle into a rotating disk configuration around the center of the dark matter halo. The change in the total vector angular momentum of the gas during a timestep reads as follows

$$\Delta\vec{J}_{\rm gas} = \delta\vec{J}_{\rm gas,cooling} + \delta\vec{J}_{\rm gas,acc} + \delta\vec{J}_{\rm gas,SF}, \tag{4.9}$$

where $\delta\vec{J}_{\text{gas, cooling}}$, $\delta\vec{J}_{gas,acc}$ and $\delta\vec{J}_{\text{gas, SF}}$ are the change for the angular momentum due to addition of gas by cooling, to accretion from minor mergers, and to gas removal through star formation.

The gas in the rotating disk is subject to various instabilities, such as gravitational instability and fragmentation. These instabilities can lead to the formation of clumps or substructures within the disk, which can subsequently evolve into stars or star-forming regions. The critical gas mass required to form stars is [16]

$$M_{\text{crit}} = 11.5 \times 10^9 \left(\frac{V_{\text{max}}}{200\text{km}/s}\right)\left(\frac{R_{\text{gas,d}}}{10\text{ kpc}}\right) M_\odot, \tag{4.10}$$

where V_{max} is the maximum velocity of an assumed flat rotation curve and $R_{\text{gas,d}}$ is a scale radius. Under this model, stars can be formed from a cold gas in the disk. The amount of gas that is converted into stars per unit of time is expressed as follows

$$\dot{M}_* = \frac{\alpha(M_{\text{gas}} - M_{\text{crit}})}{t_{\text{dyn}}}, \tag{4.11}$$

where $t_{\text{dyn}} = \dfrac{3R_{\text{gas,d}}}{V_{\text{max}}}$. The star formation involves different baryonic processes which modify the dynamics of the disk, such as supernova feedback, disruption, black hole growth and AGN feedback, metal enrichment, and dust extinction.

Bulge formation

Within the simulation regime, three different models have been considered in the literature, major mergers, minor mergers, and disk buckling. A *major merger* occurs when two galaxies of roughly equal mass interact with each other and subsequent merger into a single and more massive galaxy. In cosmological simulations, in this process, all the newly formed stars are assumed to end up in a spheroidal component.

On the contrary, a *minor merger* happens when there is a component more much massive than the other. During a minor merger, the smaller galaxy is influenced by the gravitational field of the larger galaxy, causing it to be tidally disrupted and its stars, gas, and dust to be pulled toward the larger galaxy. In this process, the structure of the largest galaxy generally retains its dominant characteristic. For instance, the disk is not modified but the bulge acquires all the pre-existing stars from the minor progenitor, while the newly formed stars are added to the disk. In both cases, the bulge component gets more massive. In fact, the virial theorem can be used to estimate the change in size

$$C\frac{GM^2_{\text{new,bulge}}}{R_{\text{new,bulge}}} = C\frac{GM_1^2}{R_1} + C\frac{GM_2^2}{R_2} + \alpha_{\text{inter}}\frac{GM_1M_2}{R_1+R_2}, \tag{4.12}$$

where C is the structure parameter relating the binding energy of a galaxy to its mass and radius, the α_{inter} quantifies the effective interaction energy deposited in the stellar components.

For instance, the formation of a galactic bulge might occur due to a major or minor merger [17]. Also, in these processes, pre-existing and newly formed stars play an important role since, after the merger, all the stars from the progenitors are added into a bulge component of the remnant galaxy. Additionally, it is assumed that in a galaxy merger, the gas contained within the progenitors becomes part of the resulting galaxy disk and the specific angular momentum of this component is equal to that of the halo in which it is embedded [18, 19, 20].

Another channel for the formation of galaxy bulges, particularly when the system has a dominant disk, is the instability of the disk criterion. Here, the schematic expression reads as follows

$$V_{\text{max}} < \sqrt{\frac{GM_{*,d}}{3R_{*,d}}}, \tag{4.13}$$

where $M_{*,d}$ and $R_{*,d}$ are the stellar mass and exponential length of the stellar disk. When this criterion is met, then a transfer of mass from the disk to the bulge stars to keep the disk stable. This produces a new bulge that can merge into the existing one in the same way as in the galaxy mergers, increasing the size of the original bulge.

4.1 Machine Learning Algorithms to estimate the mass components of galaxies

As we can notice, on one hand, there are different ways of computing the mass and properties of different galactic components. The bulge-disk decomposition can be done by using pure observation of the morphology, or by light information such as the photometric and /or spectroscopic measurements, either in a synthetic way by using mock catalogs. On the other hand, having information about the total mass implies making strong assumptions regarding at least one specific model of dark matter, or about the total kinematics of the system. In this section, we propose a method based on artificial intelligence (AI) designed to single out the bulge and disk components of the baryonic mass as well as the total mass of the galaxy by using information about luminosity and features inferred from the kinematics.

The aim of this section is to implement and test different machine learning algorithms in order to predict the stellar mass $M_\star$, the total mass $M_{\rm tot}$, and the disk mass $M_{\rm disk}$, which represent the most prominent components in a galactic system, this is achieved by using data associated to the luminosity of visible components and the kinematics from the Guo's galaxy catalog [18], which is a synthetic catalog derived from the Millennium simulation [21]. Here, it is worth pointing out that the bulge mass $M_{\rm bulge}$ is not within the prediction set since it can be easily derived in terms of $M_{\rm disk}$ from the following expression [18, 13]

$$M_\star = M_{\rm bulge} + M_{\rm disk}. \tag{4.14}$$

Therefore, in some cases only the $M_{\rm disk}$ will be considered.

4.1.1 The Guo's galaxy catalog

In order to train our machine learning algorithms, we have used Guo's galaxy catalog [18] derived from the Millennium Simulation. The latter is a dark matter-only simulation carried out under the ΛCDM prescription [21], by using the Gadget 2 code [22].

In this case, we are considering the information at $z = 0$. Due to the fact we are interested in studying the mass of the bulge and the disk, we only selected those galaxies whose disk and bulge components are different from zero in the mock catalog. The masses values for each component are delimited by the resolution of the cosmological simulation, then, once the filter mentioned before has been applied, the range of the total mass is between $10^{10} M_\odot/h$ and $10^{13} M_\odot/h$, while the baryon and disk masses are between $10^9 M_\odot/h$ and $10^{11} M_\odot/h$. Notice that, the total mass range does not involve galaxies of low or high masses, given that they do not fulfill the condition of having both bulge and disk. Indeed, very massive galaxies tend to be elliptical [23].

Features importance

It is well known that the physical and photometric properties of the stellar population of a galaxy are closely related to its dynamics and the spatial mass distribution of different components within the system. Specifically, this relation is reflected in the color-magnitude relation. For instance, it has been shown that bulge-dominant galaxies have a color-magnitude diagram mainly described by red galaxies [24]. Besides, in [25] it has been shown that the bulge is redder than the disk in galaxies within a cluster.

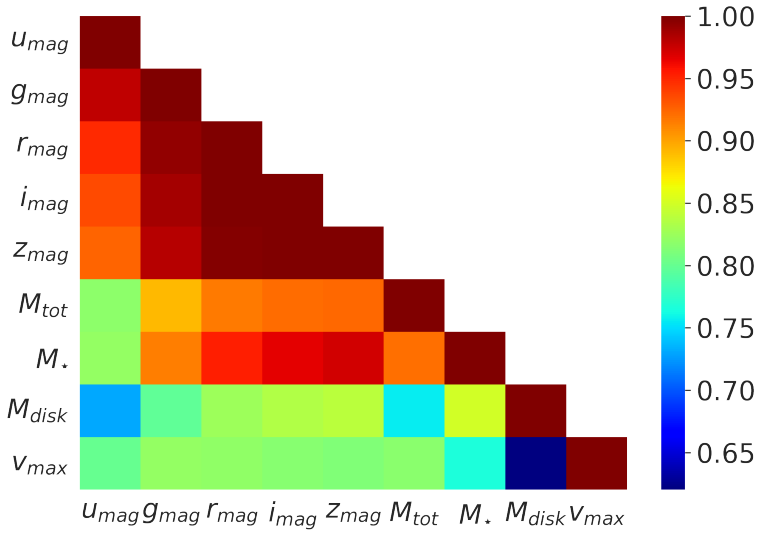

Figure 4.5: Heat map of the absolute value of the Pearson correlation coefficient between the galaxy parameters considered in this work. Number 1 represents a strong correlation. The stronger correlations occur between the stellar mass and the magnitudes in different bands, as expected. However, there exists a relation between the total mass and the magnitudes as well, although to a lesser extent.

In this work, we consider different sets of features, the first one corresponding to the u, g, r, i, z absolute magnitudes that we dub hereafter as Set I. Such magnitudes are also available within Sloan Digital Sky Survey (SDSS) dataset [26], so they have an observational counterpart. Within a second set (Set II) the same features as Set I are considered in addition to $V_{\rm max}$, in order to include information about the kinematics. In both cases, the algorithm predictions turn out to be the $M_{\rm disk}$, $M_\star$, and $M_{\rm tot}$.

In fig. 4.5 the correlation matrix is shown for our set of features and it illustrates the extent that each feature contributes to the algorithm prediction. An exploration of the data is performed by using Pearson's correlation ratio which is defined for two sets of data X and Y as

$$r_{X,Y} = \frac{\sum_{i=1}^{n}(X_i - \bar{X})(Y_i - \bar{Y})}{(n-1)s_X s_Y}, \tag{4.15}$$

where barred symbols stand for the mean values and $S_{X,Y}$ for the standard deviation. When this quotient is $r_{X,Y} = \pm 1$ we have a perfect positive (negative) correlation, whereas for $r_{X,Y} = 0$ parameters are not correlated at all. In figure 4.5 we show the absolute value of this ratio since we are only interested in values that can contribute to a regression.

As expected, we can see that $M_\star$ is highly correlated to the magnitudes, especially with the z and i bands which correspond to the infrared and near-infrared regions of the spectrum, respectively. Actually, observational inferences of the luminous mass are strongly affected by the presence of dust given that emissions within the optical band are reddened while in the near-infrared this effect is negligible [27].

The $M_{\rm disk}$ is less correlated to the magnitudes in comparison to $M_\star$. We can notice that it also shows a weak relation with the remaining quantities. Additionally, $M_{\rm tot}$ shows a strong link with $M_\star$, this is due to the way mock catalogs are created. Then, the correlation of it with $V_{\rm max}$, which encodes information about the dynamics of all components of the system, is the highest in comparison to the masses of the rest of the components. Finally, the importance of the correlations

with $M_{\rm disk}$ is weak. This suggests that the dark matter component affects the stellar one as a whole instead of each component separately.

4.1.2 Description of the algorithms

Below, we present a brief description of each as well as their main parameters used.

- **K Neighbors**. This method defines the predicted value as a function of the similarities in their neighbors. In the regression case, the algorithm takes the average of the values of the corresponding neighbors and the measure is defined by the Euclidian distance between two points. Additionally, the main parameter that controls this algorithm is precisely the number of neighbors. In this case, we found that the highest accuracy is reached when the number of neighbors is around 19 and after the value the error starts to increase.

- **Linear Regression**. This is one of the most famous methods of regression. The implemented technique attempts to model the relation between a dependent variable and one or more independent variables by means of the following linear equation

$$\hat{y} = w[0]x[0] + w[1]x[1] + \ldots + w[p]x[p] + b \tag{4.16}$$

  where $\hat{y}$ is the prediction, $x[i]$ denotes the features of a single point and w, b are parameters the model learn. The coefficients (or weights) w assigned to each feature are estimated in such a way that minimizes the mean squared error between predictions and true values. Although we implemented different variations of this method such as Lasso and Ridge regressor, the two of them converged to linear regressor, showing the values for the parameters which controls the regularization methods close to zero. This method can be applied to multiple dimensions where the features are highly correlated.

- **Decision Tree Regresor**. This corresponds to a hierarchy leading to an if/else decision. It separates the data into smaller and smaller subsets to predict the target value. The tree starts with the root node, containing the whole data point. After that, decision nodes split the data, giving place to different branches. When the decision node does not split data anymore, there is a leaf, that corresponds to the final result of the tree. It is possible to select the option where the leaves are pure, this means the data cannot be split anymore. The main parameters involved in this algorithm are the maximum depth of the tree, the maximum number of features to consider when splitting the data, and the minimum number of samples required for each node.

- **Random Forest Regressor**. This is a collection of tree regressors, where each of them corresponds to a hierarchy leading to an if/else decision. It separates the data into smaller and smaller subsets until predicting the target value In the form the trees are built, it is possible to have overfitting. That is why it is better to use a collection of trees instead. A forest is an estimator that uses the number of regressor trees and averages the results to improve the predicting accuracy and avoid the learning of specific non-representative patterns. The main parameters on which it depends the method are the number of decision trees, the maximum depth of each tree, and the minimum number of data to split to the next node. Here, the best accuracy was reached when using 700 trees each one with a depth of seven and the minimum number of samples required to split in two.

- **Neural Network**. Networks involve various architectures and learning algorithms. The processing units are neurons also known as nodes. Each node is stored in a layer and connected to other nodes in the network by unidirectional connections of different weights. Patterns learned in a layer are transferred to the next activated nodes. This results in the output of one node becoming the input of the next node. The input layer activates neurons in the

inner layers until the output layer gives the smallest error. The NN depends mainly on the number of layers, the number of neurons per layer, the learning rate, the activation function, and possibly the regularization method.

4.1.3 Testing the algorithms performance

In fig. 4.6 we present the relative percentage difference between the logarithm of $M_{\rm actual}$ within the mock catalog and the logarithm of the predicted value $M_{\rm pred}$ by each algorithm, computed as follows

$$\Delta = 100\left[\frac{\log M_{\rm pred}}{\log M_{\rm actual}} - 1\right]. \tag{4.17}$$

The left side panel shows the result when the training was carried out using Set I while on the right side that corresponds to Set II. The dashed lines correspond to the mean values for the whole set whereas the width of shaded regions corresponds to the standard deviation around the mean value $\mu \pm \sigma$. Also, the histogram for the quantities in the Mock catalog is shown.

It can be noticed in the uncertainty bands for the histogram become thinner as data counts are larger and hence the prediction is more accurate. Therefore, the highest error for the $M_{\rm disk}$ and $M_\star$ predictions (Figs. 4.6 (a) and 4.6 (c)) lay below $10^9 M_\odot/h$. Besides, for $M_{\rm tot}$ in Figs. 4.6 (e) and 4.6 (f), the error increases for larger values of the mass, which means the prediction is reliable in the central region of the range around $10^{11}/M_\odot$. In fact, it is worth mentioning that the distribution of $M_{\rm tot}$ is narrower compared to the distribution of $M_{\rm disk}$, as we can see in figs. 4.6 (a) and 4.6 (e). This can be explained given that galaxies within the sample chosen from the mock catalog passed the strong condition of holding a bulge and this requirement is only fulfilled by sufficiently massive galaxies.

In general, all predictions have statistical errors around a central value equal to zero. However, $M_\star$ in fig. 4.6 (c) and 4.6 panel (d) show the smallest percentage difference in both cases since there is a linear correlation between the magnitudes and the luminous mass. For that reason, the LR model shows the best score since it was trained by directly fitting a scaling relation. In some algorithms like NN and RF, the error increases around 1% for masses $10^{10} M_\odot/h$, when Set II is considered.

Now, for the mass of the disk, figs. 4.6 (a) and 4.6 (b), we can notice that the percentage difference is higher than for the $M_\star$ case, but still, it is within a good prediction range for medium and high masses. In this case, the predictions for both sets of features are similar. Also, the LR method is no longer the best, since it is not a linear fit. Here, the NN and RF show the best training for Set I, and the first one improves then Set II is taken into account.

Finally, the $M_{\rm tot}$ is predicted similarly in both cases, fig. 4.6 (e) and fig. 4.6 (f). Here, the correlation between Set I, which corresponds to the magnitudes and $M_{\rm tot}$, is not straightforward. However, given that the mock catalogs were created following a halo abundance matching relation, there exists a correlation to $M_\star$ and therefore, to the magnitudes. This allows having good training for $M_{\rm tot}$. Something interesting is that the prediction for Set II does not show an improvement, even though this set includes information about the kinematics of the system. Here, the best score corresponds to NN for Set I, given the lack of an explicit scale relation, while for Set II, all predictions are very similar.

By analyzing the behavior of the predictions for Set I and Set II, we can conclude the latter does not show a significant improvement in the results. Actually, the major contribution is in the $M_{\rm tot}$ as we can see in figure 4.6 (f) where the curve is closer to zero above $10^{12} M_\odot$. Besides, having information about the $V_{\rm max}$ for real galaxies can be complicated because of the complexity of the dynamics of the system. For that reason, in order to keep the set of features as simple as possible, we decided to use Set I only from now on.

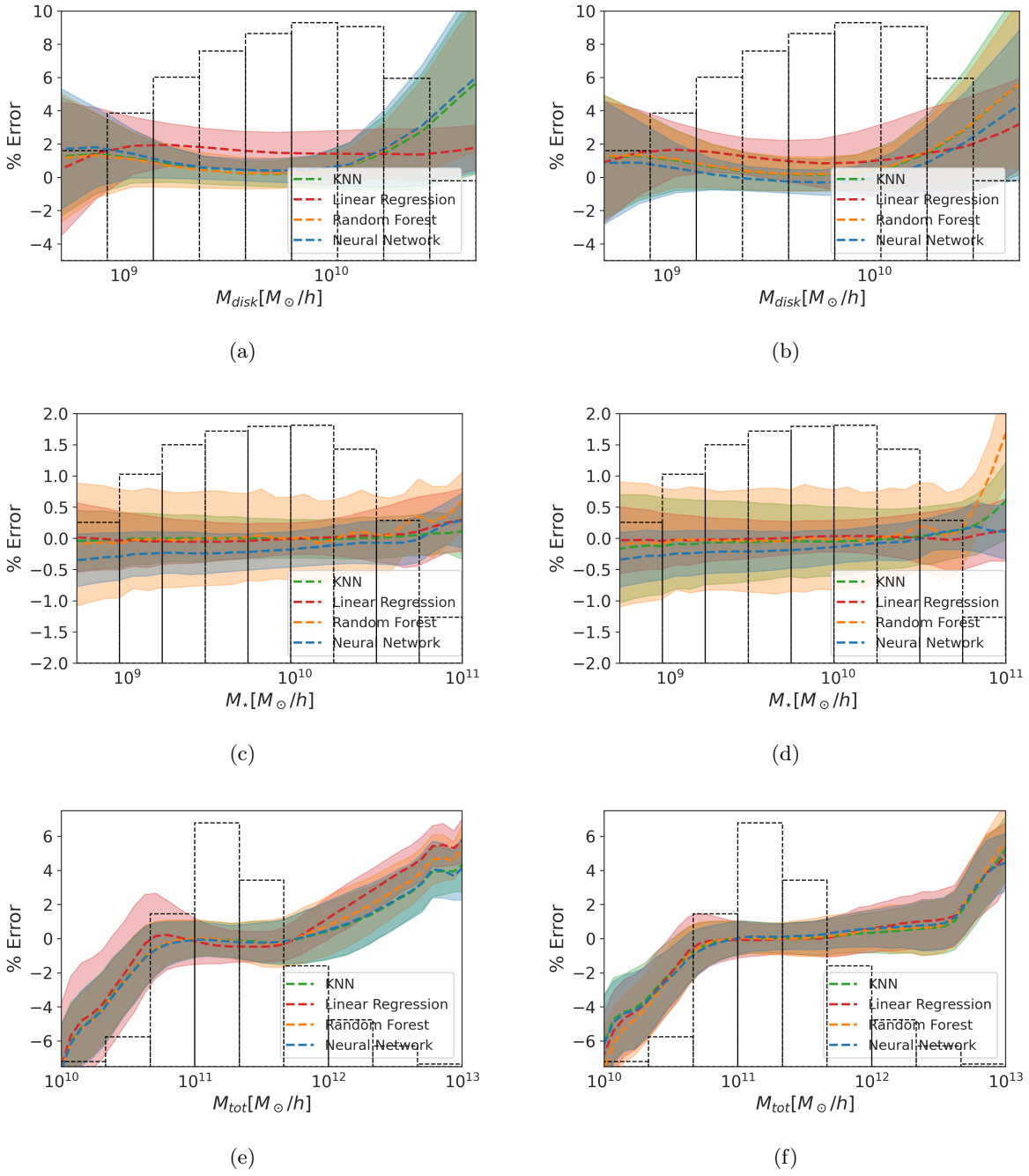

Figure 4.6: Relative percentage difference for the predictions of different Machine Learning algorithms with respect to the actual values in the mock catalogs. Set I is displayed on the left, the Set II on the right. The histograms in the figures represent the distribution of the data. As expected, the predictions are better where the density of data is higher. The lines represent the mean value μ and the bands are one standard deviation away from the mean value $\mu \pm \sigma$.

4.1.4 Comparison with the SDSS catalog

Up to this point, we have assessed the training performance by using data from the mock catalog. Now, such trained algorithms are ready to predict masses of different components in real galaxies by using observational data as input features. With that purpose in mind, we took data from the SDSS galaxy catalog [28], which contains data from around 660 000 galaxies. Nevertheless, we only used a portion of the total data $\sim 70\%$, which corresponds to the galaxies whose u, g, r, i, z magnitudes are known. The bulge-disk brightness profiles were reconstructed by using the Sersic profile photometric decomposition method. In order to compare the predictions of our algorithms with this observational data, we took into consideration the information on the bulge, disk, and stellar masses.

Additionally, we considered the SPARC database which contains information on irregular galaxies observed with the Spitzer telescope whose photometry lies at 3.6 μm. The catalog contains information about the observed rotation curves either for the dark matter or for each baryonic component and they were derived by using photometric and spectrometric methods. Particularly, we used the Mass Models Supplement (MMS) table to obtain the mass of the disk and the bulge. We inferred the observational total mass from the total rotation curve.

The apparent magnitudes used in the predictions stage were obtained from the SDSS DR7 [26], we converted the apparent to absolute magnitudes following the equation [29]

$$M = m - 5\Big(\log_{10} d - 1\Big), \tag{4.18}$$

where M and m are the absolute and apparent magnitudes, respectively, and d is the distance to the source. Distances were computed using the library Astropy [30] with the redshift reported in NED[1] and assuming the concordance cosmological model with the Planck 2018 cosmological parameters $H_0 = 67.66$ km/Mpc/s, and $\Omega_{m0} = 0.26$. A valuable piece of information for describing the evolution and structure of galaxies is the scaling relations between different physical quantities of a galaxy sample. In this section, we are interested in obtaining some of those relations from the input and output parameters of our algorithms. Specifically, we focus on analyzing the relation between mass components and the r-magnitude. We choose the magnitude in this color since is a common practice in different works. Furthermore, the relations for magnitudes in other colors are similar to the former. In addition, we study the $M_{\rm bulge} - M_{\rm disk}$ relation as well as the $M_\star - M_{\rm tot}$.

4.1.5 Mass-magnitude relation

In fig. 4.7 we show the distributions projected in $M_\star$- r-magnitude, $M_{\rm disk}$- r-magnitude and $M_{\rm bulge}$- r-magnitude planes. In all cases distributions for three datasets are plotted: firstly, that from the original Mock catalog in color blue, secondly that for the SDSS from the original catalog in green and the third one corresponds to predictions for the SDSS galaxies in color red.

In fig. 4.7 panel (a), the scaling relation between $M_{\rm disk} - r_{\rm mag}$ is shown. It can be noticed that a large fraction of the SDSS sample lies inside the region corresponding to the Mock catalog distribution, except galaxies with masses above $10^{11} M_\odot/h$. NN predictions for SDSS galaxies agree with observational data from the original catalog. Dashed lines represent the best fit for the three sets of data shown in the figure.

The best fit for all data sets is shown as follows

$$M_\star = -0.427 r_{\rm mag} + 1.370 \quad \text{Mock catalog,} \tag{4.19}$$
$$M_\star = -0.461 r_{\rm mag} + 0.916 \quad \text{SDSS catalog,} \tag{4.20}$$
$$M_\star = -0.457 r_{\rm mag} + 0.954 \quad \text{NN prediction.} \tag{4.21}$$

[1]The NASA/IPAC Extragalactic Database (NED) is operated by the Jet Propulsion Laboratory, California Institute of Technology, under contract with the National Aeronautics and Space Administration.

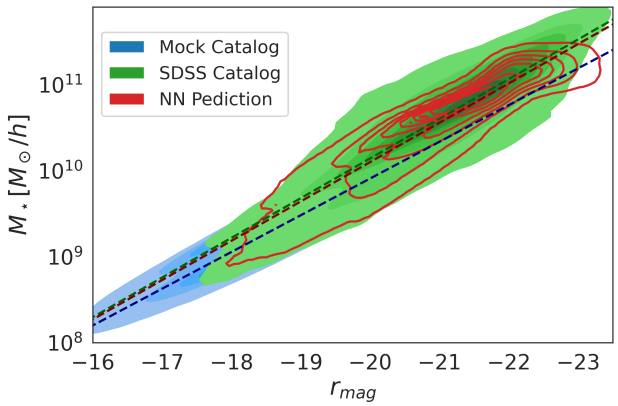

(a)

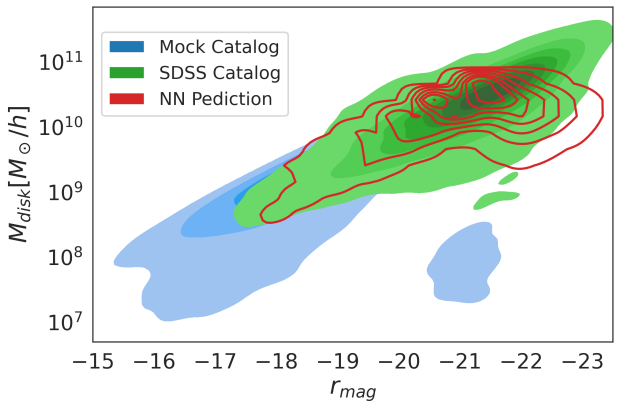

(b)

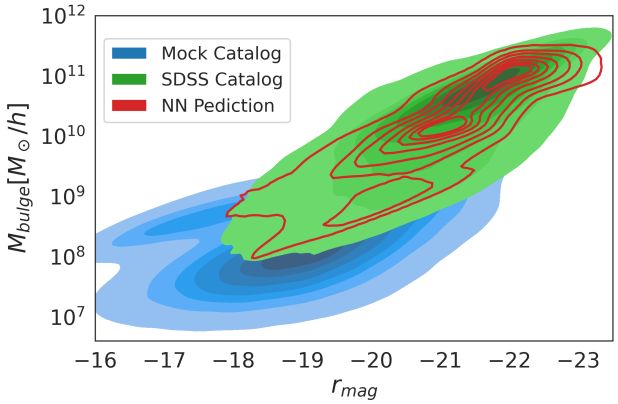

(c)

Figure 4.7: Kernel density estimation (KDE) plots of the stellar (a), disk (b), and bulge (c) masses components versus the r-magnitude. In the first case, we have a linear relation, and the best-fit fo each dataset is represented by the dashed lines.

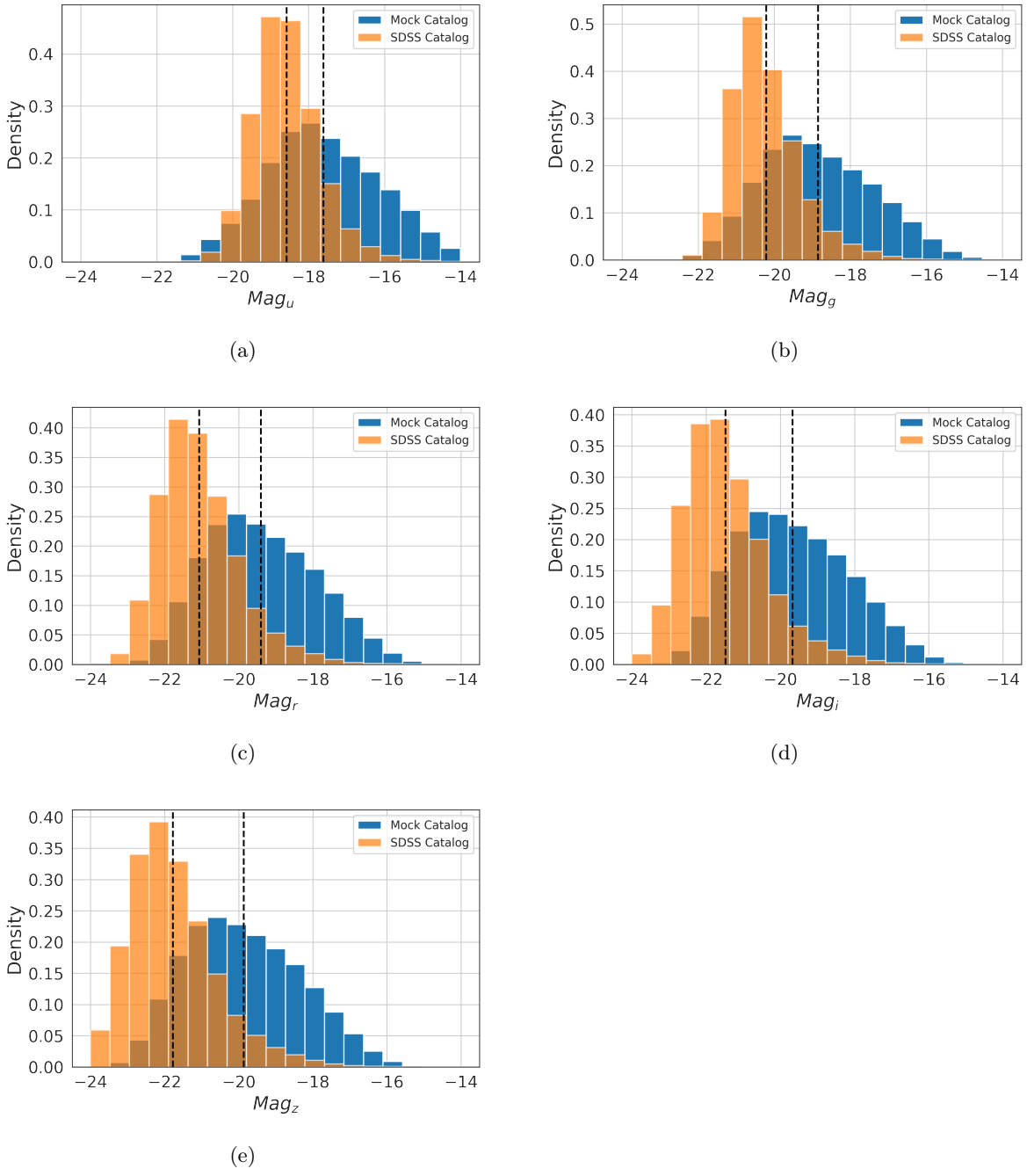

(a) (b) (c) (d) (e)

Figure 4.8: These histograms clearly show that within the mock sample, the distribution of magnitudes for galaxies significantly differs from that for the SDSS sample. This suggests that the algorithms shall be able to obtain generalized predictions given the extended range of features of the SDSS sample and the combinations between them. Vertical dashed lines show the mean value of each distribution.

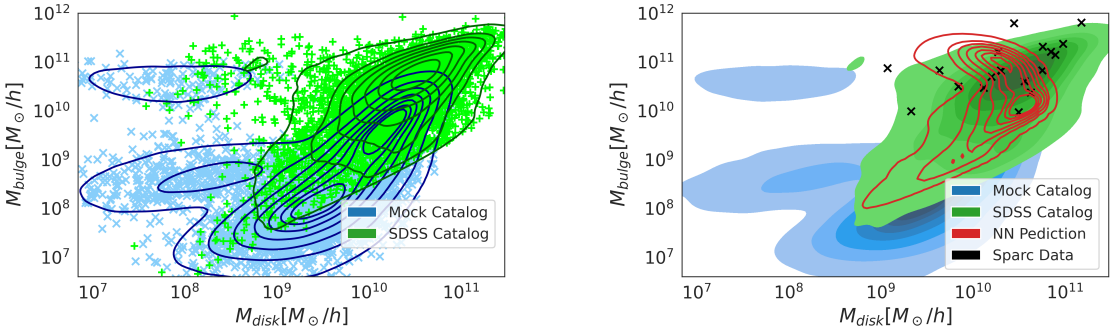

(a) (b)

Figure 4.9: KDE plots of the Bulge-Disk decomposition. In (a) the distribution for both simulated (blue) and observational (green) data are shown as well as the solid contour levels. We observe a trimodal distribution for the mock catalog, whereas the observations show a bimodal distribution. In (b) we show the contour levels from the previous figure and in addition we report the prediction for the NN for observational data (red) and the galaxies selected from the SPARC database (black crosses).

For $M_{\rm disk}$ in fig. 4.7 panel (b), the SDSS galaxies reach higher values than the mock catalog, so it clearly confirms that the neural network is capable to generalize values beyond the training data. We also observe a small blob separated from the largest one, since the values for the magnitude in that region correspond to large $M_\star$ values above $10^{10} M_\odot/h$ and by following eq. (4.14), we can conclude that these galaxies have large values for the bulge in order to compensate for the stellar mass. This sort of galaxy is usually dubbed as cD−like galaxies (central dominant) [18]. Interestingly the KNN algorithm correctly avoids predicting values in this region since cD−like galaxies are absent within the SDSS catalog. For $M_{\rm bulge}$ in 4.7 panel (c) the generalization is actually more evident. In this case, the relationship is not as simple as a linear regression as in the $M_\star - r_{\rm mag}$, but it shows the capability of NN to predict more complex relations.

As we can see, the regions embedding the distribution for the virial mass (and consequently the baryonic mass) corresponding to the mock catalog sample, are delimited by the numerical resolution of the Millenium simulation. However, the observations can go beyond those limits, showing higher masses and different magnitudes outside those regions.

Histograms describing the distribution of the absolute magnitudes in different bands in the ugriz-photometric system, for both SDSS and the mock catalog, are shown in Fig. 4.8. Distributions of magnitudes u, g, r, i, and z used for the training are reported, in Figs. 4.8 (a), (b), (c), (d), and (f), respectively. The dashed lines correspond to the mean values for each catalog. We can observe that in all cases the mean value for the observed galaxies is shifted to the left for high luminosities. The combination of these values in each band gives rise to values for baryonic masses higher than the mock catalogs as shown in Fig. 4.7.

4.1.6 Bulge-disk relation

The bulge-disk decomposition is delimited by the eq. (4.14). At the same time, $M_\star$ can be directly determined given the magnitude, by using a scaling relation as that shown in Fig. 4.7. Thus, for a specific value for $M_{\rm bulge}$, its counterpart, $M_{\rm disk}$, will only take values within certain intervals, and vice versa.

Figure 4.9 (a) shows masses of the bulge and the disk of galaxies from the mock and SDSS catalogs whereas all information is contained inside the contour levels. As in the previous sections, the observations lie inside a region beyond the mock catalog data.

Nevertheless, we observe an interesting behavior for both datasets: The mock catalog shows

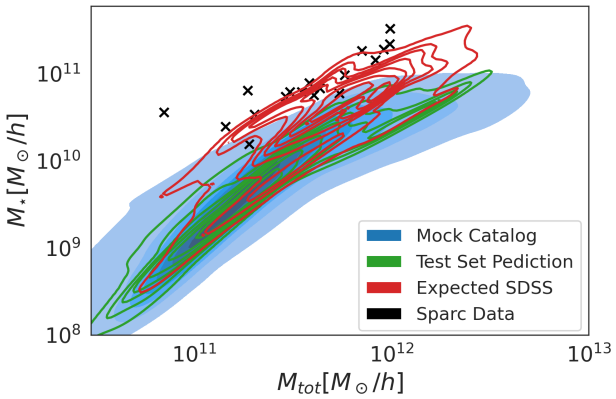

Figure 4.10: Predicted halo abundance matching relationship between $M_{\rm tot}$ and $M_\star$ for both the mock catalog test set and the SDSS Mendel catalog. We observe the prediction for the SDSS galaxies in red curves, which follows the same behavior as the synthetic catalog. Moreover, the crosses represent the galaxies in SPARC, which lie within the regions delimited by the predictions.

a trimodal distribution while the SDSS data has a bimodal one. The most prominent region, for $M_{\rm disk} > 10^9 M_{\odot/h}$, corresponds to low values for $M_{\rm bulge}$, and it is associated to disk-dominated galaxies. The second region, for $M_{\rm bulge} > 10^{10} M_{\odot/h}$ is the bulge-dominated region. This sort of morphology arises in both observed and simulated galaxies. Although disk-dominant galaxies are more abundant in both cases, within the SDSS data, the number of bulge-dominant galaxies is too small to be considered in the contour levels.

The third region in the $M_{\rm bulge} - M_{\rm disk}$ plane reveals an interesting fact and it is only visible for the synthetic data and corresponds to galaxies with low disk and bulge masses. Nevertheless, these galaxies are not reported in the SDSS catalog. This discrepancy suggests that there may be an observational bias. This difference may be due to the fact that current telescopes might not be able to detect the low-luminosity galaxies that actually appear in the numerical simulations.

Fig. 4.9 (b) shows data from both catalogs together with the NN prediction. Additionally, crosses in that panel correspond to data for galaxies from SPARC. For this last sample, the relationship between disk and bulge is nonlinear and not readily fitted with an analytic function as it happens with scaling relations derived, nevertheless, the machine learning algorithm is able to make good predictions. Furthermore, it is interesting to note that the NN algorithm gives rise to mass predictions consistent with the SDSS distribution and does not predict bulge-dominant galaxies as expected.

4.1.7 Halo abundance matching

This work presents a prediction for halo abundance matching using galaxies within the SDSS dataset. In this case, we lack information about the total mass of the galaxies in this dataset. However, with the SPARC data, we can derive $M_{\rm tot}$ from the total rotation curve. Fig. 4.10 shows the relation between $M_\star - M_{\rm tot}$. It is evident that the relationship is not linear; instead, the stellar mass increases faster than the total mass. However, once $M_* > 11 M_\odot/h$, it becomes approximately constant. This parameter space region corresponds to galaxies with a significant amount of dark matter.

Some of the galaxies in SPARC are also contained in the SDSS sample. Interestingly, the SPARC data fall inside the range of predicted values in the $M_* - M_{\rm tot}$ plane for SDSS, red curves. And both observational datasets show higher values for M_* than those in the mock catalog, as in the previous relations. This corresponds to another observational bias, due to the actual telescopes

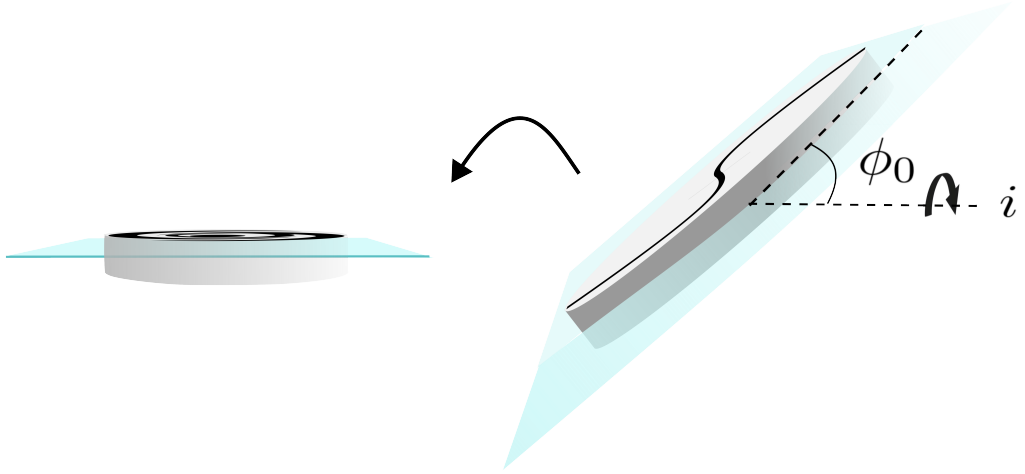

Figure 4.11: To describe the position of a galaxy for the line-of-sight it is necessary to identify two angles, the first one is the measure respect from the horizon, and the second one is the inclination angle.

being capable to observe more luminous objects than those reported in the synthetic data, see Fig. 4.8. However, the M_{tot} values are within the same regions delimited by the mock catalog.

4.2 Rotation curves for observational galaxies

In this section, we will study the bulge-disk decomposition in observational data. For this reason, the MaNGA catalog will be used to construct the rotation curves and therefore, continue exploring the properties of dark matter. MaNGA is the newest survey component of the Sloan Digital Sky Survey. Its goal is to map the detailed composition and kinematic structure of 10,000 nearby galaxies. MaNGA uses integral field unit (IFU) spectroscopy to measure spectra for hundreds of points within each galaxy. In particular, we will only focus on spiral galaxies, in order to obtain the rotation curve.

For this model, a disk will be considered whose rotation curve $V_{\text{ROT}}(R)$ from our point of observation. We will assume that the systematic velocity relative to us is zero, otherwise, just add a constant to all observed velocities. In order to study the speed of stars in galaxies, it is necessary to see them edge-on. However, usually, the galaxies seen from our line of sight have an angle ϕ_0 with respect to the horizon, as well as an inclination i, as shown in Fig. 4.11. Therefore, it is necessary to position them as the sketch on the left in order to reconstruct the rotation curve. Fig. 4.12 shows the coordinate systems used. First, (x_0, y_0) is the system on the sky plane. For convenience, a rotation of the axis will be performed such that the x-component lies on the major axis of the galaxy, and the galaxy center matches the origin. Namely

$$\begin{pmatrix} x \\ y \end{pmatrix} = \begin{pmatrix} \cos(-\phi_0) & -\sin(-\phi_0) \\ \sin(-\phi_0) & \cos(-\phi_0). \end{pmatrix} \tag{4.22}$$

Additionally, we have the coordinate system on the galactic plane, given by (x', y'). In the latter, it is also convenient to use polar coordinates (R', θ'). A component located at radius R will have velocity $\vec{r} = -V_{\text{ROT}}(R)(\hat{\vec{R}} \times \hat{\vec{n}})$, where $\hat{\vec{R}}$ is the unit vector pointing from the center of the galaxy to the component and $\hat{\vec{n}}$ is the unit vector to the plane of the disk, as shown in Fig. 4.12. The

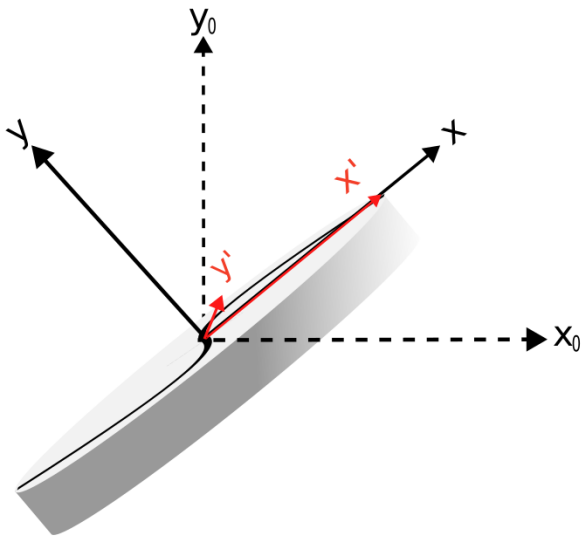

Figure 4.12: Skecth to describe the position of a galaxy in the sky. The coordinate system x_0, y_0 is associated with the sky, but for simplicity, it is convenient to rotate it such that the $x-$axis lies along the major axis of the galaxy and the origin matches the galaxy center. The other system is on the galaxy plane, that is x', y'.

observed velocity along the line of sight (LOS) is expressed as the dot product between the velocity $\vec{v}$ and the direction along the line of sight $\hat{r}$, pointing from the observer to the galaxy as follows

$$V = \hat{\vec{r}} \cdot \vec{v} \tag{4.23}$$
$$= V_{\rm ROT}(R)\hat{\vec{R}} \cdot (\hat{\vec{r}} \times \hat{\vec{n}}) \tag{4.24}$$
$$= V_{\rm ROT}(R)\hat{\vec{R}} \cdot \hat{\vec{k}} \sin(i) \tag{4.25}$$

where i is the inclination angle of the galaxy (defined such that the edge-on galaxy would have $i = 90$). Here $\hat{\vec{k}} = (\hat{\vec{r}} \times \hat{\vec{n}}) \sin(i)$ is the normal vector to $\hat{\vec{r}}$ and $\hat{\vec{n}}$, which resides in the plane of the sky.The vector $\hat{\vec{R}}$ also lies in that plane and has coordinates $(\cos\theta, \sin\theta)$. For simplicity, the center of the stellar coordinate system is defined in such a way that the center of the galaxy is at $(x, y) = (0, 0)$, and the major axis of the galaxy will be aligned at y =0. The polar coordinates in the sky plane will be denoted by (r, ϕ).

Considering the previous information, we have

$$V(x, y) = V_{\rm ROT}(R)\cos(\theta)\sin(i). \tag{4.26}$$

As it was mentioned previously, in case of having systematic velocity different from zero, then, it is necessary to add a constant, as follows

$$V(x, y) = V_{\rm SYS} + V_c(R)\cos(\theta)\sin(i). \tag{4.27}$$

It is worth mentioning that $V_{\rm SYS}$ is precisely the one that has been subtracted in the filtered mask to obtain the values in the right panel, so it is an important parameter to obtain the appropriate rotation curve in each of the samples.

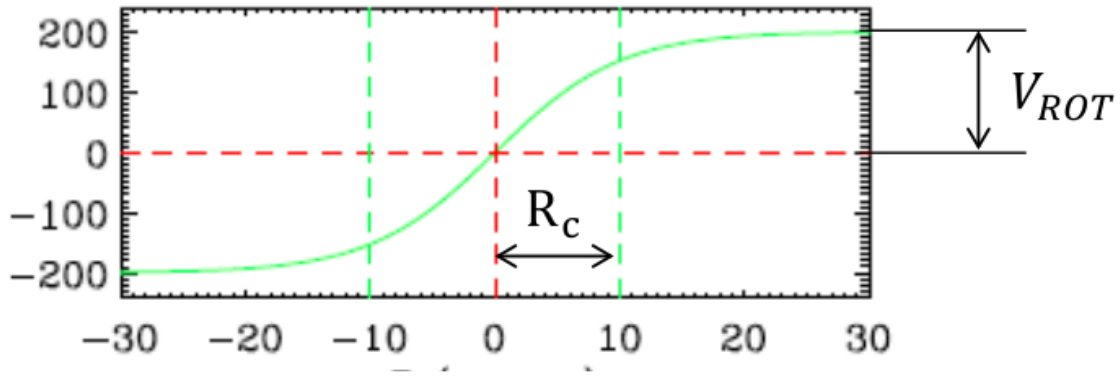

Figure 4.13: Functional form of the rotation curve defined by a hyperbolic tangent. We can observe two important parameters, the first R_c corresponds to the radius before the curve begins to have an asymptotic behavior. The second value $V_{\rm ROT}$ is just the asymptotic value of the velocity.

Below is the relationship between the two coordinate systems, which are important to be able to make the adjustment

$$x' = x, \tag{4.28}$$
$$y' = \frac{y}{\cos(i)}, \tag{4.29}$$
$$\tan(\theta) = \frac{\tan\phi}{\cos(i)}. \tag{4.30}$$

However, there are different functional forms for $V(R)$ reported in the literature. Various studies have shown that the rotation curve has different slopes in the inner and outer parts, which also depend on the properties of the galaxies. In this case, we take a functional form in terms of a hyperbolic tangent, expressed as

$$V(R) = V_{\rm ROT}\tanh\left(\frac{r}{R_c}\right) + s_{\rm out}r, \tag{4.31}$$

where the term $s_{\rm out}$ is the slope of the rotation curve when the condition $r \ll R_c$ is fulfilled, feel R_c the radius where the hyperbolic tangent begins to be flattened. (See Fig. 4.13)

4.2.1 Stellar velocity maps for galaxies in MaNGA

Data pre-processing

The observational data was taken from the SDSS survey, particularly from MaNGA, which provides two-dimensional maps of stellar velocity and velocity dispersion, mean stellar age and star formation history, stellar metallicity, element abundance ratio, stellar mass surface density, ionized gas velocity, ionized gas metallicity, star formation rate, and dust extinction for a statistically powerful sample, as shown in Fig. 4.14. In this case, the stellar maps provide the necessary information to be able to reconstruct the rotation curve, however, such maps are not filtered from objects positioned along the line of sight as well as from background noise.

The first selection criteria before the fitting are applied over the total flux. It is convenient to select those velocities where the flux compared to the error (signal-to-noise ratio), is greater than a certain threshold, that is [31]

$$\frac{S}{N} \geq 5. \tag{4.32}$$

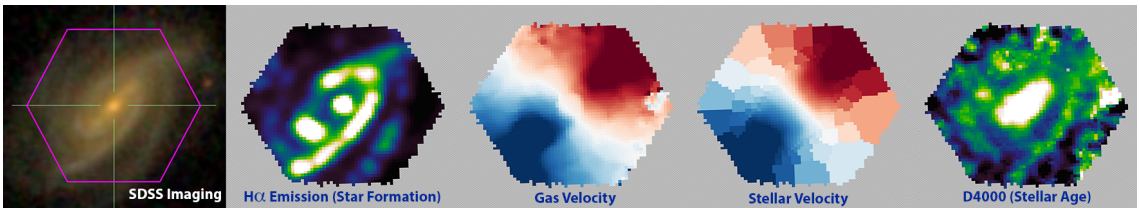

Figure 4.14: Different maps reported in MaNGA involve the main parameters derived from the analysis of the stellar populations, including the LW and MW ages, metallicities, dust attenuation, and stellar kinematics properties. Here we can see the image in the visible, the $H\alpha-$emission, the gas velocity, the stellar velocity, and the stellar age. Source `https://www.sdss4.org/surveys/manga/`.

Indeed, the spaxel at large R_c could be noise, which means low $\frac{S}{N}$, therefore the stellar velocity obtained from them could be unreliable. In particular, spaxels around the minor axis and large R_c typically have low $\frac{S}{N}$ and including them in the subsequent process can disturb the fitting. To illustrate this, we can select randomly a galaxy from the MaNGA data, namely 8329-6103. Fig. 4.15 shows the optical image in panel (a), there, the pink hexagon shows the size of the MaNGA integral size unit (IFU). In panel (b), the flux intensity of the $H\alpha$ map is displayed after applying the signal-to-noise ratio threshold. Indeed, only the pixels that are part of the galaxy are the ones that survive this filter, so they fall within the contour lines.

Additionally, in order to remove objects along the line-of-sight as well as background noise it is necessary to implement a filter over the stellar velocity map. First, the histogram of velocities is identified, and then, the valleys where the velocity count is equal to zero. These gaps in the distribution help to identify astrophysical objects that are not gravitationally bound to the galaxy or just noise. In Fig. 4.16 (a) the optical image of the galaxy is shown. Then, in 4.16 (b) the original velocity map is shown before the filter, there we can observe the regions in blue where the velocity is lower than in the rest of the map. Here, the numeric panel has values of the order of 1×10^4, which corresponds just to the systematic velocity $V_{\rm SYS}$. In Fig. 4.16 (c), we observe the stellar velocity map once the filter has been applied, now the contours of the galaxy are visible and we can easily distinguish between the speeds that are moving away (in red) and those that are approaching (in blue), with respect to the observer. Finally, in 4.16 (d) the corresponding density mass map is reported.

4.2.2 MCMC Method for Rotation Curve Fitting

Taking into account the results of the previous section and regarding the geometric parameters of the 2D stellar velocity map, the projected velocity along the line-of-sight takes form.

$$V_{\rm LOS} = V_{\rm SYS} + V(r)\sin(i)\cos(\theta), \tag{4.33}$$

therefore, the parameters to fit are $V_{\rm SYS}$, $V_{\rm ROT}$, R_c, $s_{\rm out}$, i, ϕ_0, $X_{\rm cent}$ and $Y_{\rm cent}$. Where the last two quantities represent the central values where $V_{\rm SYs}$ is measured. There are 8 free parameters in total. It is worth mentioning that the fitting is very sensitive to the initial values of $X_{\rm cent}, Y_{\rm cent}$ given that those values determine the rest of the fitting.

In [31] a study of the rotation curves for the galaxies in MaNGA, from photometric data, was performed. They reported giving very accurate initial values to the free parameters in order to obtain a good fitting. In this work, we applied an MCMC method to reconstruct the rotation curve. First, the initial value for $X_{\rm cent}, Y_{\rm cent}$, and therefore the $V_{\rm SYS}$, is obtained by smoothing the density mass map 4.16 and finding the maximum value. Moreover, since the stellar velocity map is already filtered, and the regions where the velocity moves away from or approaches the observer

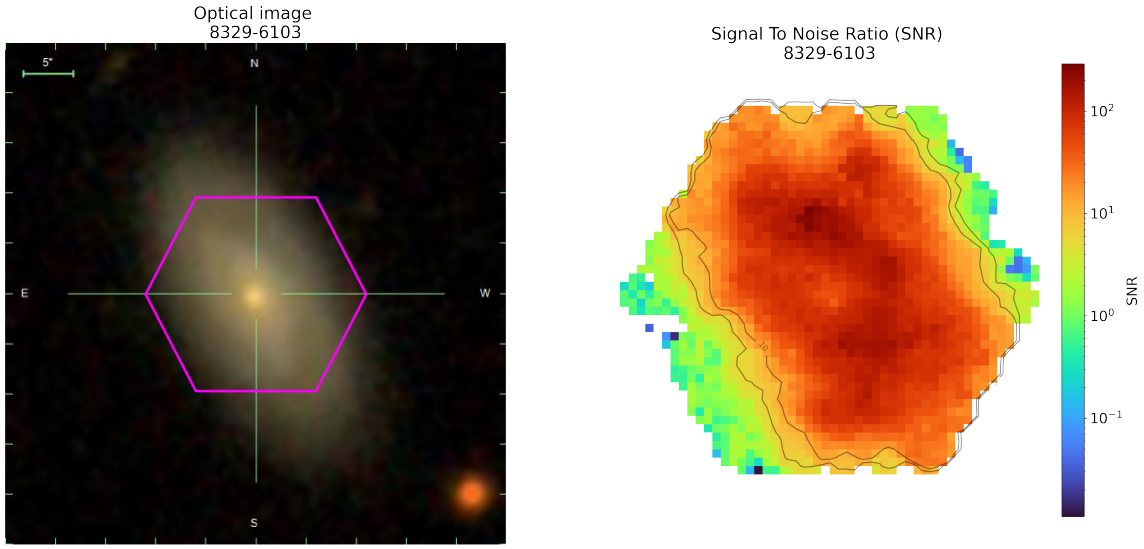

(a) (b)

Figure 4.15: (a)The optical image of the 8329-6103 galaxy in MaNGA. (b)Flux intensity of the $H\alpha$ analyzed emission line map once the signal-to-noise ratio has been applied. The contour lines indicate two thresholds: $\frac{S}{N} = 5, 10$. The inner contour represents the most restrictive limit, while the outer contour is the weaker one. We can see that both contours delimit the shape of the galaxy shown in the optical image.

can be easily identified, it is possible to give an estimated value of the parameter ϕ_0. The rest of the free parameters are given randomly within the following ranges

$$i \in \left[0, \frac{\pi}{2}\right] \text{ pixels}, \tag{4.34}$$
$$R_c \in [0, 40] \text{ pixels}, \tag{4.35}$$
$$s_{\text{out}} \in [-5, 5] \text{ pixels}, \tag{4.36}$$
$$V_{\text{rot}} \in [0, 400] \text{ km}/s. \tag{4.37}$$

4.2.3 Bulge-disk decomposition

Once the rotation curve has been fitted from the stellar velocity map, it is possible to find the mass distribution by considering the distance measure in the galactic plane. Here we will use the mass density map as well as the luminous mass relationship described in eq. (4.14).

In the literature, different density profiles have been proposed to adjust the baryonic components. As mentioned in sec. 4.0.2, for the disks of the *late-type* galaxies, exponential fit better. In this way, for the disk, we are assuming that the mass is distributed following the same functional form as the Sersic profile

$$\rho_d(R, z) = \frac{m_d}{4\pi z_0 h} \text{sech}^2\left(\frac{z}{z_0}\right) \exp\left(-\frac{R}{h}\right), \tag{4.38}$$

and the Plummer profile for the bulge

$$\rho_b(r) = \frac{3m_b}{4\pi a^3}\left(1 + \frac{r^2}{a^2}\right)^{-5/2}. \tag{4.39}$$

In the case of the MaNGA Fits, the mass information is available as $[M] = M\odot/\text{spixel}^2$, which makes it difficult to estimate the contribution of each component separately since the data is projected on the observer's plane. For that reason, first, it is necessary to compute an integral over z

$$\rho_\star(x,y) = \int_{-\infty}^{\infty} \left[\gamma_d \rho_d(x,y,z) + \gamma_b \rho_b(x,y,z)\right] dz, \tag{4.40}$$

where $r = \sqrt{x^2+y^2+z^2}$ and $R = \sqrt{x^2+y^2}$.

For the case of the disk, the integration of the dependency on z simply reduces to $-2z_0$. For the Plummer profile, we have

$$\int \left(1 + \frac{R^2+z^2}{a^2}\right)^{-5/2} dz = \frac{a^2 z\left(3a^2+3R^2+2z^2\right)}{3\left(a^2+R^2\right)^2\left(\frac{a^2+R^2+z^2}{a^2}\right)}. \tag{4.41}$$

Here, $f(r)$ has the following limits

$$lim_{z\to\pm\infty} f(R) = \pm\frac{2a^5}{3(a^2+R^2)^2}. \tag{4.42}$$

Therefore, the density profiles can be rewritten as follows

$$\rho_b(R) = \frac{a^2 m_b}{\pi(a^2+R^2)^2} \tag{4.43}$$

$$\rho_d(R) = \frac{m_d}{2\pi h}\exp\left(-\frac{R}{h}\right). \tag{4.44}$$

where R is the distance from the galactic plane center. Fig. 4.17 shows the density profile constructed from the best fit of the stellar velocity map. The crosses represent the data and the blue line is the best fit following the eq. (4.33). From the density mass map, the best fit for the bulge and disk are shown in green and red, respectively. Here we can see that the dominant component is the disk. In fact, the bulb has its maximum contribution close to $r = 0$, as expected, but then it starts to decrease substantially.

4.2.4 Dark matter rotation curve

The total rotation curve of the stars in a galaxy reads as

$$V_{\text{tot}}(r) = \sqrt{\frac{GM_{\text{tot}}(r)}{r}}, \tag{4.45}$$

where the total matter component is expressed as the sum of the baryonic components plus the dark matter one

$$M_{\text{tot}} = M_{\text{bulge}} + M_{\text{disk}} + M_{\text{gas}} + M_{\text{DM}}. \tag{4.46}$$

The contribution of the baryonic components depends on the rotation curve of each component, weighted by the mass-luminosity ratio of the bulb, disk and gas

$$V_{\text{bar}} = \sqrt{\gamma_{\text{gas}}\left|V_{\text{gas}}\right| V_{\text{gas}} + \gamma_{\text{disk}}\left|V_{\text{disk}}\right| V_{\text{disk}} + \gamma_{\text{bul}}\left|V_{\text{bul}}\right| V_{\text{bul}}}, \tag{4.47}$$

where γ_{disk} and γ_{bul} are the Mass-to-light ratios for the disk and the bulge while γ_{gas} is a parameter which takes into account the different contribution of gas. In this work, the gas contribution will be neglected on the grounds that it is very small in most cases, so we will focus on the main contributions of the baryons, the disk, and the bulge.

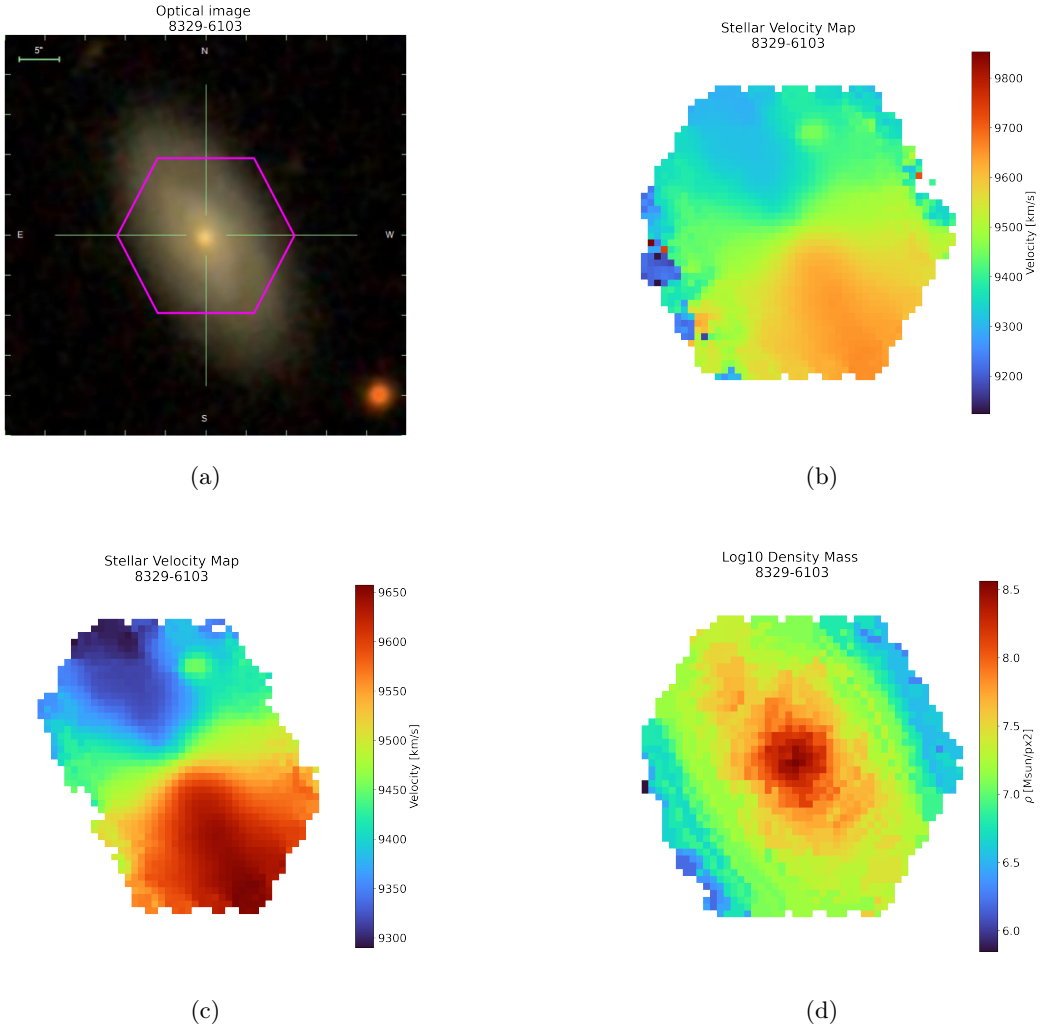

Figure 4.16: (a) The optical image of the galaxy 8329-6103. (b) the stellar velocity map before the filter. (c) The stellar velocity map once the filter and the signal-to-noise ratio threshold have been applied. (d) the density mass, we can observe the highest mass contribution is located in the galaxy's center.

According to the previous relations, the dark matter component can be expressed as

$$V_{\mathrm{DM}}^2 = V_{\mathrm{tot}}^2 - \gamma_{\mathrm{gas}} V_{\mathrm{gas}}^2 - \gamma_{\mathrm{disk}} V_{\mathrm{disk}}^2 - \gamma_{\mathrm{bulge}} V_{\mathrm{bulge}}^2. \tag{4.48}$$

In fig. 4.18 the rotation curves for the halo, disk, and bulge are shown for the galaxy we have been studying in the second part of this chapter. The black line represents the deprojected data obtained from (4.33). The error bars were calculated around 1 sigma in each radio bin. The blue line is the best fit for the data, which contains the contribution from all components. Dark matter, i.e. the halo contribution, is represented by the green line, we can see that speeds start to increase for large radii. Also, the disk is related to the dark blue line, at the beginning it has an ascending behavior, it reaches a maximum of around 2 kpc and then it begins to descend gently. For this case, the bulb, yellow line, has a negligible contribution. This is due to the fact that the value found for the mass-to-light ratio γ_b during the fitting was very small. In fact, the adjustment is very sensitive to the value of γ, so very precise values must be given in very limited ranges. In [32], fixed values for the mass-to-light ratios for baryonic components were used. Namely, $\gamma_d = 0.5 M_\odot/L_\odot$

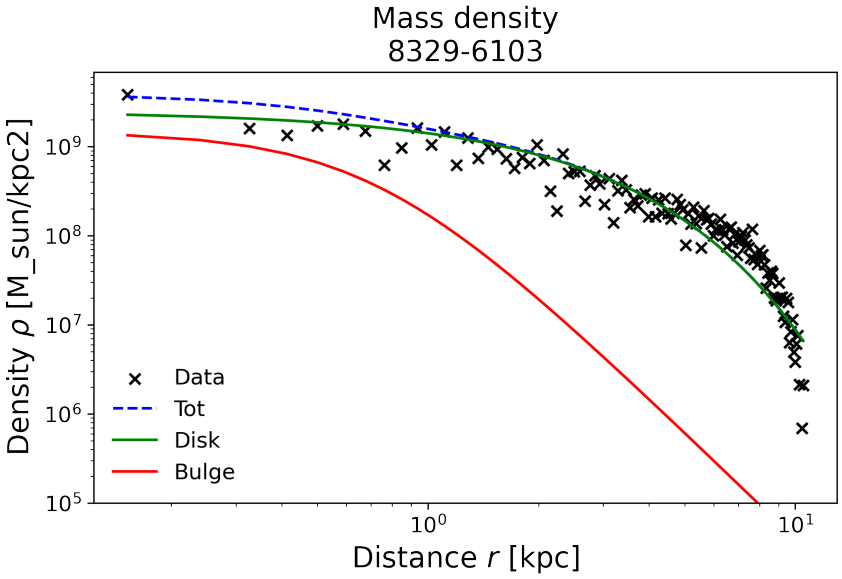

Figure 4.17: Mass density profile for the total mass (blue line), the disk (green line) and the bulge (red line) adjusted using the mass density map.

and $\gamma_b = 0.7$.

4.3 Fitting different dark matter profiles

Once the study of the rotation curve has been made from the stellar velocity maps and the baryonic components have been separated, a study will be carried out on the properties that the density profile associated with the galaxy should have. This will be a guideline for studying the properties of dark matter by considering different density profiles associated with different models. To do that, we will consider the Zhao profile (1.123) and the solitonic one (3.12) derive from the spherical approach of the Schrödinger-Poisson system.

This will allow us to carry out a statistical study based on observational data, about the characteristics of the free parameters in the density profiles, that is, α, β, γ, r_s, ρ_s for Zhao and m and r_c for the solitonic case. We can know about the most frequent values of isolated galaxies as well as those that belong to dense environments, those that are interacting, or those that are either closer or further from the observer. At the same time, this will give us tools to be able to build more realistic initial conditions when studying galaxy collisions or some other astrophysical systems such as Hickson Compact Groups of galaxies.

4.4 Conclusions

It is well known that the bulge-disk decomposition and the estimation of the total mass of galactic systems are complicated tasks that have been tackled by considering several assumptions. In the first sections of this chapter, I have presented different machine learning algorithms to estimate the mass components of the galaxies by considering cosmological simulations and Mock catalogs. In this case, the training is only considered as baryon information, the patterns it can infer from

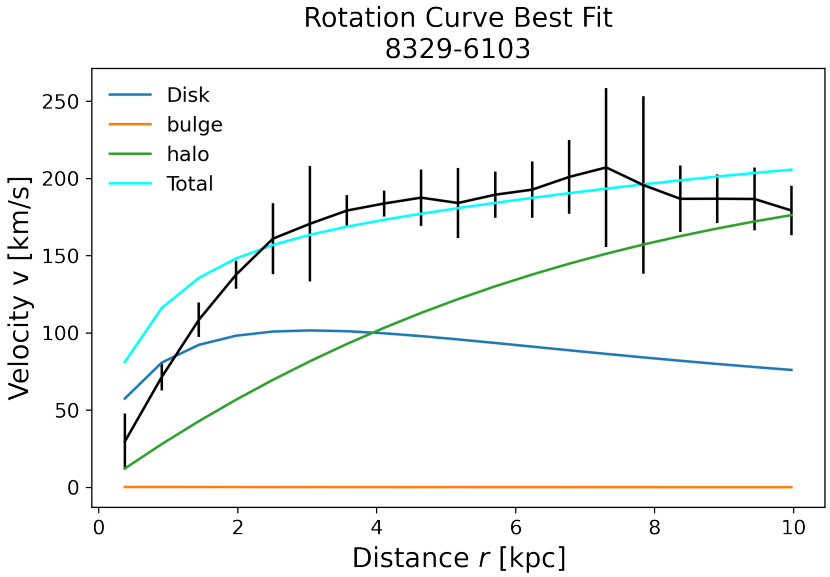

Figure 4.18: Reconstruction of the rotation curves for the galactic components. Black shows the data, blue shows the best fit to the total contribution. In green we have the rotation curve of the halo, we can see that this contribution begins to grow as the radius increases. In blue is the disk, which reaches a maximum of around 2 kpc. In this case, the fit shows a null contribution for the bulge.

the simulated data, then there are no strong considerations about baryon physics, as in the post-processing of observational data or for modeling astrophysical systems.

During the training and test stages, different algorithms not only provided the expected predictions for masses of different galaxy components but they were capable to single out scaling relations between different galaxy parameters. By using as input various magnitudes in the ugriz-photometric system, the trained IA algorithms achieved a great improvement over classical linear scale relations for stellar mass components in galaxies from different datasets. Furthermore, these methods provide good predictions of the total mass of galaxies in the sample. Moreover, the trained IA methods were used to predict masses of different components of real galaxies by means of observational data. Parameters of galaxies from SDSS hold higher values, namely, magnitudes and masses.

In the second part of the chapter, an analysis of the kinematic properties of the SDSS galaxies was carried out. In fact, the construction of rotation curves from spectroscopic data is essential and irreplaceable for the study of dark matter properties, although numerous considerations must be made in data post-processing. For that reason, it is usually complicated due to the high sensitivity of the adjustment parameters, which is why fairly precise methods must be designed in order to obtain reliable results. In this case, an MCMC method has been implemented to deproject the stellar velocity map data and thus build the rotation curve. To obtain the stellar components, it is necessary to use the density map and take into account the weights that the mass-to-light ratios contribute to the total mass density. This project is still under development, and it is planned to study the statistics of the density profiles, one of purely empirical origin, the Zhao profile, and the other that comes from the stationary solution that describes the scalar dark matter system. It is also intended to observe the influence of the environment on the dynamics of dark matter and itself on the rotation curves and associated density profiles. All this will help us to build more realistic initial conditions when carrying out numerical simulations of astrophysical systems, such

as individual galaxies, groups of galaxies, and large clusters.

Bibliography

[1] Edwin Hubble. A relation between distance and radial velocity among extra-galactic nebulae. *Proceedings of the national academy of sciences*, 15(3):168, 1929.

[2] E. Holmberg. A photographic photometry of extragalactic nebulae. *Meddelanden fran Lunds Astronomiska Observatorium Serie II*, 136:1, January 1958.

[3] S.M. Kent. CCD surface photometry of field galaxies. II. Bulge/disk decompositions. *Astrophysical Journal Series*, 59:115–159, October 1985.

[4] John Kormendy and Ralf Bender. A proposed revision of the hubble sequence for elliptical galaxies. *The Astrophysical Journal*, 464(2):L119, 1996.

[5] Ivan R. King. The structure of star clusters. III. Some simple dynamical models. *Astrophysical Journal*, 71:64, February 1966.

[6] Gerard de Vaucouleurs. Recherches sur les Nebuleuses Extragalactiques. *Annales d'Astrophysique*, 11:247, January 1948.

[7] Y. C. Andredakis, R. F. Peletier, and M. Balcells. The shape of the luminosity profiles of bulges of spiral galaxies. *Monthly Notices of the Royal Astronomical Society*, 275(3):874–888, 08 1995.

[8] Kenneth C Freeman. On the disks of spiral and s0 galaxies. *Astrophysical Journal, vol. 160, p. 811*, 160:811, 1970.

[9] Martha Tabor, Michael Merrifield, Alfonso Aragón-Salamanca, Amelia Fraser-McKelvie, Thomas Peterken, Rebecca Smethurst, Niv Drory, and Richard R Lane. SDSS-IV MaNGA: full spectroscopic bulge-disc decomposition of MaNGA early-type galaxies. *Monthly Notices of the Royal Astronomical Society*, 485(2):1546–1558, 02 2019.

[10] E. J. Johnston, A. Aragón-Salamanca, M. R. Merrifield, and A. G. Bedregal. Spectroscopic bulge–disc decomposition: a new method to study the evolution of lenticular galaxies. *Monthly Notices of the Royal Astronomical Society*, 422(3):2590–2599, 05 2012.

[11] Enrico M Di Teodoro, Lorenzo Posti, Patrick M Ogle, S Michael Fall, and Thomas Jarrett. Rotation curves and scaling relations of extremely massive spiral galaxies. *Monthly Notices of the Royal Astronomical Society*, 507(4):5820–5831, sep 2021.

[12] John Kormendy and S Djorgovski. Surface photometry and the structure of elliptical galaxies. *Annual review of astronomy and astrophysics*, 27(1):235–277, 1989.

[13] Gabriella Lucia. Lighting up dark matter haloes. *Galaxies*, 7:56, 05 2019.

[14] Volker Springel, Simon DM White, Giuseppe Tormen, and Guinevere Kauffmann. Populating a cluster of galaxies–i. results at z= 0. *Monthly Notices of the Royal Astronomical Society*, 328(3):726–750, 2001.

[15] Ralph S Sutherland and Michael A Dopita. Cooling functions for low-density astrophysical plasmas. *The Astrophysical Journal Supplement Series*, 88:253–327, 1993.

[16] Qi Guo, Simon White, Cheng Li, and Michael Boylan-Kolchin. How do galaxies populate dark matter haloes? *MNRAS*, 404(3):1111–1120, May 2010.

[17] Philip F. Hopkins, Kevin Bundy, Darren Croton, Lars Hernquist, Dusan Keres, Sadegh Khochfar, Kyle Stewart, Andrew Wetzel, and Joshua D. Younger. Mergers and Bulge Formation in LCDM: Which Mergers Matter? *Astrophysical Journal*, 715(1):202–229, May 2010.

[18] Qi Guo, Simon White, Michael Boylan-Kolchin, Gabriella De Lucia, Guinevere Kauffmann, Gerard Lemson, Cheng Li, Volker Springel, and Simone Weinmann. From dwarf spheroidals to cD galaxies: simulating the galaxy population in a LCDM cosmology. *MNRAS*, 413(1):101–131, May 2011.

[19] R. G. Bower, A. J. Benson, R. Malbon, J. C. Helly, C. S. Frenk, C. M. Baugh, S. Cole, and C. G. Lacey. Breaking the hierarchy of galaxy formation. *Monthly Notices of the Royal Astronomical Society*, 370(2):645–655, 06 2006.

[20] Gabriella De Lucia and Jérémy Blaizot. The hierarchical formation of the brightest cluster galaxies. *MNRAS*, 375(1):2–14, February 2007.

[21] Volker Springel, Carlos S. Frenk, and Simon D. M. White. The large-scale structure of the universe. *Nature*, 440(7088):1137–1144, apr 2006.

[22] Volker Springel, Simon D. M. White, Adrian Jenkins, Carlos S. Frenk, Naoki Yoshida, Liang Gao, Julio Navarro, Robert Thacker, Darren Croton, John Helly, John A. Peacock, Shaun Cole, Peter Thomas, Hugh Couchman, August Evrard, Jörg Colberg, and Frazer Pearce. Simulations of the formation, evolution and clustering of galaxies and quasars. *Nature*, 435(7042):629–636, June 2005.

[23] Gabriella De Lucia, Volker Springel, Simon D. M. White, Darren Croton, and Guinevere Kauffmann. The formation history of elliptical galaxies. *Monthly Notices of the Royal Astronomical Society*, 366(2):499–509, 02 2006.

[24] David W. Hogg, Michael R. Blanton, Jarle Brinchmann, Daniel J. Eisenstein, David J. Schlegel, James E. Gunn, Timothy A. McKay, Hans-Walter Rix, Neta A. Bahcall, J. Brinkmann, and Avery Meiksin. The dependence on environment of the color-magnitude relation of galaxies. *The Astrophysical Journal*, 601(1):L29–L32, jan 2004.

[25] S. Barsanti, M. S. Owers, R. M. McDermid, K. Bekki, J. J. Bryant, S. M. Croom, S. Oh, A. S. G. Robotham, N. Scott, and J. van de Sande. The colors of bulges and disks in the core and outskirts of galaxy clusters. *The Astrophysical Journal*, 911(1):21, apr 2021.

[26] Abdurro'uf, Katherine Accetta, and et al. Aerts. The Seventeenth Data Release of the Sloan Digital Sky Surveys: Complete Release of MaNGA, MaStar, and APOGEE-2 Data. *Astrophysical Journal Series*, 259(2):35, April 2022.

[27] R. Brent Tully, Michael J. Pierce, Jia-Sheng Huang, Will Saunders, Marc A. W. Verheijen, and Peter L. Witchalls. Global extinction in spiral galaxies. *The Astronomical Journal*, 115(6):2264–2272, jun 1998.

[28] J. T. Mendel, L. Simard, M. Palmer, S. L. Ellison, and D. R. Patton. VizieR Online Data Catalog: SDSS bulge, disk and total stellar mass estimates (Mendel+, 2014). *VizieR Online Data Catalog*, page J/ApJS/210/3, January 2014.

[29] Peter Schneider. *Extragalactic Astronomy and Cosmology.* Springer Berlin Heidelberg, Berlin, Heidelberg, 2006.

[30] The Astropy Collaboration. Astropy: A community python package for astronomy. *Astronomy and Astrophysics*, 558:A33, 2013.

[31] Yongmin Yoon, Changbom Park, Haeun Chung, and Kai Zhang. Rotation curves of galaxies and their dependence on morphology and stellar mass. *The Astrophysical Journal*, 922(2):249, dec 2021.

[32] Federico Lelli, Stacy S. McGaugh, and James M. Schombert. Sparc: Mass models for 175 disk galaxies with spitzer photometry and accurate rotation curves. *The Astronomical Journal*, 152(6):157, nov 2016.

Chapter 5

Conclusions and perspectives

In this work, the properties of dark matter in different astrophysical systems have been studied through cosmological simulations, small-scale simulations, and observations. We have seen that the dynamics of formation and evolution are determined by the nature of the dark matter candidate, then its properties can be constrained through observations.

For the cosmological part, the GDM model has been explored. Within this theoretical framework, the dark matter corresponds to a general fluid with non-vanishing sound speed c_s, viscosity $c_{\rm vis}$, and equation of state w. Specifically, three different scenarios have been studied, giving specific values to the free parameters close to CDM. As a result, the free-streaming of dark matter linear perturbations gives rise to a cut-off in the matter power spectrum on small scales. the GDM I model shows a more subtle cut-off compared to GDM III. This behavior in the power spectrum is also reflected in the growth of structures at small and medium scales. Indeed, a lower count of halos and galaxies is observed, and this effect becomes more pronounced at higher redshifts. The stellar mass functions obtained were compared with the mass function of galaxies observed by the Spitzer telescope. The GDM I and GDM II scenarios show a better fit for small scales halos in both the halo and stellar mass functions compared to CDM. In some regions, a better match is observed for one model or the other. However, GDM III falls well below the observations. Since this model was built with values a little further from those of CDM, therefore, in order to fall within the error bars of the observed mass functions, very small values of the free parameters are needed.

Subsequently, the effect of the different GDM models on the formation and evolution of Hickson Compact Groups was studied. First, the compact groups identified in the GDM III model have more massive members than those found in the rest of the models, in fact, CDM has the lightest member galaxies, followed by GDM I and GDM II. The main relevance of this criterion is that there are different galaxy clustering mechanisms in different models, in this work we identified self-agglomeration (mainly for CDM) and clustering induced by a falling into a dominant gravitational potential well (as in GDM III). Additionally, the analysis was performed by considering $N = 3$ and $N = 4$ members of HCG. An interesting result is that, when the standard algorithm of classification with $N = 4$ is used, a larger amount of HCG is counted in the GDM I simulation in comparison to CDM even though the first one has less structure. Also, GDM II has a very close number of groups to CDM. However, GDM III shows a very small number since the beginning of the classification. This indicates that despite the reduced presence of small structures, HCGs can proliferate. This suggests the need for modifications in either the characteristics of field galaxy populations or the clustering behavior of these galaxies to form HCGs. These modifications are particularly relevant in models where the dark matter component is not entirely cold or exhibits some degree of viscosity within the fluid limit. This may be related to the problem that compact groups present, since, due to their very active dynamics, it would be expected to have fewer clusters than currently observed.

Next, a small-scale study was carried out to study the dynamics of different systems in detail. For this case, the SFDM model has been considered. This model has become popular in recent decades, then, the investigation regarding the dynamics of halos and their comparison at the observational level continues nowadays. Here, different examples have been presented, some of them already mentioned in the literature, through the implementation of a new Adaptive Moving Mesh Method. It was shown the ability of the method to provide adaptability to the numerical resolution to desired high-density regions in the physical domain. Particularly, a simple but fairly complex scenario, a configuration embedded inside a soliton halo was studied. The goal was to monitor the development of a configuration that acted as a subhalo on a galactic scale in the context of SFDM (Scalar Field Dark Matter). This configuration experienced a disrupting effect due to the gravitational forces exerted by a host halo. The main achievement was to track the evolution of a configuration playing the role of a galactic-sized SFDM-subhalo suffering a disrupting effect produced by the gravity of a host halo. The main conclusion was that the largest the angular momentum the stronger disruption of the subhalo and there are two possible fates of the subhalo after being disrupted: it remains bounded or it is dissolved into the host.

Additionally, different examples of configurations have been made in both CDM and SFDM.

With this, it is intended to find the differences in both density profiles, and the virialization process, when equivalent initial conditions are established. For this, the Zhao profile was parameterized to find the values of the parameters that best describe the soliton profile. Once this has been done, the Jeans equation is solved to stabilize the system. Therefore, both models start from stable configurations before evolving. In general, all SFDM collisions show interference patterns due to the wave nature of the scalar field. In addition, more violent and dispersed interactions are shown given the pressure effects of the system. Nevertheless, the result of the collision is similar for both models, that is, they merge with a certain initial velocity, and they manage to separate if that velocity is higher. This type of simulation will continue to be studied but impose more realistic initial conditions that try to emulate astrophysical systems. For this, an analysis of the observed galaxy rotation curves must be carried out to adjust density profiles, and with it find the best value for the mass of the boson. It is also planned to simulate density profiles that fit a certain type of galaxies, for this it would not only be enough to use the soliton profile, but an NFW-type tail would have to be added, in order to work on the external part of the halo. In short, in order to be able to perform more sophisticated initial conditions, it is necessary to explore the observational systems and their dynamics.

To analyze the observational part it is necessary to also separate also the baryons, since the properties of dark matter are inferred through the dynamics of luminous matter. First, a neural network has been built and trained with synthetic catalogs of galaxies from a cosmological simulation to estimate the mass of galactic components. We observe that the predictions are good and manage to reproduce some scale relationships that are commonly studied in the literature, such as magnitude-mass, bulge-disk decomposition, and halo abundance matching. That is, the neural network recognizes patterns between baryons and dark matter. This represents an alternative to investigate even more about the properties of dark matter. Because, on one hand, at the observational level, the processing of galaxy data turns out to be complicated and several properties of baryons must be assumed. On the other hand, carrying out simulations with baryons requires the implementation of baryonic processes such as feedback, star formation rate, and ionization, which depend on numerous parameters, which is why they will affect the properties of dark matter. For the artificial intelligence case, although a simulation is needed for the training phase, the inferences made and the possible extrapolations in ranges of the features beyond those trained, are no longer rigorously imposed by the restrictions of baryon physics that other methods have.

Additionally, a study of the rotation curves with observed disk galaxies of the MaNGA project was carried out. For that, it is essential to first perform the bulge-disk decomposition. There lies the importance of working correctly on the properties of the baryons since the resulting component of dark matter depends on it. From the rotation curves inferred from the observations, density profiles can be fitted. The form that they take, again depends on the features of dark matter. For the adjustment of the rotation curve, the mass-to-light ratios for disk and bulge must be considered. They change the height of the baryon rotation curve, which implies that in the density profiles, the disk and the bulge can have different contributions. Something worth mentioning is that velocity maps only show information for very small radii around 10 to 15 kpc, which is why regular density profiles are needed. These models such as SFDM have a flattened profile in the center. It also adjusts for γ close to zero in the Zhao profile. However, it is a challenge to match the information coming from cosmological simulations, where the halos are very extended. In addition, the fact that the range of radios is very limited to the center makes it difficult to adjust, contrary to what would be obtained with larger radii. Therefore, the range where the parameters can vary in the Monte Carlo method must also be limited.

Finally, as a perspective, it is planned to simulate Hickson Compact Groups at small scales, considering two types of initial conditions, the first obtained from cosmological simulations and the second from density profiles derived from observed rotation curves. With this, we will continue exploring the dynamics of these agglomerations and particularly in the crossing time, the virialization, and the behavior of the velocity dispersion. Additionally, it is intended to study how the environment influences the evolution of these systems, on both small and large scales.

Appendix A

Some conditions for the ics in cosmological simulations

The initial conditions of a cosmological simulation are built from the power spectrum obtained from the linear theory. Therefore, the parameters that describe this simulation must be selected such that the initial condition remains in the same regime. Below are some of the conditions that must be imposed.

- **The Boxsize.** There is a maximum of this parameters above which thins become problematic. If one appriaches this size, of the order of $\sim Gpc/h$, then, the horizon at high redshift is exceeded, and gets deviations from Newtonian theory on the largest scales.

  On the contrary, if the boxsize is too small, then the largest wavelength contained in the box (the so-called fundamental mode) becomes non-linear at a certain redshift. From that point on, the box cannot be considered representative for the Universe any more, and one will get distortions of the subsequent growth history of objects. In fact, if there are $N^{1/3}$ particles positioned along one side of the box, the wavelenght is

  $$\lambda = \frac{2L}{N^{1/3}}. \tag{A.1}$$

  For the fundamental mode to remain in the linear regime, it must be true that

  $$1 = \frac{1}{2\pi^2}\int_0^{k_{\rm nl}} P(k, z=0)k^2 dk. \tag{A.2}$$

  As a consequence, the boxsize must be $L \leq \frac{2\pi}{k_{\rm nl}}$. The value of the boxsize when this becomes an issue depends on the final redshift of the simulation. If the simulation is stopped at high redshift (for instance $z = 20$) even $L = 1{\rm Mpc}/h$ can still be viable. But if the simulation runs down to z=0, then $L >\sim 30{\rm Mpc/h}$.

- **k-limits** The values for $k_{\rm min}$ and $k_{\rm max}$ for the matter power spectrum should meet some conditions as well. Then,

  $$k_{\rm min} = \frac{2\pi}{L}, \quad k_{\rm max} = k_{\rm min}\frac{N_{\rm tot}}{2}. \tag{A.3}$$

  Here kmax is the Nyquist frequency, assuming $N^3_{\rm tot}$ is the total particle number.

Appendix B

The DBSCAN algorithm

DBSCAN is an algorithm designed to identify overdensities in clusters of data, considering a small number of parameters. In fact, the method depends on two main parameters, the maximum distance between members ϵ, which specifies how close the points can be to be considered part of the cluster. The ϵ-neighborhodd of a point x as

$$N_\epsilon(\mathbf{x}) = |\mathbf{y} \in D : d(\mathbf{x}, \mathbf{y}) \leq \epsilon|. \tag{B.1}$$

This means that if the distance between two points is less than or equal to ϵ, these points will be considered as neighbors. On the other hand, the minimum number of points N is required to consider a region as dense.

Fig. B.1 shows the parameters which determinate the form in which DBSCAN works.

Density relations

- A point $\mathbf{x}$, contained within the set of point, is considered *density reachable* (DR), if the following criteria are fulfilled

$$\begin{aligned} \mathbf{x} &\in N_\epsilon(\mathbf{y}) \\ |N_\epsilon(\mathbf{y})| &\leq N \end{aligned} \tag{B.2}$$

  where $|N_\epsilon(\mathbf{y})|$ denotes the number of points in $N_\epsilon(\mathbf{y})$.

- Additionally, a point $\mathbf{x}$ is considered *directly density-reachable* from a core-point $\mathbf{y}$ if $\mathbf{y}$ lies within the neighborhood of $\mathbf{x}$,

$$\begin{aligned} \mathbf{x} &\in N_\epsilon(\mathbf{y}) \\ \text{Core}(\mathbf{y}) & \end{aligned} \tag{B.3}$$

- Two points $\mathbf{x}$ and $\mathbf{y}$ are called density connected, if there is a third point $\mathbf{r}$ such that $\mathbf{r}$ can be density-reach $\mathbf{x}$ and $\mathbf{y}$. Two border points can be density-connected, even though they are not density-reachable by definition due to not fulfilling the core point criteria.

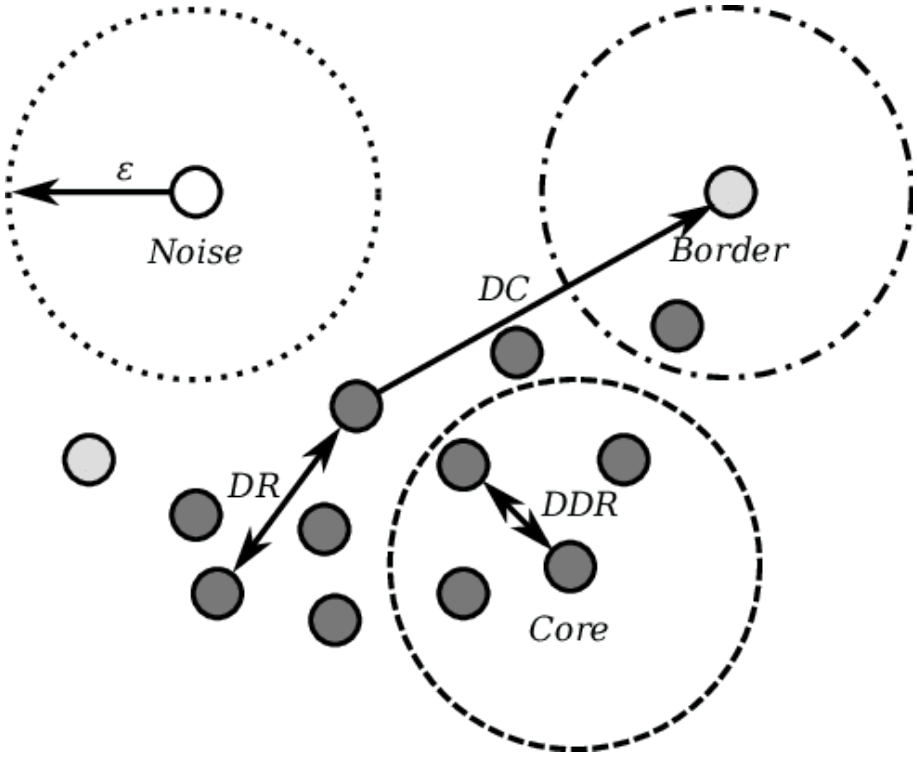

Figure B.1: DBSCAN scheme. The hollow point corresponds to a noise one, that is, it does not belong to any overdensity region because it is isolated from the rest of the points by a distance greater than ϵ. In this example $N_{\min} = 4$, as it can be seen in the down circle.

Appendix C

Numerical methods: Adaptive moving mesh refinement method

For a general description of the method, consider an Initial Value Problem (IVP) formulated within the domain $\Omega \subset \mathbb{R}^3 \times t \in [0, t_f] \subset \mathbb{R}$, for the unknown $u = u(\boldsymbol{x}), t$, $\boldsymbol{x} \in \mathbb{R}^3$, whose evolution equation reads

$$u_t + \nabla \cdot \boldsymbol{f} = \nabla \cdot (a \nabla u) + s, \tag{C.1}$$

with appropiate initial conditions $u(\boldsymbol{x}, 0)$ and boundary conditions $u(\partial\Omega, t)$ for u, and unknown functions a, s and $\boldsymbol{f}$. The solution can be obtained by discretizing the problem on a discrete domain and employing an evolution method. This involves using specific finite differentiation schemes to approximate the spatial operators that act on fluxes, the parabolic term, and the sources. By integrating this discrete version of the problem, we can obtain the desired solution.

Mesh Refinement is motivated by the need for accuracy in certain regions of the domain where the solution function u is possibly developing structure or important features to the problem in turn. Particularly, the Adaptive Moving Mesh refinement method needs for accuracy in certain region of the spatial domain Ω_d it uses the a different approach, instead of defining new discrete sub-domains with higher resolutions as Mesh Refinement methods do, it redefines the equation associated with the IVP in terms of new coordinates.

Here, we can distinguish between two domains, the logical $\Omega_L = \{(\xi_i, \eta_i, \kappa_k)\}$ where the set of points is uniformly distributed, and the physical $\Omega_P = \{(x, y, z)\}$, where the discretization is not necessarily uniform. With this in mind, the nabla operator in the physical domain, written in terms of the logical coordinates is expresssed in two possible forms

$$\nabla = \sum_i \boldsymbol{a}^i \frac{\partial}{\partial \xi_i} \quad \text{non-conservative,} \tag{C.2}$$

$$= \frac{1}{J} \sum_i \frac{\partial}{\partial \xi_i} J \boldsymbol{a}^i \quad \text{conservative,} \tag{C.3}$$

where $J = \det\{\mathcal{J}\}$. Here, $\mathcal{J}$ is defined in terms of the a_i vectors by means of

$$\mathcal{J} = [\boldsymbol{a}_1, \boldsymbol{a}_2, \boldsymbol{a}_3], \quad \mathcal{J}^{-1} = \begin{bmatrix} (\boldsymbol{a}^1)^T \\ (\boldsymbol{a}^2)^T \\ (\boldsymbol{a}^3)^T. \end{bmatrix} \tag{C.4}$$

Here, we have

$$\boldsymbol{a}_i = \frac{\partial \boldsymbol{x}}{\partial \xi_i}, \quad \boldsymbol{a}^i = \nabla \xi_i. \tag{C.5}$$

The parabolic term in Eq. (C.1) involves second order derivatives and can be calculated using (C.2) as follows

$$\nabla \cdot (a \nabla u) = \frac{1}{J} \sum_{i,j} \frac{\partial}{\partial \xi_i} \left(a J \boldsymbol{a}^i \cdot \boldsymbol{a}^j \frac{\partial u}{\partial \xi_j} \right). \tag{C.6}$$

The method becomes Adaptive-Moving if the transformation depends on time, in which case the coordinate transformation reads $\boldsymbol{x} = \boldsymbol{x}(\xi, t)$, and then (C.1) is modified as

$$u_t = \dot{u} - \nabla u \cdot \dot{x}. \tag{C.7}$$

A popular choice for $\dot{x}$ is the so-called *adaptative moving mesh partial differential equation* given by

$$\dot{\boldsymbol{x}} = \frac{1}{\tau} \nabla_\xi \cdot (\rho \nabla_\xi \boldsymbol{x}), \tag{C.8}$$

where τ controls the mesh speed of response. With equations (C.6) and (C.7) it is possible to rewrite the expressions for the Schrödinger equation for a general change of coordinates. Here, $\rho = |\omega|^{3/2}$ is known as the mesh density. This function can take different forms and the choice depends on the Partial Differential Equation (PDE) to be solved. For illustration two possible expressions will be consider

$$\omega = \omega_1 = \sqrt{1 + \alpha v^2}, \tag{C.9}$$

$$\omega = \omega_1 = \sqrt{1 + \alpha |\nabla_\xi v|^2}, \tag{C.10}$$

where α parameter regulates the mesh strees through the function v. Again, for illustration let's consider the followins relations

$$v(x, y, z) = v_1 = \exp\{-(5x^2 + 7y^2 - 1)^2/10\}, \tag{C.11}$$

$$v(x, y, z) = v_2 = \exp\{-10(y - x^2 + 0.5)^2\} \tag{C.12}$$

The physical domain mesh obtained by using the four combinations of ω_1, ω_2, v_1, v_2 is shown in Fig. C.1

A particular setup useful to solve the SP system uses functions v and ω that concentrate a nearly constant high resolution at the center of the domain and a constant coarse resolution in the outskirts. A function v that helps this purpose, is the following

$$v = A \left(2 + \tanh\left(\frac{R - r_c}{\delta} \right) - \tanh\left(\frac{r_c}{\delta} \right) \right). \tag{C.13}$$

The results for $\omega = \omega_1$, ω_2 $R = \sqrt{x^2 + y^2 + z^2}$, 2.7, $r_c = 15$, $\delta = 1$, on the physical domain $[-20.8, 20.8]^3$, discretized with $N_\xi = N_\eta = N_\kappa = 104$ cells along each direction is shown in Fig. C.2.

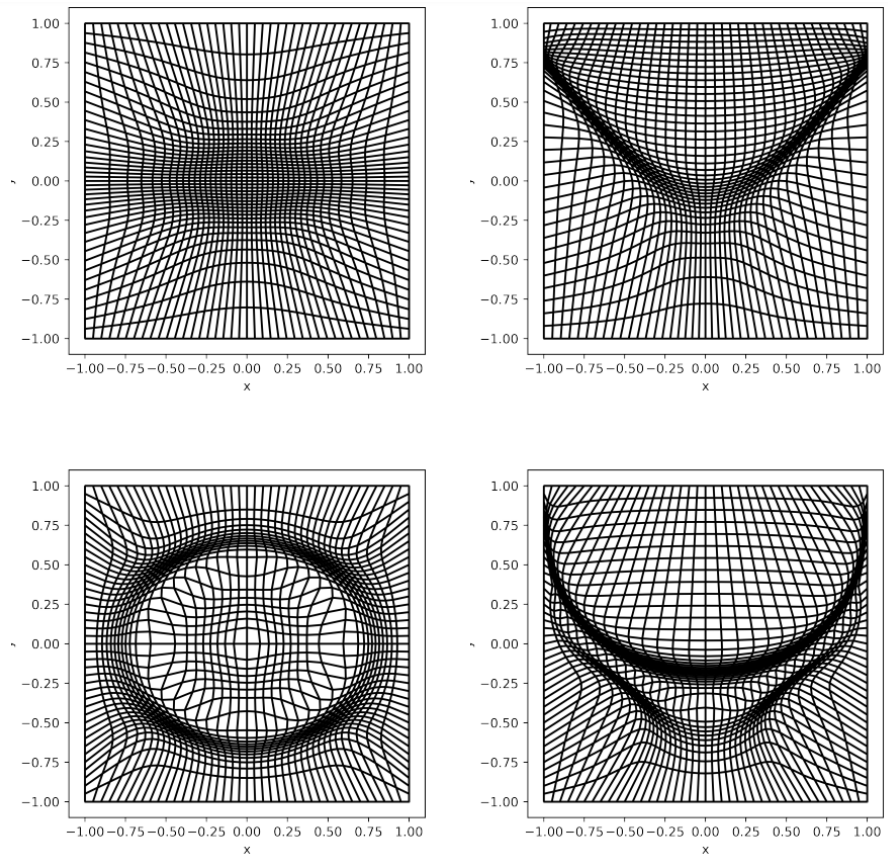

Figure C.1: Physical mesh in the $\kappa = 0$ plane for the four combinations of ω_1, ω_2, v_1, v_2. At the top we show the two combinations for ω_2, at the bottom the cases for ω_2, at the left column the cases v_1 and at the right those for v_2. For these meshes we fix the parameter $\alpha = 100$.

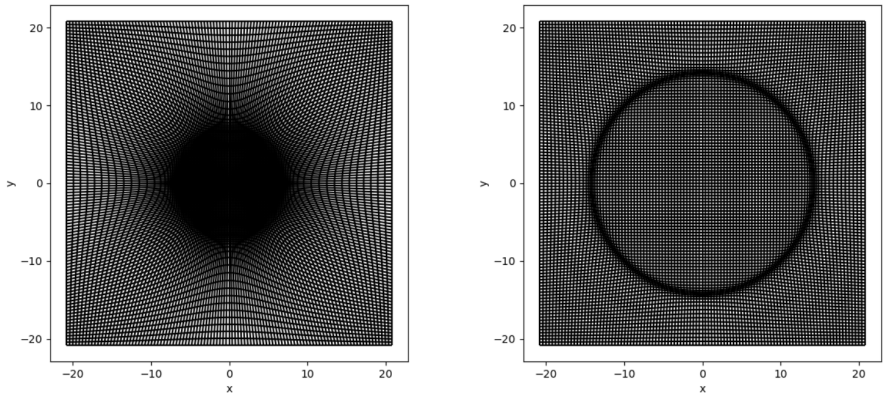

Figure C.2: Example of a physical domain projected at $\kappa = 0$. At the left we show the result for $\omega = \omega_1$ which defines a region with high resolution ~ 0.2 in the center and a coarse resolution near the boundary of ~ 0.4. At the right we show the result for $\omega = \omega_2$ that defines a spherical shell of high resolution.